

TECHNICAL DIGEST

1 9 9 5

# SEMICONDUCTOR LASERS

## ADVANCED DEVICES AND APPLICATIONS

AUGUST 21-23, 1995  
KEYSTONE, COLORADO

1995 TECHNICAL DIGEST SERIES  
VOLUME 20

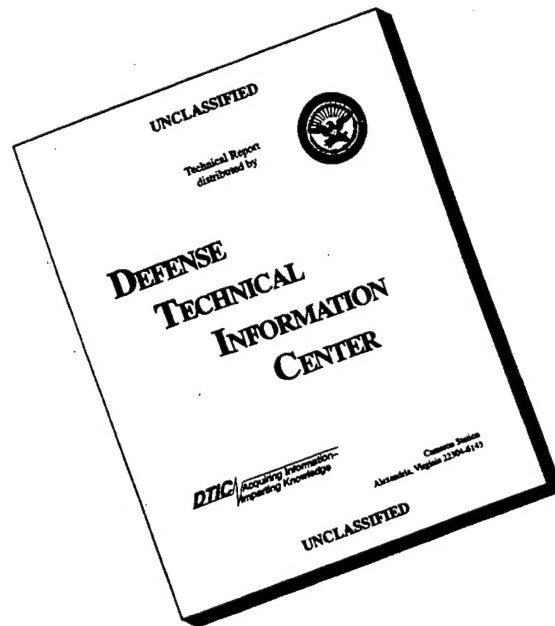
COSPONSORED BY  
OPTICAL SOCIETY OF AMERICA



IEEE/LASERS AND ELECTRO-OPTICS SOCIETY

DISTRIBUTION STATEMENT A  
Approved for public release;  
Distribution Unlimited

# DISCLAIMER NOTICE



**THIS DOCUMENT IS BEST QUALITY AVAILABLE. THE COPY FURNISHED TO DTIC CONTAINED A SIGNIFICANT NUMBER OF PAGES WHICH DO NOT REPRODUCE LEGIBLY.**

CONFERENCE EDITION

1 9 9 5

*Summaries of the papers  
presented at the topical meeting*

# SEMICONDUCTOR LASERS

## ADVANCED DEVICES AND APPLICATIONS

August 21–23, 1995  
Keystone, Colorado

1995 Technical Digest Series  
Volume 20

COSPONSORED BY  
OPTICAL SOCIETY OF AMERICA



IEEE/LASERS AND  
ELECTRO-OPTICS SOCIETY

Optical Society of America  
2010 Massachusetts Avenue NW  
Washington DC 20036-1023

**DISTRIBUTION STATEMENT A**

Approved for public release;  
Distribution Unlimited

Articles in this publication may be cited in other publications. To facilitate access to the original publication source, the following form for the citation is suggested:

Name of Author(s), "Title of Paper," in *Coherent Laser Radar*, Vol. 19, 1995 OSA Technical Digest Series (Optical Society of America, Washington DC, 1995), pp. xx-xx.

Optical Society of America

ISBN

Conference Edition	1-55752-407-6
Postconference Edition	1-55752-408-4
(Note: Postconference Edition includes postdeadline papers.)	
1995 Technical Digest Series	1-55752-368-1

Library of Congress Catalog Card Number

Conference Edition	95-68684
Postconference Edition	95-68685

Copyright © 1995, Optical Society of America

Individual readers of this digest and libraries acting for them are permitted to make fair use of the material in it, such as to copy an article for use in teaching or research, without payment of fee, provided that such copies are not sold. Copying for sale is subject to payment of copying fees. The code 1-55752-368-1/95/\$6.00 gives the per-article copying fee for each copy of the article made beyond the free copying permitted under Sections 107 and 108 of the U.S. Copyright Law. The fee should be paid through the Copyright Clearance Center, Inc., 21 Congress Street, Salem, MA 01970.

Permission is granted to quote excerpts from articles in this digest in scientific works with the customary acknowledgment of the source, including the author's name and the name of the digest, page, year, and name of the Society. Reproduction of figures and tables is likewise permitted in other articles and books provided that the same information is printed with them and notification is given to the Optical Society of America. In addition, the Optical Society may require that permission also be obtained from one of the authors. Address inquiries and notices to Director of Publications, Optical Society of America, 2010 Massachusetts Avenue, NW, Washington, DC 20036-1023. In the case of articles whose authors are employees of the United States Government or its contractors or grantees, the Optical Society of America recognizes the right of the United States Government to retain a nonexclusive, royalty free license to use the author's copyrighted article for United States Government purposes.

Printed in the U.S.A.



## Contents

Agenda of Sessions .....	v
<b>MA</b> High Speed Communications .....	1
<b>MB</b> Spectroscopic Applications .....	15
<b>MC</b> High Power Lasers: Applications and Devices .....	35
<b>TuA</b> Novel-Function Devices .....	49
<b>TuB</b> Lidar Applications .....	63
<b>TuC</b> High Brightness Lasers .....	79
<b>TuD</b> Vertical-Cavity Lasers .....	99
<b>TuE</b> Poster Session .....	123
<b>WA</b> Telecommunications Lasers .....	175
Key to Authors and Presiders .....	193

19960325 105

**SEMICONDUCTOR LASERS  
TECHNICAL PROGRAM COMMITTEE**

**Thomas M. Baer**, *General Chair*  
*Biometric Imaging*

**Thomas L. Koch**, *General Chair*  
*AT&T Bell Laboratories*

**Peter F. Moulton**, *Program Chair*  
*Schwartz Electro-Optics, Inc.*

**David F. Welch**, *Program Chair*  
*SDL, Inc.*

**Connie J. Chang-Hasnain**  
*Stanford University*

**P. Daniel Dapkus**  
*University of Southern California*

**Russ Dupuis**  
*University of Texas at Austin*

**Renny A. Fields**  
*Aerospace Corporation*

**Edward Gage**  
*Eastman Kodak Corporation*

**Leo William Hollberg**  
*National Institute of Standards and Technology*

**Paul Morton**  
*AT&T Bell Laboratories*

**Robert Olson**  
*Schwartz Electro-Optics, Inc.*

**John D. Ralston**  
*SDL, Inc.*

**Peter Roenpten**  
*IBM Research Division, Switzerland*

**Alan C. Stanton**  
*Southwest Sciences, Inc.*

**Wolfgang Stutius**  
*Polariod Corporation*

**Dick Williamson**  
*MIT Lincoln Laboratory*

**Mori Yoshifumi**  
*Sony Corporation, Japan*

SUNDAY

AUGUST 20, 1995

PREFUNCTION AREA

6:00pm-8:00pm

Conference Registration

MONDAY

AUGUST 21, 1995

PREFUNCTION AREA

7:00am-12:00m

Conference Registration

TORREYS PEAK I-III

8:20am-8:30am

Opening Remarks

8:30am-9:45am

**MA • High Speed Communications**

Paul A. Morton, AT&T Bell Laboratories, *Presider*

8:30am (Invited)

**MA1 • High-speed laser-based fiber-optic systems**, Radha Nagarajan, *SDL, Inc.* We discuss our progress in the implementation of high-temperature high-speed data links at both 0.98 and 1.3  $\mu\text{m}$ . (p. 2)

9:00am (Invited)

**MA2 • Strain-compensated 1.55- $\mu\text{m}$  DBR lasers for operation at high speed with low drive current**, U. Öhlander, O. Sahlén, *Ericsson Components AB, Sweden*; O. Kjebon, S. Lourdudoss, J. Wallin, K. Streubel, S. Nilsson, L. Bäckbom, *Royal Institute of Technology, Sweden*. Single-mode DBR lasers at 1.55- $\mu\text{m}$  wavelength with strain-compensation are reported with low thresholds, 1.4–1.9 mA, and high resonance frequencies, 2.7–2.9 GHz/mA<sup>1/2</sup>. (p. 5)

9:15am

**MA3 • Minimizing the operating current of quantum well lasers with modulation bandwidth and optical power requirements**, M. McAdams, B. Zhao, T. R. Chen, J. Feng, A. Yariv, *California Institute of Technology*. Analysis of the operating current of quantum well lasers shows that microcavity lasers are not favored in systems with fixed bandwidth and optical power requirements. (p. 8)

9:30am

**MA4 • Reduction of the frequency chirp of two-section distributed feedback laser without suppressing spatial hole-burning**, Jing Feng, T. R. Chen, Bin Zhao, Amnon Yariv, *California Institute of Technology*. We present experimental and theoretical studies of the reduction of the frequency chirp in a two-section DFB laser. (p. 11)

SHAVANO PEAK

9:45am-10:15am

Coffee Break/Exhibits

TORREYS PEAK I-III

10:15am-12:00m

**MB • Spectroscopic Applications**

Peter Moulton, *Schwartz Electro-Optics, Inc., Presider*

10:15am (Invited)

**MB1 • Diode lasers for industrial spectroscopy**, Alan C. Stanton, David S. Bomse, Joel A. Silver, David C. Hovde, Daniel J. Kane, Daniel B. Oh, Mark E. Paige, *Southwest Sciences, Inc.* Progress in development of visible/near-infrared diode laser-based instrumentation to address industrial gas sensing problems is reviewed. Required laser device characteristics are discussed. (p. 16)

10:45am

**MB2 • Transient molecular spectroscopy with a frequency-doubled diode laser**, R. W. Fox, L. W. Hollberg, *NIST-Boulder*; M. Hunter, NOAA. Absorption at a wavelength of 427.2 nm is used to measure transient molecular iodine-monoxide concentrations. A 150-mW injection-locked AlGaAs laser is frequency-doubled in a build-up cavity using potassium niobate, generating 40 mW. (p. 19)

11:00am

**MB3 • Stimulated Raman spectroscopy with a modulated external cavity diode laser**, C. S. Wood, S. C. Bennett, D. Cho, C. E. Wieman, *Univ. Colorado*. An external cavity diode laser was used to perform stimulated Raman spectroscopy. The current was modulated synchronously with the external cavity at 4.6 GHz to achieve the necessary frequencies. (p. 22)

11:15am

**MB4 • Tunable infrared source by difference frequency mixing diode lasers and diode-pumped YAG, and application to methane detection**, S. Waltman, L. Hollberg, *NIST-Boulder*; K. Petrov, U. Simon, F. Tittel, R. Curl, *Rice Univ.* Single-frequency, tunable infrared radiation is generated between 3.1 and 3.4  $\mu\text{m}$ . This source is used to detect methane with high sensitivity in normal air samples. Detection sensitivity is noise-limited to  $\sim 15$  ppb-m/ $\sqrt{\text{Hz}}$ . (p. 25)

11:30am

**MB5 • Tunnel-injection laser based on type II broken-gap p-GaInAsSb/p-InAs single heterojunction**, Yu. P. Yakovlev, K. D. Moiseev, M. P. Mikhailova, O. G. Ershov, A. F. Ioffe *Physical Technical Institute, Russia*. New physical approach to design of mid-IR diode laser with high operating temperature is proposed. Single-mode laser was realized at  $\lambda = 3.26 \mu\text{m}$  with high characteristic temperature  $T_0 = 60$  K at 77–120 K by using interface radiative transitions at type II broken-gap p-GaInAsSb/p-InAs heterojunction. (p. 29)

MONDAY

AUGUST 21, 1995

11:45am

**MB6 • Theoretical analysis of gain in compressive strained quantum well InAlAsSb/GaSb structures for 3–4- $\mu$ m lasers**, R. F. Nabiev, C.J. Chang-Hasnain, *Stanford Univ.*; H. K. Choi, *MIT Lincoln Laboratory*. An analysis of gain and differential gain in InAlAsSb quantum well lasers emitting between 3 and 4  $\mu$ m is presented. In compressive strained structures, the carrier density as low as  $5.5 \cdot 10^{17} \text{ cm}^{-3}$  can provide an optical gain of  $500 \text{ cm}^{-1}$ . (p. 31)

12:00m–7:00pm

**Free Time**

**PREFUNCTION AREA**

---

6:30pm–9:00pm

**Conference Registration**

**TORREYS PEAK I–III**

---

7:00pm–9:00pm

**MC • High Power Lasers: Applications and Devices**

Dick Williamson, *Massachusetts Institute of Technology*, *Presider*

7:00pm (Invited)

**MC1 • High power lasers for medical and graphic arts printing applications**, W. Stutius, L. Heath, *Polaroid Corp.* The application of high power lasers in a variety of high speed printing environments of digital image files on dry-processed non-silver halide media will be discussed. (p. 36)

7:30pm (Invited)

**MC2 • Diode-pumped solid-state lasers for high power precision machining**, Leonard J. Marabella, *TRW*. The next-generation laser machine tools, based upon diode-pumped solid-state laser technology with fiber optic beam delivery, and beam clean-up are being developed. (p. 39)

8:00pm

**MC3 • Strained-layer InGaAs-GaAs-AlGaAs buried-heterostructure lasers with nonabsorbing mirrors by selective-area MOCVD**, R. M. Lammert, G. M. Smith, D. V. Forbes, M. L. Osowski, J. J. Coleman, *Univ. Illinois*. Design, fabrication and operation of buried-heterostructure lasers with nonabsorbing mirrors fabricated by selective-area epitaxy are presented. (p. 40)

8:15pm

**MC4 • Non-imaging laser diode array beam shaper**, David Caffey, *Opto Power Corp.*; W. A. Clarkson, *Univ. Southampton, UK*. Non-imaging, multiple-bounce reflective beam shapers improve beam qualities of fiber-lensed laser diode broad stripes and bars. 15-W, 350- $\mu$ m, .2NA spots are produced. (p. 43)

8:30pm (Invited)

**MC5 • Diode laser systems for photodynamic therapy**, Daniel R. Doiron, *PDT Systems, Inc.* Engineering and design considerations for high-power diode laser systems for photodynamic therapy are reviewed and initial clinical system development presented. (p. 45)

## PREFUNCTION AREA

8:00am-5:45pm

Conference Registration

## TORREYS PEAK I-III

9:00am-10:00am

## TuA • Novel-Function Devices

Connie Chang-Hasnain, *Stanford University, Presider*

9:00am

**TuA1 • Simultaneous demultiplexing and wavelength conversion of NRZ optical signals using a side-injection-light-controlled bistable laser diode**, Takashi Kurokawa, Koji Nonaka, *NTT Opto-electronics Laboratories, Japan*. We have demonstrated optical demultiplexing of NRZ signals with simultaneous wavelength conversion using a side-injection-light-controlled bistable laser diode (SILC-BLD) module with pigtailed fibers and a monitoring pin-phodiode. (p. 50)

9:15am

**TuA2 • 4 GHz all-optical clock recovery using a self-pulsating multielectrode DFB laser**, P. Landais, G. Pham, G. H. Duan, C. Chabran, P. Gallion, *Ecole Nationale Supérieure des Télécommunications, France*; J. Jacquet, *Alcatel Alsthom Recherche, France*. 3.8-Gbit/s all-optical recovery using a self-pulsating three-section distributed feedback laser is obtained with 13 nm wavelength deviation. (p. 53)

9:30am

**TuA3 • TE/TM polarization switching with single longitudinal mode operation in GaAs/AlGaAs MQW DFB lasers**, Toshihiko Ouchi, Masao Majima, Sotomitsu Ikeda, Takeo Ono, Mamoru Uchida, Yuichi Handa, *Canon Inc. Research Center, Japan*. TE/TM polarization switching between single longitudinal modes has been successfully demonstrated in GaAs/AlGaAs MQW distributed feedback lasers with two electrodes. (p. 56)

9:45am

**TuA4 • Optical bistability and NOR-gate operation in intracavity-coupled in-plane and vertical-cavity surface-emitting lasers**, D. B. Shire, C. L. Tang, *Cornell Univ.*; M. A. Parker, *USAF Rome Laboratory*. The output power versus input power characteristic of intracavity-coupled multiple in-plane and vertical cavity surface emitting lasers shows hysteresis, leading to optical bistability and NOR-gate operation. (p. 59)

## SHAVANO PEAK

10:00am-10:30am

Coffee Break/Exhibits

## TORREYS PEAK I-III

10:30am-12:00m

## TuB • Lidar Applications

Renny Fields, *The Aerospace Corporation, Presider*

10:30am (Invited)

**TuB1 • Miniature lidar using diode lasers modulated with PN codes**, James B. Abshire, Jonathan A. R. Rall, *NASA Goddard Space Flight Center*. Diode-based lidar with pseudonoise code (PN) modulation has been previously used to remotely sense clouds and atmospheric aerosol distributions. We have developed the theory for and demonstrated both an aerosol and H<sub>2</sub>O DIAL lidar. (p. 64)

11:00am

**TuB2 • Antarctic miniature lidar**, Jonathan A. R. Rall, James B. Abshire, *NASA Goddard Space Flight Center*. A compact, laser-diode-based lidar has been installed at the NOAA Clean Air Facility at the Amundsen-Scott South Pole Station. This paper reports on the design and preliminary performance of the instrument. (p. 67)

11:15am

**TuB3 • High-power diode laser transmitter for aerosol lidar and laser ranging**, Donald M. Cornwell, Jr., Pamela S. Millar, *NASA Goddard Space Flight Center*; Anthony W. Yu, *Hughes-STX*; Gary L. Harnagel, *SDL, Inc.*; Daniel E. Hopf, *Science Systems and Applications, Inc.* A laser transmitter has been developed for lidar applications that emits a 130-mW (avg.) collimated, single-mode beam at up to 100 Mbit/s NRZ. An incorporated etalon results in single frequency operation (<0.3 nm) under large signal modulation. (p. 70)

11:30am

**TuB4 • Demonstration of high precision semiconductor laser ranging system**, Pamela S. Millar, *NASA Goddard Space Flight Center*; Kent D. Christian, *Alliedsignal Technical Services Corp.*; Christopher T. Field, *Johns Hopkins Univ.* We report on the design and preliminary performance of a continuous wave semiconductor laser ranging system for spaceflight application. (p. 73)

11:45am

**TuB5 • Semiconductor laser-based ranging instrument for earth gravity measurements**, James B. Abshire, Pamela S. Millar, *NASA Goddard Space Flight Center*; Xiaoli Sun, *Johns Hopkins Univ.* A laser ranging instrument is being developed to measure the spatial variations in the Earth's gravity field. It will range in space to a cube corner on a passive co-orbiting sub-satellite with a velocity accuracy of 20 to 50  $\mu$ m/s by using AlGaAs lasers intensity modulated at 2 GHz. (p. 76)

12:00m-1:30pm

Lunch

## TORREYS PEAK I-III

1:30pm-3:15pm

### **TuC • High Brightness Lasers**

John Ralston, *SDL, Inc.*, *Presider*

1:30pm (Invited)

**TuC1 • High-power (>1 W) semiconductor lasers**, Robert J. Lang, Ross Parke, David Mehuys, Steve O'Brien, Jo Major, Julian S. Osinski, Gary Harnagel, Frank Shum, David F. Welch, *SDL, Inc.* This talk will describe continuing advances in diffraction-limited diodes at wavelengths from 630 nm to 2  $\mu$ m including advances in tunability, fiber coupling, and more. (p. 80)

2:00pm

**TuC2 • Monolithic stable-resonator semiconductor laser**, S. A. Biellak, Y. Sun, S. Wong, A. E. Siegman, *Stanford Univ.* We report to our knowledge the first experimental results on monolithic wide stripe stable-resonator semiconductor lasers. (p. 83)

2:15pm

**TuC3 • A high-power (~2 W) external-cavity cw diode laser tunable from 960 to 980 nm**, S. Gupta, R. J. Jones, R. K. Jain, *Univ. New Mexico*; J. N. Walpole, *MIT Lincoln Laboratory*. Tunable single-longitudinal-mode operation of 960-980 nm, in a near-diffraction-limited beam, was achieved at ~1.8 W cw powers in an external-cavity diode laser using a tapered-amplifier. (p. 86)

2:30pm

**TuC4 • Spectral properties of an AlGaAs MOPA laser under large signal modulation of the oscillator or the amplifier**, Michael A. Krainak, Donald M. Cornwell, Valerie Dutto, *NASA Goddard Space Flight Center*; Anthony W. Yu, *Hughes STX Corp.*; Stephen O'Brien, *Spectra Diode Laboratories*. We report the performance of an AlGaAs monolithic flared amplifier (MFA-MOPA) laser with large signal modulation applied to the master oscillator or power amplifier. (p. 89)

2:45pm

**TuC5 • Beam propagation model of tapered amplifiers including nonlinear gain and carrier diffusion**, P. Chazan, *Fraunhofer-Institut für Angewandte Festkörperphysik, Germany*; J. D. Ralston, *SDL, Inc.* A FD-BPM model is used to simulate filamentation in tapered amplifiers. Improved beam quality is expected by reducing the  $\alpha$ -factor using advanced epitaxial layer structures. (p. 92)

3:00pm

**TuC6 • Operating characteristic simulation of high-power broad-stripe quantum-well semiconductor traveling wave amplifiers**, Zheng Dai, Rainer Michalzik, Peter Unger, *Univ. Ulm, Germany*. Nonlinear material properties under large current injection condition and residual facet reflectivities are found to significantly influence the operation characteristics of semiconductor traveling wave amplifiers. (p. 95)

## SHAVANO PEAK

3:15pm-3:45pm

*Coffee Break/Exhibits*

## TORREYS PEAK I-III

3:45pm-5:45pm

### **TuD • Vertical-Cavity Lasers**

Thomas M. Baer, *Biometric Imaging, Presider*

3:45pm

**TuD1 • Blue-green electron-beam-pumped VCSEL using MBE grown modulated ZnCdSe/ZnSe superlattice**, N. G. Basov, V. I. Kozlovsky, A. B. Krysa, A. S. Nasibov, Yu. M. Popov, P. N. Lebedev *Physical Institute, Russia*; E. M. Dianov, A. M. Prokhorov, P. A. Trubenko, E. A. Shcherbakov, *The General Physics Institute, Russia*. Room-temperature operation of the VCSEL ( $\lambda = 484$  nm) with the threshold current density of 60 A/cm<sup>2</sup> based on the MBE grown modulated Zn<sub>0.88</sub>Cd<sub>0.12</sub>Se/ZnSe superlattice has been demonstrated under scanning electron-beam pumping. (p. 100)

4:00pm

**TuD2 • 1.5- $\mu$ m vertical-cavity surface-emitting lasers**, M. A. Fisher, Y.-Z. Huang, A. J. Dann, D. J. Elton, M. J. Harlow, S. D. Perrin, J. Reed, I. Reid, H. J. Wickes, M. J. Adams, *BT Laboratories, UK*. Pulsed operation of 1.5- $\mu$ m VCSELs is described. Photo-pumped lasing up to 357 K and electrically injected lasing up to 240 K are achieved. (p. 103)

4:15pm

**TuD3 • Accurate growth of submilliampere threshold current vertical-cavity surface-emitting laser using diode laser reflectometry in a molecular beam epitaxy system**, G. S. Li, W. Yuen, S. F. Lim, K. Toh, L. E. Eng, C. J. Chang-Hasnain, *Stanford Univ.* Accurate diode laser reflectometry calibrated growths result in 0.29 mA threshold current vertical-cavity lasers. We obtained 100% wafer yield, 0.25% average growth accuracy and 0.4% standard deviation. (p. 106)

4:30pm

**TuD4 • Low threshold current VCSELs with enhanced resistance to heating**, Gye Mo Yang, Michael H. MacDougall, P. Daniel Dapkus, *Univ. Southern California*. VCSELs fabricated by selective oxidation from an all-epitaxial structure show a record low threshold current of 8.7  $\mu$ A and an output power greater than 1.9 mW in 212- $\mu$ A-threshold device. (p. 109)

4:45pm

**TuD5 • High-power highly efficient vertical-cavity surface-emitting laser diodes with an Au-plated heat spreading layer**, T. Wipiejewski, M. G. Peters, B. J. Thibeault, D. B. Young, L. A. Coldren, *UC-Santa Barbara*. We demonstrate vertical-cavity lasers with a Au-plated heat spreading layer showing high output power levels up to 42 mW for unmounted devices. (p. 112)

5:00pm

**TuD6 • Impurity-induced disordering for improved vertical cavity lasers**, P. D. Floyd, M. G. Peters, L. A. Coldren, *UC-Santa Barbara*; J. L. Merz, *Univ. Notre Dame*. We have explored Zn-impurity-induced disordering for spatial mode filters and carrier confinement in vertical cavity lasers. High-order transverse modes are effectively suppressed. (p. 115)

5:15pm

**TuD7 • Robust and wavelength-insensitive performance of selectively oxidized vertical-cavity lasers**, Kent D. Choquette, R. P. Schneider, Jr., K. L. Lear, M. Hagerott Crawford, K. M. Geib, J. J. Figiel, *Sandia National Laboratories*; Robert Hull, *Univ. Virginia*. We report the performance of selectively oxidized vertical-cavity lasers, including submilliamp threshold over a 55-nm wavelength range, efficiencies at 1 mW of >20% over a 40-nm range, and device lifetime of >650 hours. (p. 118)

5:30pm

**TuD8 • High-performance folded-cavity surface-emitting InGaAs/GaAs lasers fabricated by ion-beam-etching technique**, Yong Cheng, Gye Mo Yang, P. Daniel Dapkus, *Univ. Southern California*. Monolithic folded-cavity surface-emitting InGaAs/GaAs lasers that employ high quality internal 45° deflectors are demonstrated with threshold current density of 112.5 A/cm<sup>2</sup> and surface-emission external quantum efficiency of 65% (0.82 W/A). (p. 121)

5:45pm–7:00pm

Free Time

SHAVANO PEAK

7:00pm–8:30pm

Conference Reception

SHAVANO PEAK

7:30pm–8:30pm

TuE • Poster Session

**TuE1 • Efficiency and spectral properties of integrated optoelectronic laser-diode-based rf frequency mixers**, E. A. Avrutin, I. G. Thayne, D. A. Barrow, J. H. Marsh, *Univ. Glasgow, UK*; E. L. Portnoi, A. F. Ioffe *Physico-Technical Institute, Russia*; V. B. Gorfinkel, *Univ. Kassel, Germany*. Efficiency and spectral properties of integrated optoelectronic rf frequency converters based on passively Q-switched and mode-locked diode lasers are studied theoretically and experimentally. (p. 124)

**TuE2 • Dynamics of electro-optical synchronization of self-pulsating laser diodes**, A. Egan, P. Rees, J. O'Gorman, J. Hegarty, *Trinity College, Ireland*; G. Farrell, *Dublin Institute of Technology, Ireland*; P. Phelan, *Opto-electronica, INESC, Portugal*. We examine the behavior of the pulse jitter of and phase difference between synchronized self-pulsating laser diode emission and injected electrical or optical signals. (p. 127)

**TuE3 • Numerical analysis of distortions in directly modulated semiconductor lasers in the presence of weak optical feedback**, M. K. Haldar, F. V. C. Mendis, J. Wang, *National Univ. Singapore*. It is shown that distortions produced by directly modulated semiconductor lasers with weak reflections is better predicted by numerical analysis than by small signal analysis. (p. 130)

**TuE4 • Correct way to model arbitrary complex distributed feedback (DFB) lasers in the above threshold regime**, Wei Hsin, *National Chiao Tung Univ., Taiwan*. Many of the published above-threshold simulation results for DFB lasers were incorrect. We developed a new and correct approach for any complex DFB laser structure. (p. 133)

**TuE5 • High-power diffraction-limited ultrashort pulse generation from double tapered semiconductor laser diodes**, Ziping Jiang, I. H. White, F. Laughton, R. V. Penty, *Univ. Bath, UK*; M. W. McCall, *Imperial College, UK*; H. K. Tsang, *Chinese Univ., Hong Kong*. Double tapered-stripe diode lasers have been simulated using a dynamic beam propagation method and shown to generate high-power ultrashort pulses without filamentation. (p. 136)

**TuE6 • Influence of small radiation doses on the parameters of injection lasers**, A. V. Khaydarov, A. I. Koifman, I. V. Mart'yanova, *Scientific-Research Institute of Applied Physics*. Irradiation with gamma-ray up to 10<sup>4</sup> R and with neutron doses up to ~10<sup>14</sup> cm<sup>-2</sup> reduced the threshold current of InGaAsP/InP and AlGaAs/GaAs laser diodes by 5–15%. Micromechanisms of the radiation influence and possible application of the radiation technology in the development of the injection lasers are discussed. (p. 139)

**TuE7 • Theory of subpicosecond semiconductor lasers**, Jan A. Leegwater, *Vrije Univ. Amsterdam, The Netherlands*. In a theoretical study we show that the shortest obtainable pulsewidth from a modelocked semiconductor laser is about eight times the inverse gain bandwidth. (p. 141)

**TuE8 • Selected multiwavelength oscillation of a semiconductor laser in an external cavity**, Ching-Fuh Lin, *National Taiwan Univ., Taiwan*. A Fabry-Perot laser diode is controlled to oscillate at selected multiple wavelengths using a reflected-type grating telescope configuration in an external cavity. (p. 144)

**TuE9 • Thermal modeling of VCSEL-based optoelectronic modules**, N. D. Morozova, Y. C. Lee, *Univ. Colorado*. Thermal model for application-specific VCSEL-based optoelectronic modules has been developed. Optoelectronic modules performance can be predicted under a variety of operation conditions. (p. 147)

**TuE10 • Development of a tritium powered semiconductor laser**, H. E. Ruda, L. Jedral, *Univ. Toronto, Canada*; L. Mannik, *Ontario Hydro Technologies, Canada*. GaInAsP photo-, cathodo- and radio-luminescence studies identified limitations for efficient visible tritium-luminescence, providing the first demonstration of strong tritium-powered luminescence required for developing radio-luminescent lasers. (p. 150)

**TuE11 • A cw external cavity surface-emitting laser**, J. V. Sandusky, A. Mukherjee, S. R. J. Brueck, *Univ. New Mexico*. We report the first operation of a cw external cavity surface emitting laser. Input-output, polarization, and modal characteristics are investigated. (p. 153)

**TuE12 • Jitter measurements in gain-switched DFB semiconductor lasers coupled to optical fibers**, Adalberto Sapia, Jaime Dellunde, *Fondazione Ugo Bordoni-ISPT, Italy*. Jitter measurements in a repeatedly gain switched distributed feedback laser diode are reported. An optical fiber reflector close to the laser output facet can induce switch-on time and jitter variations up to 25 and 6 ps respectively when the chip-fiber distance is changed by tiny amounts. (p. 156)

**TuE13 • Oscillation wavelength shift characteristics of a semiconductor laser in a magnetic field—observation using a beat note,** Takashi Sato, Shin'ya Matsuda, Kazunori Shibata, Shigeki Yamamoto, Masashi Ohkawa, Takeo Maruyama, *Niigata Univ., Japan*; Minoru Shimba, *Tokyo Denki Univ., Japan*. The observed wavelength shift shows time delay about 0.07 s, which is discussed with the temperature increase around the active layer owing to a magnetic field. (p. 159)

**TuE14 • Asymmetric cladding ridge waveguide laser by selective area MOCVD,** G. M. Smith, D. V. Forbes, R. M. Lammert, J. J. Coleman, *Univ. Illinois*. Fundamental mode ridge waveguide lasers with a thin upper cladding layer are fabricated with a two-step selective area MOCVD growth. (p. 162)

**TuE15 • Analysis of segmented tapered rib-waveguide semiconductor optical amplifiers,** P. S. Spencer, I. Middlemast, R. Balasubramanyam, J. Sarma, K. A. Shore, *Univ. Bath, UK*. A theoretical model for semiconductor tapered rib-waveguide optical amplifiers demonstrates that a segmented device offers superior current-gain performance over an unsegmented structure. (p. 165)

**TuE16 • Quantum interference effect and electric field domains in multiple quantum well structures,** Yuanjian Xu, Ali Shakouri, Amnon Yariv, *California Institute of Technology*. Novel observations of quantum interference in photocurrent spectra of a superlattice are reported, and were used to investigate electric field domain formation in the structure. (p. 168)

**TuE17 • Lasing characteristics of pillar-type microcavity lasers,** H. Yoshida, T. Tezuka, S. Nunoue, *Toshiba R&D Center, Japan*. Lasing characteristics have been studied for micron size pillar-type microcavities fabricated by reactive ion beam etching. Lasing was realized up to 2.5  $\mu\text{m}$  in diameter. (p. 171)



## PREFUNCTION AREA

8:00am-12:30pm

Conference Registration

## TORREYS PEAK I-III

9:00am-11:00am

## WA • Telecommunications Lasers

P. Daniel Dapkus, *University of Southern California, Presider*

9:00am (Invited)

**WA1 • Market requirements on semiconductor lasers for telecommunications**, N. A. Olsson, R. L. Hartman, D. P. Wilt, *AT&T Bell Laboratories*. We review the key market and technological requirements on semiconductor lasers for commercial applications in telecommunications. We will cover high volume applications for access systems as well as high-reliability and high-performance requirements. (p. 176)

9:30am (Invited)

**WA2 • High-temperature uncooled lasers**, C. E. Zah, R. Bhat, T. P. Lee, *Bellcore*. Design considerations for fabricating highly efficient uncooled semiconductor lasers for loop applications are discussed. The emphasis is on the temperature characteristics of threshold current, quantum efficiency, and modulation speed. (p. 177)

10:00am

**WA3 • Theoretical and experimental study on the temperature sensitivity of high-efficiency 1.3- $\mu$ m InP-based strained MQW lasers**, S. Seki, H. Oohashi, H. Sugiura, T. Hirono, K. Yokoyama, *NTT Opto-electronics Laboratories, Japan*. We study the temperature-dependence of the differential quantum efficiency and threshold current of 1.3- $\mu$ m InP-based strained MQW lasers. On the basis of the theoretical and experimental results, the dominant mechanism for determining the temperature sensitivity is discussed. (p. 180)

10:15am

**WA4 • A bi-directional transceiver PIC for Ping-Pong local loop configurations operating at 1.3  $\mu$ m wavelength**, R. Ben-Michael, U. Koren, B. I. Miller, M. G. Young, T. L. Koch, M. Chien, R. J. Capik, G. Raybon, K. Dreyer, *AT&T Bell Laboratories*. We proposed and demonstrated a potentially low cost PIC transceiver for Ping-Pong optical data link configurations. The device is designed for uncooled operation, with a gain section, a detector, and a beam expander. (p. 183)

10:30am

**WA5 • Fe-InP buried 1.3- $\mu$ m double heterostructure laser heteroepitaxially grown on Si**, T. Yamada, M. Tachikawa, T. Sasaki, H. Mori, Y. Kadota, S. Matsumoto, K. Kishi, *NTT Opto-electronics Laboratories, Japan*. A 1.3- $\mu$ m DH laser buried with semi-insulating InP was heteroepitaxially grown on Si for the first time. Its performance is compared to that of ridge-waveguide lasers. (p. 186)

10:45am

**WA6 • Wavelength uniformity in  $\lambda/4$ -shifted DFB laser array WDM transmitters**, M. G. Young, T. L. Koch, U. Koren, D. M. Tennant, B. I. Miller, M. Chien, K. Feder, *AT&T Bell Laboratories*. Six-element quarter-wave-shifted DFB arrays have been fabricated using holographic printing with e-beam generated quartz phase masks. A standard deviation of  $\sigma = 0.18$  nm from a uniform WDM channel spacing has been achieved, a dramatic improvement over the values associated with wafer-wide DFB wavelength distributions. (p. 189)

## SHAVANO PEAK

11:00am-11:30am

Coffee Break/Exhibits

## TORREYS PEAK I-III

11:30am-12:30pm

## Postdeadline Paper Session

Thomas Koch, *AT&T Bell Laboratories, Presider*

12:30pm-12:40pm

Closing Remarks

Monday, August 21, 1995

# High Speed Communications

**MA** 8:30 am-9:45 am  
Torreys Peak I-III

Paul A. Morton, *Presider*  
*AT&T Bell Laboratories*

## High Speed Lasers Based Fiber Optic Systems

Radhakrishnan Nagarajan, Robert Marsland\*, Benjamin Li, Marc Verdiell

Paul Wen, Peter Braid, Kenneth Dzurko and Richard Craig

SDL, Inc., 80 Rose Orchard Way, San Jose CA 95134

Tel: (408) 943 4211 Fax: (408) 943 1070

\* New Focus, Inc., 2630 Walsh Avenue, Santa Clara, CA 95051

### Introduction

The transmitter in a high speed fiber optic system typically consists of a semiconductor laser that is either directly or externally modulated. Although, the small signal modulation bandwidth in semiconductor lasers have exceeded 30 GHz (Fig. 1), external modulation is the preferred method for systems operating at 10 GBit/s and beyond. This has to do with the detrimental effects of laser wavelength chirp under modulation which tends to limit the transmission distance in silica fiber [1]. In long distance fiber transmission using directly modulated lasers at 10 GBit/s, the dispersion limit has also been overcome by techniques [2,3] other than traditional dispersion compensation.

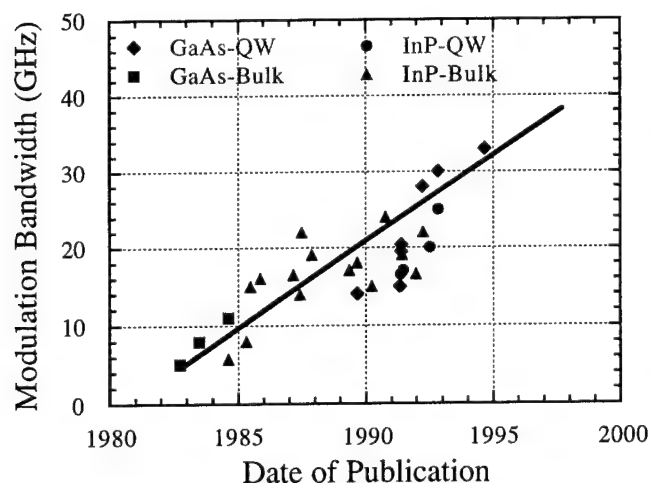


Fig. 1 Room temperature small signal CW modulation bandwidth of semiconductor lasers as a function of publication date.

Despite the problem of wavelength chirping, directly modulated laser transmitters have the advantage of being less expensive and simpler in design. They are used extensively in fiber optic systems operating up to about 2.5 GBit/s. Another area of interest is the use of directly modulated lasers for inexpensive, high temperature 'uncooled' transmitters for computer interconnects and local area networks. Uncooled operation of laser diodes is desired because it eliminates the need for thermoelectric coolers which are

major contributors to operational complexity and poor reliability (especially at high temperatures) in packaged fiber optic transmitters. In recent years there has been a lot of progress in the design and fabrication of laser diodes that operate uncooled at high temperatures at 0.98  $\mu\text{m}$  [4], 1.3  $\mu\text{m}$  [5] and 1.5  $\mu\text{m}$  [6] wavelengths. Despite many publications of CW laser operation at high temperatures, there has not been a report of a complete fiber optic link operating uncooled at high temperatures. Here we present some of our results with a 1  $\mu\text{m}$  wavelength fiber optic transmitter as well as a receiver operating uncooled at temperatures in excess of 125°C at link bit error rates of  $10^{-11}$ . We also present some preliminary results on the operation of laser diode arrays at 1.3  $\mu\text{m}$ .

# Uncooled Fiber Optic Systems Operating at 1.0 $\mu\text{m}$

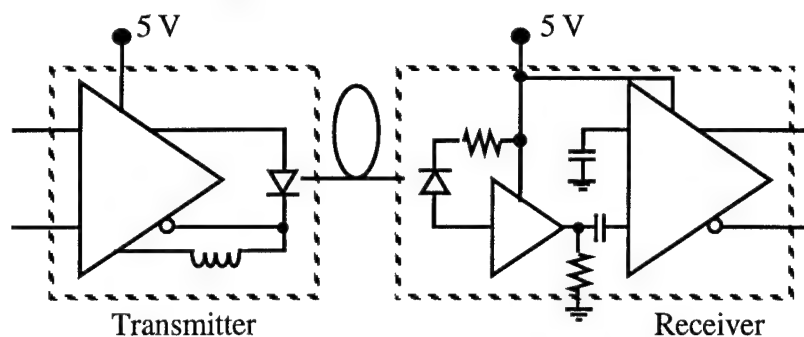


Fig. 2 Schematic diagram of the transmitter and receiver modules. They are both of the Silicon bipolar technology and use a 5 V supply.

Figure 1a shows the schematic diagram of the transmitter and receiver packages used in the fiber optic link. The transmitter consists of a commercial high speed laser driver chip and a Fabry

Perot InGaAs/GaAs quantum well laser operating nominally

at a wavelength of 1  $\mu\text{m}$  at room temperature. The driver chip provides the laser DC bias as well, and the isolation for the RF drive output is provided within the package. The transmitter is single mode fiber coupled and the coupling scheme is very stable at high temperatures.

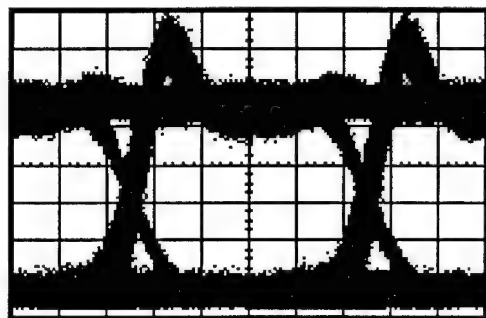


Fig. 3 The eye diagram of the transmitter at 130°C.

The eye diagram of the transmitter at 130°C is shown in Figure 3. This is for  $(2^{31}-1)$  pseudo random bit sequence (PRBS) at 1.24416 GBit/s. The optical signal swing between logic '0' and logic '1' levels is 3.5 mW. The risetime is about 210 ps and the falltime is about 250 ps. The sensitivity measurements are done at a data rate of 1.24416 GBit/s with the transmitter and receiver connected back to back and the results are shown in Fig. 2.

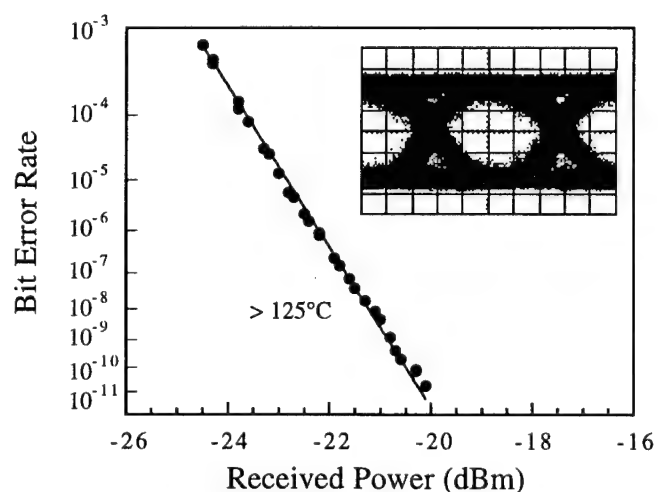


Fig. 3 Sensitivity curves at a data rate of 1.24416 GBit/s for the back to back operation of the fiber optic link at temperatures exceeding 125°C.

Figure 2 indicates a -20.8 dBm sensitivity at temperatures about 130°C for a bit error rate (BER) of  $10^{-9}$ . The inset in Figure 2 shows the high temperature eye diagram at the output of the receiver for an average input optical power of -20.1 dBm. The sensitivity of the fiber optic link is limited by the thermal noise of the receiver which was designed for low cost fiber channel applications. There are no optical isolators in the package or the link, and despite this, the laser relative intensity noise is not a problem.

### Laser Arrays for Parallel Links

Apart from point to point links, there has been considerable attention paid to laser arrays for parallel fiber links. These are for computer cluster or back plane interconnect applications.

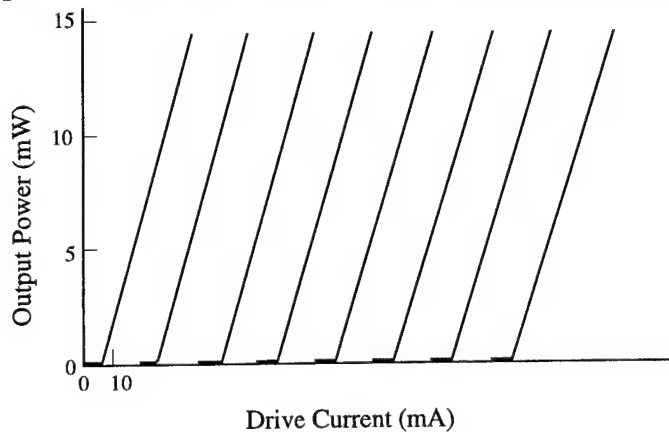


Fig. 4 Uniformity of 8 laser arrays at 1.3  $\mu\text{m}$ .

98%/70% coatings. The array was bonded p-up on a ceramic submount. The average threshold current was 7 mA with a maximum dispersion of  $\pm 1$  mA. Laser efficiency was 0.36 mW/mA. Maximum power of 40 mW at 160 mA was obtained from p-up mounted, uncooled lasers (1 mm long lasers from the same wafer operated up to 220 mW with a 0.5 mW/mA efficiency). In preliminary high temperature measurements, the threshold current increase for a temperature rise from 20°C to 53°C was 4.8 mA, and  $T_0$  value extracted from this measurements was 63K.

Preliminary high speed measurements indicate these laser arrays are capable of being modulated at data rates up to 2.48 GBit/s.

Fig. 4 shows the L-I curves for an array of eight lasers operating at a wavelength of 1.3  $\mu\text{m}$ . The active region consists of compressively strained InGaAsP multiple quantum wells. Similar arrays operating at 1  $\mu\text{m}$  wavelength (using compressively strained InGaAs/GaAs) have also been made. The 1.3  $\mu\text{m}$  wavelength, 8 element array had a

cavity length of 325  $\mu\text{m}$  and the facet had

### References

1. G. P. Agrawal, *Fiber-Optic Communication System*, John Wiley:New York, 1992.
2. U. Fischer, *Electron. Lett.* **28**(14), 1305 (1992).
3. B. Wedding and B. Franz, *Electron. Lett.*, **29**(4), 402 (1993).
4. P. L. Derry, et al., *IEEE Photon. Tech Lett.*, **4**(11), 1189, (1992).
5. C. E. Zah, et al., *IEEE J. Quantum Electron.* **30**(2), 511 (1994).
6. B. Stegmüller, et al., *Electron. Lett.* **29**(19), 1691 (1993).

# Strain-compensated 1.55 $\mu\text{m}$ DBR lasers for operation at high speed with low drive current

U. Öhlander and O. Sahlén

Ericsson Components AB, S-164 81 Kista, Sweden

Tel. + 46 8 75 74461

Fax. + 46 8 75 74764

O. Kjebon, S. Lourdudoss, J. Wallin, K. Streubel, S. Nilsson and L. Bäckbom

Laboratory of Photonics and Microwave Engineering

Royal Institute of Technology, Electrum 229, S-164 40 Kista, Sweden

Tel. + 46 8 75 21281

Fax. + 46 8 75 21240

Strained-layer quantum well (QW) technology allows band-engineered active material to improve threshold current and output power [1], speed [2-4], chirp [2] and temperature performance [5]. A distributed Bragg reflector (DBR) section can be used to obtain longitudinal single-mode operation [6] and improve temperature performance [7]. High-reflectivity (HR) coatings can be employed for better temperature performance [7] and threshold current [1]. We report a combination of DBR rear section, short-cavity QW active section and HR-coated front facet, which improves the properties for direct modulation.

The laser structure is schematically shown in Figure 1. All layers except the semi-insulating are grown with MOVPE.

In the active section are 8 InGaAsP wells, 7 nm thick with 1 % compressive strain, separated by 7 InGaAsP barriers, 8 nm thick with 1 % tensile strain. Outside each of the two outermost wells is a 8 nm layer of the same material as in the barriers. The wells and barriers were grown with the same As/P-ratio, so-called constant  $y$ , (CY)  $y = \text{As-fraction}$ , which allows strain-compensation [8]. The compositions of the wells and the barriers are nominally ( $x=0.745$ ,  $y=0.85$ ) and ( $x=0.465$ ,  $y=0.85$ ), respectively, where  $x = \text{In-fraction}$ . Surrounding this QW package, was formed a symmetrical step-graded index separate confinement heterostructure. The step-grading on each side consists of one 14 nm step closest to the QW structure, followed by three 22 nm steps, with corresponding bandgap wavelengths of 1.30, 1.22, 1.14 and 1.08  $\mu\text{m}$ , respectively.

The grating section consists of a 10 nm InP buffer layer, a waveguide consisting of 20 lattice-matched 10 nm thick wells, with corresponding bulk bandgap wavelength of 1.45  $\mu\text{m}$ , and InP barriers of 10 nm thickness. On top of the waveguide is an InP spacer layer of 50 nm thickness followed by a lattice matched grating layer, with a bandgap wavelength of 1.45  $\mu\text{m}$ . The designed coupling strength of the buried grating is 135  $\text{cm}^{-1}$ .

Mesas  $\sim 1.5 \mu\text{m}$  wide and  $\sim 5 \mu\text{m}$  high, were fabricated by reactive ion etching and selectively regrown with semi-insulating InP:Fe by hydride vapor phase epitaxy. After p- and n-contact metallisations, lasers were cleaved with active and grating section lengths of 70-110 and 170-180  $\mu\text{m}$ , respectively.

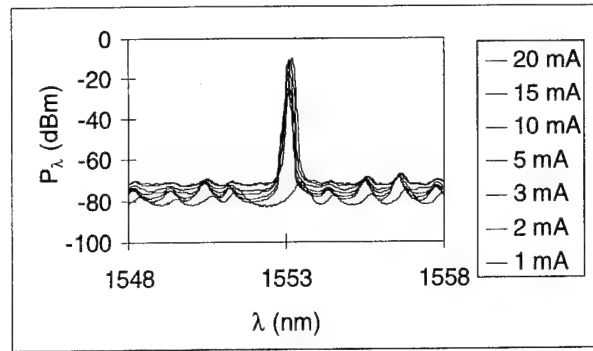
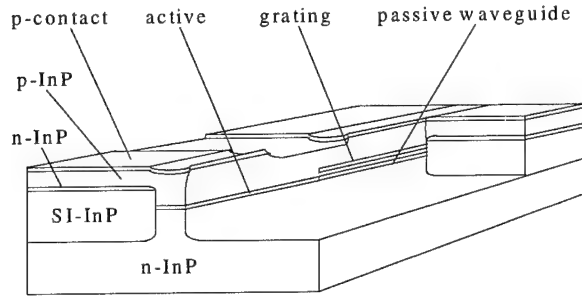


Figure 1. Schematic DBR-QW laser structure. Figure 2. Spectra for laser # 5 @  $T=20^\circ\text{C}$  at different bias levels.

The CW threshold currents,  $I_{th}$ , and front facet external differential efficiencies,  $\eta_{ext,F}$ , at  $20^\circ\text{C}$ , before coating, were 3.0-4.0 mA and 37-39 %, respectively. Coatings with 90% reflectivity were then deposited on the front facets (DBR section at the rear facet) of five lasers.

The relaxation oscillation frequency,  $f_r$ , depends linearly on the square root of bias current above threshold,  $(I - I_{th})^{1/2}$ . The  $D$ -parameter we define as:

$$D = \frac{f_r}{(I - I_{th})^{1/2}} \quad (1)$$

After coating,  $I_{th} = 1.4$ -1.9 mA,  $\eta_{ext,F} = 11$ -15 % and  $D = 2.7$ -2.9 GHz/mA<sup>1/2</sup> were obtained at  $20^\circ\text{C}$ , for the five lasers. The mode spectra of laser #5 at  $20^\circ\text{C}$  and at different bias levels are displayed in Figure 2. Above threshold the lasers were longitudinal single-mode, except for laser #3 which exhibits a mode-jump at  $60$ - $65^\circ\text{C}$ . Figures 3 and 4 show the temperature dependence of threshold currents and  $D$ -parameters, respectively, in the regime  $10$ - $80^\circ\text{C}$ . The performance of laser #3 deteriorates above  $\sim 40^\circ\text{C}$  due to the mode-jump. Below  $40^\circ\text{C}$  the performances of all lasers are excellent (the  $D$ -parameter of laser #21 was only measured at  $20^\circ\text{C}$ ).

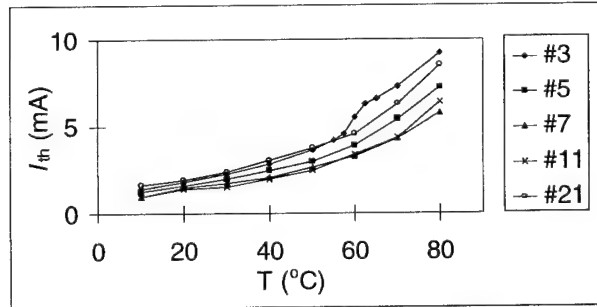


Figure 3. Threshold current vs. temperature for lasers 3, 5, 7, 11 and 21.

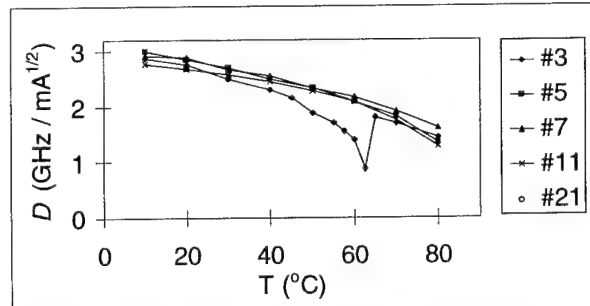


Figure 4. Resonance frequency parameter ( $D$ ) vs. temperature for lasers 3, 5, 7, 11 and 21.

A 2.4484 Gb/s transmission experiment was performed on laser #3 at  $20^\circ\text{C}$ , using a  $2^{15}-1$  pseudo-random NRZ bit-stream. The DC bias current, intermediate between the one and the zero, was as low as 8.2 mA, while the AC-coupled drive current was just 13 mA p-p. The extinction ratio was

10.5 dB. Measured BER curves, corresponding to transmission over 0, 50 and 100 km of standard fibre, are displayed in Figure 5.

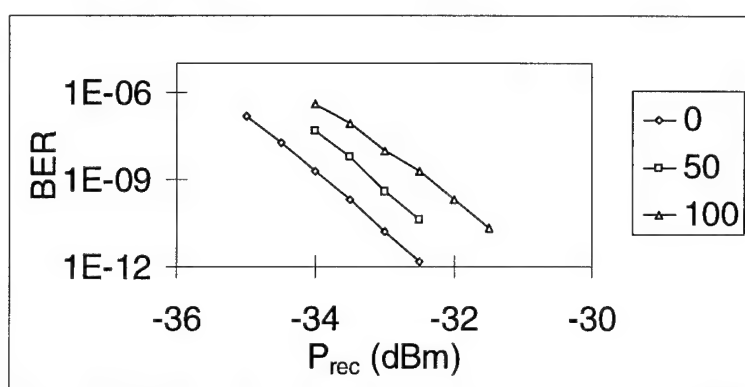


Figure 5. Bit error rate vs. received mean power after 2.4484 Gb/s transmission over 0, 50 and 100 km standard fibre, with 10.5 dB extinction and using low bias and drive currents.

In conclusion, 1.55  $\mu\text{m}$  single-mode lasers with improved threshold current and speed at low drive current have been reported.

## References

1. P. J. A. Thijs, J. J. M. Binsma, L. F. Tiemeijer and T. van Dongen: "Submilliamp threshold current (0.62 mA at 0 °C) and high output power (220 mW) 1.5  $\mu\text{m}$  tensile strained InGaAs single quantum well lasers", *Electronics Letters* vol. 28, no. 9, pp. 829-830, April 1992.
2. K. Uomi, S. Sasaki, T. Tsuchiya, H. Nakano and N. Chinone: "Ultralow chirp and high-speed 1.55  $\mu\text{m}$  multi-quantum well  $\lambda/4$ -shifted DFB lasers", *IEEE Photonics Technology Letters*, vol. 2, no. 4, pp. 229-230, April 1990.
3. H. Yasaka, R. Iga, Y. Noguchi and Y. Yoshikuni: "Pure strain effects in strained-layer multiple-quantum-well lasers", *IEEE Photonics Technology Letters*, vol. 4, no. 8, pp. 825-828, August 1992.
4. O. Kjebon, U. Öhlander, S. Lourdudoss, J. Wallin, K. Streubel, S. Nilsson and T. Klinga: "Multi quantum well 1.55  $\mu\text{m}$  DFB lasers with low threshold current, high resonance frequency and bandwidth at low current injection", 14th IEEE International Semiconductor Laser Conference, September 19-23, 1994, Maui, Hawaii, USA, Proceedings, pp. 221-222, Sept. 1994.
5. H. Oohashi, T. Hirono, S. Seki, H. Sugiura, J. Nakano, M. Yamamoto, Y. Tohmori and K. Yokohama: "High temperature operation InAsP-based MQW lasers", Post-deadline Paper PDA3, presented at 6th International Conference on InP and Related Materials, March 27-31, 1994, in Santa Barbara, California, USA.
6. G. P. Agrawal and N. K. Dutta: *Long-wavelength semiconductor lasers*, text book, Van Nostrand Reinhold Company, ISBN 0-442-20995-9, New York, 1986.
7. W. T. Tsang, F. S. Choa, R. A. Logan, T. Tanbun-Ek, A. M. Sergent and K. W. Wecht: "Reduced temperature dependence of threshold current by broadband enhanced feedback: A new approach and demonstration", *Applied Physics Letters*, vol. 60, no. 1, pp. 18-20, January 1992.
8. A. Mircea, A. Ougazzaden, J. Barrau, J. -C. Bouley, B. Calvas, J. Charil, C. Kazmierski and G. Leroux: "Quantum-well structures with compensated strain for optoelectronic applications", *Proceedings of the Conference on InP and Related Materials*, Paris, pp. 41-44, 1993.



## Minimizing the Operating Current of Quantum Well Lasers with Modulation Bandwidth and Optical Power Requirements

M. McAdams, B. Zhao, T.R. Chen, J. Feng, and A. Yariv

*T. J. Watson Sr. Laboratories of Applied Physics*

*MS 128-95*

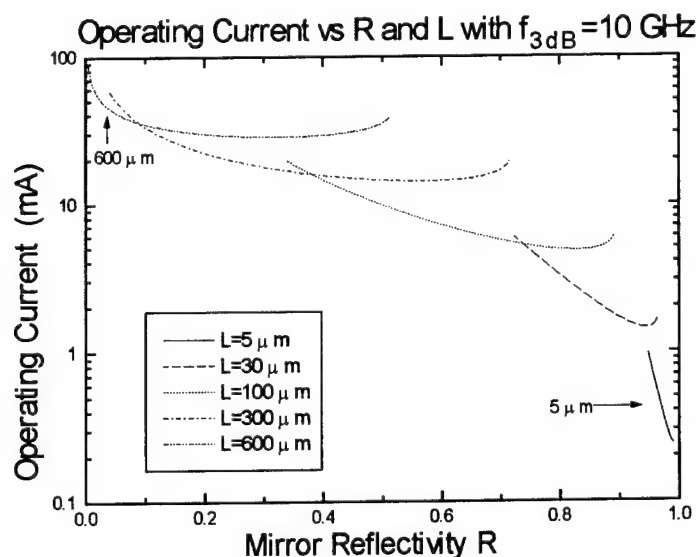
*California Institute of Technology*

*Pasadena CA 91125*

TEL (818) 395-4830 FAX (818) 405-0928

When semiconductor lasers are used in optical telecommunication and optical interconnect applications, it is desirable to have as low an electrical power consumption as possible, i.e. a low operating current. However, if used in a high data transmission rate system, there may be a minimum requisite modulation bandwidth. In addition, signal-to-noise considerations often demand a minimum optical output power. While lowering the threshold current often improves the bandwidth and output power at a given operating current, it is not true that a laser optimized solely for the lowest threshold current will have the lowest operating current when biased to meet the requirements of a particular system. In this talk we discuss how the laser device parameters are optimized to produce the lowest operating current in applications with given bandwidth and optical power requirements.

The laser devices under study were strained InGaAs/AlGaAs single quantum well lasers with graded index separate confinement heterostructures. The gain (including non-linear gain), differential gain, and spontaneous lifetime have been calculated with consideration of the bandmixing and strain effects, in order to quantify the laser performance as a function of the device parameters. All quantities involved in the analysis were either calculated directly from



the assumed structure or chosen from typical values.

We analyzed the scenario in which the laser must have a minimum modulation bandwidth  $f_{3dB}$ . Figure 1 shows the operating current versus  $R$  and  $L$  for a 10 GHz bandwidth requirement. Short cavity lasers have lower optimized operating currents at any  $f_{3dB}$ , but the range of  $R$  in which the optimum current lies is more restrictive--compare, for example, the  $L=5\text{ }\mu\text{m}$  and  $L=30\text{ }\mu\text{m}$  lines in Figure 1. The range of solutions is limited on the high- $R$  end, because beyond a certain  $R$ , a laser is incapable of a 10 GHz bandwidth at any bias--gain saturation prevents any bandwidth increase above some large operating current. On the low- $R$  side, thermal effects preclude selecting a laser whose operating current density exceeds practical limits. Thus, short lasers have lower operating currents in fixed-bandwidth systems, but the choice of  $L$ , and hence  $R$ , will depend upon the degree of control of  $R$  during fabrication.

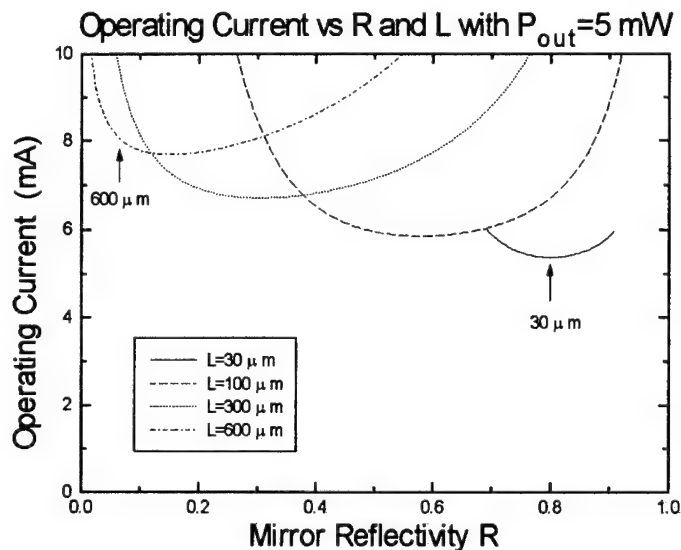
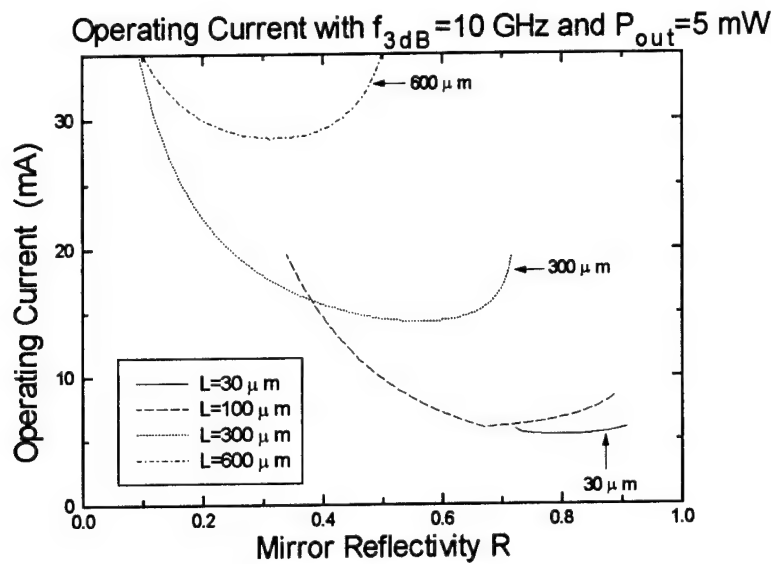


FIGURE 2

The short cavity lasers that look favorable in Figure 1 unfortunately have very low output powers. Therefore we now relax the  $f_{3dB}$  requirement and instead demand a minimum optical output power  $P_{out}$ . Figure 2 shows the current disadvantage attendant with high-reflectivity mirrors, which becomes more severe for large  $P_{out}$ . Short lasers again have the smallest optimized operating current, but their advantage dwindles away as the required output power increases above about 10 mW. In Figure 1, the  $30\text{ }\mu\text{m}$  cavity has a minimum operating current that is a factor of 6 less than for the  $100\text{ }\mu\text{m}$  cavity; but in Figure 2, that factor is only 10%. In addition, the  $30\text{ }\mu\text{m}$  cavity has a quite large optimized current *density* of  $8950\text{ A/cm}^2$ , a factor of 3 larger than for the  $100\text{ }\mu\text{m}$  cavity. Consequently, thermal effects now make the  $100\text{ }\mu\text{m}$  cavity more preferred. The  $L=5\text{ }\mu\text{m}$  cavity laser would have an operating current density so high it is impractical, so it is not plotted as a viable solution. The smaller cavities again have smaller tolerances in  $R$ .

When we combine an  $f_{3dB}$  requirement with a  $P_{out}$  requirement, the result could be dubbed the worst of both worlds--the operating current is the larger of the currents needed to produce  $f_{3dB}$  alone and  $P_{out}$  alone. Figure 3 shows the result of combining the bandwidth requirement of Figure 1 with the output power requirement of Figure 2. One new feature is that at some  $L$  values, for which the  $P_{out}$  criteria produces a large minimum current, that current is too high to produce the desired  $f_{3dB}$  (because of gain saturation), even if that  $f_{3dB}$  is attainable at a lower current. Thus there is only a certain  $L$  range in which solutions exist for  $R$  that will satisfy the bandwidth and output power requirements. The 30  $\mu m$  and 100  $\mu m$  cavities in Figure 3 have nearly equal operating currents, so thermal effects again make the 100  $\mu m$  cavity preferable.



In conclusion, minimizing the threshold current of a laser is not the best way to minimize the operating current in a system with realistic bandwidth and power requirements that must be met. The optimum cavity length and mirror reflectivity depend strongly upon the bandwidth and power specifications, and the choice of these device parameters will be influenced by the degree of control of  $R$  during fabrication. Thermal effects arising from large operating current densities force the conclusion that short- $L$ , high- $R$  microcavity lasers are not favored.

# The Reduction of the Frequency Chirp of Two Section Distributed Feedback laser without Suppressing Spatial Hole Burning

J. Feng , T. R. Chen , B. Zhao, and A. Yariv

*T. J. Watson Sr. Laboratories of Applied Physics , 128-95 ,California Institute of Technology  
Pasadena, California 91125  
phone (818)395-3983, fax (818)405-0928*

The spectral linewidth of a DFB laser increases significantly when directly modulated at a high frequency , a phenomenon known as frequency chirping . Means for reducing the frequency chirp have included the use of laser with a smaller linewidth enhancement factor of the active material and methods which reduce the spatial hole burning (SHB) . The second approach involves fabrication of either complex laser structures which introduce gain coupling or quarter wavelength shift three section DFB lasers. We report here on the measurement of the frequency chirp of a two section DFB laser under large signal modulation . It was found that the frequency chirp of a two section laser can be minimized by simply adjusting the injection current distribution in the laser. The unique advantage for using two section DFB lasers is that frequency chirp can be reduced even when SHB is not suppressed.

A two-electrode 1.3  $\mu\text{m}$  InGaAsP/InP DFB laser has been fabricated. Its front facet was AR coated and the rear front was left as-cleaved. The two sections are 400 $\mu\text{m}$  and 100 $\mu\text{m}$  long with an electric isolation of 1.4K $\Omega$ . The threshold current for section one was measured as a function of the injection current in section two and is shown in

The two sections are pumped with DC currents while the longer one is also AC pumped. In all measurements section one is biased above threshold. The laser output is collimated and divided by a beamsplitter into two beams, one beam is focused onto an Ortel 2516A high speed photodiode, the other beam on a SPEX 1870 monochromator slit with a resolution of 0.5  $\text{\AA}$  to observe modulated light spectrum . The monochromator detection system consists of a Ge detector and a lock-in amplifier. The wavelength of the monochromator was scanned at a low speed of 0.1  $\text{\AA}/\text{s}$  so that the envelope of the dynamic wavelength shift was recorded. The full width of half maximum of the optical spectrum was measured to evaluate the frequency chirp. The output of the photodiode was fed to a sampling oscilloscope with which the time waveforms for the modulated light were observed . The current in the section one was biased at  $I_1/I_{th}=1.8$  for  $I_2=0$  , and the optical power is then maintained at that level for various  $I_2$  values by changing current  $I_1$  . The optical modulation index  $m$  monitored by the sampling oscilloscope and was fixed at 100 percent by adjusting the AC microwave power (typically 10 dBm) into the section one.

The frequency chirp was measured at a modulation frequency of 5 GHz, and the result is shown in Fig. 1 . A minimum near 1.2 $\text{\AA}$  when  $I_2$  is in the range of 14 mA to 18 mA . A dip around  $I_2 = 4\text{mA}$  is due to the mode switching of the laser. We found the chirp to be strongly dependent on the modulation frequency . The chirp of the laser was also measured at a modulation frequency of 3 GHz, 2 GHz . The chirp at those modulation frequencies is much smaller than that at 5 GHz; the features of the chirp at those frequencies can not be obtained because for some of the cases the chirp is less than the resolution of the monochromator. It was observed that the distortion of output optical waveform becomes serious when either the modulation current or the modulation frequency increases. The distortion is a result of the relaxation oscillation which is accompanied by a large chirp.

We studied the chirp of multisection DFB lasers with a model based on time-dependent coupled mode wave equations. The model explains the basic observed features of the frequency chirp of the two section DFB lasers. Taking into account the SHB along the laser axis<sup>[1],[2]</sup>, the carrier density  $N$ , photon density  $P$ , and refractive index  $n$  of the active layer, all vary along the  $z$ -axis. The refractive index is related to the optical gain by linewidth enhancement factor. We divided the DFB laser into sufficiently short segments in each of which the carrier and photon density were assumed constant. We then calculated the complex reflectivities of a two section DFB laser by means of the propagator  $F$  matrices<sup>[3]</sup>. The dynamics of the laser under high frequency, large signal modulation is calculated with the coupled mode equations

$$\begin{aligned} \frac{\partial E^+}{\partial z} + \frac{1}{v_g} \frac{\partial E^+}{\partial t} &= i\kappa E^- - (i\delta + i\Delta\omega/v_g - g + \alpha_{loss})E^+ + T^+ \\ \frac{\partial E^-}{\partial z} - \frac{1}{v_g} \frac{\partial E^-}{\partial t} &= i\kappa E^+ - (i\delta + i\Delta\omega/v_g - g + \alpha_{loss})E^- + T^-, \end{aligned} \quad (1)$$

and the rate equation

$$\frac{dN}{dt} = \frac{J}{ad} - \frac{N}{\tau} - BN^2 - CN^3 - \frac{a(N-N_{tr})}{(1+\epsilon P)} v_g P, \quad (2)$$

here the transverse electric field can be represented by

$$F(z,t) = E^+(z,t) \exp[-i\beta_0 z + i(\omega_0 + \Delta\omega)t] + E^-(z,t) \exp[+i\beta_0 z + i(\omega_0 + \Delta\omega)t] \quad (3)$$

where  $E^+$ ,  $E^-$  are the complex field amplitudes of the forward and backward wave, respectively, and  $\omega_0$  is the reference frequency.  $\beta_0 = 2\pi/\Lambda_0$ , where  $\Lambda_0$  is the Bragg wavelength.  $\Delta\omega = \omega - \omega_0$ ,  $\omega$  is the lasing frequency,  $v_g$  is the group velocity of light in the active region,  $\kappa$  is the coupling coefficient,  $g$  is the optical gain,  $\alpha_{loss}$  is the internal loss, and  $\delta = \beta - \beta_0$  with  $\beta$  as propagation constant.  $T^\pm$  are the terms due to the spontaneous emission coupled into the lasing mode, and  $T^\pm = \frac{J_{sp}}{|E^\pm|^2} E^\pm$ , where  $J_{sp}$  is a constant related to spontaneous emission.

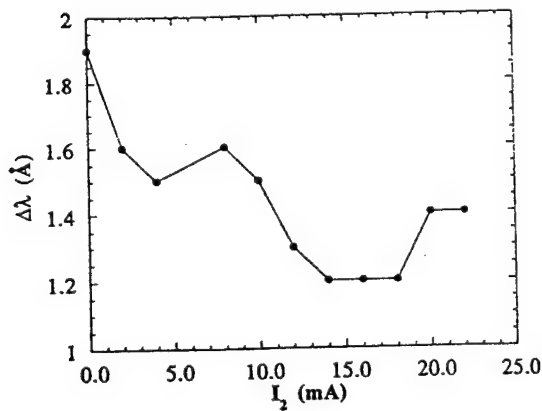


FIG. 1. The measured frequency chirp of the two section DFB laser with optical modulation index  $M=100\%$ , average optical power is kept the same level as that of  $I_1=1.8I_{th}$  and  $I_2=0$ .  $I_{th}$  is the threshold current for section one when  $I_2=0$ .

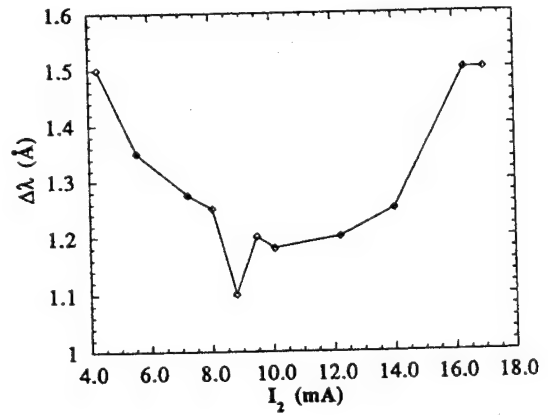


FIG. 2. The calculated frequency chirp for the two section DFB laser used in the experiment with optical modulation index  $M=100\%$ , average optical power kept the same. The peak to peak modulation current is about 10 mA. The parameters used were a linewidth enhancement factor of 4.8, a nonlinear gain suppression coefficient of  $10^{-17} \text{ cm}^3$ , a spontaneous emission factor of  $10^{-4}$ , a carrier life time of 2ns, and a photon lifetime of 1ps.

The calculated frequency chirp of the laser is shown in Fig. 2 . The modulation frequency is set to be 5 GHz, and the optical modulation index at 100% with the average optical power kept a constant. In Fig. 2 , we observe that the calculated frequency chirp also has a minimum value of 1.1 Å when  $I_2=9.5$  mA . Because the computation of each data in the figure is highly time-intensive, very limited points were obtained to construct the curve on which a sharp dip appears. For values of  $I_2$  less than 1 mA or greater than 14 mA, we had difficulty with the convergence of the solution for the dynamic lasing condition because the photon density distribution is very asymmetrical . We found that the calculated chirp is hardly changed when other values of the phases of the facet reflectivities are used in the calculation. In our calculation, the phases are assume to be zero. Considering the complexity of the structure of the DFB laser and the large number of parameters involved in the calculation, we can say that the basic features and the range of values of the numerical analysis are in agreement with the observation.

To explain to the reduction of the chirp in two section DFB laser, we use the average photon densities in each section and the mode frequency shift  $\Delta\omega_i$  due to average gain change  $\Delta G_i$  in the two sections is then given by [4]

$$\Delta\omega_l = A ( L_1^{eff} \Delta G_1 + L_2^{eff} \Delta G_2 ) / ( L_1^{eff} + L_2^{eff} ) . \quad (4)$$

Here A is the material constant of the active layer, and we define the effective lengths of the sections  $L_i^{eff} \equiv (v_g/2) \frac{\partial \phi_i}{\partial \omega_l}$ .

To maintain oscillation, the gain change in one section must be compensated by an opposite change in the other section (  $\Delta G_1$  ,  $\Delta G_2$  have the opposite values ) , and  $L_i^{eff}$  depends on gain or injection current and detuning . The small chirp of two section DFB lasers can be realized when one section contributes positive chirp and the other one equal amount of negative chirp. However, when taking SHB into account, a finite frequency chirp  $\Delta\omega_l$  results.

In conclusion, the reduction of the frequency chirp of a two section DFB laser by nonuniform current injection is demonstrated. The reduction of the chirp was realized without using complicated laser structures to suppress SHB. The technique in our experiment is practical for commercial used DFB lasers because of its simplicity. We also analyzed the frequency chirp of the two section DFB laser with a numerical simulation based on a dynamic model for multisection DFB lasers.

- [1] J. I. Kinoshita, and K. Matsumoto, *IEEE J. Quantum Electron.* **QE-24**, 2160(1988)
- [2] P. Vankwikelberge, G. Morthier, and R. Baets, *IEEE J. Quantum Electron.* **QE-26**, 1728(1990)
- [3] M. Yamada, and K. Sakuda, *Appl. Opt.* **26**, 3474(1987)
- [4] M. Kuznetsov, A. E. Willner and I. P. Kaminow, *Appl. Phys. Lett.* **55**, 1826 (1989)



Monday, August 21, 1995

## Spectroscopic Applications

**MB** 10:15 am-12:00 m  
Torreys Peak I-III

Peter F. Moulton, *Presider*  
*Schwartz Electro-Optics, Inc.*



## Diode Lasers for Industrial Spectroscopy

Alan C. Stanton, David S. Bomse, Joel A. Silver, D. Christian Hovde,  
Daniel J. Kane, Daniel B. Oh, and Mark E. Paige

Southwest Sciences, Inc.  
1570 Pacheco St., Suite E-11  
Santa Fe, NM 87505

phone (505) 984-1322  
fax (505) 988-9230

### 1. Introduction

Visible/near-infrared diode lasers are well-suited for use as spectroscopic light sources in detection of a wide variety of gases by measurement of optical absorption. The high spectral resolution of these devices permits the selective detection of targeted species, while their characteristics of relatively low cost, room temperature operation, and compatibility with fiber optics make them attractive for instrument development. The nominal range of available wavelengths (presently  $\sim 0.63 - \sim 2.0 \mu\text{m}$  for commercially available devices that operate at room temperature) includes absorption bands of numerous gas species that need to be monitored to meet various industrial objectives (e.g. process control, emissions monitoring, toxic gas detection, etc.) While the molecular absorption bands in this spectral region consist mostly of relatively weak overtone or combination bands (some electronic bands are accessible at the shorter wavelengths), detection sensitivities of about 1 ppm-meter or better can be achieved for many gases using frequency or wavelength modulation techniques that permit routine measurement of small optical absorbances.<sup>1-2</sup> Sub-ppm measurement sensitivities are easily achieved using simple optical multipass designs if necessary. A partial list of industrially significant gases that may be measured by this approach includes oxygen, water vapor, methane, acetylene, carbon monoxide, carbon dioxide, hydrogen halides, ammonia, hydrogen sulfide, and nitrogen oxides (both NO and NO<sub>2</sub>). Diode laser-based instruments for measurement of some of these species in process control or environmental monitoring applications are now commercially available.

This paper describes recent progress in development of diode laser-based instrumentation for industrial applications by presenting two examples: perimeter monitoring of a toxic gas in a refinery environment and measurement of trace moisture contamination in high purity process gases. The paper then turns to a discussion of diode laser device characteristics that are desirable for present and contemplated industrial gas sensing applications.

### 2. Perimeter Monitoring in a Refinery Environment

We have developed and field-tested a diode laser-based toxic gas perimeter monitor. The field test, at a commercial oil refinery, spanned a six month period from October, 1993 – March, 1994. Located outdoors, this instrument continuously monitored hydrogen fluoride gas over an open path line of sight that was subject to steam, rain, and snow, using a telescope/retroreflector arrangement. A fiber-pigtailed DFB diode laser operating in the  $1.31 \mu\text{m}$  region was used. The instrument featured extensive error checking, internal calibration, and continuous line-locking to the HF absorption feature.<sup>3</sup> The instrument showed almost flawless operation throughout one of the harshest winters on record in the Northeast. The

diode laser perimeter monitor is being commercialized by Spectrum Diagnostix, Inc. under license from Southwest Sciences, and its detection capability is being extended to other gases.

### 3. Trace Moisture Detection in Process Gases

Process gases for semiconductor applications must meet high standards for purity. Water is especially troublesome due to its physical properties and its high abundance in the atmosphere. Although trace water vapor levels can be quantified by several methods, they are either slow, expensive, or cannot be applied in corrosive gases. We have constructed and tested a prototype trace moisture sensor based on absorption of near-infrared diode laser radiation. This sensor comprises a multiple-pass absorption cell attached to a sealed compartment housing the laser and detector. The laser is a custom-fabricated DFB device operating near  $1.393\ \mu\text{m}$ . Wavelength modulation spectroscopy with  $2f$  detection near 100 kHz was used in our initial tests. The sensor system was tested in-house and calibrated at the research facilities of a major semiconductor gas supplier.

The sensor exhibited a linear response across the full test range of 20 ppb to 50,000 ppm mixture ratio. Water vapor concentrations as low as 41 ppb were detected with excellent signal to noise, as shown in Fig. 1. From the noise within a single spectral scan, the estimated minimum detection limit ( $S/N=3$ ) is 12 ppb. Design improvements are expected to result in sensitivity better than 1 ppb.

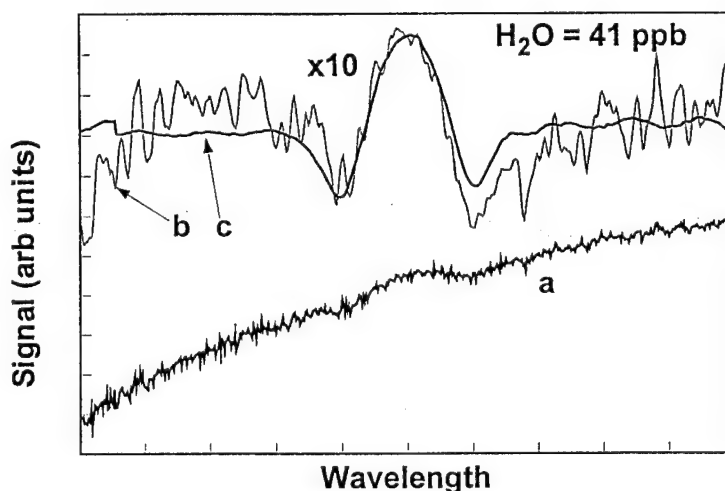


**Figure 1** - Spectrum of trace water in nitrogen. a) raw measured spectrum, b) measured spectrum minus best-fit quadratic background, c) reference spectrum scaled to 41 ppb.

### 4. Diode Laser Device Characteristics Needed for Spectroscopic Gas Sensing

The three most important diode laser device characteristics for spectroscopic gas sensing applications are wavelength, single frequency output, and tunability. Output power is generally not an issue: mW power levels are easily adequate for achieving high sensitivity in absorption measurements; higher power levels might be needed if the output of one laser is distributed via fiber optics to many gas detection points.

For researchers who have been involved in the early development of visible/near-infrared diode laser-based spectroscopic sensors, the overwhelming issue has been the availability of required laser wavelengths. Standard "off the shelf" wavelengths are rarely optimum for detection of a particular gas (HF in the  $1.31\ \mu\text{m}$  region is a possible exception), so researchers usually are faced with surveying the various laser manufacturers to determine if they will search their inventories for wavelength outliers (only a handful of manufacturers have been willing to do this). In some instances, the wavelength

requirement has been sufficiently unique that custom fabrication of lasers has been required, as in the case of the trace moisture application described earlier. It seems likely that development of commercial diode laser-based gas sensors will usually require such custom fabrication efforts, as the laser wavelength needs to be tightly specified to obtain the desired sensitivity or to avoid spectroscopic interferences.

Commercial availability of room temperature (or at least thermoelectrically cooled) semiconductor lasers at longer wavelengths is also eagerly anticipated by gas sensor developers. The antimonide-based laser systems appear to hold substantial promise in achieving this goal. TE-cooled devices beyond 2.5  $\mu\text{m}$  have been fabricated. As these lasers become available in the 3  $\mu\text{m}$  region and beyond, the fundamental C-H stretching frequencies found in most hydrocarbons would be accessible. In addition, stronger absorption bands of several of the species mentioned in the introduction could be accessed.

Single frequency output is very important to gas sensing applications. The presence of multiple longitudinal modes reduces detection sensitivity, increases the probability of spectroscopic interference, and makes the calibration stability of the instrumentation questionable. Fortunately, laser structures (DFB, DBR) are available that address this problem. Vertical cavity surface emitting lasers (VCSELs) provide single frequency output and hold promise for ultimately having lower manufacturing costs than DFB lasers. Presently, such devices are available only at the shorter wavelengths where gas detection applications are limited principally to  $\text{O}_2$  and  $\text{NO}_2$ , but extension of this laser structure to the longer wavelength InGaAsP domain is eagerly anticipated.

A third important device requirement for diode laser-based gas sensors is reasonable continuity of tuning of the single frequency output. Generally, this need is met by DFB InGaAsP lasers, where continuous temperature tuning of the laser output over at least  $20\text{ cm}^{-1}$  is seen. This tuning continuity allows modest relaxation of the wavelength tolerance specification and guarantees that wavelength modulation detection schemes will not be compromised by mode hops. VCSELs also appear promising in meeting this need. In contrast, Fabry-Perot edge emitting lasers, such as the very inexpensive compact disc player lasers, make very poor spectroscopic light sources. These devices tend to operate at an essentially single frequency if driven at currents well above threshold, but the continuous tuning intervals between mode hops are very small (about 1 or 2  $\text{cm}^{-1}$ ) and the mode hops shift. Although these lasers have been used in many laboratory demonstrations of gas detection applications, it is unlikely that they will ever see application in commercial gas sensors.

## 5. Acknowledgments

This work was supported by the Petroleum Environmental Research Forum under Agreement No. 91-10 and by the U. S. Department of Commerce under Contract No. 50-DKNA-4-00123. We also thank Dr. James McAndrew of American Air Liquide for providing laboratory facilities for testing the sensitivity of the trace moisture sensor.

## 6. References

1. D. S. Bomse, A. C. Stanton, and J. A. Silver, *Appl. Opt.* **31**, 718 (1992).
2. D. E. Cooper and R. E. Warren, *J. Opt. Soc. Am. B* **4**, 470 (1987).
3. D. S. Bomse, *Appl. Opt.* **30**, 2922 (1991).

## TRANSIENT MOLECULAR SPECTROSCOPY WITH A FREQUENCY-DOUBLED DIODE LASER

R. W. Fox, M. Hunter<sup>a</sup>, and L. Hollberg

National Institute of Standards and Technology  
325 Broadway, Boulder, CO 80303

<sup>a</sup>National Atmospheric and Oceanic Administration

**Introduction.** A tunable cw low-amplitude noise laser is useful in the measurement of reaction rate constants of short-lived molecules. We are using an injection-locked diode laser together with a potassium niobate (KNbO<sub>3</sub>) crystal in a build-up cavity to generate tunable blue light. The blue light is then used to measure absorption due to iodine-monoxide (IO). This molecule is believed to play a role in the atmospheric ozone cycle.<sup>1</sup> Chemical reactions involving IO are studied by monitoring transmittance through a flow cell in the wavelength range near 427 nm. IO is produced in the cell by photolysis of I<sub>2</sub> and ozone with an excimer laser pulse; subsequent decay of the IO concentration takes place in approximately 10 ms. To accurately measure these fast reaction rates in low concentrations, optical absorptions of less than 10<sup>-4</sup> are monitored with a 40 kHz bandwidth. Amplitude stabilization of the doubled light is necessary and is implemented with an electro-optic modulator.

**Laser System.** More than 40 mW of tunable, single frequency blue light in the range of 421 to 428 nm is generated by this system, which is based on an injection-locked 150 mW diode laser. The laser power is built-up in a ring cavity containing a 15 mm long KNbO<sub>3</sub> crystal which is temperature controlled to provide a 90° noncritical phase-match for second harmonic generation. A second diode laser, AR coated and built into an extended cavity, is used as a master-laser for injection locking of the high-power diode. As shown in Fig. 1, optical isolators are used to prevent feedback from the ring cavity to the high-power diode and to isolate the master from the high-power diode.

The spectral linewidth of the build-up cavity is approximately 1 MHz, which is narrower than the linewidth of the high-power AlGaAs diode emission. To efficiently couple the diode power to the cavity requires that the laser's linewidth be narrowed, which is accomplished by injection locking with the extended-cavity grating laser (ecl). The injection locking also allows wavelength tuning, since the ecl can be tuned by the diffraction grating over a much wider range than the high-power laser can be with temperature. The ecl is a grazing-incidence type with about 10 mW of output power. By adjustment of the ecl wavelength, the temperature of the

---

<sup>1</sup> S. Solomon, R. R. Garcia, and A. R. Ravishankara, "On the role of iodine in ozone depletion," *J. Geophys. Res.* **99**, 1994.

high-power laser, and the crystal temperature, tuning to any wavelength in the range from 421 to 428 is possible. This range is limited on the long wavelength end by the temperature of the high-power laser, and on the short wavelength end by the tuning of the ecl. With different lasers, the system should be able to generate light down to approximately 417 nm, limited by the phase-matching of the  $\text{KNbO}_3$  crystal.

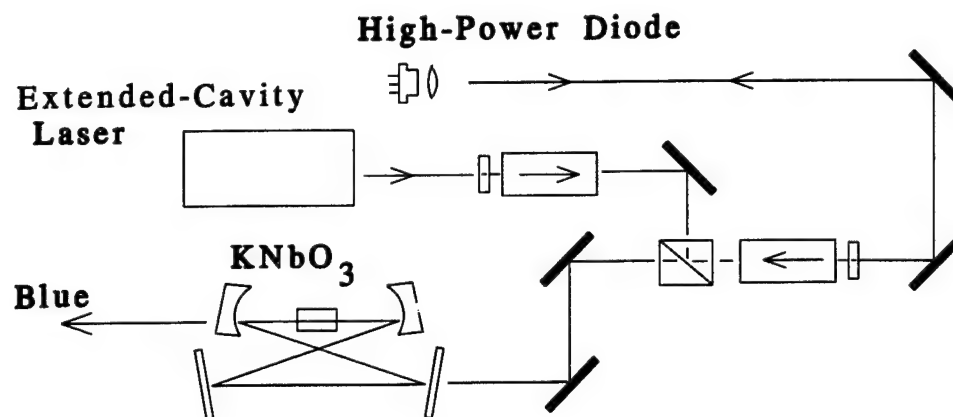


Fig. 1. The optical system to generate 427 nm light. Injection-locking of the high-power diode narrows its linewidth and allows coupling to the build-up cavity. The cavity is resonant in the IR, not the blue. The IR power is nominally in one direction only as shown, however scatter from the crystal and mirrors drives a lower-power backward-travelling wave in the cavity. Optical isolator 1 prevents this backward-travelling wave from returning to the high-power laser and optically locking it. The cavity is electronically locked to the master laser.

The crystal temperature to phase-match 427.2 nm light is about 13°C. This system has also been used for calcium spectroscopy experiments using 422.7 nm light, which requires a crystal temperature of -14°C. The frequency-doubled diode system has been used for cooling calcium atoms in a thermal beam (and for chromium spectroscopy at 425.5 nm). A two-stage Peltier cooler with flowing nitrogen gas was sufficient to achieve -14°C and keep the crystal surfaces free from condensation.

The resonance frequency of the build-up cavity is electronically locked to the master by piezo-electric control of the cavity length. To provide an error signal, a small dither at 50 kHz is imposed on the cavity length and the IR transmittance is phase-sensitively detected, then fed back to the cavity piezo. Without external perturbations the system will remain locked for many hours. When locked, frequency sweeps of approximately 4 GHz are possible by tuning the ecl wavelength; the limitation on single-mode tuning is the range of the piezo-electric transducer.

A cylindrical lens, telescope, and anamorphic prisms are used to spatially mode-match the high-power laser into the cavity. IR power transmitted from the cavity's higher-order spatial modes is less than 3% of the fundamental mode. The losses of the cavity are dominated by the nonlinear generation. A 96.1% input coupler transmission is used. After the mode-matching optics and the isolator, there is 115 mW of IR at the cavity input which produces 40 mW of blue power.

**Detection System.** The double-diode light is relayed to the absorption cell with a 30 m long single-mode fiber, as shown in Fig. 2. Approximately one-half of the power is diverted from the experiment beam and used for an intensity-control servo using an electro-optic modulator. The servo control signal is generated by subtracting a stable offset current from the detected photocurrent, followed by a wideband high-voltage amplifier stage. A loop bandwidth of 1 MHz was achieved. The noise of the experiment beam photocurrent is near the shot noise limit at frequencies well within the loop bandwidth, as expected.<sup>2</sup> In practice the detection sensitivity has been limited by extraneous noise in the experiment arm (after the beamsplitter pick-off). This noise is due to vibration of the optics and cell windows, and by dust particles crossing the beam path.

The IO absorption signal is co-added with a boxcar averager triggered with the excimer laser pulse.

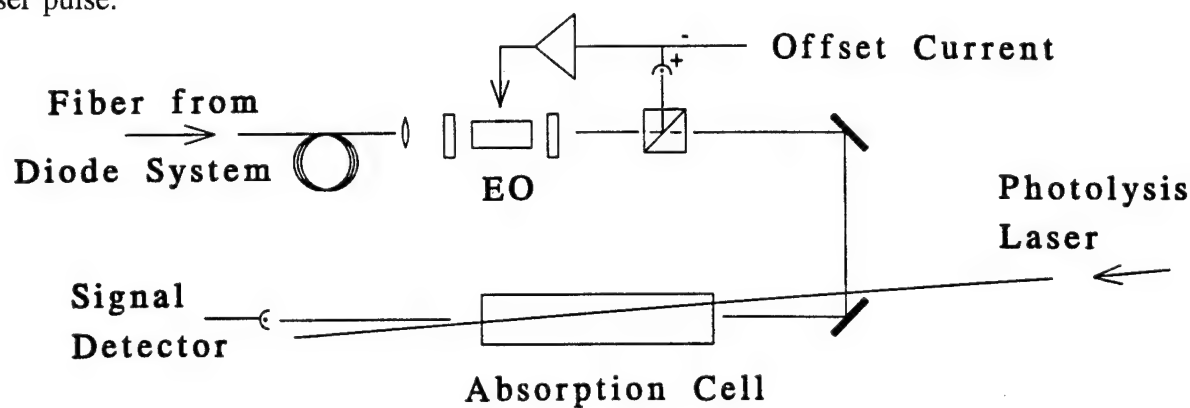


Fig. 2. A 30 m single-mode fiber delivers the 427 nm beam to the absorption cell. Amplitude noise is controlled after the fiber with an electro-optic (EO) modulator and polarizers. Approximately 50% of the doubled-diode power from the fiber is used for intensity control with a 1 MHz servo bandwidth. The diode laser wavelength was fixed at the IO absorption peak of 427.2 nm, and the absorption was detected synchronously with the excimer trigger.

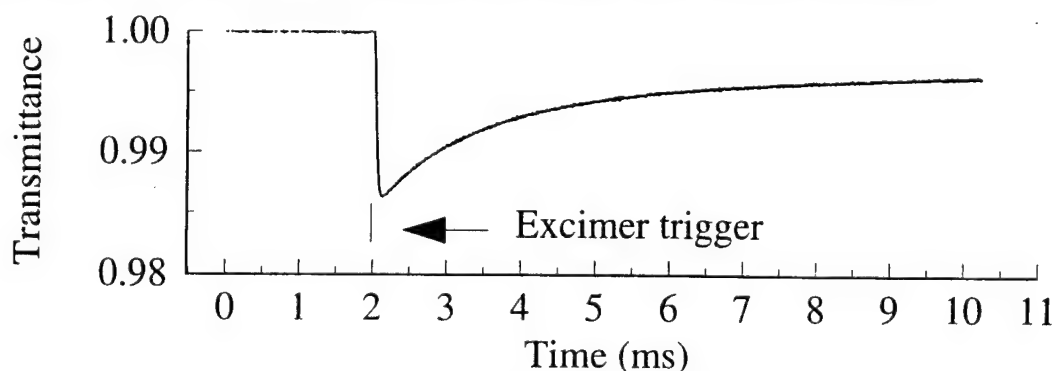


Fig. 3. A representative IO absorption, co-added 10 times with a boxcar averager triggered on the excimer pulse. The path length through the flowing gas cell is 86 cm, and the peak absorption shown is about 1.4%.

<sup>2</sup> R. W. Fox, L. D'Evelyn, H. G. Robinson, C. S. Weimer, and L. Hollberg, "Amplitude modulation on frequency locked extended cavity lasers," SPIE Proc. 2378, 1995.

## **Stimulated Raman Spectroscopy with a Modulated External Cavity Diode Laser**

C. S. Wood, S. C. Bennett, D. Cho, C. E. Wieman

*Joint Institute for Laboratory Astrophysics, and Dept. Of Physics,  
Campus Box 440, University of Colorado, Boulder, Colorado 80309  
(303) 492-6839, fax: (303) 492-8994*

The usefulness of stimulated Raman transitions has been demonstrated in a variety of different applications. These two-photon transitions have the capability of very high resolution because the transition linewidths depend on the relative jitter between two frequencies, rather than absolute jitter on either one. Recent demonstrations include laser cooling and atomic interferometry [1]. They may also be needed for improved atomic clocks [2]. Due to this high resolution, stimulated Raman transitions can be a direct replacement for a microwave cavity and are often more compatible with optical experiments because a laser beam requires less space.

The most difficult requirement for stimulated Raman spectroscopy is the generation of two optical frequencies which have relative jitter much less than the linewidth of the transition of interest. For applications in atomic physics the linewidths of Raman transitions are on the order of a few kHz or less, which virtually excludes the possibility of using two independent lasers. One common method is to use a microwave electro-optic modulator (EOM) to generate correlated sidebands. For atoms with large hyperfine splittings, this method becomes costly. As an example, experiments with cesium (9 GHz splitting) frequently use low power diode lasers, and a microwave EOM is much more expensive than the diode lasers. Another, more difficult alternative in this case is the use of two diode lasers in an optical phase-locked-loop to reduce the relative jitter between the lasers to an acceptable level [3].

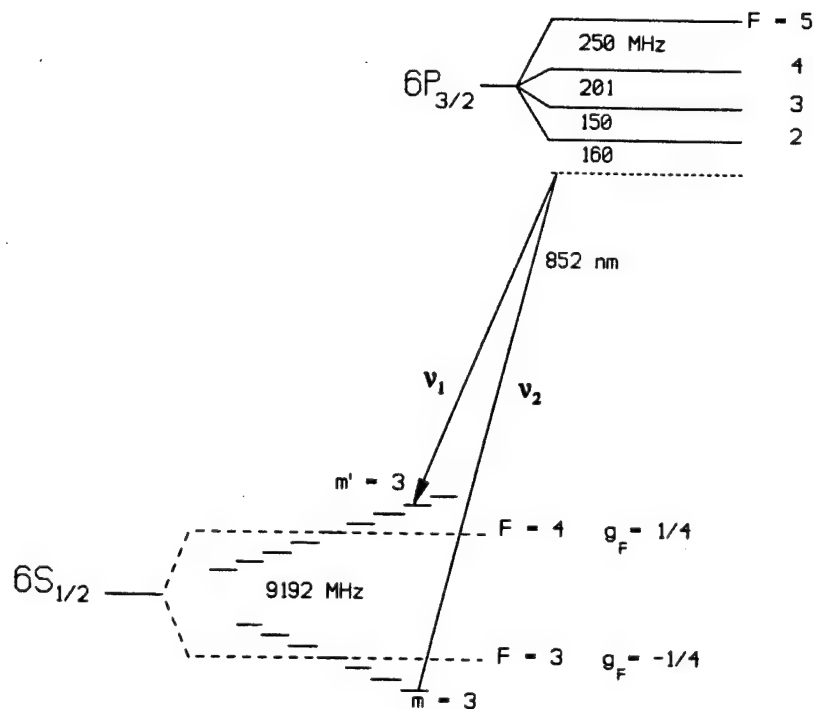
A simpler, less expensive alternative is to use a single diode laser, and modulate its injection current to produce correlated sidebands. This is very easy at low frequencies, but typical diode lasers have relaxation oscillations in the 2-3 GHz range and above that the modulation response drops rapidly. With an external-cavity diode laser, though, a significant enhancement in the modulation at microwave frequencies can be realized by matching the external cavity free spectral range with the modulation frequency [4]. The external-cavity-enhanced modulation can be understood as a kind of mode locking. This technique dramatically reduces the cost and complexity of the optical/microwave setup necessary to perform Raman transitions in cases where diode lasers are available.

The free spectral range of the external cavity diode laser used to generate the Raman frequencies is set near 4.6 GHz. The tunable microwave source used to modulate the



injection current is a YIG oscillator driven by a homemade current supply. There is a resonant enhancement in the modulation response when the modulation frequency is near the external cavity free spectral range, or near a harmonic of it. Multi-mode behavior (random phases between external cavity modes) can be distinguished from "mode-locked" behavior (same phase between external cavity modes) by adjusting the injection current and observing the instability of the sideband amplitudes in the multi-mode case.

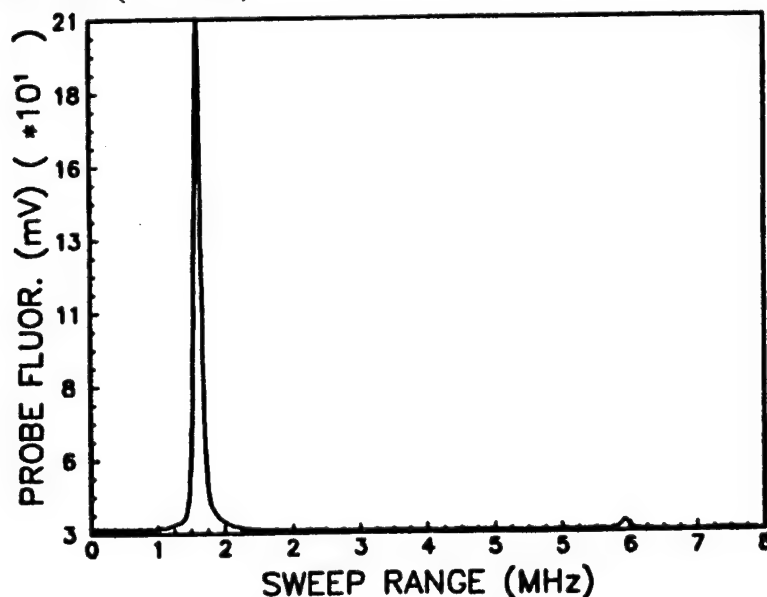
To observe Raman transitions in a cesium beam with only a few microseconds of interaction time, an intensity of about  $50 \text{ mW/cm}^2$  is required. For typical diode lasers this means that a significant fraction of the light must be placed in the first order sidebands. With the external cavity enhancement, 50% of the laser power can easily be placed in the first order sidebands without using elaborate microwave coupling techniques. By modulating the laser current at 4.6 GHz the two first order sidebands have the proper separation of 9.2 GHz to drive Raman transitions in cesium. The relevant lowest lying levels of cesium are shown below, as well as a specific Raman transition.



A parity non-conservation (PNC) measurement being performed in our lab utilizes an optically pumped cesium beam. The optical pumping, done with three external cavity diode lasers, forces nearly all of the atoms (98%) into the magnetic sublevel under investigation. The remaining 2% in nearby states contribute to an important potential systematic error in the PNC measurement, and must be precisely measured. Previously, state-selected atomic beams have been analyzed using a microwave cavity. This technique had several complications which prevented us from using it. The equivalent



Raman system works much better. The following figure shows a graph of the  $\Delta m=0$  Raman transitions observed when optical pumping is performed to put the atoms into the  $6S F=3, m_F=3$  state. Together with a precise calibration of the Raman linestrengths, this graph implies  $98.3 \pm 0.3\%$  of the atoms in  $6S F=3, m_F=3$  and  $1.7 \pm 0.3\%$  in  $6S F=3, m_F=2$ . All other states contain negligible population. The transition linewidths are determined by the interaction time with the Raman laser beam, and are narrower than the absolute linewidth of the laser ( $\leq 1$  MHz).



We have demonstrated that a single diode laser can be used to perform precision Raman spectroscopy in cesium. The optical frequencies required are derived from a modulated, external cavity diode laser whose free spectral range is set to match the modulation frequency. The technique, which is analogous to mode-locking, significantly decreases the cost of the Raman setup. Our system has been used to perform precision measurements of magnetic sublevel population distributions in an optically pumped cesium beam. This system has a further advantage over traditional techniques such as a microwave cavity because it requires only that a laser beam be sent into the vacuum chamber. Possible applications of this technology include single-laser traps [5], velocity selective Raman transitions, optical Ramsey fringes, and an all-optical atomic clock.

- [1] M. Kasevich, S. Chu, Phys. Rev. Lett., 70, 2706 (1993).
- [2] K. Gibble, S. Chu, Phys. Rev. Lett., 70, 1771 (1993).
- [3] Chul-Ho Shin, Motoichi Ohtsu, IEEE J. Quan. Elec., 29, 374 (1993), G. Santarelli, A. Clairon, S. N. Lea, G. M. Tino, Optics Comm., 104, 339 (1994), D. S. Weiss, B. C. Young, S. Chu, Phys. Rev. Lett., 70, 2706 (1993).
- [4] C. E. Wieman, L. Hollberg, Rev. Sci. Instrum., 62, 1 (1991).
- [5] C. J. Myatt, N. R. Newbury, C. E. Wieman, Optics Letters, 18, 651 (1993).

# Tunable Infrared Source by Difference Frequency Mixing Diode lasers and Diode pumped YAG, and Application to Methane Detection

S. Waltman<sup>2</sup>, K. Petrov<sup>1</sup>, U. Simon<sup>1</sup>,  
L. Hollberg<sup>2</sup>, F. Tittel<sup>1</sup>, and R. Curl<sup>1</sup>

<sup>1</sup> Departments of Electrical and Computer Engineering, and Chemistry  
Rice University, Houston, Texas 77251-1892

<sup>2</sup> National Institute of Standards and Technology  
325 Broadway, Boulder CO 80303  
fax 303-497-7845

Tremendous potential exists for the application of diode laser sources for high sensitivity detection of atoms and molecules. Some of the obvious applications include pollution monitoring, medical diagnostics, industrial process monitoring, and analytic and atmospheric chemistry applications. Room-temperature, tunable diode laser sources provide the opportunity for constructing compact, transportable instrumentation. Unfortunately the wavelengths of most of the atomic and molecular transitions are not directly accessible with commercially available, room-temperature diode lasers. In particular many of the important molecular transitions are in the mid-infrared spectral region. However, this spectral region is accessible with difference-frequency-generation (DFG) using visible and near-IR lasers.

We have constructed a DFG system that generates about 10  $\mu\text{W}$  of IR that is tunable between 3.1 and 3.4  $\mu\text{m}$  (3076 to 3183  $\text{cm}^{-1}$ ). The basic structure of the DFG system is diagramed in Fig. 1. The input frequencies come from a diode laser, tunable near 800 nm, and a diode-pumped YAG at 1064 nm. The difference frequency radiation is generated in a 5 mm long  $\text{AgGaS}_2$  crystal that is located at the waist of a ring buildup cavity. The buildup cavity is used to enhance the power of the 1064 nm beam. The diode laser light is collinear with the 1064 nm beam but is not resonated in the ring cavity. This arrangement allows us to tune the diode laser and hence the DFG wavelength without having to synchronously track the buildup cavity resonance frequency. The broad wavelength coverage between 3.1 and 3.4  $\mu\text{m}$  is accomplished with a single diode laser using a grating in an extended-cavity configuration. The mixing crystal is angle tuned using a rotation stage. With 40 mW of diode laser power and 230 mW of Yag power the system generates about 6  $\mu\text{W}$  of infrared.

A number of techniques were evaluated for the methane spectroscopy and high sensitivity detection. These include: direct absorption in a single pass configuration, FM derivative spectroscopy, Fabry-Perot cavity-enhancement of the 3  $\mu\text{m}$  radiation, and active noise suppression of the 3  $\mu\text{m}$  power by using an AO-modulator in the diode laser beam. Each of these systems has advantages and disadvantages but all of them demonstrated very good detection sensitivities for methane. Figure 2 shows example spectra of methane taken with the derivative method for three different methane concentration levels in air. These data were taken at a sample pressure of about 100 Torr in a single pass through a 59 cm sample cell. Our best results so far have been with direct detection and active noise suppression, and resulted in an excellent noise-limited detection sensitivity of approximately 20 ppb $\cdot\text{m}/\sqrt{\text{Hz}}$ .

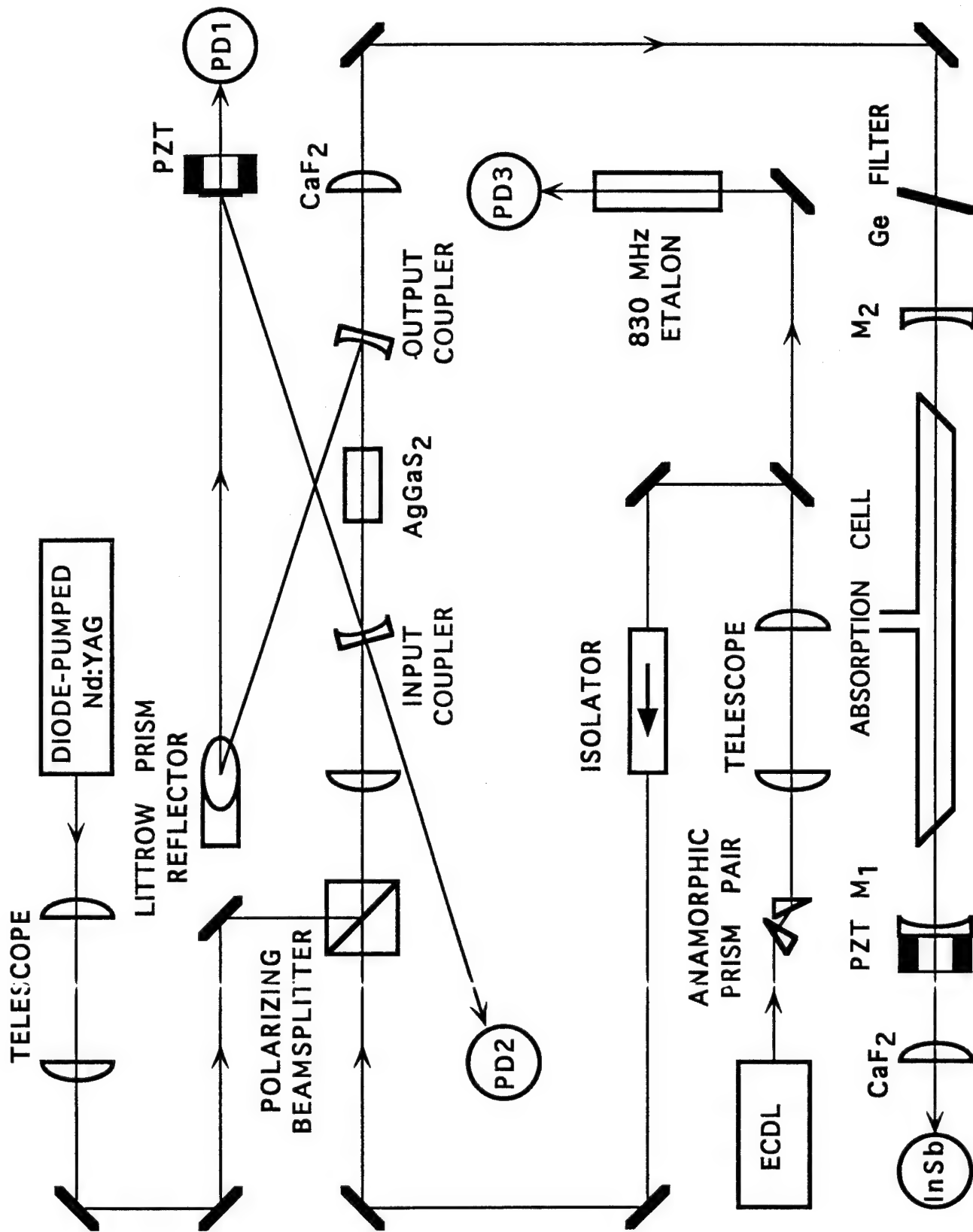


Figure 1

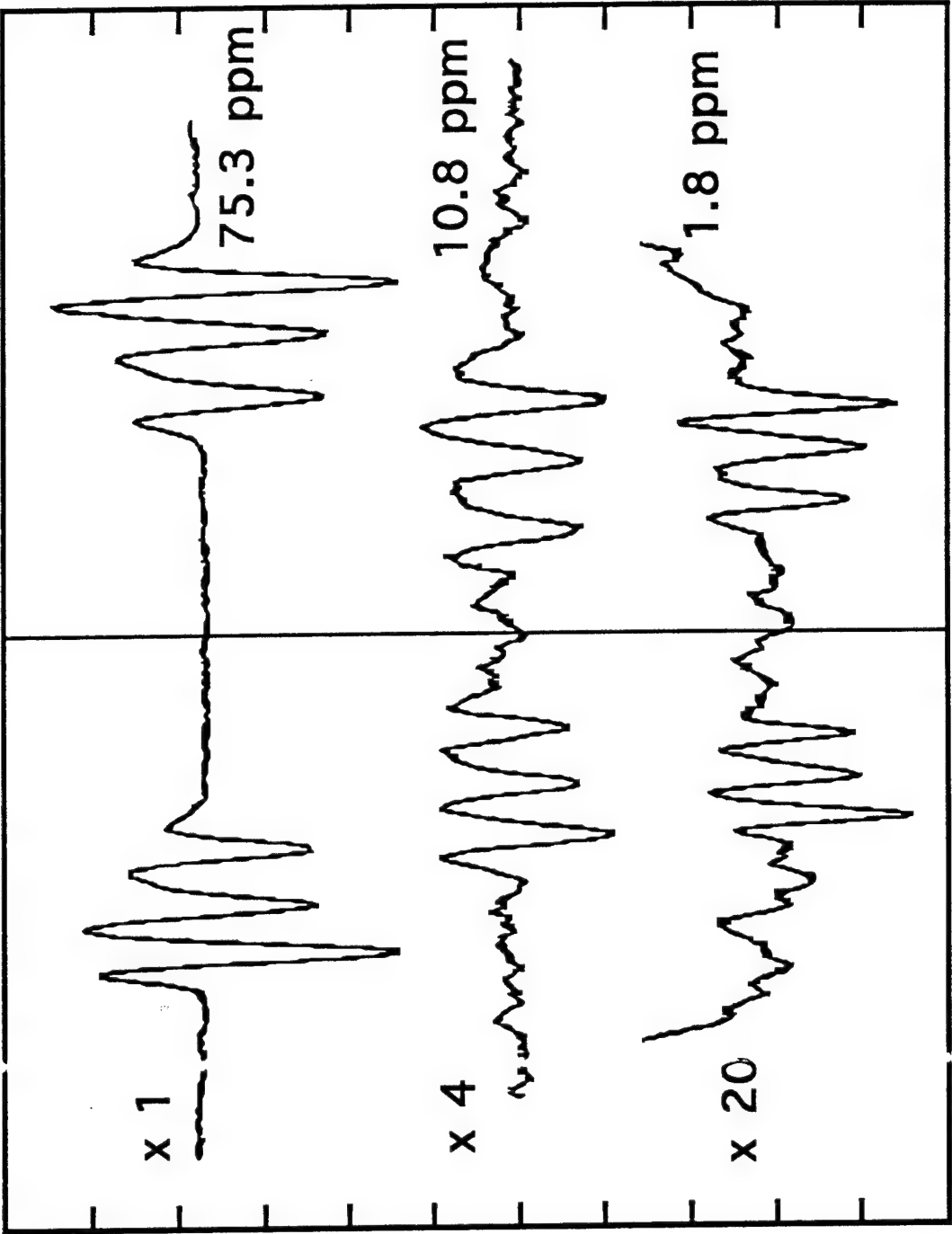


Figure 2

# TUNNEL-INJECTION LASER BASED ON TYPE II BROKEN-GAP p-GaInAsSb/p-InAs SINGLE HETEROJUNCTION

Yu.P.Yakovlev, K.D.Moiseev, M.P.Mikhailova, O.G.Ershov

A.F.Ioffe Physical Technical Institute, RAS,  
26, Polytechnicheskaya st., St.Petersburg, 194021, Russia  
phone: (812) 247-9956, fax: (812) 247-1017, E-mail: yak@les.pti.spb.su

We present a new physical approach to design of III-V middle-infrared diode lasers which can lead to increasing operating temperature of InAs-based lasers. Main peculiarity of proposed method is using interface radiative recombination of spatially-separated carriers in type II broken-gap p-p heterojunctions (HJs). Lattice-matched nondoped and doped  $\text{GaIn}_{0.17}\text{As}_{0.22}\text{Sb}$  layers with high quality interface were grown on p-InAs (100). It was established that  $\text{GaIn}_{0.17}\text{As}_{0.22}\text{Sb}/\text{InAs}$  HJ is type II with broken-gap alignment.

Intensive spontaneous electroluminescence (EL) was first observed in isotype p- $\text{GaIn}_{0.17}\text{As}_{0.22}\text{Sb}/\text{p-InAs}$  structure in the range of  $T=77\text{-}300\text{ K}$  at applied bias  $0.4\text{-}4.0\text{ V}$ . Two narrow emission bands with full width at half maximum (FWHM) 10 and 20 meV were found in EL spectra in the spectral range 3-4  $\mu\text{m}$  (fig.1). Energy band scheme of the p-p single HJ under external electric field was considered for analyse of EL experimental results (fig.1, insert). We found that unusual EL due to indirect (tunnel) radiative recombination of 2D-electrons localized in quantum well at InAs-side with holes confined in quaternary layer. Existence of 2D-electron channel in p- $\text{GaIn}_{0.17}\text{As}_{0.22}\text{Sb}/\text{p-InAs}$  heterostructure was established by Shubnikov-de-Haas oscillations and was confirmed by scanning electron microscopy of the HJ cleaved surface.

Using observed phenomenon we proposed and realized new laser structure on the base of InAs solid solutions. Mesa-stripe laser structure consisting of 6 layers was grown by LPE on InAs substrate (see fig.2, insert) and contained in an active layer type II broken-gap structures based on two quaternary alloys: wide-gap p- $\text{GaIn}_{0.17}\text{AsSb}$  ( $E_g=0.63\text{ eV}$  at  $T=77$

K) and narrow-gap p-GaIn<sub>0.83</sub>AsSb ( $E_g=0.39$  eV at  $T=77$  K) HJ. For improving electron and optical confinement we used wide-gap GaInAsSb and InAsSbP cladding layers. Single-mode coherent emission was obtained with wavelength  $3.26 \mu\text{m}$  at  $77$  K (fig.2). Threshold current density ( $J_{th}=J_0\exp(T/T_0)$ ) depended slightly on temperature in the range of  $77$ - $110$  K. High characteristic temperature  $T_0=30$ - $60$  K and  $J_{th}=2\text{kA/cm}^2$  were achieved. It is highest  $T_0$  value for InAs-based lasers [1].

This result is due to using interface recombination transitions at type II heteroboundary. It leads to a weaker temperature dependence of Auger-recombination rate [2] and, in addition, to suppressing of Auger-recombination caused spin-orbit splitting valence contribution.

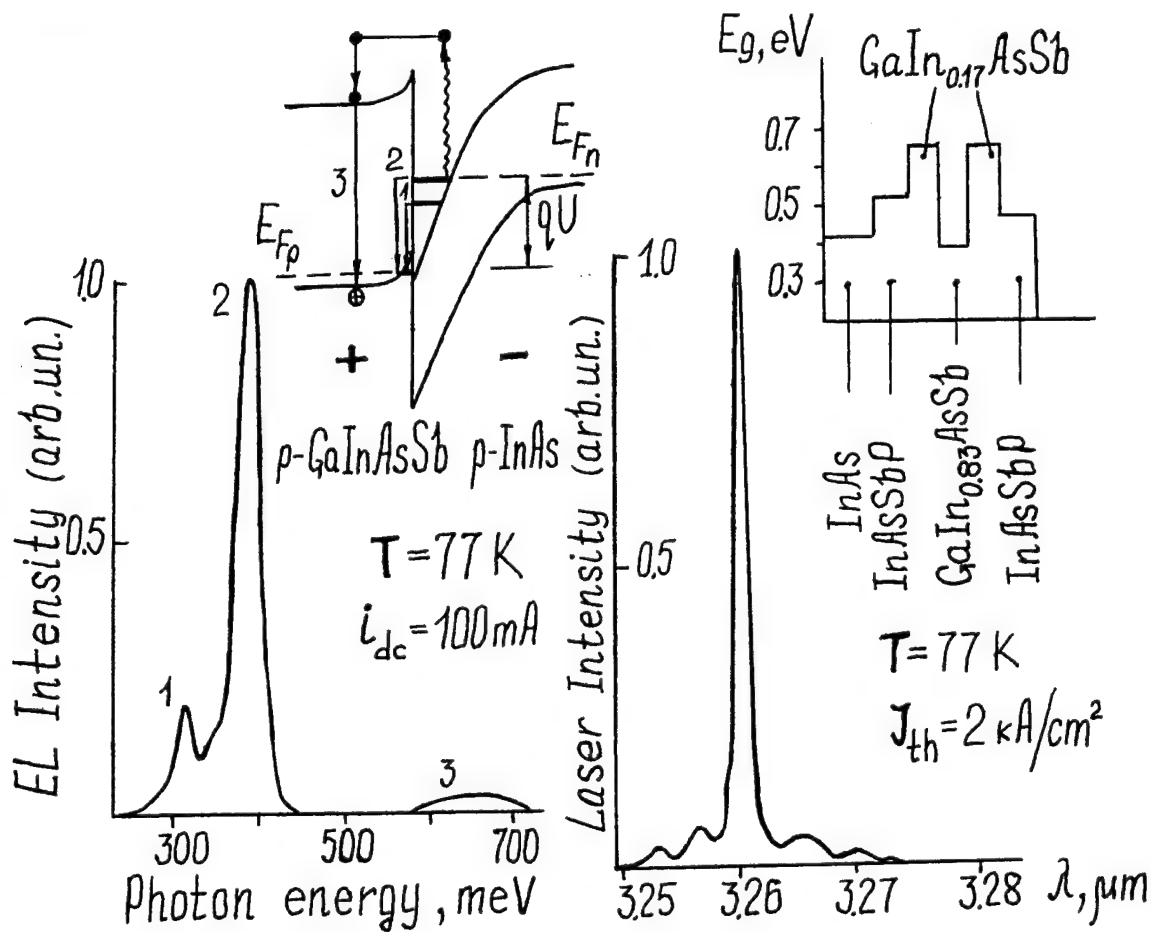


Fig.1. Electroluminescence spectra of p-GaIn<sub>0.17</sub>AsSb/p-InAs HJ under applied bias

Fig.2. Novel laser structure

1. A.N. Baranov, T.N. Danilova, O.G. Ershov, A.N. Imenkov, V.V. Sherstnev, Yu.P. Yakovlev // Sov. Tech. Phys. Lett., 1993, v.18, 725
2. G.G. Zegrya, A.D. Andreev // JETP, 1995, v.75, in print

# Theoretical Analysis of Gain in Compressive Strained Quantum Well InAlAsSb/GaSb Structures for 3-4 $\mu\text{m}$ Lasers

R.F. Nabiev, C.J. Chang-Hasnain  
E.L. Ginzton Laboratory, Stanford University  
Stanford, CA 94305-4085

H.K. Choi  
MIT Lincoln Laboratory  
244 Wood St., Lexington, MA 02173-9108

**Introduction.** Mid-infrared laser diodes are important sources for laser radar systems, molecular spectroscopy, and remote sensing of pollution and gases. InGaSbAs/GaAlSbAs lasers emitting at 2  $\mu\text{m}$  are explored in detail since first room-temperature (RT) lasers [1-3] were demonstrated. However, a breakthrough in 3-4  $\mu\text{m}$  lasers was made only recently [4-6]. Long wavelength lasers exhibit low characteristic temperature ( $T_0 \leq 30$  K [6]), preventing them from operation at RT. One of the possible reasons of high threshold current at RT is Auger-recombination, which is proportional to cube of carrier density. Therefore, for long-wavelength lasers, it is especially important to decrease the carrier density at threshold.

In this paper, we present for the first time, to our knowledge, an analysis of quantum well (QW) InAlAsSb lasers emitting at 3-4  $\mu\text{m}$  wavelengths grown on a GaSb substrate. We show that, in compressive strained QW structures, the carrier density as low as  $6 \cdot 10^{17} \text{ cm}^{-3}$  can provide an optical gain of  $500 \text{ cm}^{-1}$ . The differential gain is as high as  $2.5 \cdot 10^{-15} \text{ cm}^2$  for a lattice mismatch of 1.5%. Such a structure promises increased operating temperature for mid-infrared lasers.

**Structure.** We use 10 nm thick  $\text{In}_x\text{Al}_{1-x}\text{As}_y\text{Sb}_{1-y}$  quantum wells with  $\text{In}_x\text{Al}_{1-x}\text{As}_y\text{Sb}_{1-y}$  barrier with different compositions. Using quaternary QW one can match the desirable energy gap and strain. An increase in Sb content in QW results in a higher compressive strain and a decrease of energy gap, while an increase of As content results in a tensile strain and an energy gap increase. Energy gap dependence on composition is  $E_g[\text{eV}] = 2.22 - 2.478 \cdot x + 0.43 \cdot x^2 + 0.798 \cdot y - 1.458 \cdot x \cdot y + 0.268 \cdot x^2 \cdot y + 0.58 \cdot x \cdot y^2$ . In and As contents used in this work are listed in Table 1. For the unstrained material, the QW depth in valence band is only 26 meV. Therefore, we do not consider this case. We choose  $\text{In}_{0.8}\text{Al}_{0.2}\text{As}_{0.73}\text{Sb}_{0.37}$  as a barrier. Its refractive index is 3.48 and 3.45 at  $\lambda = 3.2 \mu\text{m}$  and  $4 \mu\text{m}$ , respectively. Cladding material of  $\text{AlAs}_{0.08}\text{Sb}_{0.92}$  with index 3.22 at  $\lambda = 3.2 \mu\text{m}$  (3.21 at  $\lambda = 4 \mu\text{m}$ ) provides an optical confinement factor about 0.8-1% for a 10 nm thick QW.

**Model.** Valence subband structure is calculated using a 4x4 Hamiltonian for complex valence band structures [7]. Radiative recombination current is calculated by integrating the spontaneous recombination rate over all photon energies. Luttinger and strain parameters, and relative position of valence bands are calculated as a linear interpolation of corresponding values for binaries taken from Refs. [7-10]. Quantized states in conduction band are calculated by taking account of different electron masses in QW and barrier.

**Table 1.** In and As contents in  $\text{In}_x\text{Al}_{1-x}\text{As}_y\text{Sb}_{1-y}$  QW material for different values  $\epsilon$  of lattice mismatch. Barrier material is  $\text{In}_{0.8}\text{Al}_{0.2}\text{As}_{0.73}\text{Sb}_{0.37}$

	$\epsilon = -0.5\%$		$\epsilon = -1.0\%$		$\epsilon = -1.1\%$		$\epsilon = -1.5\%$	
$\lambda, \mu\text{m}$	x	y	x	y	x	y	x	y
3.2	0.967	0.808	0.951	0.721			0.940	0.640
4.0					1.0	0.75	0.988	0.682



**Results and discussion.** Figs. 1a and 1b show the valence subbands and hole density-of-states (DOS) dispersion for two compressive strained QWs with  $\epsilon = -0.5\%$  and  $-1.5\%$ , respectively. Strong band mixing in  $\epsilon = -0.5\%$  QW results in effectively larger hole mass, and higher DOS. In the case of  $\epsilon = -1.5\%$ , the hole mass is about  $0.03m_0$  over  $\sim 30$  meV near band edge, and the DOS is considerably lower (cf. Figs. 1a and 1b).

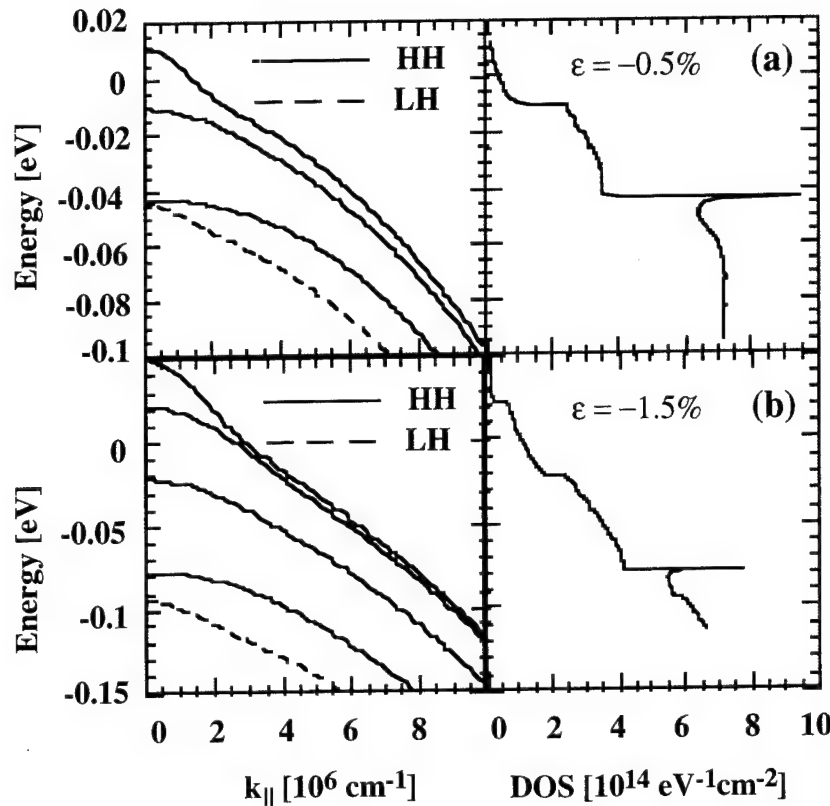


Fig. 1. Valence subband and hole density-of-states dispersions in 10 nm InAlAsSb QW of 3.2  $\mu\text{m}$  laser. Strains are  $-0.5\%$  (a) and  $-1.5\%$  (b).

Dependence of gain on the carrier density and radiative recombination current is shown in Fig. 2. The compressive strain results in a considerable decrease in transparent carrier density and an increase in differential gain. For a given strain  $\epsilon$ , the gain at 4  $\mu\text{m}$  is larger than that at 3.2  $\mu\text{m}$  because QW in the former case is deeper. Radiative current density (Fig. 2b) is only 20-30 A/cm<sup>2</sup> in strained QW.

Dependence of gain on the carrier density can be approximated by a function  $g = a + b \cdot \log_{10}(n/10^{18} \text{ cm}^{-3})$  fairly accurately in a gain region from 0 to 1000 cm<sup>-1</sup>. The stress dependence of  $a$  and  $b$  parameters is shown in Fig. 3. These curves are convenient tool for a QW design.

To decrease Auger-recombination in the active region, one must keep the threshold carrier density low. Fig. 4 shows temperature dependence of the carrier density in QW and differential gain at a gain  $g$  of 500 cm<sup>-1</sup> for different strain parameters  $\epsilon$  for lasers emitting at  $\lambda = 3.2 \mu\text{m}$  (a) and 4  $\mu\text{m}$  (b). At the confinement

factor of 1% such a material gain corresponds to the modal gain of 5 cm<sup>-1</sup>, and 8-10 QWs are necessary to achieve a

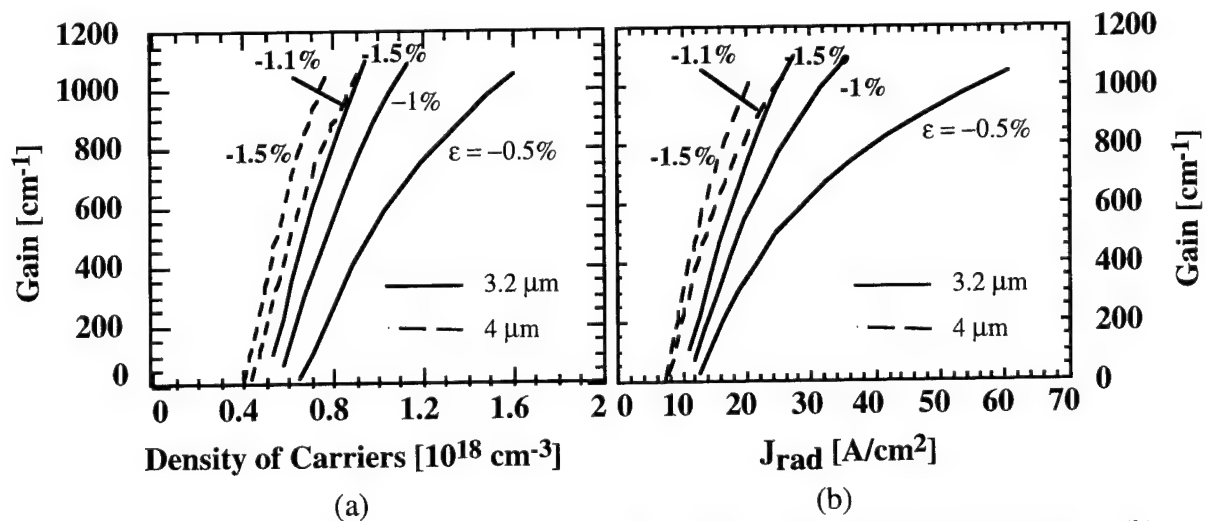


Fig. 2. Dependence of gain on the carrier density (a) and the radiative recombination current density  $J_{\text{rad}}$  (b) in InAlAsSb QW emitting at 3.2  $\mu\text{m}$  and 4  $\mu\text{m}$ .

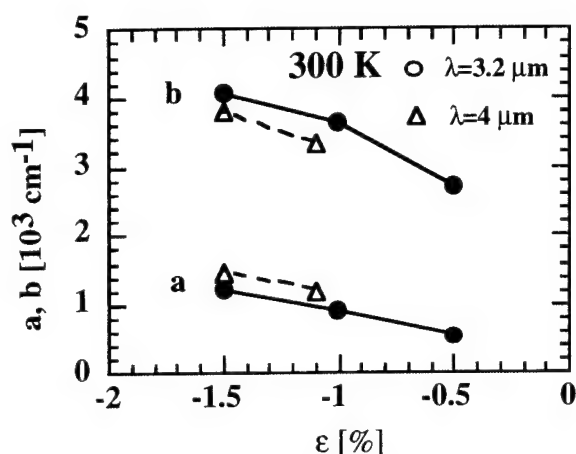


Fig. 3. Dependence of gain parameters  $a$  and  $b$  on strain in 10 nm InAlAsSb QW. Optical gain is  $g = a + b \cdot \log_{10}(n/10^{18} \text{ cm}^{-3})$ .

lasing threshold. In the strained QW with  $\epsilon = -1.5\%$ ,  $n = 5.5 \cdot 10^{17} \text{ cm}^{-3}$  and  $6.8 \cdot 10^{17}$  for 3.2 and 4  $\mu\text{m}$  QW, respectively. The strain considerably reduces the carrier density and increases the differential gain for a given gain value. Therefore, the Auger-recombination rate should be much lower in the strained QW. The differential gain  $dg/dn = (2.5-3) \cdot 10^{-15} \text{ cm}^2$  in the strained QW with  $\epsilon = -1.5\%$  and this value is 2.5 times larger than that for QW with  $\epsilon = -0.5\%$ . The value of characteristic temperature  $T_0$  for the carrier density is about 160K which corresponds to 55 K for Auger recombination rate. The value of characteristic temperature for the decrease in differential gain is about 120 K.

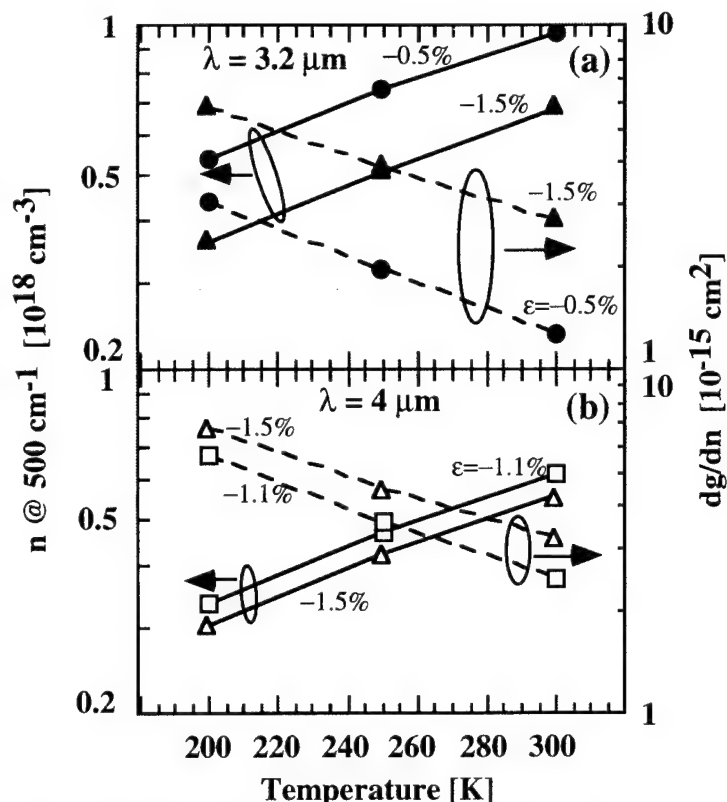


Fig. 4. Temperature dependence of carrier density  $n$  and differential gain  $dg/dn$  in 10 nm QW at gain of  $500 \text{ cm}^{-1}$

**In conclusion**, our calculations based on Luttinger-Kohn Hamiltonian show that the compressive strain considerably improves parameters of 3-4  $\mu\text{m}$  InAlAsSb QW lasers. In the strained structure with  $\epsilon = -1.5\%$  optical gain of  $500 \text{ cm}^{-1}$  can be achieved at carrier densities of  $5.5 \cdot 10^{17} \text{ cm}^{-3}$ . Differential gain in strained QW is as high as  $2.5 \cdot 10^{-15} \text{ cm}^2$ . Further improvement of gain characteristics of QW can be achieved in structures with additional tensile strain in barriers, and this structures are under current investigation.

**Acknowledgement:** The authors acknowledge the support from the Powell and Sloan Foundations (Stanford) and Phillips Laboratory, the Department of the Air Force (MIT Lincoln Laboratory).

#### References:

1. A.E. Bochkarev et al. Sov. J. of Quant. Electron., **18**, 1362 (1988).
2. A.N. Baranov et al. Sov. Tech. Phys. Lett., **14**, 798 (1988).
3. S.J. Eglash, H.K. Choi. Appl. Phys. Lett., **57**, 1292 (1990).
4. S.J. Eglash, H.K. Choi. Appl. Phys. Lett., **64**, 833 (1994).
5. H.K. Choi, G.W. Turner, Z.L. Liao. Appl. Phys. Lett., **65**, 2251 (1994).
6. H.K. Choi, G.W. Turner, H.Q. Le. "GaSb-based semiconductor lasers in the 4- $\mu\text{m}$  band". Paper presented at the International Narrow Bandgap Conference. Santa Fe, New Mexico, Jan. 1995.
7. D. Ahn et al. J. Appl. Phys., **64**, 4056 (1988). S. L. Chuang. Phys. Rev., B **43**, 9649 (1991).
8. C.G. Van de Walle. Phys. Rev., **B39**, 1971 (1989).
9. A. Ghiti, E.P. O'Reilly. Semicond. Sc. Technol., **8**, 1655 (1993).
10. A.T. Meney, E.P. O'Reilly. Phys. Rev., **B50**, 10893 (1994).



Monday, August 21, 1995

# High Power Lasers: Applications and Devices

**MC** 7:00 pm-9:00 pm  
Torreys Peak I-III

Richard Williamson, *Presider*  
*MIT Lincoln Laboratory*

## High power lasers for medical and graphic arts printing applications,

W. Stutius\* and L. Heath\*\*,

\* *Polaroid Corporation, N1-1C, Norwood, MA 02062*

\*\* *Polaroid Corporation, W4, Waltham, MA 02154*

Ecological concerns and time and cost saving measures have started a trend towards dry-processed, high quality image recording media for digital medical and graphic arts imaging applications. As compared to silver-halide film based systems, the photosensitive layers in most of these media are considerably less sensitive than traditional wet-processed film and therefore require a high laser power for exposure. In addition, advanced screening methods, like FM or stochastic screening, require an extremely well controlled laser spot size. The most recent developments in the graphic arts industry are directed towards eliminating film as an intermediate step for plate-making altogether and instead writing the image (comprising text, line art and pictures) directly onto plates. What these technological developments have in common is that, independent of the specific method for implementation, they all rely on various high power laser sources with extremely well controlled beam properties for writing the image. This talk will address the present status of laser requirements for non-silver-halide-based medical and graphic arts printing, as well as impending industry-wide technological changes and the resulting "wish list" for advanced laser sources.

### Dry (non-silver halide) media

Wet-processed, silver halide photographic film is still unsurpassed in terms of its sensitivity to exposure to light. Energies in the order of  $\text{ergs/cm}^2$  will expose the silver grains. Increasing ecological concerns and regulatory restrictions are accelerating an industry-wide trend towards completely "dry" processing and finishing, even eliminating water in a rinse step. The "dry" systems are based on electrophotography, dry silver, photopolymers or strictly thermal media, all of which have sensitivities many orders of magnitude less than photographic film ( $\sim 10^7$   $\text{ergs/cm}^2$  for thermal media). As a result, "dry" systems require powerful, modulatable exposure sources for high speed writing of images.

### Generation of digital gray scale

The various gray levels are almost exclusively created by "halftoning", i.e. a portion of an area in an image is rendered opaque to the transmission of light. The transmitted light intensity is directly proportional to the ratio of the transparent over the opaque areas. It was found empirically that the human eye will notice changes in lightness (or optical density, OD) between 9 bit (512) gray levels equally spaced in perceived OD. Because of the logarithmic relationship between OD and the transmitted intensity, extremely small dots are required in order to properly render  $D_{\text{max}} - 1$  with the spatial resolution demanded by modern printing applications (several hundred to several thousand lines per inch). Minimum dot sizes with areas of  $\sim 15 \mu\text{m}^2$  are now becoming the norm.

In digital halftoning, opaque areas can be created in two ways: by varying the area coverage of a specific dot (AM screening) or by varying the distance between dots of equal area (FM or stochastic screening). FM screening results in fewer artifacts, especially Moiré patterns, but requires stringent control of dot size during dot generation and processing. It is easily appreciated that lateral dimensions dots of  $\sim 5 \mu\text{m}$  are difficult to maintain in a controlled and repeatable fashion, especially with affordable optical elements, suitable working distance, and a reasonable depth of focus.

Conventional analog recording on photographic film will in many applications not result in the required high MTF (Modulation Transfer Function) due to diffusion (exacerbated by wet processing) and stochastic processes. Digital halftone images on "dry" media, exposed by lasers, provide a highly deterministic imaging mechanism, in addition to being environmentally friendly.

## Digital Medical Printers

Medical digital imaging modalities, such as computed tomography, magnetic resonance imaging and digital radiofluoroscopy, have proliferated, and high-resolution digital x-ray imagers are also expected to displace traditional x-ray technology. Most silver-halide film based printers operate very much like conventional office laser printers, i.e. employing low power single-mode IR laser diodes. The "dry" Polaroid Helios™ Medical Imaging System, on the other hand, due to its much lower sensitivity, uses a print head with a total of 4 laser diodes, each emitting ~1 Watt CW; it images the demagnified near-fields of these lasers onto an external drum. Finished prints range in size from 8" x 10" to 14" x 17", with print speed between 1 - 2 prints/minute. We will discuss the principle of operation of the Helios™ medical printer, as well as advanced print head concepts and associated laser requirements.

## Graphic Arts Printers

The name "Graphic Arts" comprises the creation, composition, and printing of image and text information. In these days, information is created and processed by computers which in turn render digital output files. These files are then outputted by a variety of printers, ranging from desktop laser and ink jet printers to offset printers for printing magazines and newspapers. We will here describe the application of lasers in commercial printing, where tens and hundreds of thousand impressions are made from a single printing plate.

In the "traditional" plate making, a film is exposed photographically, and then this photographic film is used as a mask for exposing a plate coated with a layer sensitive to UV light. Most recently, for cost saving reasons, a new technology, called Computer-to-Plate, is gaining ground, where film as an intermediate carrier is eliminated and plates are exposed directly with laser light. Depending on the chemistry of the light sensitive layer used in either film-based or filmless applications, different kinds of lasers are employed. Silver halide and photopolymer based imaging layers use Ar or IR diode lasers, often in multibeam configuration, whereas media based on photothermal or phototackification effects require more powerful lasers, mainly solid state lasers. In another, recently developed printing method for prepress and proofing applications, called "Laser Ablation Transfer" or LAT, a powerful short laser pulse evaporates an absorptive layer in a microscopic "explosion" and transfers actual printing inks onto actual printing stock. We will discuss the requirements for beam properties of these lasers (wavelength, power,  $M^2$ , stability, etc.) and compare these requirements with the performance of semiconductor lasers.

## Print engines

Digital printers for dry-processed media can basically be divided into two different groups based on their inherent design: *external drum* and *internal drum* printers. Because of the very different working distances, the two types of printers require different lasers and different optics.

In an external drum printer, the media is secured to the outside of a rotating drum, and a laser-based exposure system travels along the outside parallel to the axis of rotation, thereby exposing the media along a helical track. This is the principle of operation for Polaroid's Helios™ Medical Imaging System and for the Heidelberg/Presstek GTO-DI Computer-to-Plate printing press. Exposure sources in external drum machines are presently diode lasers or diode laser arrays, with fiber pigtails or free space optics delivering the optical energy to the media. The print spot is basically defined by the near-field image of the diode.

In an internal drum printer, the media is positioned in a semicircle inside a stationary drum. A spinning lens/mirror assembly travels along the center axis of the stationary drum, thereby exposing the media along a helical track. Because of the long working distances of several 10 cm and the small spot size, the laser beam has to be single spatial mode ( $TEM_{00}$ ). The writing speed can exceed 250 m/sec.

### **Requirements for laser sources**

From the foregoing discussion it becomes obvious that the availability of high power, CW lasers with predictable and controlled beam properties is the gauging item for the development of printers for the medical and graphic arts market. Modulatable optical power output of  $>5$  Watt in a  $TEM_{00}$  mode in the IR or of several 100 mW in the UV (for UV plate imaging) is desirable. Their cost is dictated by competitive choices of printing systems. Alternately, inexpensive multiwatt laser diodes or laser diode bars with small NA and uniform near-fields are finding applications in external drum printers. Here, better mode control and higher brightness would significantly simplify the design of the optical system. Finally, lasers emitting at shorter wavelengths, from green to UV, would allow the use of more sensitive photochemistry. Performance requirements for this "wish list" of lasers, including semiconductor lasers and diode-laser-pumped solid state and fiber lasers, will be discussed.

**Diode Pumped Solid State Lasers for High Power Precision Machining**

Leonard J. Marabella  
TRW  
Space and Electronics Group  
Redondo Beach, California

The objective of the Precision Laser Machining Technology Reinvestment Project (PLM TRP) is to develop the next generation laser machine tools and advanced manufacturing processes for both commercial and military applications. This is a government-industry cost share program sponsored by the Advanced Research Projects Agency (ARPA) to provide the most advanced and affordable US military systems, and the most competitive commercial products in the global marketplace for the automotive, aircraft/aerospace, heavy equipment, and shipbuilding industries. To accomplish the objective a Consortium of 20 organizations that represent industrial users, process developers, system integrators and technology developers has been established forming a user-driven, horizontally and vertically integrated team.

The next-generation laser machine tool is based upon diode pumped solid state laser technology with fiber optic beam delivery, and beam clean-up. The technical objective is to produce multi-kW lasers with excellent beam quality, and offer the option of fiber optic delivery with equally good beam quality. The machining capabilities of PLM lasers will be established through extensive process tests that will be conducted. Process data will be published in a Laser Machining Handbook and disseminated through an Outreach program.

Two PLM lasers will be built and integrated into laser machine tools and operated at beta test sites. A 2.5 kW high peak power laser will be assembled and operated with an emphasis on the drilling of precision holes. In addition, a 6 kW high average power laser, that can run pulsed or continuously, will be built and used to perform welding, cutting and surface treatment process tests. Beam clean-up techniques are being developed to produce excellent beam quality through multi-mode fiber optics. The manufacturing users have identified numerous high pay-off process applications that will be addressed; for example, welding of aluminum; high speed welding; drilling of precision holes for aircraft engine, airfoils and fuel injectors; cutting of composite materials; deep penetration welding for ships; and cutting of coated steels.

The organizations participating in the PLM program are as follows:

**Users:** Boeing, Caterpillar, Chrysler, Cummins Engines, Ford, GE Aircraft Engines, GM, Hughes Missile Systems, Newport News Shipbuilding, TRW Vehicle Safety Systems, United Technologies.

**Process Developers:** Edison Welding Institute, University of Illinois, Penn State University

**System Integrators:** Process Equipment. Utilase Systems

**Technology Developers:** Fibertek, GE, Hughes, Northrop Grumman, SDL, TRW



## Strained-Layer InGaAs-GaAs-AlGaAs Buried-Heterostructure Lasers with Nonabsorbing Mirrors by Selective-Area MOCVD

R.M. Lammert, G.M. Smith, D.V. Forbes, M.L. Osowski, and J.J. Coleman

Microelectronics Laboratory  
University of Illinois  
208 N. Wright St.  
Urbana, IL 61801 USA  
Phone: (217) 333-2555  
FAX: (217) 244-7645  
e-mail: jcoleman@ux1.cso.uiuc.edu

Optical absorption in the active region near the facets of semiconductor lasers during high-power operation may result in catastrophic optical damage (COD). Several schemes to increase the COD limited optical power have been reported. One scheme entails forming non-injection regions near the facets to reduce the nonradiative recombination at the facets [1], [2]. A disadvantage of this scheme is that the non-injection region acts as a saturable absorber which may effect the L-I curve near threshold. Another scheme to increase the output power at which COD occurs involves forming a region at the laser facets which has a higher band gap energy than the energy of the emitted laser light. One method to produce these nonabsorbing mirrors (NAMs) utilizes bent-waveguides fabricated using nonplanar substrates [3], [4]. Although this method produces NAMs with broad near-fields, the coupling of the optical field between the window region and the light-emitting region is low due to the optical beam diffracting freely in the window region. In addition, accurate cleaving is necessary to achieve the relatively short window regions needed ( $<15\text{ }\mu\text{m}$ ). Another method to produce NAMs uses an etch and regrowth technique, but this method also allows the optical beam to diffract freely in the window region and accurate cleaving is again needed [5].

The QW laser material system is also an important factor which determines the COD limit of the laser. For example, the strained InGaAs QW lasers have been shown to have a COD limit which is three to four times higher than that of conventional unstrained GaAs/AlGaAs QW lasers [6], [7]. In this paper we report the design, fabrication and operation of strained-layer InGaAs-GaAs-

AlGaAs buried-heterostructure (BH) lasers with nonabsorbing mirrors fabricated by an atmospheric pressure metalorganic chemical vapor deposition (MOCVD) three-step selective-area growth process. The wavelength tunability of selective-area epitaxy (SAE) [8] is utilized to form the quantum well (QW) at the facets with a quantum-confined-state wavelength which is  $350\text{ }\text{\AA}$  less than the emission wavelength of the device. The NAM-SAE lasers exhibit over a 40% increase in maximum optical output power when compared to conventional SAE lasers. The optical field is guided by the active region throughout the entire device which enables the coupling loss of the optical field in the nonabsorbing region to be low (optical coupling coefficient  $C \sim 0.914$ ). Furthermore, the nonabsorbing region can be relatively long ( $>100\text{ }\mu\text{m}$ ), reducing the accuracy necessary for cleaving and resulting in a higher yield of devices.

The strained-layer InGaAs-GaAs-AlGaAs lasers with nonabsorbing mirrors utilize a BH configuration formed by a three-step selective-area growth [8], [9]. Figure 1(a) is the schematic diagram of the dual oxide stripe mask used during the selective growth of the active region for the conventional SAE lasers. Each oxide stripe is  $25\text{ }\mu\text{m}$  wide along the entire device. Figure 1(b) is the schematic diagram of the dual oxide stripe mask used during the selective growth of the active region for the NAM-SAE lasers. The oxide stripe width in the gain region is  $25\text{ }\mu\text{m}$  and is linearly tapered down in the nonabsorbing region to a width of  $13\text{ }\mu\text{m}$  at the facets. This geometry relates to a calculated quantum-confined-state wavelength of  $1.063\text{ }\mu\text{m}$  in the

gain section ( $\lambda_1$ ) and a calculated quantum-confined-state wavelength of  $1.028 \mu\text{m}$  at the facet ( $\lambda_2$ ) for a nominal  $40 \text{ \AA}$   $\text{In}_{0.21}\text{Ga}_{0.79}\text{As}$  QW. Thus the quantum-confined-state wavelength at the facet is  $\sim 350 \text{ \AA}$  less than the quantum-confined-state wavelength in the gain region enabling the QW at the facet to be transparent to the light generated in the gain region. The space between the stripes for both the conventional SAE laser and NAM-SAE laser is  $4 \mu\text{m}$  which defines the BH mesa width. Both the gain region and the nonabsorbing region of the NAM-SAE lasers are biased during operation.

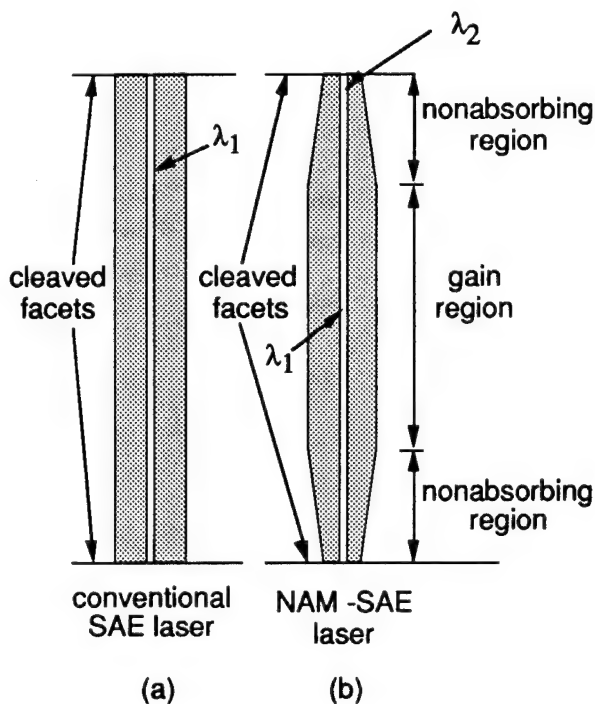


Figure 1. Schematic diagram of a dual oxide stripe mask used during the selective growth of the active region for (a) a conventional SAE laser (b) a NAM-SAE laser.

Figure 2 shows the pulsed ( $1.5 \mu\text{s}$  pulses,  $2 \text{ kHz}$  repetition rate) output power versus current ( $L-I$ ) characteristics for a NAM-SAE laser and a conventional SAE laser from the same cleaved bar. Both lasers are  $1000 \mu\text{m}$  long and have  $4 \mu\text{m}$  wide BH mesas. The NAM-SAE laser has a  $700 \mu\text{m}$  long gain region and two  $150 \mu\text{m}$  long nonabsorbing regions. The conventional SAE laser and the NAM-SAE laser have a threshold current of

$24.5 \text{ mA}$  ( $613 \text{ A/cm}^2$ ) and  $25.5 \text{ mA}$  ( $638 \text{ A/cm}^2$ ), respectively, and both have a peak emission wavelength of  $1.068 \mu\text{m}$ . The peak output optical power per uncoated facet of the NAM-SAE laser and the conventional SAE laser are  $326 \text{ mW/facet}$  and  $228 \text{ mW/facet}$ , respectively. Thus, the NAM-SAE laser exhibits over a 40% increase in maximum optical output power when compared to the conventional SAE laser.

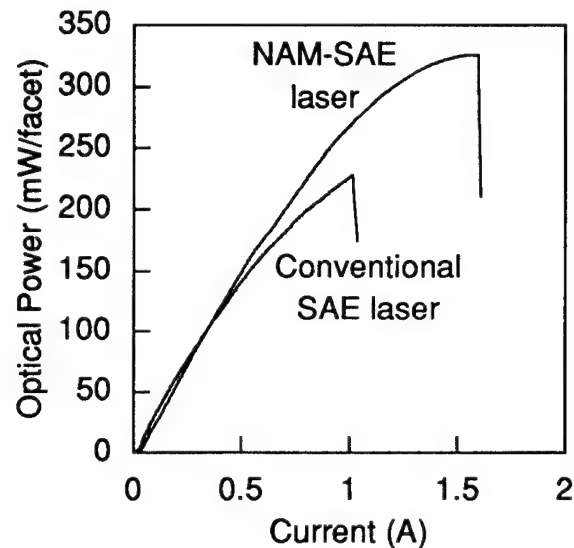


Figure 2. Pulsed light output vs. current at for an uncoated NAM-SAE laser and an uncoated conventional SAE laser from the same cleaved bar. The peak output power per facet of the NAM-SAE laser and the conventional SAE laser are  $326 \text{ mW/facet}$  and  $228 \text{ mW/facet}$ , respectively. Both lasers have an output aperture width of  $\sim 4 \mu\text{m}$ .

The same selective-area enhancement design which enables the QW to be thinner in the nonabsorbing region than in the gain region also produces thinner GaAs barriers in the nonabsorbing region than in the gain region. As a result, there will be a coupling loss of the optical field between these two regions. To calculate the coupling loss, a NAM-SAE device was cleaved such that one facet is located at the end of the nonabsorbing region, and the other facet is located in the gain region (see inset of Fig. 3). Figure 3 shows the  $L-I$  characteristics for both facets of this  $490 \mu\text{m}$  long  $4 \mu\text{m}$  wide device ( $I_{th} = 17.5 \text{ mA}$ ). The round trip unity gain model which solves for the self-consistent variation of the

intensity inside the laser cavity yields the expression [4], [10]:

$$C = \frac{P_{\text{gain}}^2}{P_{\text{nam}}^2} \quad (1)$$

where  $P_{\text{nam}}$  and  $P_{\text{gain}}$  are the light output from the nonabsorbing region facet and gain region facet, respectively, and  $C$  is the optical coupling coefficient. From the L-I characteristics of Fig. 3, a coupling coefficient of 0.914 is calculated.

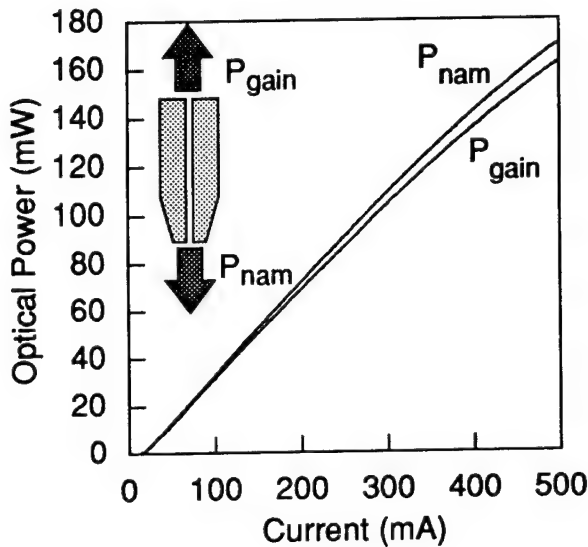


Figure 3. Light output versus current for an uncoated NAM-SAE device with one nonabsorbing facet and one conventional facet. The inset is a schematic diagram of this device.

- [1] M. Sagawa, K. Hiramoto, T. Toyonaka, K. Shinoda, and K. Uomi, "High Power COD-free Operation of 0.98  $\mu\text{m}$  InGaAs/GaAs/InGaP lasers with Non-injection Regions Near the Facets," *Electron. Lett.*, vol. 30, p. 1410, 1994.
- [2] S.A. Maranowski, E.I. Chen, N. Holonyak, Jr., and T.A. Richard, " $\text{Al}_x\text{Ga}_{1-x}\text{As}$ -GaAs-In<sub>y</sub>Ga<sub>1-y</sub>As Quantum Well Heterostructure Lasers with Native Oxide Current-Blocking Windows Formed on Metallized

- Devices," *Appl. Phys. Lett.*, vol. 64, p. 2151, 1994.
- [3] R.P. Bryan, L.M. Miller, T.M. Cockerill, and J.J. Coleman, "Nonplanar Quantum Well Heterostructure Window Laser," *Appl. Phys. Lett.*, vol. 54, p. 1634, 1989.
- [4] F.R. Gfeller, P. Buchmann, P.W. Epperlein, H.P. Meier, and J.P. Reithmaier, "High-Power Single-Mode AlGaAs Lasers with Bent-Waveguide Nonabsorbing Etched Mirrors," *J. Appl. Phys.*, vol. 72, p. 2131, 1992.
- [5] J.E. Ungar, N.S.K. Kwong, S.W. Oh, J.S. Chen, and N. Bar Chaim, "High Power 980 nm nonabsorbing facet lasers," *Electron. Lett.*, vol. 30, p. 1766, 1994.
- [6] L.S. Heath, K. Meehan, A.K. Chin, P. Gavrilovic, J.H. Zarrabi, M. Wober, and J.E. Bisberg, "980 nm Ridge Waveguide Laser Reliability at 100 mW," *Appl. Phys. Lett.*, vol. 62, p. 1869, 1993.
- [7] T. Takeshita, M. Okayasu, and S. Uehara, "High-Power Operation in 0.98- $\mu\text{m}$  Strained-Layer InGaAs-GaAs Single-Quantum-Well Ridge Waveguide Lasers," *IEEE Photon. Technol. Lett.*, vol. 2, p. 849, 1990.
- [8] T.M. Cockerill, D.V. Forbes, J.A. Dantzig, and J.J. Coleman, "Strained-Layer InGaAs-GaAs-AlGaAs Buried-Heterostructure Quantum-Well Lasers by Three-Step Selective-Area Metalorganic Chemical Vapor Deposition," *IEEE J. Quantum Electronics*, vol. 30, p. 441, 1994.
- [9] R.M. Lammert, T.M. Cockerill, D.V. Forbes, G.M. Smith, and J.J. Coleman, "Submilliampere Threshold Buried-Heterostructure InGaAs/GaAs Single Quantum Well Lasers Grown by Selective-Area Epitaxy," *IEEE Photon. Technol. Lett.*, vol. 6, p. 1073, 1994.
- [10] T. Takamori, L.A. Coldren, and J.L. Merz, "Folded-Cavity Transverse Junction Stripe Surface-Emitting Laser," *Appl. Phys. Lett.*, vol. 55, p. 1053, 1989.

## Non-imaging Laser Diode Array Beam Shaper

David Caffey, Opto Power Corporation, 15251 E. Don Julian Road, City of Industry, CA, 91745, (818) 369-6886, FAX (818) 369-4812

W. A. Clarkson, Optoelectronics Research Centre, University of Southampton, Southampton, SO9 5NH, U.K., 44 703 59 3141, FAX 44 703 59 3142.

Laser diode arrays are inexpensive, compact, efficient, and reliable light sources. However, the output beam, which is highly elliptical, is difficult to both efficiently collect and concentrate. This has limited continuous wave (CW) diode sources to power levels under 100 Watts. The fast axis of the laser diode array output tends to have good beam quality,  $M^2 \sim 2$ , and a source size of  $\sim 1$   $\mu\text{m}$ . The slow axis of laser diode broad stripes and of array bars is highly multimode, typically having an angular distribution of 10 degrees at the  $1/e^2$  power points. The slow axis beam quality for a 500  $\mu\text{m}$  wide stripe is thus  $M^2 \sim 70$ , and  $M^2 \sim 1400$  for a one centimeter array. One means of improving the brightness is to individually fiber couple broad stripe diodes, and then bundle the fiber ends together. Another is to collimate the fast axis of one centimeter arrays using a fiber lens<sup>1</sup>, and then fiber couple into a linear array of fibers. The output ends of the fibers are also bundled together. Both techniques are compact and relatively simple, and power is scaled by increasing the number of fibers in the bundle.  $M^2 \sim 350$  are available at 60 Watts output using the latter technique. It is difficult to scale beyond 100 Watts without increasing  $M^2$  to values greater than 500. This is due to loss of brightness in fiber coupling, as an essentially linear source is being coupled into a round fiber, or in mode mixing as light propagates through the fiber. Brightness is further reduced in fiber bundling by the presence of the fiber cladding, and by the less than unity packing factor of round fibers.

A new technique for improving diode array beam quality has recently been described by Clarkson, et al<sup>2</sup>, in which the output of a 20 Watt, fiber lensed, one centimeter bar is imaged into a multiple reflection beam shaper (MRBS), consisting of a pair of offset, tilted, parallel plane mirrors, separated by a small gap. The MRBS optically translates a row of 24 individual beams, having overall slow and fast axis beam qualities of  $M^2 \sim 1400$  by  $M^2 \sim 2$ , into a stack of 24 beams, having beam qualities  $M^2 \sim 50$  in both axes. The throughput was over 75%. This result was obtained by magnifying the output image of the fiber lensed bar into the MRBS. Image magnification requires optics and some space in order to accommodate the one centimeter source size while using reasonable numerical aperture optics.

In this paper, we describe a simplified MRBS design in which a one centimeter, 20 Watt array is fiber-lens collimated, and this output is reshaped and focused into a delivery fiber. The non-imaging technique works in the far field of the diode output, while the imaging technique described above works in the near field. The non-imaging approach removes imaging optics from the input side of the MRBS, reducing overall size and complexity. Rather than translating individual emitter images into a stack, as is the case with the imaging MRBS approach, our approach chops a wide stripe of light into segments, and then stacks the segments. Edge aperture effects are minimized by making the input aperture larger than beam height in the fast axis. The mirrors used are high reflectors at 808 nm, separated by 0.5 mm air gap, and tilted at 45 degrees and 25 degrees to the slow and fast axes, respectively. The output beam consists of a stack of about 25 individual segments. MRBS throughput is over 80%, slow axis beam quality  $M^2 \sim 89$ , fast axis beam quality 106. Using one cylindrical lens and one spherical lens, the 13 Watt output is focused to 300  $\mu\text{m}$ , .176 NA in the fast axis, and 250  $\mu\text{m}$ , .172 NA in the slow axis. Further improvements are expected to increase throughput to over 15 Watts.

We also describe the non-imaging technique when used on a 500  $\mu\text{m}$ , 3 Watt, broad stripe emitter. The emitter is fiber lensed, and the output is allowed to expand in the slow axis to asymmetrize the beam. The mirror spacing is about 2.5 mm, and the beam is chopped into about 9 segments. Output beam quality is  $M^2 \sim 15$  by  $M^2 \sim 25$ , while MRBS throughput is about 90%. This source is suitable for pumping fiber lasers and fiber amplifiers.

The non-imaging MRBS technique allows power scaling of fiber coupled laser diode broad stripes and linear arrays to over 100 Watts with  $M^2 \sim 350$ , suitable for many medical procedures, including urological, endoscopic, and orthopedic surgeries, as well as for pumping solid state lasers, fiber lasers, and fiber amplifiers. The MRBS technique can be applied to all wavelengths currently of interest, from 670-1000 nm, by selecting suitable coatings for mirrors and optics.

#### REFERENCES

1. J. J. SNYDER, P. REICHERT, and T. M. BAER, "Fast Diffraction-limited Cylindrical Microlenses," *Appl. Opt.* **30**, 2743-2747 (1991).
2. W. A. Clarkson, A. B. Neilson, D. C. Hanna, "Novel Beam Shaping Technique for High-power Diode Bars," in *Technical Digest, Conference on Lasers and Electro-Optics*, (Optical Society of America, Washington, DC, 1994), paper CThL2.

## DIODE LASER SYSTEMS FOR PHOTODYNAMIC THERAPY

Daniel R. Doiron, PDT Systems, Inc., 7408 Hollister Ave., Santa Barbara, California, 93117  
Phone: (805) 685-9880, Fax (805) 685-2959

Diode lasers have long been viewed as the future technology for clinical light sources for use in Photodynamic Therapy (PDT). This has been based on their small size, high efficiency, potential reliability and potential low cost. The requirement for a laser source in PDT is based on their ability to deliver light efficiently through small single optical fibers. This in turn allows for endoscopic and interstitial use. The wavelength of the diode source must match that of the absorption of the photosensitizer used, which are chosen to provide good tissue penetration. Due to the high tissue penetration requirements wavelengths in the red and near infrared are used. At present the photosensitizers in clinical testing and commercial development have peak absorptions in the 630nm to 695nm range, while preclinical testing includes photosensitizers with absorption extending up to 800nm. Above 800nm the photophysics of the compounds tend to make them less desirable for use in PDT. The accuracy and stability of the center wavelength of the light source, and its bandwidth, must match to the action spectrum of the photosensitizer in-vivo. For example the first generation photosensitizer Photofrin® activation is specified as 630 $\pm$ 3nm while for the second generation photosensitizer SnET2 it is 664 $\pm$ 7nm.

Power requirements for PDT light sources depend on the specific application. Low power application such as in ophthalmology require less than 0.2W, while single fiber endoscopic or interstitial application require up to approximately 2W, and multifiber applications can use 5W or more. The actual power required is determined by the surface area or volume to be treated and the need to have reasonable time exposure of less than half an hour. Irradiance levels used are generally kept below levels that induce significant hyperthermic condition, though PDT does show a synergistic effect when combined with low level hyperthermia, <45°C.

For viable commercial clinical systems, the mean time between service must be at least 2000 hours with longer times being highly desirable. The systems must operate in a variety of environmental conditions, such as temperatures from 10°C to 30°C, and high or low humidity, while maintaining wavelength and power stability. The system should be small and light weight, <25lbs, portable, and require no special utilities. It would also need to meet all domestic and international medical device regulatory requirements.

The user interface for a clinical system is a key component that will determine its success to a great degree. It must be simple and easy to use while providing versatility to meet the requirements of the different PDT applications. The system must provide adjustable power and time controls or some other means of measuring the fluence at the treatment site to achieve the desired light dose. In the case of large asymmetrical treatment areas, multiple exposures or the use of simultaneous multiple exposures are generally required



which further complicate the light dosing controls. Also as the applications for PDT grow and the methodologies for delivering the therapy expand, the user interface should be adaptable.

Preliminary clinical diode laser systems for PDT have been developed and are currently in clinical use. Due to the present limitation of the availability of commercial red diodes of sufficient power for PDT, the present systems are limited to use with second generation photosensitizers in the 660nm to 695nm range. The systems, though, could be directly adaptable to use at other wavelengths should the diodes become commercially viable. To date, systems delivering either 0.5W or 2W to tissue have been released as production units. This makes the units viable for most cutaneous type treatments as well as for single fiber endoscopic applications in the fields of urology, gastroenterology and pulmonology. At present they are being used in clinical trials with the photosensitizer SnET2. The 0.5W system is 18" x 16" x 5" and weighs 22lbs while the 2W system is 18" x 18" x 7" and weighs 40lbs. Both systems can operate on either 110VAC or 220VAC and are designed to meet all CDRH and IEC regulations for medical laser devices. The 0.5W unit is based on the use of a single discrete diode while the 2.0W system uses a single diode array device. A higher power system, >6W, is presently being developed using multiple discrete arrays that will meet the same size and weight specifications of the 2W system. Both systems are power stabilized and include active temperature stabilization of the diodes to assure wavelength stability and extended reliability.

The user interface for the 0.5W system is analog based and provides for simpler power and exposure time control which have been used in PDT to date. Such a system is simple in nature and low cost. The 2W system uses a microprocessor for control and provides a more advanced user interface. The main user interface provides both a Power/Time control similar to that of the 0.5W unit, in addition to a Light Dose mode. In the Light Dose mode the system uses an isotropic fluence sensor probe in the light treatment field to set both the delivered power and exposure time to achieve the user chosen light dose. Such on-line feed back controls allow for compensation of parameters affecting the fluence at the treatment site on a real time basis. The sensor probes are small, <0.8mm, and can be placed either at the irradiated surface or within the tissue to determine the fluence at depth. In addition, the 2W system includes a GPI IEEE488 interface for more sophisticated user interface development.

Development of these initial clinical systems has shown the need for significantly greater developments in a number of areas if laser diodes are to meet their full potential in the PDT field. First, the reliability and performance of the high power visible diodes, discrete and array, need to be significantly improved. Testing of diodes from a number of commercial sources showed the majority of these devices to be unsuitable for use in a clinical system due to limited reliability and output performance. Secondly, the concepts for coupling diode arrays, single or multiple units, into reasonable NA optical fibers, needs to be further developed and commercialized. Currently available fiber coupled arrays exhibit low overall efficiency while giving high launch angles from the delivery fibers. A number of concepts using microlensing and binary optics have been described that could

greatly improve the array to fiber coupling but they have yet to be made commercially available. Thirdly, the cost of the diodes are very high, in the \$4000 per watt range out of the diode, which translates to a high system price considering the losses to tissue and the overall system cost. Fourth, the wavelength range for the diodes needs to be expanded to include the 630nm to 660nm and the 695nm to 780nm region in order to meet the requirements of the other photosensitizers.

In addition, regulatory issues associated with devices must be considered. The FDA considers PDT a combined drug and device therapy in which the drug is the lead regulatory element. As such, the devices are tied to the photosensitizer for regulatory purposes and therefore can not be approved for marketing by themselves. This means that diode laser systems must be submitted under the photosensitizer IND, for clinical testing and the associated PMA for its market approval. This also means that the device will only be cleared for marketing with the specific photosensitizer with which it was tested. The implications of this are that, at least in the USA, a device company needs to have either a close association with the PDT pharmaceutical company or have its own photosensitizer under clinical development.

In summary the future of laser diodes in PDT looks promising but there are still a number of issues that must be resolved before they can reach their real potential.





Tuesday, August 22, 1995

## Novel-Function Devices

**TuA** 9:00 am-10:00 am  
Torreys Peak I-III

Connie Chang-Hasnain, *Presider*  
*Stanford University*

## Simultaneous Demultiplexing and Wavelength Conversion of NRZ Optical Signals using a Side-Injection-Light-Controlled Bistable Laser Diode

Takashi Kurokawa and Koji Nonaka

NTT Opto-electronics Laboratories

3-1 Morinosato Wakamiya, Atsugi, Kanagawa 243-01, Japan

Phone: +81-462-40-3233, Fax: +81-462-40-3259

Photonic digital switches will be indispensable in future all-optical nodes for both time- and wavelength-division processing of optical signals for digital regeneration, Mux/Demux, and wavelength conversion. A bistable laser diode has the potential to achieve time- and wavelength-division processing simultaneously because it is inherently capable of digital regeneration due to its memory characteristics and of wavelength conversion when a side-injection structure is used [1,2]. This paper reports optical demultiplexing of 1 Gbps NRZ signals with simultaneous wavelength conversion using a side-injection-light-controlled bistable laser diode (SILC-BLD) module with pigtailed fibers and a monitoring pin-photodiode.

Figure 1 shows the structure of the SILC-BLD module. It consists of a main waveguide DFB laser for output and an orthogonally crossed sub-waveguide for input. The sub-waveguide amplifies input light and conduct it to the saturable absorption region in the main laser cavity. Both the main laser and the sub-waveguide have a pn-buried structure grown by LPE. The optical signal from the input fiber is focused onto the sub-waveguide by collimating and focusing lenses. One of the output signals from the BLD is focused to the output fiber with the same-type lenses. The other output signal is monitored by a pin-photodiode. Typical module performance is as follows. The input light sensitivity is 10  $\mu$ W for the wavelength range of 1540 to 1570 nm. The output light power and wavelength are 0.7 mW and 1583 nm, respectively. The electric power consumption is about 100 mW.

Figure 2 shows how the module achieves optical demultiplexing with wavelength conversion, which could be applied to the photonic switching nodes of TDM/WDM hybrid transmission networks. There are many reports on optical demultiplexing. However, most of them describe only gating without pulse width conversion, which is not applicable for NRZ signals. In addition, demultiplexing with simultaneous wavelength conversion has not been achieved yet. To demultiplex NRZ optical signals simultaneously with wavelength conversion, the photonic device must have integrated functions for gate operation, memory and wavelength conversion [3]. In the SILC-BLD, input light signals from a fiber are selected by the sub-waveguide which operates as a optical gate, and are memorized in the main BLD. The output light signals with longer pulse widths and the converted wavelength are read from the output fiber by the voltage control part of the saturable absorption region. Clock pulses are produced by the trigger pulses obtained from the pin-photodiode in the module.

In the experiment, 1 Gbps NRZ input signals with wavelength of 1560 nm were generated by a LN modulator. DC bias currents of 31 mA and 80 mA were applied to the main laser and the sub-waveguide, respectively. A 1 ns gate pulse with 0.4 V<sub>pp</sub> was applied to the sub-waveguide to select the light pulses to be memorized, and a 1 ns reset pulse with 0.5 V<sub>pp</sub> was applied to the saturable absorption region. Both control signals had a demultiplexed signal frequency of 250 MHz synchronized to the clock pulses. This small voltage swing of gate pulses

is enough for the fast switching of the BLD since the small amplification change of the sub-waveguide switches the BLD due to its thresholding characteristics.

The result is shown in Fig. 3, where the upper profile shows the 250 Mbps NRZ output signals demultiplexed from the 1 Gbps NRZ input signals. The input and output light power were -8.5 dBm and -0.4 dBm, so the optical gain was 8.1 dB. The wavelength of the input signal was converted from 1560 nm to 1584 nm, so not only demultiplexing but also amplification and wavelength conversion were simultaneously achieved. Note that no optical isolator or filters were used in this experiment because of the excellent isolation between input and output. Multiplexing would be possible by using an array of SLC-BLDs.

In conclusion, using a SILC-BLD module with pigtailed fibers and a photodiode monitor, we have demonstrated optical demultiplexing of NRZ signals with simultaneous wavelength conversion. This module has the versatility for use in TDM/WDM hybrid switching nodes because of its integrated functions in both time- and wavelength-division processing. I expect this functional laser will be useful for constituting compact optical nodes with small power consumption in the future distributed networks.

#### References

1. K. Nonaka, H. Tsuda, H. Uenohara, H. Iwamura, and T. Kurokawa: IEEE Photon. Technol. Lett., vol. 5, pp. 139-141, 1993.
2. K. Nonaka, Y. Noguchi, H. Tsuda, and T. Kurokawa: IEEE Photon. Technol. Lett., vol. 7, pp. 29-31, 1995.
3. H. Tsuda, T. Kurokawa, H. Uenohara, and H. Iwamura: IEEE Photon. Technol. Lett., vol. 4, pp. 760-762, 1992.

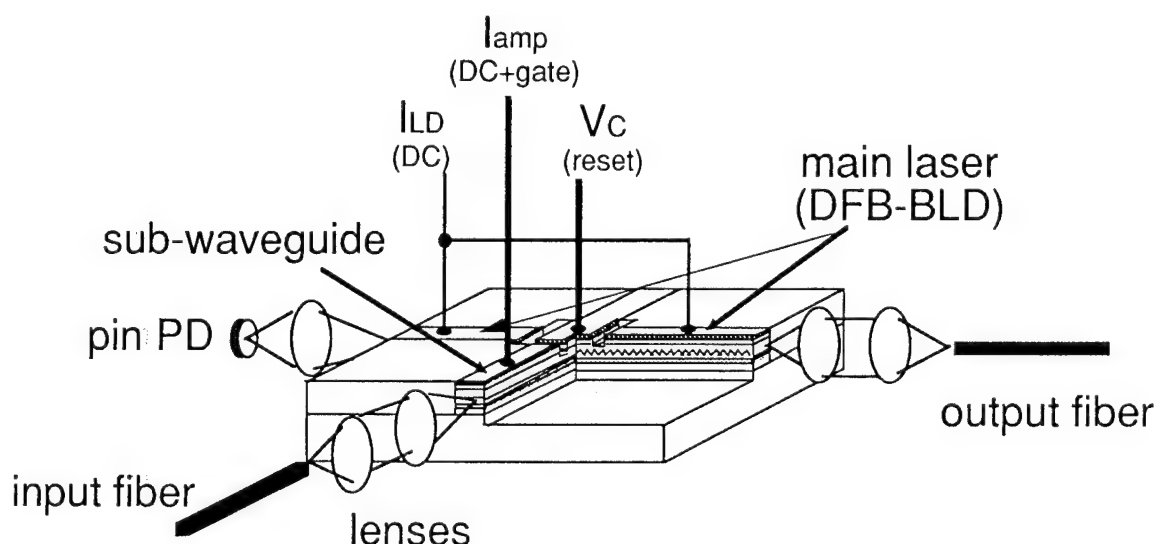


Fig. 1. Schematic structure of the SILC-BLD module.

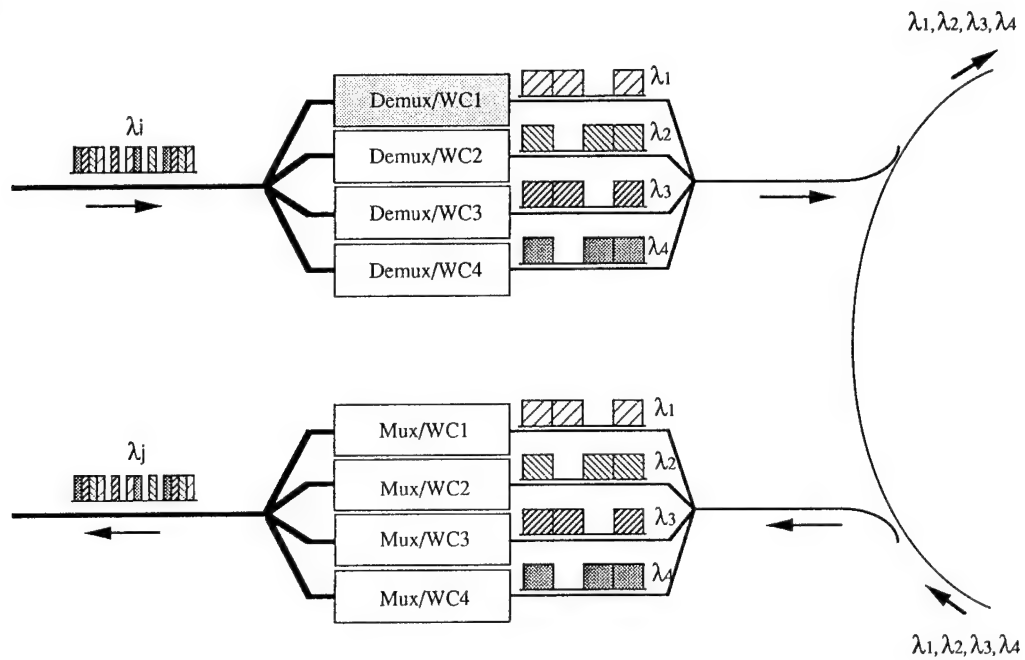


Fig. 2. Optical demultiplexing with wavelength conversion in TDM/WDM switching networks.

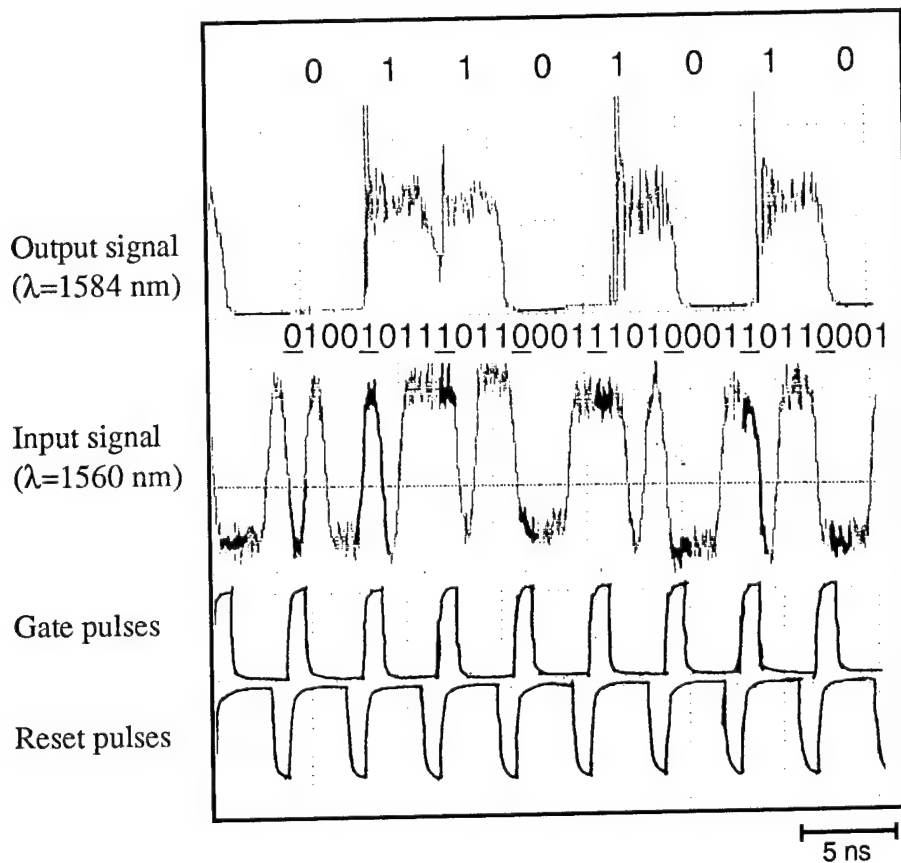


Fig. 3. Optical demultiplexing from 1 Gbps to 250 Mbps NRZ signals.

## 4 GHz All-Optical Clock Recovery Using a Self-Pulsating Multielectrode Distributed Feedback Laser

P. Landais, G. Pham, G. H. Duan, C. Chabran, P. Gallion, and J. Jacquet \*  
 Département Communications, Ecole Nationale Supérieure des Télécommunications,  
 46, rue Barrault, 75634 Paris Cedex 13, France,

Phone: (33-1) 45 81 75 67      Fax: (33-1) 45 89 00 20

\* Division des Composants Optoélectroniques, Groupe Composants Fonctionnels,  
 Alcatel Alsthom Recherche, Route de Nozay, 91460 Marcoussis, France,  
 Phone: (33-1) 64 49 15 57      Fax: (33-1) 64 49 14 22

**Introduction:** Clock recovery is a major key function of any transmission systems. All-optical devices are very attractive due to their high speed and their simplicity as electro-optic conversion is not necessary. It has been shown experimentally that the self-pulsation (SP) in a multielectrode distributed feedback (DFB) laser can be synchronised to the data clock rate of an incoming optical return to zero (RZ) signal. This property makes SP lasers (SPL) good candidates for clock recovery in transmission systems. Jinno *et al.* [1] have shown a clock extraction at 200 Mbit/s and Barnsley *et al.* [2] at 5 Gbit/s. They both have used multielectrode SPL with one section operated as saturable absorber section, which limits SP frequency due to the limitation of carrier lifetime. Feiste *et al.* [3] have extracted 18 GHz clock by using a SP DFB laser without saturable absorber. We can note that in these experiments, the clock recovery occurs in injection locking conditions where the wavelength of the injected optical signal is nearly identical to the SPL wavelength. Despite the fact that such configuration allows optical carrier recovery with a few  $\mu\text{W}$  injected, it seriously limits the application of the SPL to clock recovery. This paper reports for the first time that a 3.8 GHz clock extraction with low time-jitter can be obtained even under conditions of large wavelength difference.

**Experimental set-up:** The SPL used is a 1518 nm three-electrode DFB laser without absorber region. Each section is 100  $\mu\text{m}$  in length. The two side-sections are connected to the same drive current, named  $I_1$ , and the central section current is denoted  $I_2$ . The laser is fabricated following a standard process for 1.5  $\mu\text{m}$  DFB-BH lasers [4]. The coupling coefficient of the grating is 70  $\text{cm}^{-1}$ , and the facets are cleaved without anti-reflection coating. The self-pulsating frequency could be varied from 3 to 5 GHz by adjusting the biasing current.

The master laser is a 1531 nm DFB laser mounted on a 50  $\Omega$  impedance matched circuit. This laser is large-signal modulated by a 3.8 GHz sinusoidal signal of 12 dBm modulation power delivered by the electrical microwave signal generator. The output light corresponding to 3.8 Gb/s '11111111' RZ data stream is injected in the 1518 nm SPL through a 60 dB isolator, a polarisation controller (PC) and an end-focused fibre. The average power measured at the output of the PC is 540  $\mu\text{W}$  and the power injected into the active layer is estimated to be approximately 145  $\mu\text{W}$ . The output of the SPL from the other side is detected by using a 15 GHz bandwidth photodiode (HP 11982A) followed by a 20 GHz digitising oscilloscope (HP 54120A), or by using a 3 nm bandwidth tunable band-pass filter tuned to 1520 nm and followed by a microwave spectrum analyser (HP 7000, HP 70206A) integrating a 15 GHz bandwidth photodiode. The function of the filter is to eliminate the direct transmission of data from the pump laser. It can be noted that the wavelength deviation in the present experiment is 13 nm. Current experiment with longer wavelength deviation shows similar results.

**Experimental results:** Fig. 1.(a) shows the microwave spectrum of the SPL without optical injection. The biasing condition is  $I_1 = 36.8$  mA and  $I_2 = 21.8$  mA. In free running condition the self-pulsating frequency is 4.24 GHz and the full width at half maximum (FWHM) is about

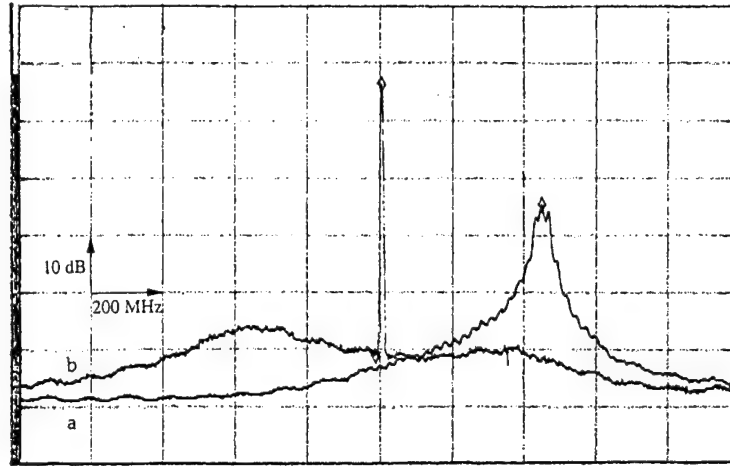


Figure 1: Microwave spectrum of self-pulsation at  $I_1 = 36.8$  mA and  $I_2 = 21.8$  mA, (a) at free running, (b) with optical injection

90 MHz. The polarisation control of the input field is very important to obtain successful synchronisation. Under optimum polarisation conditions, the typical spectrum of the SPL with optical injection is represented in Fig. 1.(b). We can see the narrow peak at the intensity-modulation frequency of the pump laser and a flat region between two side peaks which define the locking-range. The self-pulsation is synchronised to the input optical data signal and is moved from 4.24 GHz to 3.8 GHz. The FWHM is reduced to very small value which cannot be determined due to the limited resolution bandwidth of the analyser. The locking-range is approximately 800 MHz. The ratio between the peak and the flat region is 45 dB. This high value exhibits the high quality of the synchronisation.

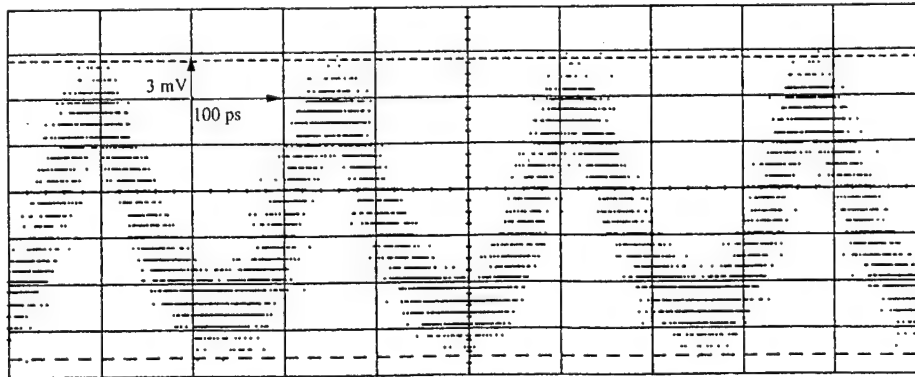


Figure 2: Temporal trace of the extracted clock signal for  $I_1=36.8$  mA and  $I_2=21.8$  mA

In Fig. 2 the temporal trace of the extracted clock is shown. The time-jitter is evaluated to be 11.5 ps by a function of the digitising oscilloscope. This value is very satisfactory in comparison with the 9.5 ps measured time-jitter of the input signal. It is observed that for our component a large wavelength deviation is not a drawback in clock recovery. We can also remark that the extinction-ratio is slightly less than 7 dB. Such temporal responses have been recorded in order to derive the values of the time-jitter for different modulation power and modulation frequencies, at fixed biasing currents. Changing the modulation power does not affect the average optical power emitted by the master laser but changes the spectral density of its fundamental and higher-order overtone frequencies. The variation of the time-jitter against the modulation frequency for different modulation power is shown in Fig. 3. The injection currents are  $I_1 =$

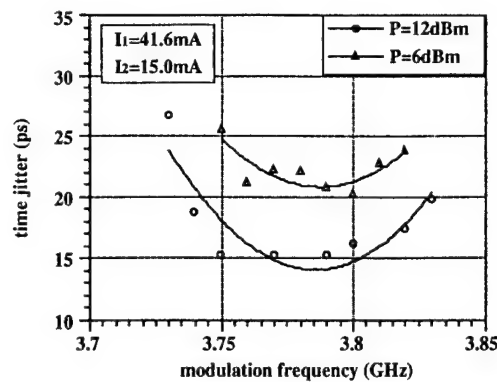


Figure 3: Time-jitter as function of the modulation frequency and for different modulation power at  $I_1=41.6$  mA and  $I_2=15.0$  mA for a constant optical input power.

41.6 mA and  $I_2 = 15.0$  mA. The output power after the isolator is  $460 \mu\text{W}$  and the estimated injected-power is  $53.4 \mu\text{W}$ . The free running self-pulsating frequency is 3.83 GHz. For a fixed modulation power, at first the time-jitter decreases with the increase of modulation frequency, reaches a minimum value, and finally increases with the modulation frequency. We can observe that the synchronisation of the SPL is better at a particular modulation frequency. It is to be noticed that this frequency is not the free running self-pulsating frequency. This can be explained by the fact that the injected optical power modifies the photon and carrier densities of the SPL and therefore its SP frequency. At a fixed value of the modulation frequency the time-jitter decreases with the increase of modulation power. We can also remark an increase of the locking range with this power. Therefore the clock recovery quality is improved when the modulation power increases. For this biasing condition, the lowest time-jitter is approximately 15.3 ps greater than the 11.5 ps previous value. This confirms the importance of the optical power injected for the clock recovery.

**Conclusion:** It has been demonstrated that a 3.8 GBit/s all-optical clock extraction with 11.5 ps time-jitter can be achieved by using a self-pulsating three-section DFB laser even under conditions of 13 nm wavelength deviation. It also has been shown that the clock recovery quality becomes better with the increase of the injected power. The high quality of the extracted clock makes this kind of device of a potential application for future optical retiming regenerator and switch synchronisation.

- [1]: M. Jinno and T. Matsumoto, "Nonlinear operations of  $1.55\text{-}\mu\text{m}$  wavelength multielectrode distributed-feedback laser diodes and their applications for optical signal processing", *Journal of Lightwave Technol.*, vol. 10, pp. 448-457, 1992.
- [2]: P. E. Barnsley, H. J. Wickes, G. E. Wickens, and D. M. Spirit, "All optical clock recovery from 5 Gb/s RZ data using a self-pulsating  $1.56 \mu\text{m}$  laser diode", *IEEE Photonics Technology letters*, 1991, vol. 3, pp 942-945.
- [3]: U. Feiste, D. J. As, and A. Ehrhardt, "18 GHz all-optical frequency locking and clock recovery using a self-pulsating two-section DFB-Laser", *IEEE Photonics Technology letters*, 1994, vol. 6, pp 106-108.
- [4]: D. Leclerc, J. Jacquet, D. Sigogne, C. Labourie, Y. Louis, C. Artigue, and J. Benoit, "Three-electrode DFB wavelength tunable FSK transmitter at  $1.53 \mu\text{m}$ ", *Electron. Lett.*, vol. 25, pp. 45-47, 1989.



## TE/TM polarization switching with single longitudinal mode operation in GaAs/AlGaAs MQW DFB Lasers

Toshihiko OUCHI, Masao MAJIMA, Sotomitsu IKEDA,

Takeo ONO, Mamoru UCHIDA, and Yuichi HANDA

CANON INC. Research Center

5-1, Morinosato-Wakamiya, Atsugi-shi, Kanagawa, 243-01, Japan

Phone: +81-462-47-2111, Fax: +81-462-48-0306

**Introduction:** Experimental and theoretical studies on polarization bistability or switching in laser diodes have been investigated[1]-[3]. Using a tensilely strained quantum-well structure, highly efficient polarization switching has been demonstrated in multi-electrode Fabry-Perot lasers[4]. For these devices, however, the switching has been observed with multi longitudinal mode operation, which are not suitable for optical frequency division multiplexing systems.

This paper shows highly efficient TE/TM polarization mode switching in GaAs/AlGaAs multi-quantum-well distributed feedback lasers with two electrodes. The device exhibits a complete polarization switching between the stable single longitudinal modes, corresponding to the distributed feedback modes of two orthogonal polarizations, and shows no evident bistabilities.

**Device structure:** A schematic drawing of the fabricated laser diode is shown in Fig.1. The laser structure is composed of an n-Al<sub>0.45</sub>Ga<sub>0.55</sub>As lower cladding layer, an undoped multi-quantum-well graded index separate confinement structure (GRIN-SCH) active layer, a p-Al<sub>0.4</sub>Ga<sub>0.6</sub>As carrier blocking layer, a p-Al<sub>0.15</sub>Ga<sub>0.85</sub>As guide layer, a p-Al<sub>0.45</sub>Ga<sub>0.55</sub>As upper cladding layer and a p-Al<sub>0.07</sub>Ga<sub>0.93</sub>As contact layer. The multi-quantum-well consists of three 6nm-thick GaAs wells and four 10nm-thick Al<sub>0.22</sub>Ga<sub>0.78</sub>As barriers. A grating corrugation of 100nm-height is fabricated on a guide layer by Cl<sub>2</sub> ECR plasma etching. The pitch of the grating is set to 246nm (2nd order) so that the TM mode Bragg wavelength should be around 835nm. That is the peak wavelength of its gain spectra. The laser has a BH waveguide structure with 2.1μm-mesa stripe. The cavity length is 600μm and the electrode is divided even into two contacts. Anti-reflection coating is applied on one of cleaved facets.

**Experimental:** We measured the TE and TM polarized output power individually against the injection current. Figure 2 (a) and (b) shows the contours of output power, for TE and TM mode, respectively. I<sub>1</sub> and I<sub>2</sub> are designated as the current values into the non-coated cleaved

side, and AR-coated one, respectively. As shown in Fig.2, while the TE mode is lasing, the other TM mode is extinguished, and *vice versa*. The boundary is clear and can be delimited by a dotted straight line as shown in Fig.2. The device temperature is controlled at 20°C.

If the bias currents are set near this boundary line, an efficient TE/TM mode switching is achieved by applying the modulation current into one of the electrodes. Figure 3 shows the switching characteristics while bias  $I_1$  is fixed at 40mA. Increasing the current of  $I_2$  from 34mA to 35mA, the TM mode oscillation is switched to the TE mode oscillation, with push-pull manner. No evident hysteresis is observed in the experiments.

In particular, TE/TM mode switching is occurred between the single longitudinal modes, corresponding to the each DFB mode. Figure 4 (a) and (b) shows the lasing and ASE spectra of the TE and TM polarizations, respectively, the former is under the condition that  $I_1=40\text{mA}$ ,  $I_2=37.5\text{mA}$  and the latter is  $I_1=40\text{mA}$ ,  $I_2=32.5\text{mA}$ . The lasing wavelength is 836.4nm for the TE mode, and 834.8nm for the TM mode. The Bragg wavelength difference of 1.6nm is due to the difference of the effective refractive index of the waveguide between the two modes. For our lasers design, the Bragg wavelength for TM mode is set to its gain peak, on the other hand, that for TE mode is 10nm shorter than its gain peak. As a result, it gives the nearly equal threshold gain for the TE and TM modes. This gain equalization design and the two electrode configuration gives an opportunity of new kind of TE/TM mode competition in the DFB structure.

We studied the TE/TM mode switching response under the current modulation. The rectangular current of 5mA amplitude was applied into one of the electrodes. The switching time less than 2nsec was confirmed. The response for further shorter pulse current is under investigation.

**Conclusion:** We have successfully achieved the TE/TM polarization switching between the stable DFB modes, in two-electrode GaAs/AlGaAs MQW DFB laser diodes. A few miliampere current modulation into one of the electrodes was enough to cause the polarization switching, and we confirmed its fast response. This new kind of polarization switching is promising for high speed optical switching systems and optical frequency division multiplexing communication systems.

## References:

- [1] Y.C.Chen and J.M.Liu, Optical and Quantum Electronics **19**, S93 (1987).
- [2] B.M.Yu and J.M.Liu, J.Appl.Phys. **69**, 7444 (1991).
- [3] A.Klehr, R Müller, M. Voss, and A. Bärwolff, Appl. Phys. Lett. **64**, 830 (1994).
- [4] H. Tanaka, J. Shimada, and Y. Suzuki, Appl. Phys. Lett. **64**, 158 (1994).

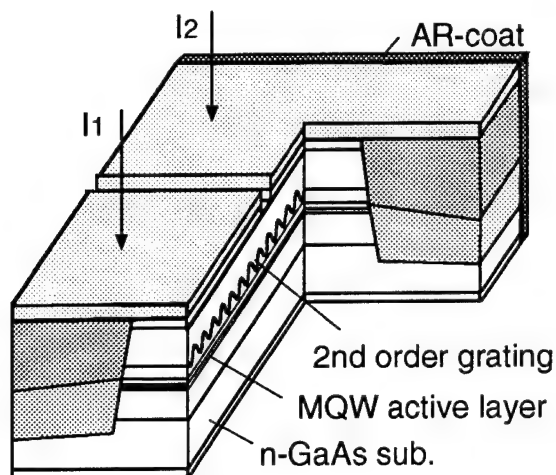


FIG.1 Schematic of the fabricated DFB laser.  $I_1$  and  $I_2$  is the current values of a non-coated cleaved side, and AR-coated one, respectively.

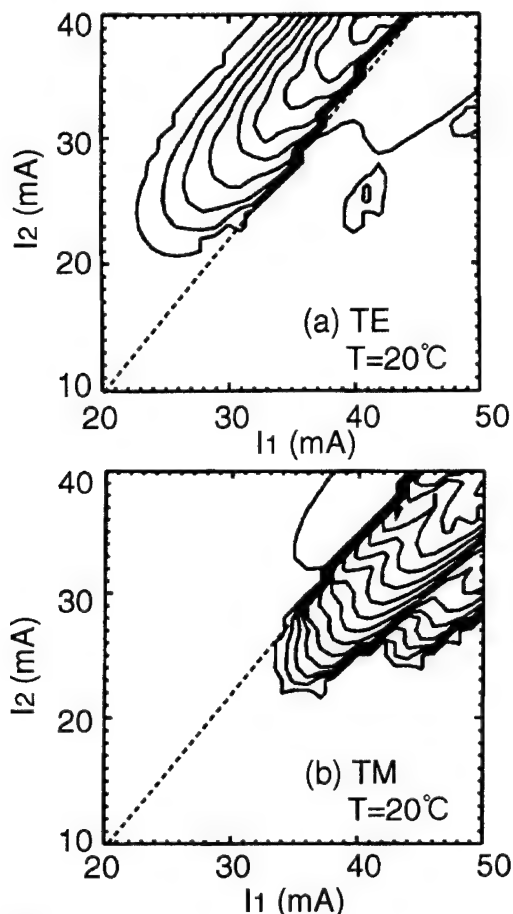


FIG.2 Light output power contour lines for TE mode (a) and TM mode (b). The contour lines are in arbitrary unit. Dotted line is the boundary of TE and TM mode lasing regions.

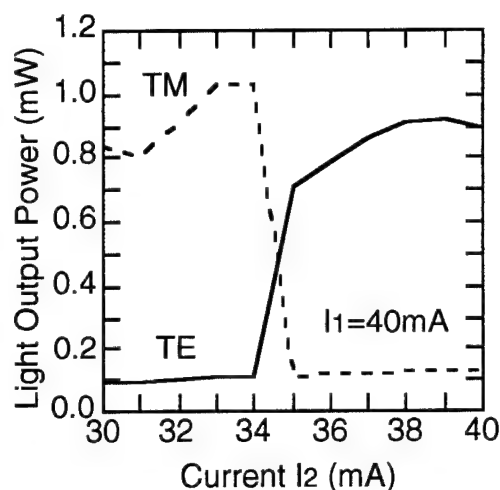


FIG.3 Light output power against the current  $I_2$ , while  $I_1$  is fixed at 40mA. Solid and dotted lines are for TE and TM modes, respectively.

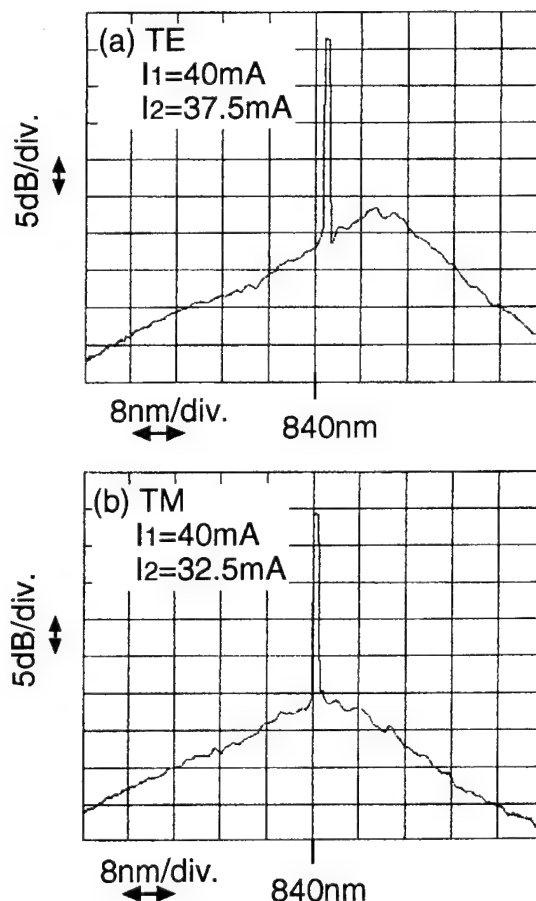


FIG.4 Lasing and ASE spectra of TE mode (a) and TM mode (b). Switching is occurred between these stable longitudinal modes.

## Optical Bistability and NOR-Gate Operation In Intracavity-Coupled In-Plane and Vertical Cavity Surface Emitting Lasers

**D. B. Shire and C. L. Tang**

*School of Electrical Engineering, Cornell University, Ithaca, NY 14853*

*Tel.: (607) 255-1448 FAX: (607) 254-4565 e-mail: shire@nnf.cornell.edu*

**M. A. Parker**

*Rome Laboratory, Griffiss AFB, NY 13441*

Gain-controlled, intracavity-coupled in-plane and vertical cavity surface emitting lasers (VCSELs) fabricated from the same epitaxial material have recently been reported<sup>1-2</sup>. Earlier work on gain quenching and bistability in intracavity coupled lasers involved in-plane devices only<sup>3-5</sup>. It has been pointed out that the conditions for bistability in cross coupled lasers depend on the individual lasers' self- and cross-saturation coefficients<sup>6-7</sup>. The cross saturation terms are highest when the overlap of the two lasers' gain sections is maximized. Consequently, the hysteresis in the power output vs. power input characteristic of cross-coupled VCSEL and in-plane lasers is expected to be larger and more easily realized than that observed in cross-coupled in-plane lasers alone. We report the first observation of optical bistability in cross-coupled VCSEL and in-plane lasers, and we present an all-optical two-input NOR gate which was fabricated to demonstrate the flexibility of this switching technology.

A conceptual sketch of a  $20\text{ }\mu\text{m}^2$  AlGaAs/GaAs VCSEL integrated with and intracavity coupled to two orthogonal  $20\times 400\text{ }\mu\text{m}$  in-plane lasers A and B is shown in Figure 1. The fabrication of these devices has been described in detail previously<sup>1-2</sup>. Coupling gaps are located between the gain sections of the in-plane lasers and the VCSEL (or output) section of the NOR gate to allow each to be independently biased. The end mirrors of the in-plane lasers are deep-etched by electron cyclotron resonance (ECR) etching. The shallow and deep etches are created in the same pumpdown using a one-step two-level etching process<sup>8-9</sup>.

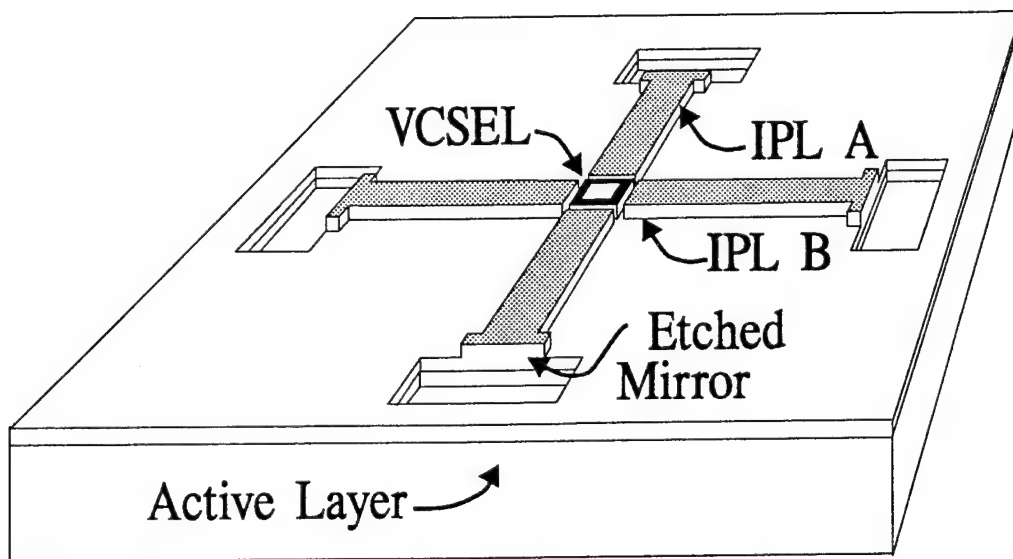
Figures 2a-c demonstrate the operation of the NOR gate. In Figure 2a, the lower, abrupt on/off oscilloscope trace is an untruncated  $1\text{ }\mu\text{s}$  voltage input pulse to the VCSEL, with the in-plane laser sections unbiased. The upper trace is the VCSEL output measured with a  $1\text{ cm}$  diameter Si photodetector. In Figure 2b, the lower trace is a  $500\text{ nsec}$  voltage pulse applied to in-plane laser A, and the upper trace again shows the VCSEL output, together with a small amount of scattered light from the in-plane laser. It is clearly seen that when the in-plane laser A is biased above threshold in the logic 1 state, the VCSEL output pulse is truncated (spontaneous emission only, or logic 0) until the time when the in-plane laser is turned off. At that point, the VCSEL output quickly rises to its lasing or logic 1 output level. During this measurement, the orthogonal in-plane laser (B) is off. Figure 2c shows another scenario, measured using in-plane laser B. The VCSEL is initially in its lasing or logic 1 state. At a later time, the output of in-plane laser B is raised from logic 0 to logic 1, or lasing. The VCSEL output, again shown as the upper trace, is then suppressed to the logic 0 state. The on/off contrast ratio between the logic states is at least 5:1. We observe that the on/off contrast ratio reaches a maximum at some VCSEL bias, at which point a further increase in VCSEL current causes the ratio to decrease. The switching speed of the devices discussed here is limited by their large RC charging time constant. The ultimate switching speed in gain quenched, bistable cross-coupled lasers should be limited by the cavity lifetime, and not by the carrier lifetime as is the case in conventional semiconductor laser operation.

Figure 3 shows the hysteresis in the power output vs. power input characteristic of a  $20\text{ }\mu\text{m}^2$  VCSEL intracavity-coupled to a  $20\times 600\text{ }\mu\text{m}$  in-plane laser. The data may be interpreted as follows. In the upper portion of the loop, the VCSEL is lasing, and the in-plane laser is off. As the top of the loop is traversed from left to right, the VCSEL output initially increases. Here, the

spontaneous emission from the in-plane laser optically pumps the VCSEL and decreases its threshold current. Eventually, the light output of the in-plane laser increases rapidly as it begins to lase at  $P_1$ , and the VCSEL output is suppressed. The VCSEL output is reduced to below 0.05 mW of spontaneous emission when the in-plane laser is at full output. When the in-plane laser power is reduced, the VCSEL remains off until  $P_2$  is reached, at which point the VCSEL begins to turn on once again. The observed hysteresis loop is approximately 20 mA wide, from inspection of the in-plane current axis of Figure 3. To ensure that the VCSEL output only was being measured, the scattered light from the in-plane laser was measured separately and subtracted from the combined in-plane and VCSEL output signal measured with the large-area photodetector. The in-plane laser power itself was measured using a reverse-biased p-n photodetector fabricated adjacent to the in-plane laser output mirror and coupled through a polyimide-filled 3  $\mu\text{m}$  gap.

Applications for the intracavity coupled laser pair include other integrated all-optical logic gates and inverters, optical interconnection between signal planes with low-divergence output beams, and sources and optical memory elements for dense wavelength division multiplexed (WDM) switching networks or time slot interchange circuits. For example, an analog or digital input signal may be amplified by a main in-plane laser with multiple intracavity VCSEL sections. The wavelength or the time slot of the output signal may then be chosen by turning off the side in-plane laser coupled to the desired VCSEL, thereby allowing that VCSEL to lase. This transfers the inverted and amplified input signal to the VCSEL's output. The intracavity coupled in-plane laser offers a wide variety of established options for controlling its associated VCSEL output, and the bistability of the coupled laser pair may be used to advantage by incorporating such elements as buffers or latches for optical memory applications.

In conclusion, we have demonstrated the first observation of optical bistability and all-optical NOR gate operation in intracavity coupled in-plane and vertical cavity lasers fabricated from the same epitaxial material. The combined device offers a wide variety of potential applications including integrated all-optical logic gates, interconnects, and memory elements.



**Fig. 1** Conceptual sketch of the all-optical NOR gate

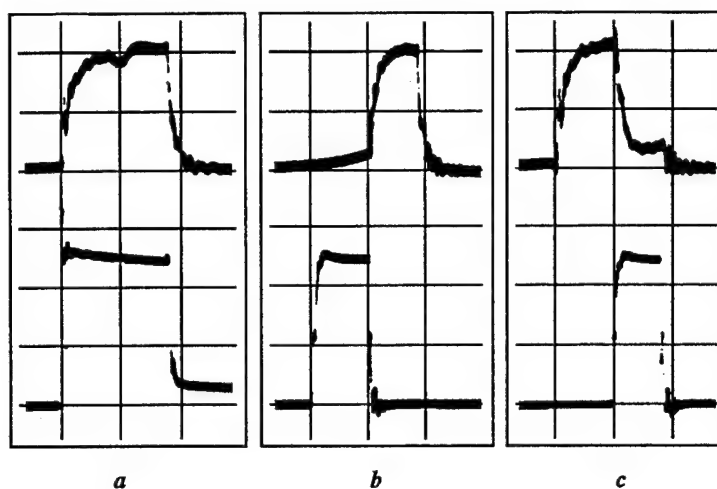


**Fig. 2** Oscilloscope traces showing NOR gate operation  
 Time (x axis): 500 nsec/division  
 VCSEL power output (Upper y axis): 0.2 mW/division  
 Input voltage (Lower y axis): 5 V/division

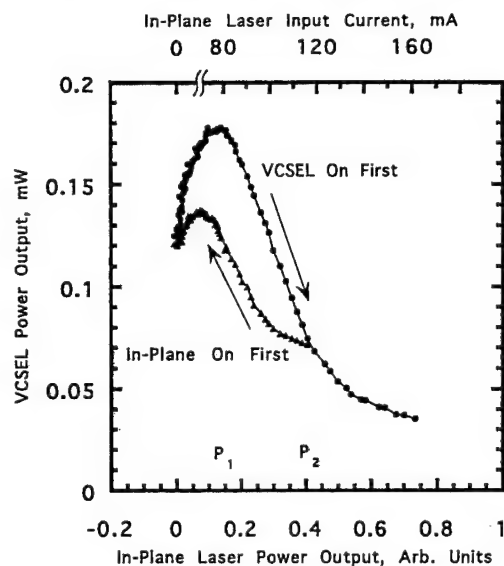


**Fig. 3** Optical bistability in intracavity-coupled in-plane and vertical cavity lasers

- VCSEL lasing first, in-plane power output increasing
- ▲ In-plane laser on first, in-plane power output decreasing

## References

1. D. B. Shire, M. A. Parker, P. D. Swanson, J. S. Kimmet, and C. L. Tang, *Appl. Phys. Lett.* **66**, 1717 (1995).
2. D. B. Shire, M. A. Parker, and C. L. Tang, *Electron. Lett.*, April 1995, submitted for publication.
3. H. Uenohara, Y. Kawamura, H. Iwamura, K. Nonaka, H. Tsuda, and T. Kurokawa, *Electron. Lett.* **28**, 1973 (1992).
4. H. Uenohara, Y. Kawamura, H. Iwamura, K. Nonaka, H. Tsuda, and T. Kurokawa, *Electron. Lett.* **29**, 609 (1993).
5. J. E. Johnson, W. J. Grande, and C. L. Tang, *Appl. Phys. Lett.* **63**, 3273 (1993).
6. C. L. Tang, A. Schremer, and T. Fujita, *Appl. Phys. Lett.* **51**, 1392 (1987).
7. H. Kawaguchi, *Bistabilities and Nonlinearities in Laser Diodes* (Artech House, London, 1994).
8. W. J. Grande, J. E. Johnson, and C. L. Tang, *Appl. Phys. Lett.* **57**, 2537 (1990).
9. P. D. Swanson, D. B. Shire, C. L. Tang, M. A. Parker, J. S. Kimmet, and R. J. Michalak, *IEEE Photonics Technol. Lett.*, June 1995, accepted for publication.



Tuesday, August 22, 1995

## Lidar Applications

**TuB** 10:30 am-12:00 m  
Torreys Peak I-III

Renny Fields, *Presider*  
*The Aerospace Corporation*



## Miniature Lidar using Diode Lasers Modulated with PN Codes

James B. Abshire and Jonathan A.R. Rall

NASA-Goddard Space Flight Center  
Experimental Instrumentation Branch, Code 924  
Greenbelt MD 20771  
Tel: (301) 286-2611, Fax: (301) 286-1761  
Internet: jba@eib1.gsfc.nasa.gov

Takeuchi et al. [1, 2] first reported aerosol lidar measurements using an AlGaAs laser modulated with a pseudo-noise (PN) code in 1986. Recently, we have reported the design, theory and measurements [3-5] made with our breadboard PN aerosol lidar, which uses a photon counting detector and histogram-correlate receiver processor.

Atmospheric H<sub>2</sub>O vapor can also be measured with DIAL techniques by using laser diode-based lidar. There are many H<sub>2</sub>O absorption lines in the 211 vibration rotation band of H<sub>2</sub>O, between 811 and 840 nm, which are sufficiently strong, well isolated and temperature insensitive to be candidates for DIAL lidar measurements. High power laser diodes and photon counting detectors are also available at these wavelengths. DIAL techniques can be used with pulsed diode lasers, although it is difficult to achieve the high peak powers with the stable narrow optical linewidths which are required.

Recently we have reported some initial DIAL H<sub>2</sub>O measurements made with our PN diode lidar [6, 7]. The block diagram of our DIAL lidar is shown in Figure 1 and its characteristics are summarized in Tables 1 and 2. The transmitter consists of an index-guided AlGaAs laser operated CW at ~100 mW, where it has ~10 MHz linewidth. The transmitted wavelength is monitored by a vacuum wavemeter with 1 pm accuracy. To lock the laser to the H<sub>2</sub>O line, a small dither current of 0.8 mA at 3 kHz is added and a few percent of laser power is sent through a multi-pass absorption cell. The cell has an optical path length of 10 m and contains only H<sub>2</sub>O vapor at a pressure of ~18 Torr. After passing through the cell, the light is detected by a Si PIN diode. We use a lock-in amplifier to synchronously detect the signal at 3 kHz and generate the first derivative error signal. A computer measures the error voltage and adjusts the laser diode's bias current to zero the error caused by the optical frequency offset. For each DIAL measurement, the on- and off-line lidar profiles are measured sequentially with the laser stabilized at each wavelength.

The PN intensity modulation is impressed by passing the CW beam through an external electro-optical modulator. The PN code is 1023 bits long and operates at 1 Mbit/sec. The modulated beam is tightly collimated and transmitted into the atmosphere. The lidar backscatter is collected by the receiver telescope and detected by a Si APD detector operated in the Geiger mode. The detector signal is passed through a threshold detector, and the output pulses are accumulated into the range bins of the receiver's histogramming memory [4]. The histogram has one range bin for each bit of the PN code, and the signal accumulates synchronously into the histogram for the integration period. After the measurements, the lidar profile is calculated by cross-correlating the histogram of photoelectron counts with the transmitted PN code.

We have used our DIAL lidar to measure the integrated water vapor in a horizontal atmospheric path at night [6, 7]. The AlGaAs laser was actively stabilized to the H<sub>2</sub>O absorption line at 811.617 nm, whose parameters are given in Table 2. The average transmitted laser power was 25 mW. Figure 2 shows the on- and off-line

lidar profiles. Each profile was measured with 75 second integration time. The peaks in both lidar profiles at 5.1 km are the reflection from the side of a water tower at the end of the path.

The integrated path H<sub>2</sub>O attenuation coefficient,  $k_w$ , can be computed from the ratio of the on- to off-line peaks in the profiles. Its value may be estimated for a target at range R by using the Beer-Lambert law,  $P_{on}(R)/P_{off}(R) = \exp(-2 k_w R)$ . For our target at 5.1 km,  $P_{on}/P_{off} = 0.268$  yielding  $k_w = 0.129 \text{ km}^{-1}$ . The surface pressure reported by a local airport at the time of the measurement was 1025 mb with a H<sub>2</sub>O vapor pressure of 5.6 mb. Assuming a pressure broadened Lorentz line shape, the absorption coefficient at line center for this vapor pressure is  $k_0 = n S_0 / \pi \gamma_0$ , and is calculated to be  $0.138 \text{ km}^{-1}$ . The 6.5% difference between the measured and calculated absorption coefficients is likely due to errors in both the lidar system and from estimating the local relative humidity from airport measurements made 30 km away.

We also made range resolved measurements of H<sub>2</sub>O with the same DIAL lidar [6,7]. These initial measurements were made over a horizontal path at night. The on-line measurements were made with the diode laser stabilized to the absorption line at 811.617 nm, and the off-line measurement was made subsequently. Both measurements utilized an average transmitted power of ~25 mW and integration times of 20 minutes. The measured lidar profiles are shown in Figure 3. The aerosols and water vapor should be well mixed along the short horizontal path through the boundary layer. This should cause both the on- and off-line attenuation coefficients to be uniform along the path, which should produce lidar profiles with a linear slope when plotted with a logarithmic Y-axis, as shown. The H<sub>2</sub>O absorption coefficient can be estimated from the ratio of slopes of the on- and off-line lidar profiles, and from Figure 3,  $k_w = 0.109 \text{ km}^{-1}$ , which corresponds to a mean H<sub>2</sub>O mixing ratio of 2.73 g/kg. The BWI airport readings for that time reported 3.47 g/kg, which means the lidar underestimated the in-situ measurements by 21%.

We have recently converted our breadboard DIAL lidar to operate at a H<sub>2</sub>O line at 828.430 nm. This line is isolated, temperature insensitive and is ~x7 stronger than the previous line. Additionally, the line-locking stability has been increased, the absorption cell path length reduced to 40 cm, and the optical bandwidth of the receiver has been reduced to 200 pm. The new line and lidar characteristics are summarized in Table 2. Our initial atmospheric measurements show the much stronger H<sub>2</sub>O extinction and lower background count rates expected. We hope to replace our electro-optic modulator with a small gain-switched optical amplifier in the near future.

There are several factors which effect the performance of a PN lidar. Since the lidar transmits continuously, the receiver's integration time is many orders of magnitude higher than for a pulsed lidar, and the effect of optical background is much more significant. The low peak power of the transmitted signal requires a photon counting detector for sensitive measurements. To reduce the background noise, the PN lidar's transmitter and receiver must be very well collimated and aligned and have narrow and stable optical linewidths and passbands. A diffraction-limited single-line diode source and telescope are highly desirable. The entire received signal also contributes to the random noise level of each bin in the lidar profile. Strong reflectors in the profile, such as clouds, can raise the total received counts and the noise levels of other range bins. Non-ideal PN modulation on the transmitted optical waveform can cause low level, but repeatable false correlation peaks in the recovered lidar profile. The height of the false peaks are proportional to the amount of distortion of the code. If the distortion is characterized and stable, this error source should be largely removable as a step in the post processing of the lidar profile.

We are developing this lidar technique and technology as a small low power instrument candidate for a NASA Mars lander mission. However, there are several applications for a small, rugged low-power lidar, which can measure both aerosol and H<sub>2</sub>O profiles. One is for use in remote unmanned stations in Antarctica to monitor the evolution and dynamics of polar stratospheric clouds. We have constructed a compact aerosol PN lidar, which we plan to install at the South Pole in January 1995. A small, autonomous low-power DIAL lidar would also be useful to measure profiles of atmospheric H<sub>2</sub>O from the Earth's surface as well as from aircraft.

#### References:

1. N. Takeuchi, N. Sugimoto, H. Baba, and K. Sakurai, "Random modulation cw lidar," *Applied Optics* 22, 1382 (1983).

2. N. Takeuchi, H. Baba, K. Sakurai, and T. Ueno, "Diode-laser random-modulation cw lidar," *Applied Optics* 25, 63 (1986).
3. J.B. Abshire, J.A.R. Rall and S.S. Manizade, "Altimetry and Lidar using AlGaAs Lasers modulated with Pseudo-Random Codes," *Proceedings 16th ILRC, NASA Conference Publication 3158, Paper J 5, Boston MA, July 1992.*
4. J.A.R. Rall, J.B. Abshire and S.S. Manizade, "Lidar Measurements of Clouds and Aerosols using AlGaAs lasers modulated with Pseudorandom Codes, *IEEE LEOS'92 Conference Proceedings, p. 206, Boston MA, November 1992.*
5. J.B. Abshire and J.A.R. Rall, "AlGaAs Aerosol Lidar: Theory and Measurements," *OSA Optical Remote Sensing of the Atmosphere, Sixth Topical Meeting, Postdeadline paper ThE29, page PD9-1, Salt Lake City UT, March 1993.*
6. J.A.R. Rall, J.B. Abshire, D. Reusser and M. Humphrey, "Measurements of Atmospheric water vapor using a compact AlGaAs laser-based DIAL Instrument," *CLEO'94 Technical Digest, Paper CWD5, Anaheim CA, May 1994.*
7. J.A.R. Rall, "Differential Absorption Lidar Measurements of Atmospheric Water Vapor using a Pseudonoise Code modulated AlGaAs Laser," *Ph.D. Dissertation, published in NASA Tech. Memo. 104610, July 1994.*

Table 1 - Common GSFC PN H<sub>2</sub>O DIAL lidar parameters.

Parameter	Value
Laser Type	AlGaAs laser diode, SDL 5410-G1
Laser divergence	8X beam expander, ~100 urad
Modulator	KD*P, Con Optics
PN code	1023 bits, 1 MHz bit rate
Lidar ave. transmit power	25 mW
Telescope	20 cm diameter, F/6.3, 160 urad FOV
Detector	Geiger mode Si APD, EG&G SPCM-200
Discriminator	Tennelec TC-453 Constant fraction

Table 2 - Characteristics of GSFC PN H<sub>2</sub>O DIAL Lidar

Parameter	Units	11/93	12/94
Absorption cell length	m	10.0	0.4
Off-line wavelength	nm	811.640	828.380
H <sub>2</sub> O On- line Wavelength	nm	811.617	828.430
H <sub>2</sub> O Line locking stability	pm	± 2	± 1
Line Strength (S)	cm <sup>-1</sup> /mole*cm <sup>-2</sup>	2.54e-24	1.95e-23
Press. Broadened Linewidth	cm <sup>-1</sup> /atm	0.0837	0.0934
Receiver Bandpass filter	nm	5.0	0.2

# Antarctic Miniature Lidar

Jonathan A. R. Rall  
James B. Abshire

Code 924  
NASA Goddard Space Flight Center  
Experimental Instrumentation Branch  
Greenbelt, MD 20771

Phone: (301)286-7397  
Fax: (301)286-1761  
email: jarrall@eib1.gsfc.nasa.gov

**Introduction** The Antarctic Miniature Lidar (AML) instrument has been assembled, tested, and deployed to the NOAA Clean Air Facility at the Amundsen-Scott South Pole Station. AML uses redundant commercially available, single element semiconductor lasers, operated CW, and a silicon avalanche photodiode (APD) operated in the Geiger or photon counting mode. We present preliminary lidar measurements made at both Goddard Space Flight Center, prior to deployment, and at the Clean Air Facility after installation at the South Pole Station in early February, 1995.

**Background** AlGaAs semi-conductor lasers have been used with pseudonoise code (PN) amplitude modulation in previous lidar instruments to remotely sense clouds and atmospheric aerosol distributions at night [1-4]. In addition, a differential absorption lidar (DIAL) based on an externally modulated AlGaAs laser has made night time measurements of integrated path and range-resolved atmospheric water vapor [5]. The AML has been designed to operate continuously during the polar night to detect the occurrence of polar stratospheric clouds (PSC's) [6] which occur at altitudes of 12 to 27 km. PSC's have been implicated in the destruction of polar stratospheric ozone [7].

**Design** The Antarctic Miniature Lidar system diagram is shown in Figure 1 and the system characteristics listed in Table 1. A 150 mW AlGaAs laser diode is used and operated with an average optical output power of 75 mW. The injected current to the laser is directly modulated with a 2047 bit PN code at a bit rate of 1.25 MHz which yields an effective range resolution of 120 meters in the atmospheric returns.

**Results** Figure 2 shows two typical night time atmospheric profiles made at Goddard with the AML prior to deployment. Each 20 minute, range-corrected profile shows enhanced particulate scattering at the planetary boundary layer and molecular Rayleigh scattering to ~7 km. A thin cloud layer at 8 km altitude either formed or moved into the field of view during the second profile.

Figure 3 shows a gray scale plot of twenty-nine lidar profiles taken at Goddard on the night of January 25, 1995. Each profile is a 20 minute integration and has been mapped to a logarithmic gray scale. A layer of broken cumulus clouds at 2-4 km altitude appears 40 minutes into the data set and lasts for ~200 minutes. The lidar

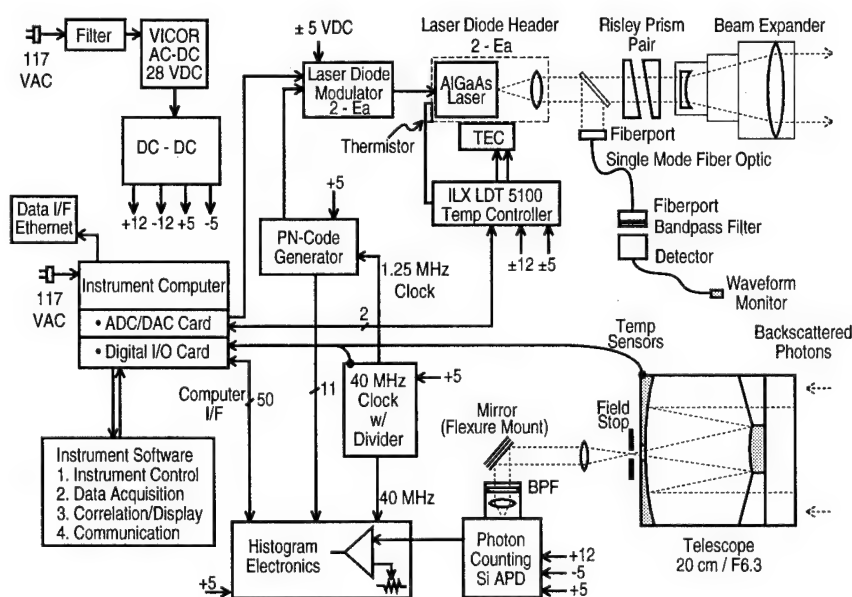


Figure 1. System diagram of Antarctic Miniature Lidar.

profiles shown in Figure 2 occur at 540 minutes and 560 minutes respectively.

Figure 4 shows twenty-eight profiles taken at the NOAA Clean Air Facility, Amundsen-Scott South Pole Station on February 9, 1995. Each profile is a 10 minute integration and has been range-corrected. The sun was at

an elevation angle of  $\sim 15^\circ$  above the horizon which produced a high background count rate on the APD. The count rate was limited to less than 300 kcounts/sec by reducing the collecting area of the telescope. This was done using concentric rings which reduced the effective telescope area to only a few square cm. Also, in the figure the gray scale has been manipulated to further suppress the noise. A cirrus cloud layer is evident at  $\sim 1.5$  km altitude for the first 120 minutes of the data set. After which, wind picked up snow and ice crystals from the surface to a height of several hundred meters, obscuring lidar returns from higher altitudes. This, however, could be accommodated for by pushing the overlap of the transmitter and receiver FOV's out further.

**Conclusion** The Antarctic Miniature Lidar has been tested and deployed to the NOAA Clean Air Facility at the Amundsen-Scott South Pole Station. The AML will continue to operate throughout the austral winter with

Laser Type	AlGaAs laser diode, SDL 5420-G1
Laser divergence	8x beam expander, $\sim 100$ urad
PN code	2047 bits, 1.25 MHz bit rate
Telescope	20 cm diam, F/6.3, 160 urad FOV
Bandpass filter	10 nm centered @830 nm
Detector	Si APD, EG&G SPCM-200
Discriminator	Tennelec TC-453 Constant fraction

Table 1. Antarctic Miniature Lidar system parameters.

data being sent regularly to Goddard via the internet for processing.

#### References

- [1] Takeuchi et al., *Appl. Opt.* **25**(63) 1986.
- [2] Abshire, Rall, & Manizade, 16th International Laser Radar Conference, NASA Conf. Pub. 3158, 1992.
- [3] Rall, Abshire, & Manizade, IEEE Lasers & Electro Optics Society Annual Meeting, EOS/SSLT/OSM 1.3, 1992.
- [4] Abshire & Rall, Technical Digest Optical Remote Sensing of the Atmosphere, Paper ThE29, 1993.
- [5] Rall & Abshire, Technical Digest -Vol 8, Conference on Lasers and Electro Optics, Paper CWD5, 1994.
- [6] McCormick, et. al. *J. Atmos. Sci.* **39** 1982.
- [7] Solomon, et. al., *Nature* **321**, 1986.

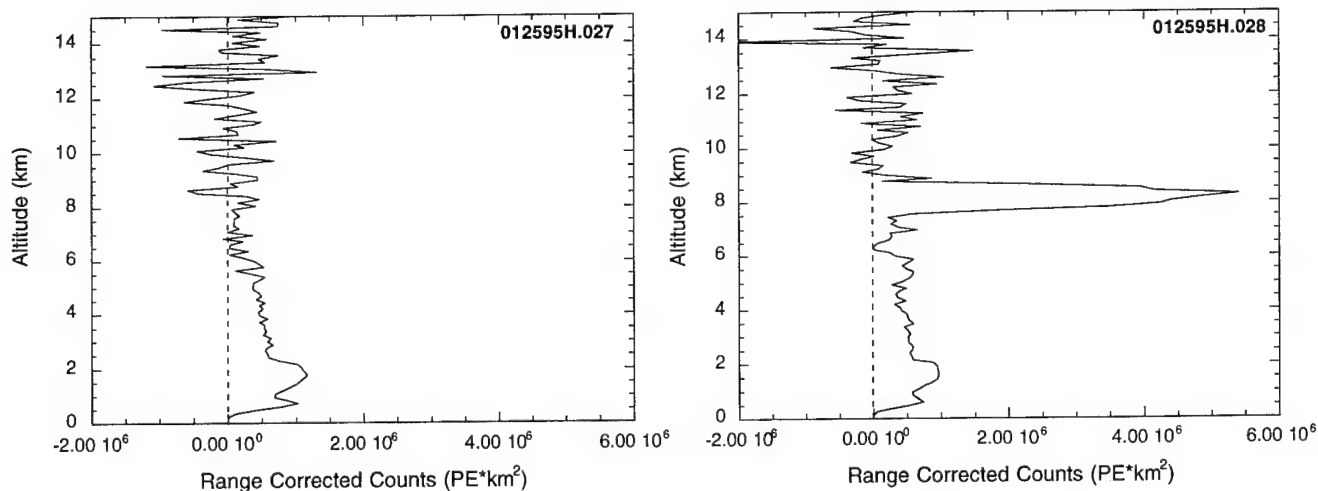


Figure 2. Atmospheric lidar profiles taken at Goddard on night of January 25, 1995.

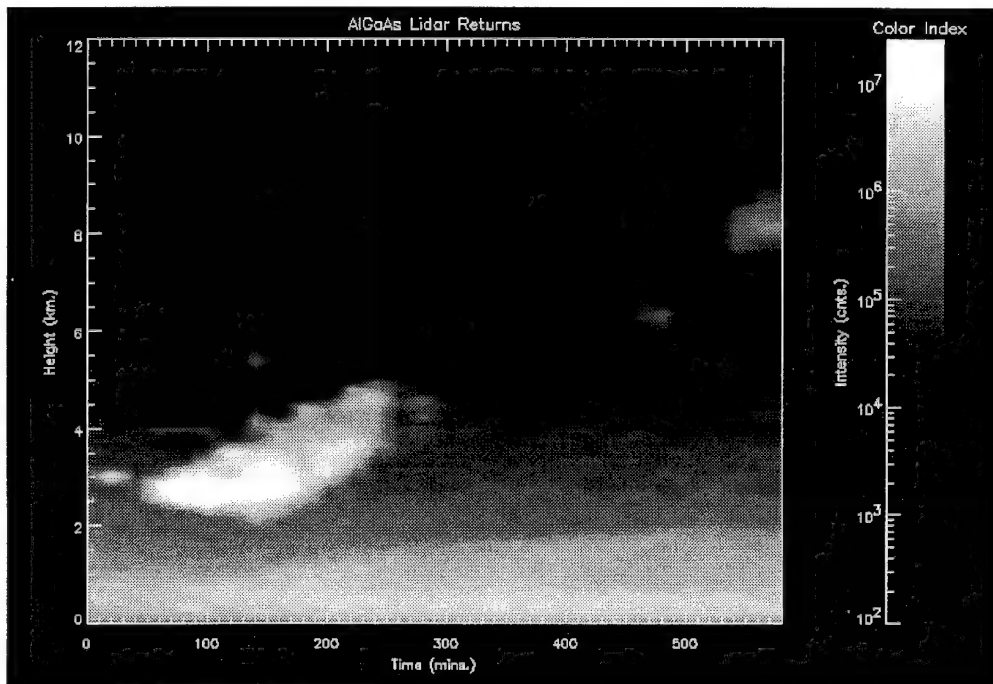


Figure 3. Gray scale representation of 29 twenty minute profiles on night of January 25, 1995 at Goddard Space Flight Center.

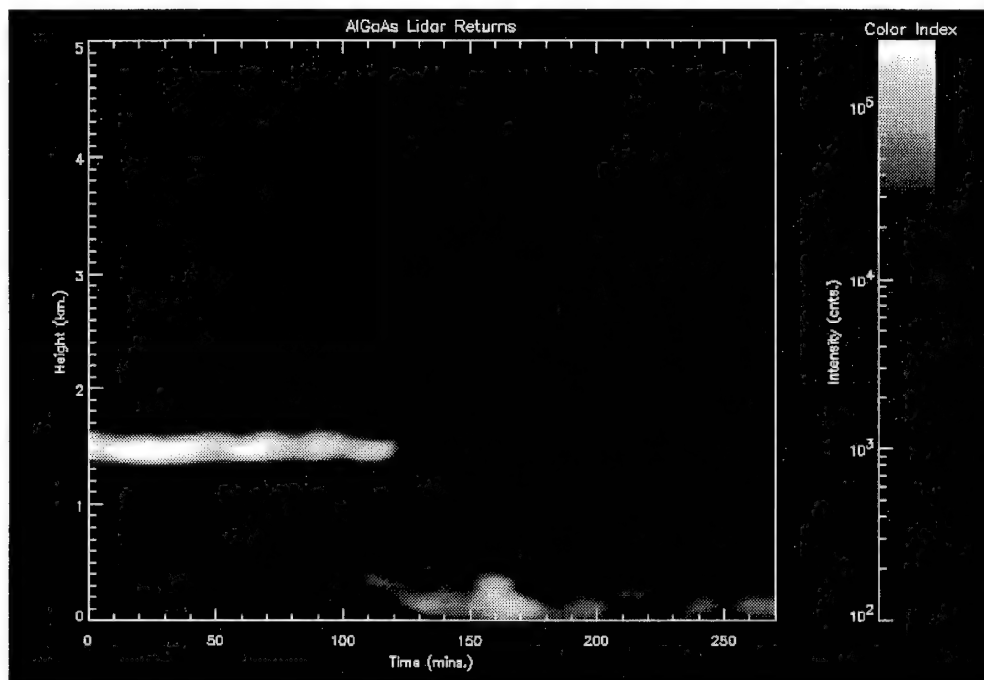


Figure 4. Gray scale representation of 28 ten minute profiles taken February 9, 1995 at the Clean Air Facility, Amundsen-Scott South Pole Station.

## High-Power Diode Laser Transmitter for Aerosol LIDAR and Laser Ranging

Donald M. Cornwell, Jr.  
*Optics Branch, Code 717,*  
*NASA Goddard Space Flight Center, Greenbelt, MD 20771*  
*(301) 286-3384 Fax: (301) 286-1750*

Anthony W. Yu  
*Hughes-STX, Lanham, MD 20706*

Gary L. Harnagel  
*SDL, Inc. San Jose, CA 95134*

Daniel E. Hopf  
*Science Systems and Applications, Inc., Seabrook, MD 20771*

Pamela S. Millar  
*Experimental Instrumentation Branch, Code 924,*  
*NASA Goddard Space Flight Center, Greenbelt, MD 20771*

The next generation of space-based instruments for NASA will be smaller and more efficient than ever before. In keeping with this requirement, LIDAR and laser ranging systems are being developed which are based on AlGaAs semiconductor laser diodes [1, 2]. These systems use pseudo-random noise (PN) intensity modulation of the laser in conjunction with a correlation receiver to improve the overall system sensitivity and allow the inherently low-power diode laser to compete with much higher power solid state and gas lasers. While the size and efficiency of diode lasers make them attractive for such applications, the high-power, quasi-CW intensity modulation of these devices can introduce deleterious effects, such as spectral linewidth broadening. In addition, the highly-divergent beams from diode lasers require fast (F/1) optical systems, which in turn place micron-level tolerances on their opto-mechanical alignment and packaging. We present here the design and performance of a high-power diode laser transmitter which addresses the problem of spectral broadening under large-signal intensity modulation and also the problem of micron-level tolerance opto-mechanical packaging. The laser transmitter is a candidate for an aerosol LIDAR system currently operating at the South Pole, and may also enable future NASA laser ranging and communication systems.

The laser transmitter consists of a laser, electronics, and optics all packaged in a compact and rugged mechanical housing (Figure 1). The physical envelope of the transmitter is 2.5 cm x 3.2 cm x 11.5 cm, with a mass of 120 g. The transmitter produces up to 130 mW cw of collimated, diffraction-limited output power, with up to 270 mW peak power under modulation. The laser diode is a AlGaAs (830 nm) device with a single quantum well (SQW) GRIN-SCH structure, commercially manufactured by SDL, Inc. of San Jose, CA (Model 5410-W). This particular laser model is a space-qualified design; related lifetesting indicates extrapolated lifetimes of up to 150,000 hours [3]. Electronics incorporated in the package include a monitor photodiode, a thermistor and heating resistor for thermal control, and a 7  $\Omega$  matching resistor such that the total package impedance appears as 10  $\Omega$ . The small-signal frequency response of the laser transmitter for 100 mW of average laser power is measured to be 470 MHz (-3 dB), with a relaxation oscillation peak at 1.2 GHz. PN code modulation current is externally supplied over a 10  $\Omega$  coaxial cable from a high-current (300 mA), high-bandwidth (200 MHz) custom-designed hybrid driver circuit; our current aerosol LIDAR system operates at a data rate of 1 Mbps NRZ with a code length of  $2^{11}$ -1 bits.



The primary optical element in the laser transmitter is the laser diode collimating lens, which is a 2.72 mm focal length, F/1 molded glass asphere. This lens is positioned in front of the lens using a vacuum chuck and then mounted to a ceramic heater pad by indium solder. This technique allows for a rough collimation of the beam to a measured divergence of  $0.66 \text{ mrad} \times 2.00 \text{ mrad}$ , implying a defocus error of only  $6 \mu\text{m}$  ( $0.000236''$ ). The  $1 \times 3$  astigmatism of the beam is a result of the elliptical emission spot of the laser. Fine collimation of the beam is achieved using a matched pair of long-focal length (100 mm) positive and negative lenses, where the adjustment is made by changing the spacing between the lens pair. The final beam divergence from the transmitter is measured to be  $0.624 (\pm 0.0010) \text{ mrad} \times 1.849 (\pm 0.0023) \text{ mrad}$ . A pair of wedge prisms allow for fine adjustment of the pointing of the beam from the package. A non-polarizing beamsplitter is also incorporated to pick off 4% of the light and direct it to another aspherical lens, which focuses the beam into a single mode optical fiber used for waveform and spectral monitoring. In order to reduce the effects of optical feedback into the laser, a quarter-wave plate is placed immediately after the collimating lens and oriented such that the polarization of any reflected light passing through is rotated to be orthogonal to the original TE polarization of the laser. Since the laser has almost no gain for this orthogonal (TM) polarization, the reflected light has no measurable effect on the laser.

As mentioned previously, intensity modulation of semiconductor lasers results in a broadening of the gain curve due to changes in the real refractive index of the device and subsequently results in multi-longitudinal mode operation. In aerosol LIDAR applications, this in turn results in a wider bandpass filter at the receiver and a corresponding reduction in the signal-to-noise ratio (SNR) of the system [2]. Single-longitudinal mode operation under large signal modulation is restored in our laser transmitter by use of a thin-film ( $25 \mu\text{m}$  thick) Fabry-Perot etalon, which is deposited on a 1 mm glass substrate and indium-soldered to within  $36 \mu\text{m}$  of the front facet of the laser [4]. The cascaded Fabry-Perot cavities (i.e. laser, air gap, and thin film) result in a frequency selective feedback mechanism which forces single longitudinal mode operation [5] with up to 175 mW of peak modulated laser power for 1 Mbps NRZ intensity modulation, as shown in Figure 2. Single frequency operation was also observed for large signal intensity modulation at rates of 10 Mbps NRZ and 100 Mbps NRZ.

As mentioned earlier, the laser transmitter is currently being evaluated for deployment in an Antarctic aerosol LIDAR system. The PN-code modulation performance of the laser transmitter as characterized using a LIDAR correlation receiver will be presented at the meeting. The BER performance of the transmitter in a 50 Mbps Q-PPM communication system may also be presented.

## References:

1. N. Takeuchi, H. Baba, K. Sakurai, and T. Ueno, "Diode-laser Random Modulation CW Lidar", *Applied Optics* 25 (1), 63, 1986.
2. J.A.R. Rall, J.B. Abshire and S.S. Manizade, "Lidar Measurements of Clouds and Aerosols using AlGaAs lasers modulated with Pseudorandom Codes, *IEEE LEOS'92 Conference Proceedings*, p. 206, Boston MA, November 1992.
3. D.R. Scifres, D.F. Welch, R.L. Craig, E. Zucker, J.S. Major, G.L. Harnagel, M. Sakamoto, J. M. Haden, J.G. Endriz, and H. Kung, "High Power, High Reliability Laser Diodes," Laser Diode Tech. & Apps. IV, *Proceedings of the SPIE*, Volume 1634, 1992.
4. R.J. Smith, "Triple Cavity Laser", U.S. Patent No. 4,805,185, awarded 1989.
5. Binder, J.O. and G.D. Cormack, "Mode Selection and Stability of a Semiconductor Laser with Weak Optical Feedback," *IEEE Journ. Quant. Electron.*, 25, 2255-2259, 1989.



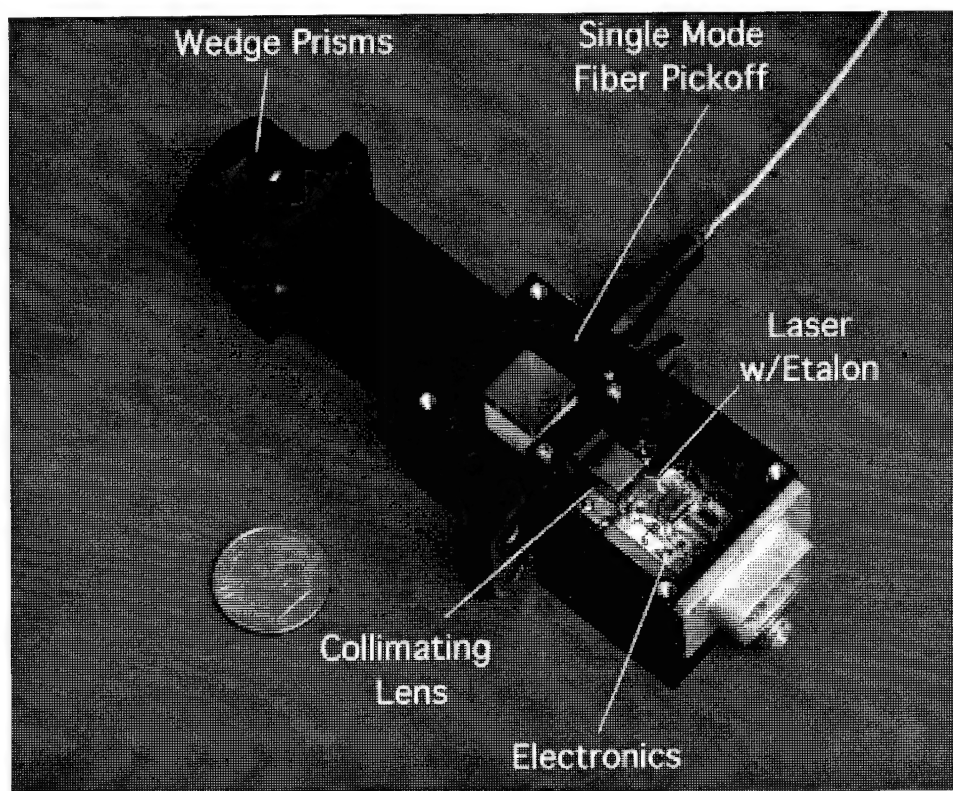


Figure 1: Photograph of laser transmitter for aerosol LIDAR system.

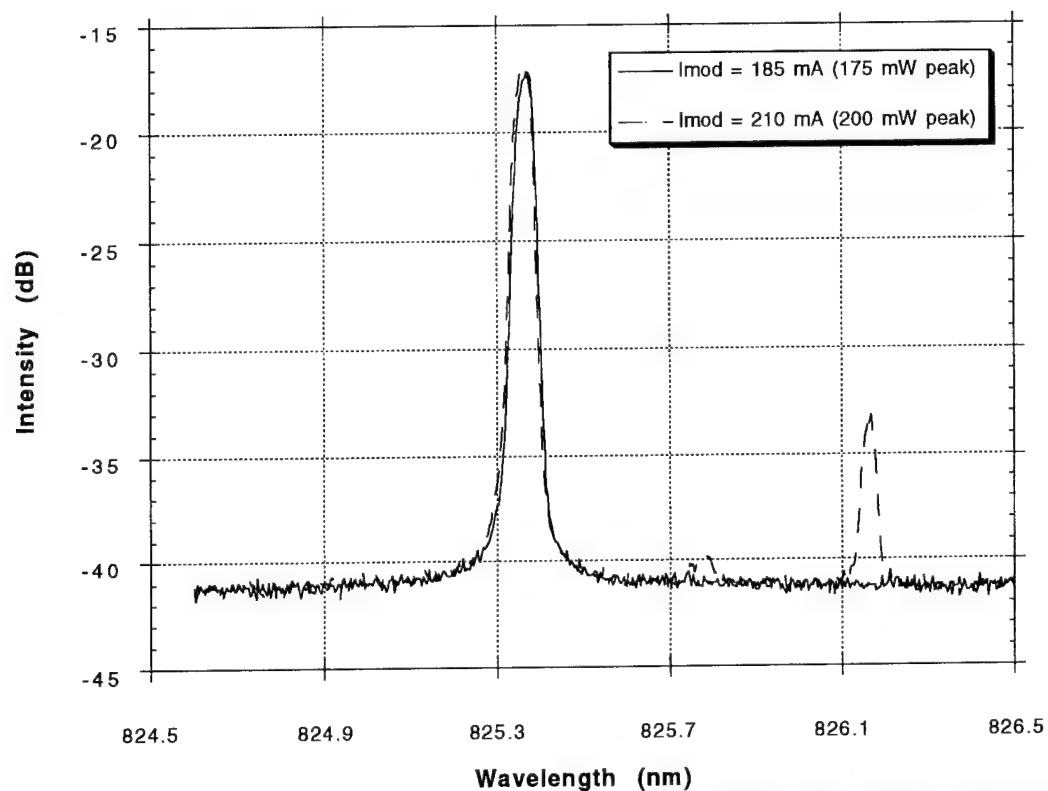


Figure 2: Optical spectrum of laser header under 1 Mbps NRZ large signal intensity modulation.

# Demonstration of High Sensitivity Laser Ranging System

Pamela S. Millar, Kent D. Christian† and Christopher T. Field††

NASA Goddard Space Flight Center,  
Experimental Instrumentation Branch, Code 924  
Greenbelt, MD 20771

phone: 301-286-3793, fax: 301-286-1761

internet: pam@eib1.gsfc.nasa.gov

† Alliedsignal Technical Services Corp.  
Lanham, MD

†† The Johns Hopkins University  
Electrical and Computer Engineering Department  
Baltimore, MD

## Background:

The small size, high efficiency, high reliability and direct modulation capabilities of semiconductor lasers make them extremely attractive for space flight applications. In this paper we report on a high sensitivity semiconductor laser ranging system developed for the Gravity And Magnetic Earth Surveyor (GAMES) for measuring variations in the planet's gravity field [1].

The GAMES laser ranging instrument (LRI) consists of a pair of co-orbiting satellites, one which contains the laser transmitter and receiver and one with a passive retro-reflector mounted in an drag-stabilized housing. The LRI will range up to 200 km in space to the retro-reflector satellite. As the spacecraft pair pass over the spatial variations in the gravity field, they experience along-track accelerations which change their relative velocity. These time displaced velocity changes are sensed by the LRI with a resolution of 20-50  $\mu\text{m}/\text{sec}$ . In addition, the pair may at any given time be drifting together or apart at a rate of up to 1 m/sec, introducing a Doppler shift into the ranging signals.

An AlGaAs laser transmitter intensity modulated at 2 GHz and 10 MHz is used as fine and medium ranging channels. Range is measured by comparing phase difference between the transmit and received signals at each frequency. A separate laser modulated with a digital code, not reported in this paper, will be used for coarse ranging to unambiguously determine the distance up to 200 km.

## Introduction:

Direct detection Laser diode-based ranging systems reported [2,3,4] to this date have been designed to measure static range. The GAMES application requires a unique ranging system capable of precise determination

of velocity changes in the presence of Doppler up to 1m/sec. In order to achieve the accuracies for this measurement, the transmitted signal is intensity modulated at 2 GHz with a modulation index of 90%, and the receiver must be capable of single photon detection. We have developed a breadboard ranging system with moving target capable of measuring these velocity changes.

## Breadboard Description:

A block diagram of the ranging breadboard is shown in Fig. 1 with nominal system parameters listed in table 1. Electrical drive signals for both the fine and medium ranging channels are derived from the 10 MHz master oscillator. Each channel has a phase lock loop (PLL) which generates a local oscillator (LO) signal offset from the main frequency by precisely 10 kHz. The 2 GHz and 10 MHz sinusoidal output signals are combined to drive the laser diode along with a DC bias. The 820 nm optical signal generated by the laser is reflected off the moving retro-reflector target onto the photocathode of a photomultiplier tube (PMT). The output signal of the detector is split into three channels and amplified. Two are filtered for 2 GHz and 10 MHz respectively and the third is reserved for photon counting.

The signal processing is similar to that described in references [2] and [4]. Each ranging signal is independently downconverted to the 10 kHz intermediate frequency (IF) by multiplying them with their respective phase-locked LO signals. The fine and medium IF signals are then independently digitized at 40 kHz each by a 16 bit analog-to-digital converter. The computer calculates phase for the signal by computing the average in-phase and quadrature fourier components of the sampled sinusoidal signal over 32 cycles (312 Hz) of the IF. The phase is then converted to range. The fine ranging chan-

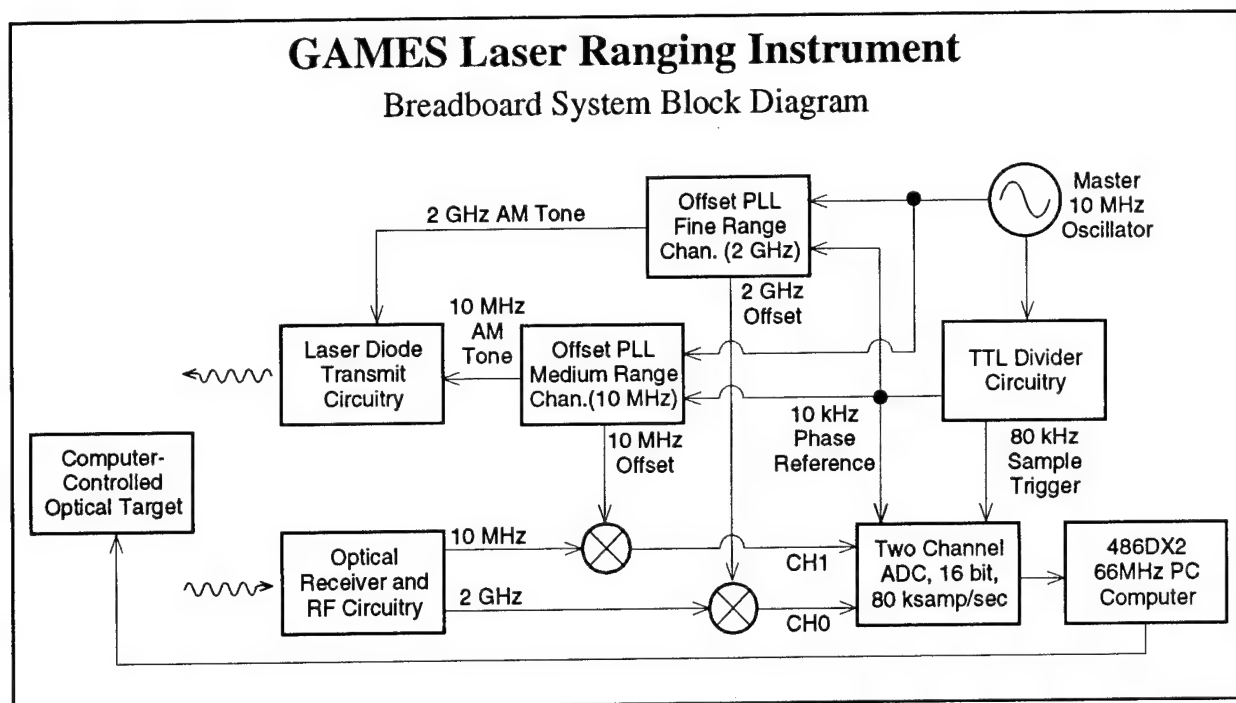


Figure 1. System block diagram of the GAMES laser ranging instrument breadboard.

nel has a cyclical range of 75 mm while that of the medium ranging channel is 15 m. In order to satisfy the range resolution for the GAMES LRI the 2 GHz cycle must be resolved to  $0.25^\circ$  (50  $\mu\text{m}$ ) while the 10 MHz cycle only needs to be resolved to  $1^\circ$  (40 mm) in order to overlap the fine ranging cycle.

#### Performance:

One of the main parameters which influences the accuracy of a range measurement is the number of cycles

averaged. Fig. 2 shows this dependence for static range. For statistically independent data, the standard deviation should decrease by the inverse of the square root of the number of cycles averaged. A linear regression fit shows that when more than 8 cycles are averaged, the standard deviation decreases as  $n^{-0.45}$  for the 2GHz channel and  $n^{-0.5}$  for the 10 MHz channel.

For our application the Fourier components computed over 32 IF cycles are recorded so as to be well above the Doppler frequency. After removing the constant

Laser Transmitter	AlGaAs laser diode, 820 nm 5 nW avg power incident on detector
Detector	MCP-PMT, Hamamatsu 3809U-11 Q.E. of detector spec'd $\sim 5\%$ @ 820 nm
Master Oscillator	10 MHz, TRAK, frequency drift $\sim 10^{-13}/\text{sec}$
Cyclical Error	$\pm 75$ mm in 37 mm cycle, due to image frequency interference at 2 GHz - 20 kHz
Fine Ranging Tone	2 GHz, 75 mm range cycle 48% optical modulation depth
Med. Ranging Tone	10 MHz, 15 m range cycle 6% optical modulation depth
IF	10 kHz
Sampling Rate	80 kHz total, 40 kHz for each channel, 4 samples/cycle
ADC	16 bit, 2 channels, $\pm 1$ volt full scale
Phase measurement	compute I & Q components from avg'd values at $\pi/2$ intervals, 312 times/sec ( $> 10\times$ max. expected Doppler shift: 26.6 Hz)
Track	Computmotor L5-A, 3 m max. optical path length controlled with Labview 3.1 software for windows velocity: 100 $\mu\text{m}/\text{sec}$ up to 1 m/sec acceleration: 100 $\mu\text{m}/\text{sec}^2$ up to 3 $\text{m}/\text{sec}^2$

Table 1. Summary of Ranging System Parameters

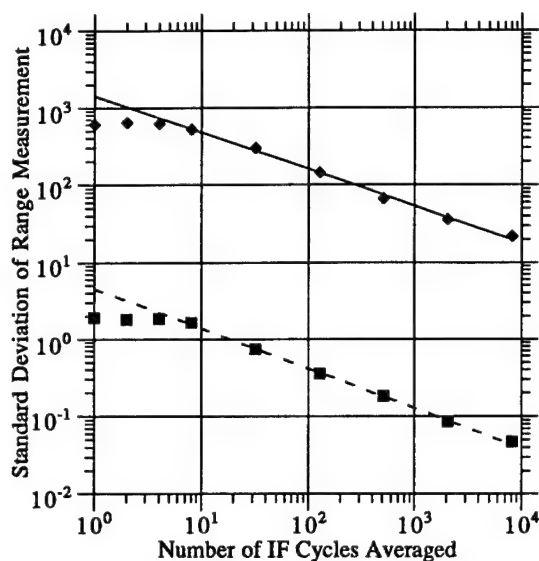


Figure 2. Range measurement standard deviation vs. IF cycles averaged. Top line is 2GHz range in microns, bottom line is 10 MHz range in meters.

Doppler velocity by linear regression, acceleration are computed by quadratic fit to 20 second long segments of the residues. The velocity changes induced by the gravity field are expected to take place over 10 second intervals and will allow us to fit the velocity data over this time period to achieve the required accuracy.

In Fig. 3 the target was computer controlled to move at 99 mm/sec for 25 seconds. A linear regression of the data yields a velocity uncertainty of 0.8  $\mu\text{m}/\text{sec}$ . This is well within the accuracy requirement for GAMES.

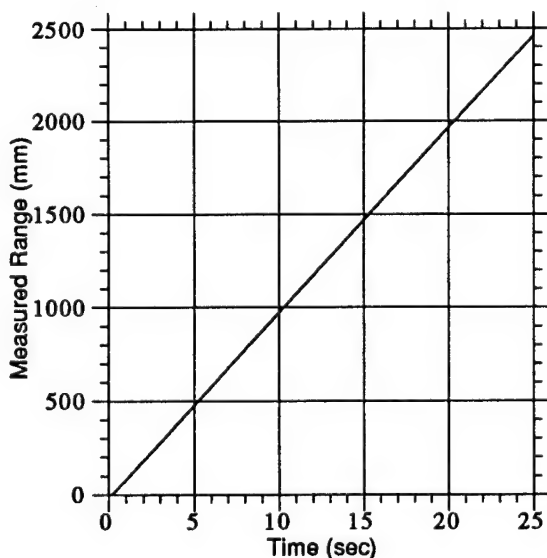


Figure 3. Constant velocity range measurements.

#### Conclusion:

A semiconductor laser ranging breadboard has been developed for the GAMES mission. Preliminary results indicate that it is possible to achieve the required velocity resolution 20  $\mu\text{m}/\text{sec}$ . A summary of system performance data will be presented.

#### References:

1. J. B. Abshire, P. S. Millar and X. Sun, 17th International Laser Radar Conference, 28PD9, July 1994
2. J. M. Payne, D. Parker, and R. F. Bradley, Rev. Sci. Instrum. **63** (6), 3311, (1992)
3. A. Greve and W. Hart, Appl. Opt. **23**, 2982, (1984)
4. K. S. Hashemi, P. T. Hurst and J. N. Oliver, Rev. Sci. Instrum. **65** (10), 3165, (1994)

## Semiconductor Laser-Based Ranging Instrument for Earth Gravity Measurements

James B. Abshire  
 Pamela S. Millar  
 Xiaoli Sun\*

NASA - Goddard Space Flight Center  
 Experimental Instrumentation Branch, Code 924  
 Greenbelt MD 20771, USA  
 Phone: (301) 286-2611 Fax: (301) 286-1761  
 Internet: jba@eib1.gsfc.nasa.gov

\*-Johns Hopkins University  
 Electrical and Computer Engineering Department  
 Baltimore MD 21218

**Abstract:** A laser ranging instrument is being developed to measure the spatial variations in the Earth's gravity field. It will range in space to a cube corner on a passive co-orbiting sub-satellite with a velocity accuracy of 20 to 50  $\mu\text{m}/\text{sec}$  by using AlGaAs lasers intensity modulated at 2 GHz.

**Need for Gravity Measurements:** Spatial variations in a planet's gravity field is an important indicator of its internal structure, which is often otherwise inaccessible. Knowledge of the spatial structure in the Earth's gravity field is also essential for the precise determination of satellite orbit heights. These are critical for space-based ocean altimetry missions, where radar measurements to the ocean surface are being used to investigate the flow of ocean currents. Spatial variations in the gravity field cause both the local sea surface and satellite orbit heights to vary with location. Lack of knowledge of the gravity field's higher order terms now limits in the spatial resolution of the Topex ocean height measurements.

**Mission Overview:** The Gravity and Magnetism Earth Surveyor (GAMES) mission has been developed by NASA-GSFC to measure the Earth's gravity and magnetic fields. The mission is planned as a small Earth-probe for a fall 1998 launch. A small rocket will be used to launch a SMEX-type spacecraft into a 325 km sun-synchronous circular polar orbit. The spacecraft carries a vector and scalar magnetometer on several meter long boom. A GPS receiver is used to determine the low degree and order terms of the gravity field.

The high degree and order gravity field terms are determined from the measurements of a satellite-to-satellite laser ranging instrument (LRI). Once in orbit, the spacecraft ejects a small passive subsatellite, which carries a laser retro-reflector. The main spacecraft then maneuvers ahead of the subsatellite and co-orbits with it, while leading it by  $\sim 150$  km. The LRI is pointed toward the

subsatellite, and it tracks and continuously measures the intersatellite range.

As the spacecraft pair pass over the spatial variations in the gravity field, they experience along-track accelerations which change their relative velocity. These time displaced velocity changes are sensed by the LRI with a resolution of 20-50  $\mu\text{m}/\text{sec}$ . When drag causes the intersatellite range to deviate outside the desired 100-200 km interval, the main spacecraft performs an orbit adjustment to re-establish the desired co-orbiting conditions.

**Instrument Description:** The LRI is laser diode-based ranging system, which is fix-mounted to the spacecraft. The present LRI configuration is shown in Figure 1 and its block diagram is shown in Figure 2. The LRI measures the range with 3 different intensity modulated signals, which determine the absolute range to the subsatellite. The fine and medium range signals are 2 GHz and 31.25 MHz sinusoids which are intensity modulated onto the 815 nm ranging laser diode. The relative ranges are measured by resolving the phase angles of the reflected ranging tones. The 2 GHz tone is used to measure the most accurate relative range to the subsatellite. The 31.25 MHz medium ranging tone is measured to better than the 75 mm ranging period of the fine tone once per second. The coarse ranging signal is a 31.25 Mbit/sec pseudo-noise (PN) code, which is intensity modulated onto the tracking laser diode at 845 nm. It is used to resolve the absolute range to the subsatellite to within a bit-time. The combined ranging signals are used for the gravity determination as well as to guide the orbit correction

maneuvers and maintain the 100 to 200 km distance to the subsatellite.

The subsatellite is passive and carries a 9 cm diameter hollow cube corner. After deployment, the spacecraft body points the LRI to the subsatellite. The spacecraft keeps the ranging beam centered on the subsatellite by using the LRI measured angular position to the control the spacecraft pointing.

**Instrument Design:** The LRI consists of the transceiver, door, electronics and the subsatellite corner reflector. The details of the LRI design are summarized in Table 1. The transceiver is attached to the spacecraft via an interface plate, which provides the common optical bench for the Laser Diode (LD) transmitters and receiver telescope. The transmitter consists of 3 ranging and 5 tracking LDs. The ranging LDs are used for both medium and fine ranging and the tracking LDs are used for both tracking and coarse ranging. The beams from all lasers are co-aligned and fixed with respect to the receiver's optical axis.

The LRI collects the reflected signal from the subsatellite with a 20 cm diameter receiver telescope. The aft optics split the received optical signal to the ranging and tracking detectors. A protective door is open during normal ranging operation, but is closed for launch and thruster firings. The door is used to prevent contamination from the spacecraft thrusters. The door also carries passive optical reflectors, which serve as a test target when the door is closed. The reflectors return attenuated LD beams to the receiver, which permits verification tests of the LRI without the subsatellite.

**Acquisition:** The tracking LDs transmit a 10 mrad wide beam at 845 nm along the spacecraft's negative velocity vector. Three tracking laser diodes are used at one time, leaving two as spares. To acquire the subsatellite, the spacecraft systematically scans its attitude in pitch and yaw. This scans the fixed-mounted LRI beam. When the subsatellite is illuminated, the reflected power is collected by the telescope, and the tracking signal is split in the aft-optics assembly. Approximately 50% of the power is focused onto the CCD array while the remainder is focused onto the coarse ranging PMT. The CCD readout is processed by the on-board computer, which generates pitch and yaw error signals proportional to the offset of the tracking spot from the array's center. These angular errors are input to the spacecraft control system, which corrects the spacecraft pointing to center the signal on the CCD array.

**Tracking:** Once acquisition occurs, the tracking algorithm continuously update the angular error

signals to the spacecraft. The spacecraft keeps the LRI pointed at the subsatellite to better than 100 urad by adjusting its pitch and yaw angles in response to the error signals.

The coarse ranging signal from the PMT is converted to a photon counting bit stream and is integrated by the receiver histogram electronics for ~ 1 sec. The histogram is correlated with a stored replica of the transmitted code to obtain the most likely range bin (the pseudo range). The multiple code length range ambiguity is resolved by alternating the PN code length between 127 and 511 bits and applying the Chinese Remainder Theorem on the pseudoranges.

**Ranging:** Ranging occurs simultaneously with tracking. The ranging LDs transmit an intensity modulated beam at 815 nm with a 1 mrad beamwidth. A single ranging LD operates at any time, leaving two as spares. Approximately 80% of the LD's intensity is modulated by the 2 GHz tone, 10% is used by the 31.25 MHz tone and the residual 10% is not modulated.

The LRI laser signals reflected by the subsatellite are collected by the telescope and directed to the ranging PMT. The PMT's electrical output is split into the fine and medium receiver electronics. Both ranging signals are independently down converted to the 7.6 KHz intermediate frequency (IF) by multiplying them with phase-locked local oscillator (LO) signals. Each LO is offset from its ranging tone by 7.6 KHz. The fine and medium IF signals are independently digitized at 30.4 kHz rate. The computer computes the in-phase and quadrature (I&Q) components from the samples at ~ 260 Hz.

The instrument computer collects the received signal components to transmit to the ground. The ground station computes the magnitude and phase angles for both ranging tones from the I&Q samples. The fine ranging phase angle is used to determine the subsatellite velocity. The medium ranging phase angle is used to measure the cycle number of the fine ranging tone to within a bit of the coarse ranging signal. The coarse ranging measurements are used to reference the medium ranging tone to absolute range.

The gravity measurement errors, which are referenced between the main spacecraft and subsatellite CG's, are summarized in Table 2. These are slightly larger than the instrument errors, since they also include the geometrical effects of the positions of the LRI and cube corner. Details on the mission and instrument design, the fine ranging breadboard measurements, and expected instrument performance will be discussed in the talk.

Table 1 - Summary of LRI Transceiver Design

Pointing:	Body pointed by spacecraft to ~ 100 urad
Laser Transmitters:	Single mode AlGaAs Laser Diodes:
Ranging:	60 mW average power, single mode, 1 mrad beam width 815 nm, 2 GHz mod., 3 each - 1 on at a time
Tracking:	90 mW average power, single mode, 10 mrad beam width 845 nm, 31.25 Mbit/sec PN code, 5 each - 3 on at a time
Telescope:	20 cm diameter Be
Ranging Detectors:	PMT with GaAs photocathode, 20% QE (810- 845 nm)
Tracking Detector:	256 x 256 CCD, ~ 10 Hz frame rate
Fine Range Receiver:	2 GHz & 31.25 MHz ranging tones
IF frequency:	7.6 KHz
Sampling rate	30.4 KHz
Phase components:	Compute I&Q, 260 times/sec
Fine Ranging Measurement Precision:	
200 km:	≈ 45 μm/sec (1.5 x signal shot noise)
100 km:	≈ 10 μm/sec (1.5x signal shot noise).
Drift rates:	≤ 2 μm/sec

Table 2 - GAMES-LRI Error Summary in Gravity Measurements

Error Source	Subsatellite Range (km)		
	200	100	Comments
LRI random ranging error (μm/sec)	45	10	From link analysis
LRI measurement drift rate (μm/sec)	2	2	LRI requirement
LRI-spacecraft CG offset (residual)	2	2	
Subsatellite (μm/sec)	12	12	Dom. error at 100 km
Cube vertex-CG offset: (2 μm/sec)			
Drag induced accel.: (10 μm/sec)			
Margin - other ranging errors	10	10	Mounting errors, etc.
RSS Gravity Ranging Errors (μm/sec)	48	18	RSS: Root Sum Square



Tuesday, August 22, 1995

## High Brightness Lasers

**TuC** 1:30 pm-3:15 pm  
Torreys Peak I-III

John Ralston, *Presider*  
*SDL, Inc.*



## High Power (>1 W) Semiconductor Lasers

Robert J. Lang, Ross Parke, David Mehuys, Steve O'Brien, Jo Major,  
Julian S. Osinski, Gary Harnagel, Frank Shum, and David F. Welch

SDL, Inc.  
80 Rose Orchard Way  
San Jose, CA 95134

### I. Introduction

Coherent semiconductor sources based on flared amplifiers — monolithic and discrete MOPAs and flared unstable resonators have demonstrated the highest cw diffraction-limited output powers from semiconductor sources at wavelengths from 630 nm to beyond 2  $\mu\text{m}$ . This talk will describe continuing advances in flared amplifier devices, including visible output powers approaching 1 W cw diffraction limited, powers up to 10 W diffraction-limited from monolithic devices, high-speed modulation, and more.

High power spatially coherent semiconductor lasers have been a goal of diode laser researchers for years. Single-stripe devices are generally limited to a few hundred mW of output power, at which point reliability problems associated with the high optical intensity at the output facet begin to limit device performance. The simple solution to the problem of facet power density has been to increase the lateral dimension of the laser facet from 3–4 to hundreds of  $\mu\text{m}$ . However, this approach simply trades one problem, facet degradation, for another: control of the spatial mode.

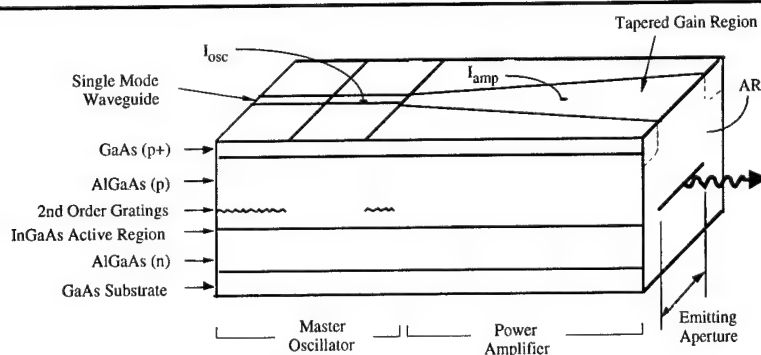


**Figure 1.** Schematic of a monolithic MOPA laser.

In the early 1990s, a discrete flared semiconductor amplifier was demonstrated [1] to produce up to 1 W diffraction-limited output. Subsequently [2–4], a distributed Bragg reflector (DBR) master oscillator was integrated with a discrete flared amplifier to realize a monolithic MOPA

(master oscillator/power amplifier) configuration operating at greater than 2 W diffraction-limited. In recent years, coherent semiconductor sources based on flared amplifiers — monolithic and discrete MOPAs and flared unstable resonators — have demonstrated the highest cw diffraction-limited output powers from monolithic semiconductor sources at wavelengths from 630 nm to beyond 2  $\mu\text{m}$ . This talk will describe continuing advances in flared amplifier devices, including visible output powers approaching 1 W cw diffraction limited, powers up to 10 W diffraction-limited from monolithic devices, high-speed modulation, and more.

Figure 1 shows a schematic view of a monolithic MOPA. The DBR master oscillator is formed by integrated grating reflectors with a single-mode waveguide. A long grating forms the high reflectivity back mirror, while a short grating forms a low-reflectivity front mirror and permits monolithic integration with the flared amplifier.

The output from the DBR master oscillator is injected into the narrow end of the flared amplifier, where it expands by diffraction to fill the aperture of the flare. The divergence of the beam reduces the intensity of the beam, which, however, is reamplified by the gain in the flared amplifier. Because of the narrow input aperture, relatively low powers (a few mW) are required to saturate the amplifier and thus extract power efficiently. The divergence of the beam suppresses the formation of filaments in the amplification region to powers over 1 W cw; thus, the output of the flared amplifier is a diffraction-limited (but

diverging) beam. Figures 2 and 3 show typical light-current and far field plots for a monolithic MOPA operating at 980 nm.

As noted above, the output from a flared amplifier is diverging and possesses a residual phase curvature that is manifested as an astigmatism. This astigmatism is fixed, however, and is easily removed by a combination of spherical and/or cylindrical optics, resulting in a circularized, collimated beam. Alternatively, the beam may be refocused after circularization for coupling into a single-mode fiber, as illustrated in figure 4.

Figure 5 shows the power coupled from the MOPA chip into the single-mode fiber. A better than 70% coupling efficiency is obtained from the main beam of the MOPA into the fiber, resulting in a peak coupled power of over 1.2 W cw.

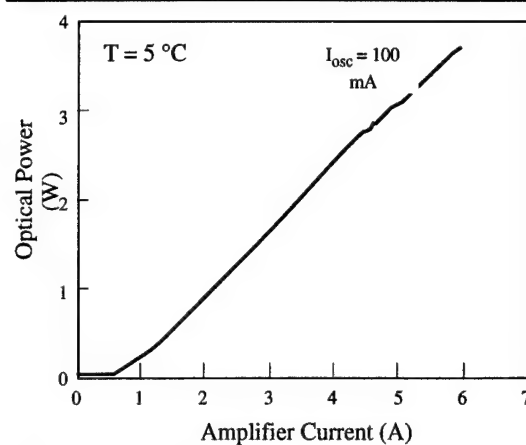


Figure 2. Light-current characteristic for a monolithic MOPA.

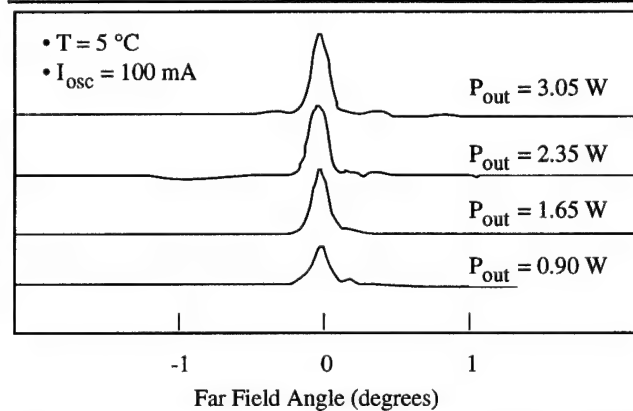


Figure 3. Far field for the MOPA after quadratic phase curvature removal.

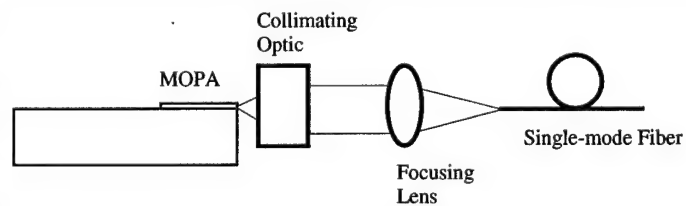


Figure 4. Schematic of a single-mode-fiber-coupled MOPA.

Over the past three years, MOPAs and their close relatives, flared unstable resonators (URs) have broken cw diffraction-limited power records at wavelengths from 630 nm to beyond 2  $\mu\text{m}$ , as illustrated in figure 6. With the fundamental properties of flared amplifiers understood, more advanced chip architectures have been demonstrated, including modulation to speeds as high as 5 GHz, mode-locked configurations, wide-band tunability, and frequency-converted devices. These and continuing demonstrations suggest that the applications of flared amplifiers are still only in their infancy and considerable new applications, configurations, and uses remain.

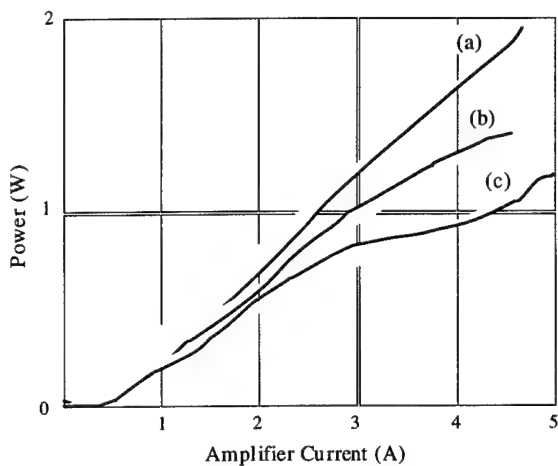


Figure 5. (a) Output power from the chip; (b) power in the main beam (after circularizing optics); (c) fiber-coupled power.

## References

- [1] J. N. Walpole, E. S. Kintzer, S. R. Chinn, C. A. Wang, and L. J. Missaggia, "High-power strained-layer InGaAs/AlGaAs tapered traveling wave amplifier," *Appl. Phys. Lett.*, **61**, pp. 740-742, 1992.
- [2] D. F. Welch, R. Parke, D. Mehuys, A. Hardy, R. J. Lang, S. O'Brien, and D. R. Scifres, "1.1 W cw diffraction-limited operation of a monolithically flared amplifier master oscillator power amplifier," *Elect. Lett.*, **28**, pp. 2011-2012, 1992.
- [3] D. F. Welch, R. Parke, D. Mehuys, A. Hardy, R. J. Lang, S. O'Brien, and D. R. Scifres, "2.0 W cw diffraction-limited operation of a monolithically master oscillator/flared power amplifier," *Appl. Phys. Lett.*, 1993.

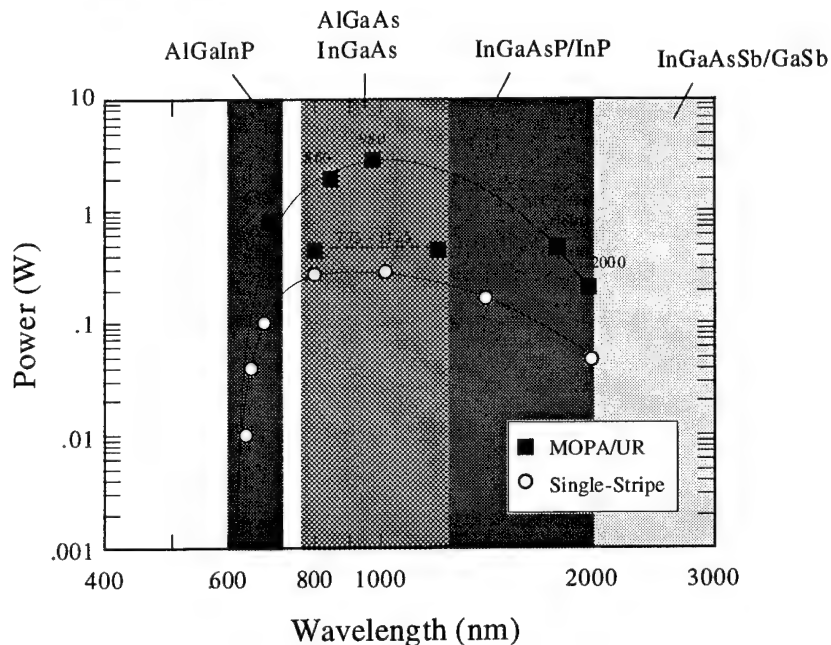


Figure 6. Table of peak diffraction-limited powers obtained from flared MOPAs and URs versus wavelength.

## A Monolithic Stable-Resonator Semiconductor Laser

S. A. Biellak, Y. Sun<sup>†</sup>, S. Wong and A. E. Siegman<sup>†</sup>

*Center for Integrated Systems, Stanford University, Stanford, California 94305*

<sup>†</sup> *E. L. Ginzton Laboratory, Stanford University, Stanford, California 94305*

*Tel: 415-723-0115 Fax: 415-725-6949*

Semiconductor lasers with a variety of cavity geometries have been studied for nearly three decades. For wide stripe monolithic lasers (width  $> 20 \mu\text{m}$ ), nearly all the resonators fabricated so far can be divided into two types: cleaved flat-mirror structures generally employing some form of gain or index guiding [1], and unstable-resonator diode lasers [2,3]. The stable-resonator geometries widely employed in ordinary gas and solid-state lasers [4] have not to date been realized in monolithic semiconductor lasers for a number of reasons. First, the technology to fabricate precisely curved end mirrors has not been widely available until recently. Second, nonlinear saturation and waveguiding effects are strong in semiconductor lasers, and hence lateral gain and index guiding can be expected to deform the modes of stable-resonator lasers at high power levels. Third, the rather weak transverse mode discrimination of stable resonators may not lead to good mode selection in diode lasers having high gain and large output coupling.

It can be instructive nonetheless to study the mode behavior of stable-resonator diode lasers (SRDLs). Before the onset of nonlinear saturation effects SRDLs should exhibit well-defined Hermite-Gaussian lateral modes determined by the resonator parameters  $g_1 = 1 - L/R_1$  and  $g_2 = 1 - L/R_2$  [4]. Careful measurements of the lateral mode properties of SRDLs as a function of oscillation level can thus yield information about the guiding properties of the stripe in both the low-level and nonlinear regimes of operation. In this paper we report the first experimental results of this type.

In order to obtain large lateral mode sizes at the laser end mirrors we elected to use near-concentric resonator designs located near the boundary of the resonator stability diagram [4] as shown in Fig. 1. This resonator design should produce Gaussian spot sizes at the end mirrors

Resonator design parameters:

cavity length:  $600 \mu\text{m}$ ;  
mirror curvature:  $303 \mu\text{m}$ .

Theoretical spot size  $w$ :

at mirror:  $15.4 \mu\text{m}$ ;  
at waist:  $1.5 \mu\text{m}$ .

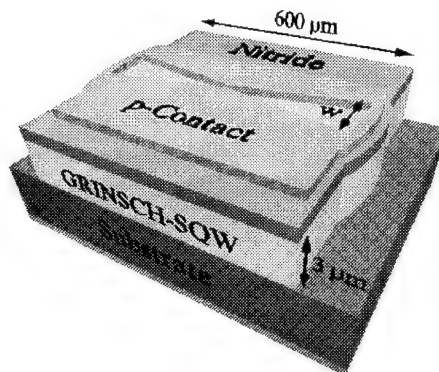


Figure 1: Structure of the stable-resonator semiconductor laser.

large enough to make catastrophic optical damage unlikely. This design also produces a very small spot at the center of the cavity, so that nonlinear effects can be expected to occur first in this region.

The material used for fabrication was a MOCVD-grown GRINSCH-SQW GaAs/AlGaAs structure with  $\lambda_0 = 824 \text{ nm}$ . A  $4000 \text{ \AA}$  thick layer of PECVD  $\text{Si}_3\text{N}_x$  was first deposited and patterned to serve as both the mask for mirror etching and as current isolation. For the mirror etch we used a Zylin ZLN-20 reactor with etch conditions of  $15 \text{ sccm SiCl}_4$  gas flow,  $20 \text{ mTorr}$  pressure,  $0.15 \text{ W/cm}^2$  power density,  $-180 \text{ V DC}$  self bias, and  $20^\circ\text{C}$  electrode temperature. This RIE technique has been previously demonstrated to yield laser diodes with high quality mirrors [3,5]. The mirrors were left uncoated, but were treated with a forming gas anneal. The

contact opening was etched in a tapered shape roughly matching the expected concentric mode pattern in order to maximize the pumping efficiency. Standard metallization steps completed the processing. Index guiding effects should be absent in these structures, at least in the absence of gain saturation, and the width of the pumped region given expected current spreading should be considerably wider than the fundamental Hermite-Gaussian cavity mode.

The lasers were tested *p* side up with 300 ns pulses at 1 kHz. Threshold currents were typically between 90 and 110 mA, or about the same as for cleaved-cavity lasers fabricated from the same material. The beam propagation factor  $M^2$  and the virtual beam waist of the lasers were measured using standard techniques. The lateral intensity distributions at the output mirror and at the virtual beam waist inside a typical diode are shown for increasing values of pump current in Fig. 2. The  $M^2$  factor, the Gaussian waist size  $w_0 = w_{meas}/M$  for the "embedded" Gaussian mode of the cavity, and the position of the beam waist behind the output mirror are all plotted as a function of diode current in Fig. 3. Based on these measurements, we deduce the existence of three regions of operation for the diode: a stable-resonator region of operation extending up to about 3 times threshold, a transition region from there to about 5 times threshold, and a saturated-gain or unstable-resonator region at still higher currents.

At low current levels, from 100 to 300 mA, where gain saturation is presumably small, the laser appears to operate in a coherent superposition of  $n = 0$  and higher-order Hermite-Gaussian wave functions. Just above threshold the  $M^2$  value is close to unity, indicating a mixture of low-order Hermite-Gaussian terms. As the current is increased, higher order terms are added to the mode profile which leads to a steady increase in  $M^2$ . The beam waist throughout this current range remains fixed at approximately  $300 \mu\text{m}$  behind the mirror or at the center of the cavity, as expected for the concentric resonator, and the waist size for the "embedded Gaussian" within the actual beam remains close to, though slightly larger than, the calculated Gaussian waist size from the resonator design parameters ( $\sim 1.54 \mu\text{m}$ ). The discrepancy between measured and calculated Gaussian waist sizes may be due to im-

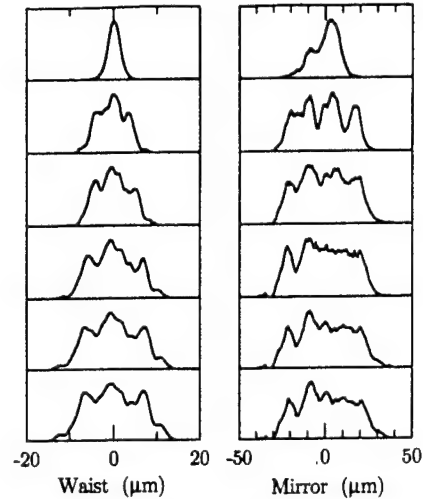


Figure 2. Lateral intensity distributions at the beam waist (left column) and at the output mirror (right column). The pump currents range from 100 mA at the top to 600 mA at the bottom with an increment of 100 mA.

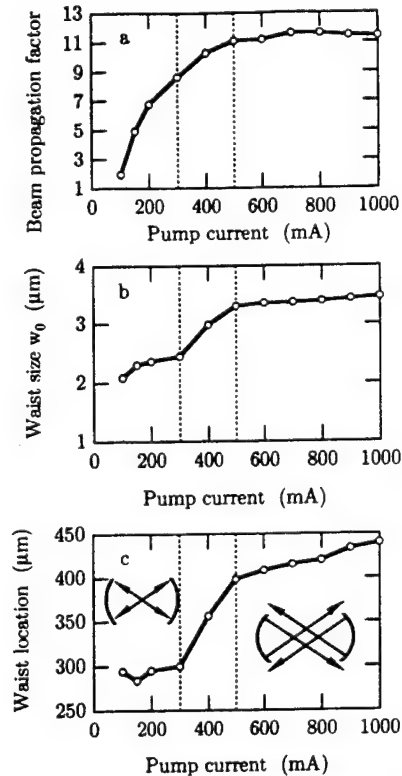


Figure 3. (a) Beam propagation factor  $M^2$ , (b) embedded Hermite-Gaussian waist size  $w_0$ , and (c) location of the beam waist behind the mirror as a function of pump current. Insets in (c) illustrate the effective stable and unstable cavity geometries.

perfect photolithography processing, or to weak carrier-induced index antiguiding in the stripe. Either of these effects would cause the effective mirror radius to be slightly larger than intended, which would broaden the waist size.

We interpret the mode profiles in this region as coherent rather than incoherent Hermite-Gaussian mixtures because the waist (= near-field) and mirror (= far-field) profiles have complementary rather than identical shapes as would be the case for simultaneous oscillations in multiple transverse modes. Also the higher-order transverse modes in near-concentric resonators are so close to degeneracy that oscillation in a locked or coherent superposition is more likely than independent oscillation in multiple transverse modes. We have successfully fit these profiles using coherent superpositions of several Hermite-Gaussian terms.

In the transition region from 300 to 500 mA gain saturation effects begin to play a role in modifying the lateral mode properties. At these higher optical power levels the carrier density in the center of the mode saturates, creating positive index guiding along the center line of the resonator via Henry's  $\alpha$  factor. This added focusing makes the laser move out of the stable region of operation and become geometrically unstable. A simple index-duct resonator calculation indicates that the transition from stable to unstable behavior in this device should occur at around 340 mA, which agrees well with our observations. Above this point the laser cavity then becomes an over-focused or "over-concentric" positive-branch unstable resonator with two internal focal points or waists [4] which are pushed backward from the center of the resonator, as is evident within the transition region in Fig. 3(c). A schematic of this effective unstable cavity geometry is inset in Fig. 3(c). The embedded spot size at the waist also increases somewhat in size, as illustrated in Fig. 3(b). We have also verified the presence of carrier saturation at pump currents above 300 mA by noting a relative decrease of ASE emission from the center of the gain region relative to the total ASE intensity.

At still higher pump currents, above 500 mA for this device, the laser operates as a strongly gain-guided positive-branch unstable resonator. Here the gain across the entire stripe is strongly saturated, and the shape of the induced index guiding profile becomes nearly fixed. As the current increases, additional longitudinal modes reach threshold, and these new lasing wavelengths keep the output power increasing. In this region the lateral mode patterns stay nearly fixed as shown in Fig. 2, as do the  $M^2$  factor and the embedded waist size as shown in Figs. 3(a) and 3(b). The waist position, however, continues to move slowly backward with increasing current as shown in Fig. 3(c), indicating that the resonator continues to become slightly more unstable.

We also fabricated other SRDLs with the same cavity length but slightly different mirror radii. For all these devices, we observed similar mode behavior, but the current levels defining the three operating regions were slightly different. Devices with longer radii of curvature were observed to reach the gain saturation regions faster, as the overall optical intensity on axis in these devices was higher at a given optical power level.

In conclusion, we have fabricated and tested what we believe to be the first monolithic stable-resonator semiconductor lasers. Precise mirror definition and etching allowed us to fabricate nearly concentric devices with large mode volumes. Three operation regions were found to exist for these SRDLs. At low currents the stable resonator modes dominate. In the transition region, gain saturation begins to play a role in determining the lateral mode. In the high current region, gain saturation is strong, the laser operates as a geometrically unstable resonator, and the lateral mode changes very slowly with increasing current. If a mode control aperture is added at the cavity waist, these devices could be expected to function as high brightness oscillators while retaining the high pumping efficiency of a stable resonator geometry.

1. G. P. Agrawal and N. K. Dutta, *Semiconductor Lasers*, V. N. R., 2nd ed., NY, 1993.
2. R. R. Craig et al, *Electron. Lett.*, **21**, 62, 1985.
3. S. A. Biellak et al, *Proc. CLEO*, Anaheim, CA, 1994.
4. A. E. Siegman, *Lasers*, Univ. Sci. Books, Mill Valley, CA, 1984, pp. 744-762 and 821-834.
5. Y. Sun et al, *Electron. Lett.*, **30**, 2034, 1994.



## A high-power ( $\sim 2$ W) external-cavity cw diode laser tunable from 960 - 980 nm

S. Gupta, R. J. Jones, R. K. Jain, and J. N. Walpole\*

Center for High Technology Materials, Rm. 125 EECE Bldg., University of New Mexico,  
Albuquerque, NM 87131 ; Tel. # (505) 277-2610 ; FAX # (505) 277-4853

\* Lincoln Laboratory, Massachusetts Institute of Technology, Lexington, MA 02173

Wavelength-tunable high-power diode lasers with narrow-linewidths and diffraction-limited outputs are needed for numerous applications including diode-based nonlinear frequency conversion, coherent radar, coherent free-space communications, and spectroscopic applications. The tapered-amplifier gain-guided design [1] has been shown to be a very effective means for achieving high output powers ( $>1$ W cw) in a single-lobed diffraction-limited beam [2,3]. Although single longitudinal mode operation using a master-oscillator-power-amplifier (MOPA) scheme, with a monolithic Bragg reflector for the master-oscillator has been demonstrated [4], these structures have very limited tuning ranges (typically  $< 3$  nm), and involve careful adjustment and regulation of the temperature. Broader tuning ranges ( $\sim 35$  nm) of  $\sim 1$  W power levels were demonstrated subsequently by using an external-cavity grating-tuned configuration at wavelengths near 860 nm [5], followed by demonstration of  $\sim 0.5$  W power levels at other wavelength ranges. *This work reports the first demonstration of broadly-tunable narrow-linewidth high-power operation ( $\sim 1.8$  W cw, and up to 3 W quasi-cw) in the 960-980 nm wavelength range*, to develop a source that is critical for a number of applications including high-power blue generation via quasi-phase matched doubling and spectroscopic study of saturation characteristics of Er-codoped amplifiers and lasers in a variety of host media.

A schematic of the external-cavity diode laser used in our experiments is shown in Fig.1. The gain medium consists of a strained layer InGaAs/AlGaAs graded-index separate confinement heterostructure (GRINSCH) configured in the form of a tapered-amplifier device structure [2]. A 4.5 mm focal length lens collects the light from the narrow end of the amplifier which is retro-reflected back to the chip from a 1700 grooves/mm diffraction grating mounted in the Littrow configuration. The active region is parallel to the lines in the grating for maximizing the dispersion; moreover, since the diode amplifier gain is predominantly TE-polarized, a half-wave plate is inserted [6] into the external-cavity to ensure that the polarization of the light incident on the grating is perpendicular to its grooves, in order to achieve a high reflection efficiency of ( $\sim 90\%$ ) in the first order across the entire tuning range of the diode laser.

The light-current (L-I) curve of the external-cavity laser operating at 970 nm is shown in Fig.2(a). The laser threshold is 0.65A with a slope efficiency of 0.8 W/A, and up to 1.8W is achieved under cw operation at 3A injected current. Due to the limitations on our heat sink, we were not able to operate cw beyond this point. Under quasi-cw conditions (duty cycle = 0.05, pulsewidths = 500 $\mu$ s), over 3W of power was obtained at  $\sim 5$ A injected current. Also no decrease in the slope efficiency was noted at these power levels under quasi-cw conditions. The far-field intensity pattern in the plane parallel to the amplifier chip was measured using a spherical lens to eliminate quadratic phase curvature due to the beam divergence. The predominantly single-lobed and  $\sim 1.5$  times diffraction-limit far-field pattern at 1.8W cw output power is shown in Fig.2(b). Figure 2(c) shows the relative flatness of the output power at 1W, as the frequency is tuned from 960-980 nm by rotating the grating.

The spectral characteristics of the tunable diode laser were studied with an optical spectrum analyzer (OSA) and a scanning Fabry-Perot interferometer. Fig.3 shows the optical spectra measured using an OSA, at the center and extremes of the tuning range. A side-mode suppression ratio (SMSR) of greater than 20 dB was obtained over the entire tuning range, with a typical SMSR value of 30 dB near the center of tuning range. Note that the linewidths shown in Fig.3 are limited by the 0.5  $\text{\AA}$  resolution of the OSA. Scanning Fabry-Perot measurements confirmed single

longitudinal mode operation over much of this tuning range. The linewidth measurements were limited by the 120 MHz resolution of our low-finesse scanning Fabry-Perot. instrument (the longitudinal mode-spacing of our external-cavity diode laser is  $\sim 1.5$  GHz).

The spectral stability of the external-cavity diode laser was observed to strongly depend on the residual modulation of the spontaneous emission spectra, observed at a period of  $\sim 2$  nm (see Fig.3). The  $1.3\mu\text{m}$  cladding layer thickness results in a leakage of the waveguide mode into the substrate which is transparent at the lasing wavelength. Reflection from the metallization results in modulation of the gain coefficient, which has been shown to result in a near-periodic modulation, with a period of 2-3 nm for similar heterostructure layer designs [7]. For wavelengths tuned near the peak of the modulation, single-longitudinal-mode operation is obtained, whose stability is dictated by the mechanical and thermal considerations of the external-cavity. For wavelengths tuned between the peaks of the gain modulation, this interference causes the laser to oscillate in a few longitudinal modes, since the grating bandwidth for the Littrow configuration ( $\sim 18$  GHz for our case) allows a number of external-cavity modes (spaced  $\sim 1.5$  GHz apart) to oscillate within the grating bandwidth. By narrowing the effective grating bandwidth to  $\sim 3$  GHz using a Littman-Metcalf configuration (double-pass grazing-angle incidence on the grating) only one longitudinal cavity-mode was observed. The spectral stability of these lasers can thus be improved by either using thicker cladding layers to eliminate the gain modulation, or by using a much narrower grating bandwidth, i.e., the Littman-Metcalf configuration.

Such narrow-linewidth high-power diode laser source are ideally suited for non-linear frequency conversion to shorter wavelengths. Preliminary measurements of second-harmonic-generation (SHG) of 976 nm diode-laser radiation, using a quasi-phase-matched (QPM)  $\text{LiNbO}_3$  waveguide ( $\sim 1$  cm long) has been demonstrated to result in the generation of 488 nm radiation in our lab. In addition, work is also in progress on a monolithic two-section tapered amplifier device incorporated in a grating-tuned external-cavity configuration, to produce tunable, high-power, narrow-linewidth modulated radiation.

In conclusion, a tapered diode amplifier has been used in an external-cavity configuration to produce a high-powered, near diffraction-limited laser source that is frequency tunable from 960-980 nm. The frequency stability is observed to strongly depend on the residual gain modulation, due to interference from the leaked waveguide mode.

## References

- [1] R. R. Craig, and R. R. Stephens, SPIE 893, 25 (1988).
- [2] J. N. Walpole, E. S. Kintzer, S. R. Chinn, C. A. Wang, and L. J. Missaggia, "High-power strained layer InGaAs/AlGaAs tapered travelling wave amplifier", Appl. Phys. Lett. 61 (7), 740 (1992).
- [3] E. S. Kintzer, J. N. Walpole, S. R. Chinn, C. A. Wang, and L. J. Missaggia, "High-power, strained-layer amplifiers and lasers with tapered gain regions", IEEE Photon. Tech. Lett. 5 (6), 605 (1993);  
- D. Mehuys, S. O'Brien, R. J. Lang, A. Hardy, and D. F. Welch, "5W, diffraction-limited, tapered-stripe unstable resonator semiconductor laser", Electron. Lett. 30 (22), 1855 (1994).
- [4] S. O'Brien, D. F. Welch, R. A. Parke, D. Mehuys, K. Dzurko, R. J. Lang, R. Waarts, and D. Scifres, "Operating characteristics of a high-power monolithically integrated flared amplifier master oscillator power amplifier", IEEE J. Quantum Electron. QE-29 (6), 2052 (1993).
- [5] D. Mehuys, D. F. Welch, and D. Scifres, "1 W cw, diffraction-limited, tunable external-cavity semiconductor laser", Electron. Lett. 29 (14), 1254 (1993).
- [6] H. Lotem, Z. Pan, and M. Dagenais, "Tunable external cavity diode laser that incorporates a polarization half-wave plate", Appl. Opt. 31 (36), 7530 (1992).
- [7] E. V. Arzhanov, A. P. Bogatov, V. P. Konyaev, O. M. Nikitina, and V. I. Shveikin, "Waveguiding properties of heterolasers based on InGaAs/GaAs strained quantum-well structures and characteristics of their gain spectra", Quantum Electronics 24 (7), 581 (1994).



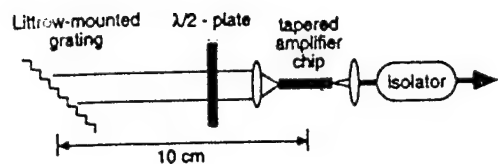


Figure 1. Schematic of external cavity design.

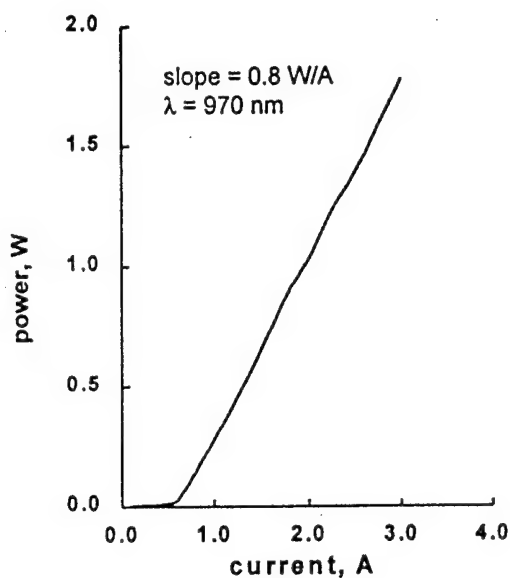


Figure 2(a). cw L-I characteristic of tunable high-power laser.

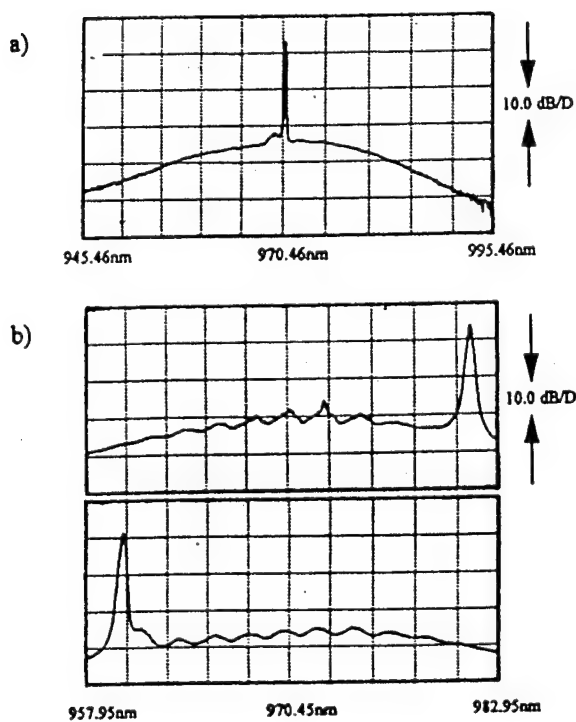


Figure 3. Frequency spectrum of laser output at (a) center and (b) extremes of tuning range as measured by an optical spectrum analyzer.

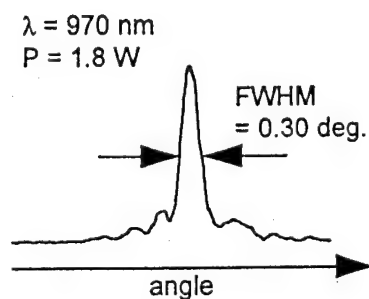


Figure 2(b). Far-field beam profile parallel to p-n junction at 1.8 W showing 1.5 times diffraction-limited performance.

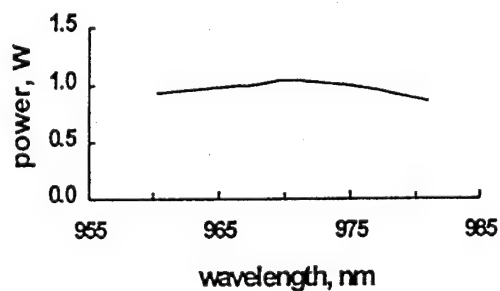


Figure 2(c). Tuning curve of the external cavity laser at 2 A injected current.

**Spectral Properties of an AlGaAs MOPA Laser**  
**Under Large Signal Modulation of the Oscillator or the Amplifier**

**Michael A. Krainak, Donald M. Cornwell, Valerie Dutto**

*NASA Goddard Space Flight Center, Photonics Branch, Code 715, Greenbelt, MD 20771*

**Anthony W. Yu**

*Hughes STX Corporation, 7701 Greenbelt Road, Greenbelt, MD 20770*

**Stephen O'Brien**

*Spectral Diodes Laboratories, 80 Rose Orchard Way, San Jose, CA 95134*

In this paper, we report on the optical spectrum characteristics of a modulated, high power ( $> 1$  W average), monolithic flared amplifier master oscillator power amplifier (MFA-MOPA) laser. The CW performance of this laser is presented in Reference 1. The master oscillator (MO) is a distributed Bragg reflector (DBR) laser operating in a single longitudinal mode under CW operation. The power amplifier (PA) is monolithically integrated with the MO and has a tapered gain region. The laser was capable of delivering over 1 W of CW power with the MO biased at 140 mA and the PA biased at 4.0 A at operating temperature of 15°C. The MFA-MOPA can be tuned with temperature at a rate of 0.07 nm/°C. The instantaneous CW linewidth of the laser was measured to be 300 MHz (0.74 pm).

The NASA application requires a 1 Mbps pseudo-noise (PN) code modulation. To investigate the performance of the MFA-MOPA laser under large signal 1 Mbps modulation, we applied modulation to (i) the MO and (ii) to the PA. With modulation applied to the MO, the MO was biased at 73 mA and a peak-to-peak modulation current of 100 mA. The power amplifier was biased at 4.0 A. Under this condition, the average power was measured as 700 mW with better than 9:1 extinction ratio. The laser spectral width measured 10 dB down from the peak is 0.3 nm (the 3 dB width is 0.14 nm). In the second case, the modulation was applied to the power amplifier (acting as an "external" modulator). The DBR MO was biased at 130

mA. The PA was biased at 2.75 A with peak-to-peak modulation current of 2.5 A. We have achieved an average power of 720 mW with a 10:1 extinction ratio. Under this condition, the spectral width measured 10 dB down from the peak is 0.16 nm (the 3 dB width is 0.07 nm). We found that the 10 dB down spectral width is more relevant for our system application. Figure 1 shows the optical spectrum as measured with a diffraction grating spectrum analyzer with 0.01 nm resolution. Note that the modulation of the amplifier, as opposed to the oscillator, provides a narrower spectral width. We believe that greater optical isolation of the oscillator and amplifier would provide an even narrower width. Another possible advantage to modulation of the amplifier (as opposed to the oscillator) is a factor of two savings in the required electrical power. However, circuit considerations may prohibit taking full advantage of these savings (i.e., due to load matching resistor requirements).

We now explain the significance of this work for NASA applications. An attractive laser ranging method for use with laser diodes is direct injection current modulation with a digital code<sup>2</sup> and/or a sinusoid. Both laser remote sensing and free space optical communications require the use of narrow band optical filters at the receiver to improve the probability of detection in environments with background radiation (e.g., Sun light), in addition to high optical power. A primary system application consideration is the wavelength range of available sensitive detectors and high power lasers. Commercial silicon avalanche photodiode detectors (APDs) used in the photon counting mode have low quantum efficiency at wavelengths longer than 860 nm.<sup>3</sup> Commercial near infrared photomultiplier tubes (PMT) also have very low quantum efficiencies at wavelengths longer than 860 nm.<sup>4</sup> These photon counting detector constraints prohibit the use of the presently available InGaAs MOPA laser technology for remote sensing applications that require photon counting. For these reasons, NASA has developed a laser diode based prototype cloud/aerosol lidar instrument operating at ~ 828 nm.<sup>5</sup> At present, the aerosol cloud lidar transmitter is a 150 mW AlGaAs laser diode with a spectral width of greater than 1 nm under 1 Mbps large signal modulation. As can be observed from the data presented in this

paper, the MFA-MOPA is a higher power and a narrower spectral width laser transmitter source for this application.

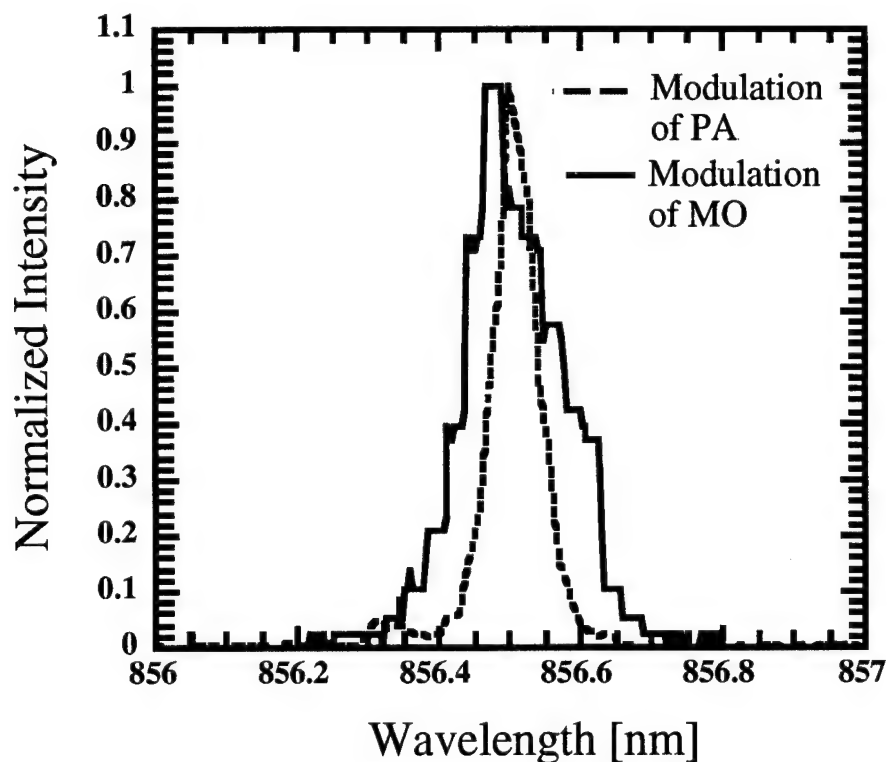


Figure 1. Optical spectrum of the MFA-MOPA under the conditions noted.

## REFERENCES

1. O'Brien, S., D. Mehuys, J. Major, R. Lang, R. Parke, D.F. Welch, and D. Scifres, "1.3 W CW, Diffraction-Limited Monolithically Interated Master Oscillator Flared Amplifier at 863 nm," *Elect. Letts.*, 29 (24), 2109, 1993.
2. Takeuchi, N., H. Baba, K. Sakurai, and T. Ueno, "Diode-laser Random Modulation CW Lidar," *Applied Optics*, 25 (1), 63, 1986.
3. EG&G Model SPCM-100-PQ single photon counting module data sheet.
4. DEP Delft Model PP0270P hybrid photomultiplier tube detector data sheet.
5. Rall, J. A. R., J. Abshire, S. Manizade, "Lidar Measurements of Clouds and Aerosols Using AlGaAs Lasers Modulated with Pseudorandom Codes," *LEOS '92 Conference Proceedings Paper EOS/SSLT/OSM1.3*, p. 206 1992.

# Beam Propagation Model of Tapered Amplifiers including Non-Linear Gain and Carrier Diffusion.

P.CHAZAN\* and J.D.RALSTON\*\*

\* Fraunhofer-Institut für Angewandte Festkörperphysik, Tullastrasse 72,  
D-79108, Freiburg, Germany, Tel: (+49) 761 5159 267, Fax: (+49) 761 5159 400.

\*\*SDL Inc. 80 Rose Orchard Way San Jose CA 95134, Tel: (408) 943 9411, Fax: (408) 943 1070

Recent interest in high-power single-mode diode lasers has led to the evaluation of a variety of semiconductor amplifier geometries [1], integrated master oscillator power amplifier (MOPA), designs and flared oscillator devices. Flared amplifiers and oscillators have been found to be less sensitive to filamentation effects than broad area devices, although filamentation still ultimately limits the performance of such devices [2]. Using a FD-BPM model we investigate the performance to be expected from various flared laser structures in terms of both output power and beam quality. We clarify the influence of such material parameters as the number of quantum wells, the differential quantum efficiency and the linewidth enhancement factor on the output beam profile of the amplifier. We point out the influence of the linewidth enhancement factor showing that a reduction of this factor improves the output beam quality, the resistance to inhomogeneous injection, and the output farfield. Furthermore, a simulation of a 2D integrated elliptical lens is presented, showing the possibility of 'on chip' correction of the astigmatism for low  $\alpha$ -factor structures. Such a lens would spare the use of an external cylindrical lens for collimation of the output signal.

## Numerical Model

We have used a 2-dimensional beam propagation model for the simulation of the optical field. The complex index function of the amplifier may be written as follow:

$$n_{\text{opt}}(x, z) = \frac{\lambda_0}{4\pi} (g(n_c(x, z)) (i - \alpha) - i\alpha_i) + n_b(x, z) \quad (1)$$

where  $\lambda_0$  is the free-space wavelength,  $\alpha$  is the linewidth enhancement factor,  $\alpha_i$  describes the internal optical losses in the waveguide,  $n_b$  is the background effective index of the structure ( $n_b=3.34$ ),  $n_c(x, z)$  is the carrier density distribution and  $g(n_c(x, z))$  is the modal gain function, which may be either linear or logarithmic to take gain saturation into account. The carrier density profile  $n_c(x, z)$  is determined by solving the diffusion equation using a 1D finite difference method in the lateral direction. In the case of a non-linear gain model, the finite difference method leads to a set of non linear coupled equations. We then use a Newton Raphson algorithm to find the solution  $n_c(x, z)$  of this non linear system.. Knowing the carrier profile  $n_c(x, z)$  at  $z$ , we deduce the complex optical index of the structure and propagate the field using the BPM method. We neglect the influence of spontaneous emission ie. we assume that the spontaneous lifetime  $\tau_{sp}$  is independant of carrier density.

## Results

We compare a typical strained InGaAs/GaAs QW structure with an  $\alpha$ -factor of 2.5, as previously modelled [2], with a structure having an  $\alpha$ -factor of 1.3, in order to obtain a quantitative performance comparison. Such low  $\alpha$ -factor lasers may be realized by combining strain and p-doping in the active region [3]. Table 1 summarizes the parameters implemented in our numerical model, together with typical values.

We first study the saturation effects arising due to an increase in the injection current. The tapered amplifier structure is 2000 $\mu\text{m}$  long, with a divergence angle of 4°; both the output beam profile and the L-I characteristic are simulated with the BPM model. As shown in Fig.1, the output optical profile is greatly improved by a decrease in the  $\alpha$ -factor. To quantify the effect of the  $\alpha$ -factor, we define an overlap factor  $\delta$  with respect to the 'top hat' profile emitted by a chirp-free ( $\alpha=0$ ) amplifier after removing the quadratic phase curvature. This profile represents the best field which can be emitted from a flared power amplifier. According to figure 2, for a beam quality corresponding to  $\delta=0.9$ , the maximum output power allowed with  $\alpha=2.5$  is only 0.8W ( $I=1.45\text{A}$ ), whereas an output power of more than 2W can be achieved for  $\alpha=1.3$  ( $I=4.3\text{A}$ ).

The influence of inhomogeneous current injection has also been simulated, by assuming a rectangular slot, 5 $\mu\text{m}$  wide and with different lengths, centered 500 $\mu\text{m}$  from the input end of the amplifier. For a 100 $\mu\text{m}$  long slot, Fig.3(a) and (b) show the evolution of the optical intensity profile for alpha factors of 1.3 and 2.5, respectively. For  $\alpha=1.3$ , the output profile is very similar to that obtained with no slot, whereas for  $\alpha=2.5$  strong filamentation has appeared.

As expected, the local reduction in gain leads to focussing of the optical beam and induces a peak in the optical profile.

Figure 4 shows the output profile of 3 structures having the same  $\alpha\beta$  product. The combination low  $\alpha$  factor and high differential gain is seen to be desirable for the standpoint of enhancing the output beam quality. For high differential gain structures, the mean carrier density to obtain a given amplification is lower than for low differential gain structures, thus the corresponding increase of optical index is reduced and, consequently, the filamentation is reduced. We have also studied the effect of the number of quantum wells (which influences the non-linear gain) and found that the lower mean carrier density of MQWs structures leads to only a slight improvement of the external quantum efficiency but not enough to compensate the disadvantage of the increase of the threshold value and higher optical losses.

Finally, we show the calculated far-field at the output of a tapered amplifier terminated with an integrated elliptical lens. This far-field is gradually broadening with increasing  $\alpha$ , from the diffraction limit ( $0.2^\circ$ ) for  $\alpha=0$  to a FWHM of  $3^\circ$  for  $\alpha=2.5$ .

To conclude, a FD-BPM model has been implemented to simulate the filamentation effects in tapered amplifiers. A dramatic improvement of the beam quality is to be expected by reducing the  $\alpha$ -factor using advanced epitaxial layer structures. We have recently been able to experimentally confirm the behaviour predicted in Fig.1, using InGaAs/GaAs tapered MQW lasers fabricated both with and without p-type modulation doping in the active region. These results will be reported elsewhere [3].

[1] L. Goldberg, D.Mehuys, M.R.Surette and D.C.Hall, "High power, near diffraction-limited large area travelling-wave semiconductor amplifiers", IEEE J. Quantum Electron., Vol.29, pp. 2048-2053,1993.

[2] R.J.Lang, A. Hardy, R. Parke, D. Mehuys, S. O'Brien, J. Major, D.F. Welch, " Numerical analysis of flared semiconductor laser amplifiers", IEEE J. Quantum Electron., Vol.29, pp. 2044-2051, 1993.

[3] J.D. Ralston, P.Chazan, M.Maier, F.R. Laughton, M.K. Abd Rahman, I.H. White, and E.C. Larkins, "Tapered InGaAs/GaAs MQW lasers with carbon modulation-doping and reduced filamentation", Electronics Letters, to be published in April 1995.

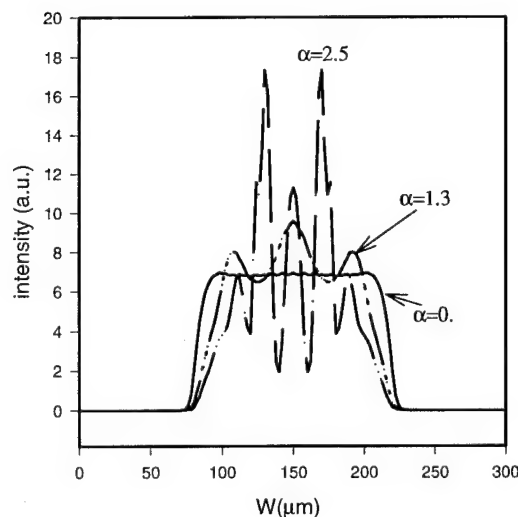


Fig.1 : Optical output profiles of the tapered amplifier for  $\alpha=0$ , 1.3 and 2.5. The injected current is 1.45A ( $1000\text{A}/\text{cm}^2$ ), and the optical input power is 10mW.

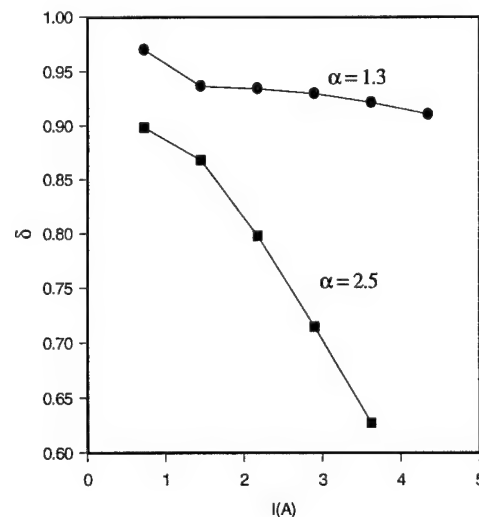


Fig.2: Overlap factors,  $\delta$ , as a function of injection current for  $\alpha=1.3$  and  $\alpha=2.5$ .

symbol	parameter	value
$L_x$	total lateral width	300 $\mu\text{m}$
$\Delta x$	lateral quantization	1 $\mu\text{m}$
$L_z$	length in longitudinal direction	2000 $\mu\text{m}$
$\Delta z$	longitudinal quantization	5 $\mu\text{m}$
$h_1$	amplifier input width	3 $\mu\text{m}$
$h_2$	amplifier output width	142 $\mu\text{m}$
$P_{in}$	input optical power	1-10mW
$W_0$	input beam waist	2.7 $\mu\text{m}$
$\lambda$	wavelength	1 $\mu\text{m}$
$\beta$	modal differential gain	$2.2 \cdot 10^{-15} \text{cm}^2/\text{s}$
$n_0$	transparency current density	$1.5 \cdot 10^{18} \text{cm}^{-3}$
$\alpha$	alpha factor	0,1.3,2.5
$\alpha_i$	internal losses	5 $\text{cm}^{-1}$
$\tau_{sp}$	spontaneous carrier lifetime	0.38ns
$D_n$	diffusion coefficient	20 $\text{cm}^2/\text{s}$
$J$	current density	1000A/ $\text{cm}^2$
$\Gamma$	overlap factor	0.024

Table 1: Parameters used in the BPM model of flared amplifier

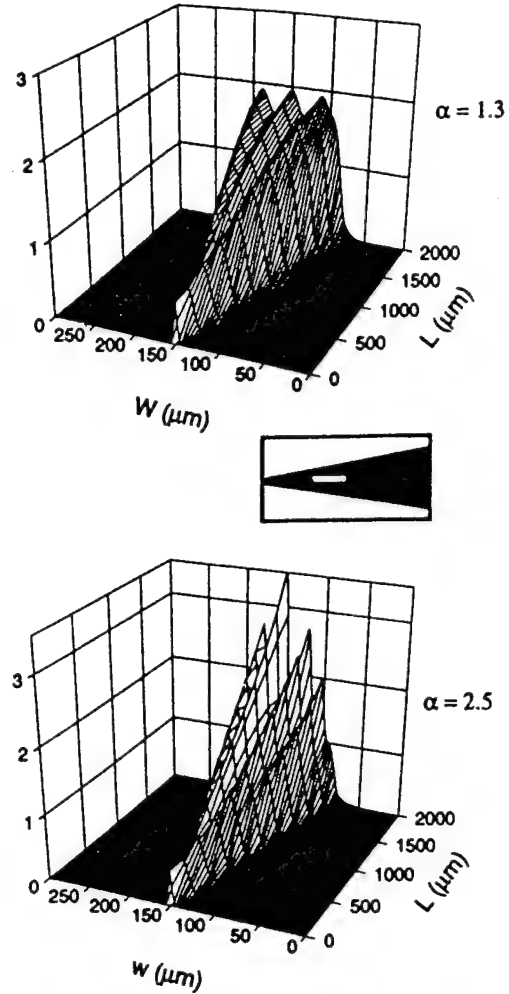


Fig.3: Evolution of the optical beam profile during propagation in a flared amplifier having a 100 $\mu\text{m}$  long slot for (a)  $\alpha=1.3$ , (b)  $\alpha=2.5$ . Injected current 1.45A (1000A/ $\text{cm}^2$ ), input optical power 1mW.

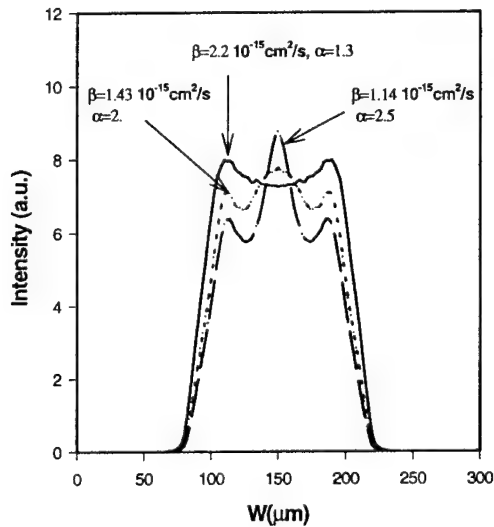


Fig4: output beam profiles of three amplifiers having the same geometry and the same  $\alpha\beta$  product, where  $\alpha$  the linewidth enhancement factor, and  $\beta$  is the differential gain.

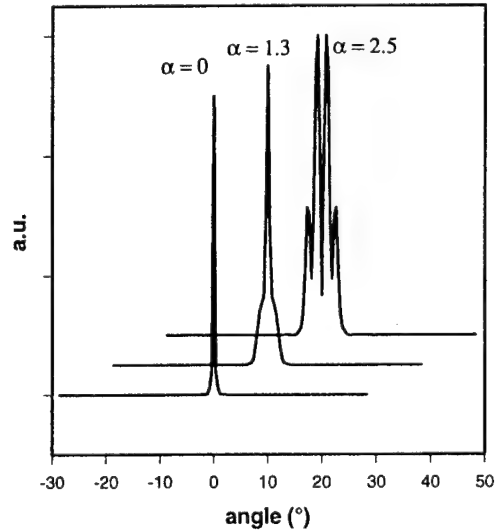


Fig5: Farfield calculation of the output of a tapered amplifier integrated with an elliptical lens. The differences in FWHM are due to phase distortions induce by filamentation

# Operating Characteristic Simulation of High-Power Broad-Stripe Quantum-Well Semiconductor Traveling Wave Amplifiers

Zheng Dai, Rainer Michalzik, and Peter Unger

Department of Optoelectronics, University of Ulm, D-89069 Ulm, Germany

Phone: +49(731)5026050, Fax: +49(731)5026049

## 1. Introduction

To design an optimized high-power semiconductor traveling wave amplifier (TWA), it is important to study the parameter dependencies of a TWA on its waveguide structure, material properties, and operating conditions. Since the degradation of the output beam profile in a broad-stripe TWA is often observed in practice, two-dimensional models employing the beam propagation method (BPM) and the effective index method have been widely used [1-2]. These models are usually based on a linearization of basic material properties. For high-power TWAs, the operating current is several times larger than the threshold current of a corresponding laser diode. Linear approximations are under these conditions no longer valid. In this paper, we consider nonlinear material properties in a self-consistent BPM model. Nonlinear gain and residual facet reflectivities are found to greatly influence the operating characteristics of the devices.

## 2. Model Description

The layer structure and the coordinate system of the quantum-well (QW) semiconductor TWA are schematically drawn in Fig. 1. Different waveguide structures and active materials influence the effective refractive index, which consists of four terms: a background effective index  $n_{eff,0}$ , a built-in effective index change  $\Delta n_{bi}$ , a carrier induced effective index change  $\Delta n_{in}$ , and an imaginary gain part  $i\lambda g/(4\pi)$ ,

$$n_{eff} = n_{eff,0} + \Delta n_{bi} + \Delta n_{in} + i\lambda g/(4\pi).$$

The gain coefficient  $g$  is composed of the material gain of the active layer  $g_a$  and the absorption of the guiding layers  $\alpha$  as

$$g = \Gamma g_a - (1 - \Gamma)\alpha,$$

where  $\Gamma$  is the confinement factor. The absorption constant can be extracted from experiments and is typically about  $\alpha = 10 \text{ cm}^{-1}$ . The optical gain for a strained InGaAs/GaAs QW active layer has been modeled according to [3] and is nonlinearly dependent on the carrier concentration (see Fig. 2). The carrier concentration  $N$  is governed by a second-order diffusion equation

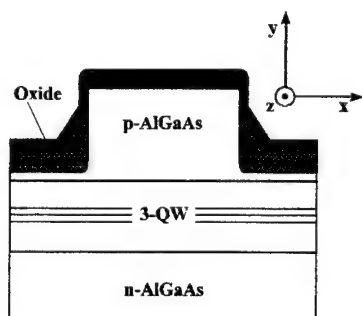


Fig 1: Schematic layer structure and coordinate system of the TWA.

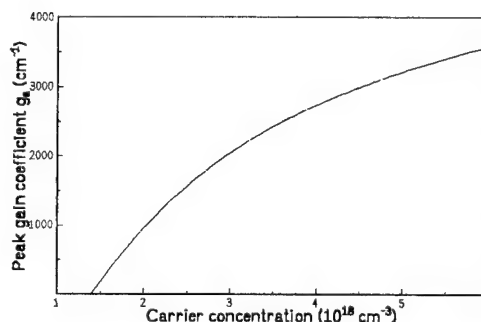


Fig. 2: Peak gain vs. carrier concentration for a strained InGaAs/GaAs QW.



$$D_e d^2 N / dx^2 = N / \tau_s - \eta J(x) / (q d_a) + g S(x, z) / (h \nu),$$

where  $D_e$  is the effective diffusion constant,  $J(x)$  and  $\eta$  denote the injected current density and the injection efficiency, respectively, and  $S(x, z)$  is the optical intensity in the active layer of thickness  $d_a$ . The recombination time  $\tau_s$  can be expressed by a nonradiative coefficient  $A$ , a spontaneous recombination constant  $B$ , and an Auger recombination coefficient  $C$  as

$$1/\tau_s = A + BN(x, z) + CN^2(x, z).$$

The current spreading is taken into account by approximating the current density as

$$J(x) = \begin{cases} J_e & \text{for } |x| \leq w_a/2, \\ J_e / [1 + (|x| - w_a/2)^2 / (\delta w_a)^2] & \text{for } |x| > w_a/2, \end{cases}$$

with a constant current density  $J_e$ , a waveguide width  $w_a$ , and a spreading width  $\delta w_a$ , respectively.

Considering the residual field reflection coefficients  $r$  and the corresponding phase shifts  $\theta$  at the front facet  $f$  and the back facet  $b$ , the optical field in the TWA is the superposition of a forward propagating field  $E_f(x, z)$  and a backward propagating field  $E_b(x, z)$ ,

$$E(x, z) = E_f(x, z) + E_b(x, z).$$

The boundary conditions of the  $k$ -th iteration at the two facets can be expressed by

$$E_f^{(k+1)}(x, 0) = r_f \exp(i\theta_f) E_b^{(k)}(x, 0) + t_f E_{inj}(x, 0),$$

and

$$E_b^{(k+1)}(x, L) = r_b \exp(i\theta_b) E_f^{(k+1)}(x, L),$$

where  $t_f E_{inj}(x, 0)$  represents the injected optical field and  $L$  is the amplifier length. We start the iteration by injecting an asymmetric Gaussian field of optical power  $P_0$ , which is reflected back and forth in the amplifier. When the carrier distribution of the  $(k+1)$ -th iteration matches that of the  $k$ -th iteration within an acceptable tolerance, a stable operation is achieved.

### 3. Numerical Results

Parameters used in the simulation are shown in Table 1. In order to focus our concentration on the operating characteristics induced by the material nonlinear properties, we neglect the carrier induced effective index change and the built-in effective index change in present investigations.

TABLE 1. Calculation Parameters

$L$	500 $\mu\text{m}$	$w_a$	20 $\mu\text{m}$	$d_a$	24 nm	$\Gamma$	0.058
$\delta w_a$	1 $\mu\text{m}$	$n_{eff,0}$	3.44	$D_e$	36 $\text{cm}^2/\text{s}$	$\lambda$	1.0 $\mu\text{m}$
$\eta$	1	$A$	$10^{-8} \text{ s}^{-1}$	$B$	$5.0 \cdot 10^{-11} \text{ cm}^3/\text{s}$	$C$	$7.0 \cdot 10^{-30} \text{ cm}^6/\text{s}$

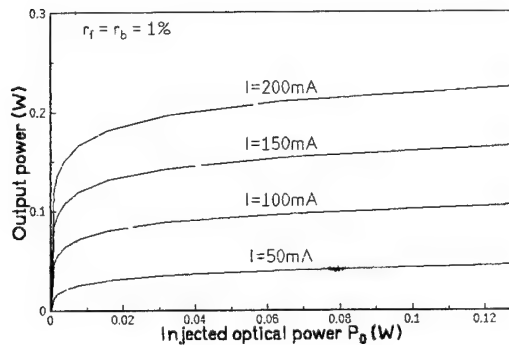


Fig. 3: Amplifier output characteristics under different driving currents.

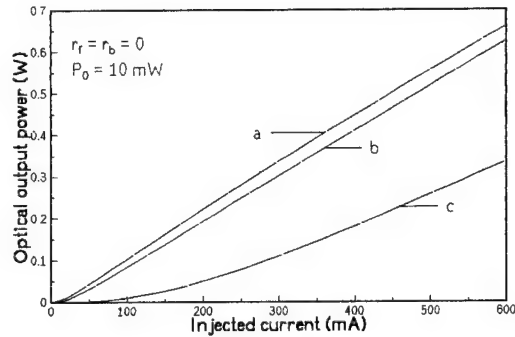
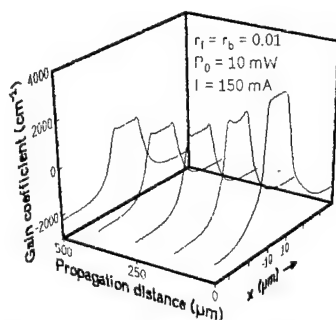
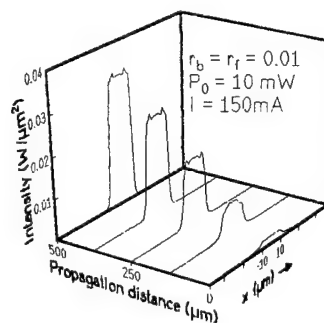


Fig. 4: Influence of the Auger coefficient on the amplified output power.

The input-output characteristics under different driving currents are shown in Fig. 3. Generally speaking, the saturation of the output power starts at a milliwatt optical input power level. The nonlinear relationship between the gain coefficient and the carrier concentration enhances the saturation phenomenon. The dependencies of the output power on the Auger coefficient are depicted in Fig. 4. Increasing the Auger coefficient  $C$ , which is not well known in the strained material system, from  $7.0 \times 10^{-30} \text{ cm}^6/\text{s}$  of curve *a* to  $5.0 \times 10^{-29} \text{ cm}^6/\text{s}$  and  $5.0 \times 10^{-28} \text{ cm}^6/\text{s}$ , we obtain curve *b* and *c*, respectively. The influence of the Auger recombination becomes significant, if the recombination rate approaches the driving term in the carrier diffusion equation.



**Fig. 5:** The gain coefficient distribution in the active layer.



**Fig. 6:** The optical intensity distribution in the active layer.

The material gain of the active layer, plotted in Fig. 5, reveals a deeply saturated gain coefficient near the output facet. With the amplification of the optical field, the gain coefficient of the active layer decreases. The amplified optical intensity in the active layer is shown in Fig. 6. Comparing the material gain coefficient distribution with the optical intensity distribution, we find that the spatial hole burning effect is considerable.

Fig. 6 also shows the deformation of the output beam profile. The superposition of the backward and forward fields construct an interference pattern in the waveguide. This pattern near the input facet will be preferably amplified in the forward propagation process. The amplified interference pattern causes distortions of the beam profile, which are intensified with increasing residual reflectivity.

As a conclusion, we have combined the nonlinear gain and recombination properties in a self-consistent BPM model for high-power traveling wave amplifiers. In addition to self-focusing, parasitic facet reflections could be identified as a reason for beam profile deformation. Especially the assumption of a linear gain model is found to lead to an overestimation of the achievable power gain.

#### 4. References

- [1] G. R. Hadley, J. P. Hohimer, and A. Owyong, *IEEE J. Quantum Electron.*, Vol. 24, pp.2138-2152 (1988)
- [2] G. P. Agrawal, W. B. Joyce, R.W Dixon, and M. Lax, *Appl. Phys. Lett.*, Vol. 43, pp. 11-13 (1983)
- [3] R. Michalzick and K. J. Ebeling, in *Physics and Simulation of Optoelectronic Devices III*, M. Osinski and W.W. Chow (Eds.), *Proc. SPIE* 2399 (1995)



Tuesday, August 22, 1995

## Vertical-Cavity Lasers

**TuD** 3:45 pm-5:45 pm  
Torreys Peak I-III

Thomas M. Baer, *Presider*  
*Biometric Imaging*

Blue-Green Electron Beam Pumped Vertical-Cavity  
Surface-Emitting Laser Using MBE Grown  
Modulated ZnCdSe/ZnSe Superlattice

N.G. Basov, E.M. Dianov\*, V.I. Kozlovsky, A.B. Krysa,  
A.S. Nasibov, Yu.M. Popov, A.M. Prokhorov\*\*, P.A. Trubenko\*,  
and E.A. Shcherbakov\*.

P.N. Lebedev Physical Institute, RAS, Moscow;  
Vavilov str., 38, 117942, Moscow, Russia.  
Ph: (095)-132-62-46, Fax: (095)-135-78-80.

(\*) Fiber Optics Research Center at the GPI, RAS,  
Vavilov str., 38, 117942, Moscow, Russia.

(\*\*) The General Physics Institute, RAS,  
Vavilov str., 38, 117942, Moscow, Russia.  
Ph: (095)-132-82-32, Fax: (095)-135-81-39.

Introduction.

The use of a broad-bandgap II-VI semiconductors and their ternary and quaternary alloys for vertical-cavity surface-emitting laser (VCSEL) fabrication open a new additional possibilities for their design and applications. In particular, one of the promising using is the realization of a large screen color high definition TV ( HDTV ) laser projection systems, and flat panel color displays [1,2]. One of the main advantages of the II-VI VCSEL's, in this case, is the possibility of the full color HDTV laser screen creation based only on this materials. The bulk II-VI compounds were used recently for the first successful demonstration of the laser cathode ray tube ( LCRT ) and color laser TV system [3]. However, one of the limitations of this scheme was the sufficiently high E-beam current threshold, in particular, for the room-temperature operation.

Essential decreasing of the threshold current can be achieved by using of multi quantum wells ( MQW's ) or superlattice structures (SLS) grown by different techniques. In particular, it is suitable to apply for this purpose of the molecular beam epitaxy (MBE) which has been successfully used for the injection current blue-green laser diode fabrication [4].

This paper presents the first results of the room temperature, E-beam pumped blue-green VCSEL based on the modulated  $\text{Zn}_{1-x}\text{Cd}_x\text{Se}/\text{ZnSe}$  SLS grown by MBE on GaAs substrate.

### Experiment and results.

The modulated  $\text{Zn}_{1-x}\text{Cd}_x\text{Se}/\text{ZnSe}$  superlattice growth was carried out by MBE on a (100)-oriented semi-insulating Cr-doped GaAs substrates. Prior to deposition of SLS, a  $0.5\mu\text{m}$  ZnSe buffer layer was grown. The details of MQWs MBE growth were described elsewhere [5]. The modulated SLS consisted of 150 periodes of  $5.6\text{nm}$ -wide  $\text{Zn}_{0.88}\text{Cd}_{0.12}\text{Se}$  wells and  $7\text{nm}$ -wide ZnSe barriers. In particular, the DBR mirrors with reflection band centered at near  $484\text{ nm}$  were composed of alternating  $\text{Zn}_{0.88}\text{Cd}_{0.12}\text{Se}/\text{ZnSe}$  SLS and ZnSe quarter-wavelength thick layers. The top mirror had 15 periods and the bottom mirror had 20 ones. Between the mirrors, one wavelength spacer superlattice of  $\text{Zn}_{0.88}\text{Cd}_{0.12}\text{Se}/\text{ZnSe}$  was used, and above the top mirror, the top  $45\text{nm}$ -wide ZnSe layer was finally deposited (see Fig.1).

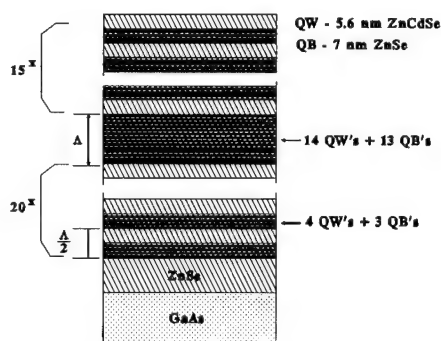


Fig.1. MBE grown modulated ZnCdSe/ZnSe SLS

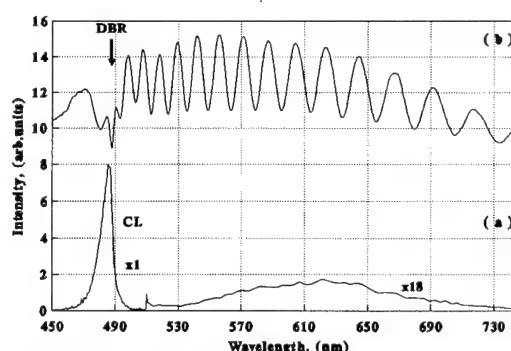


Fig.2. CL (a) and reflection (b) spectra of ZnCdSe/ZnSe SLS

The cathodoluminescence (CL) under CW excitation by electron beam ( $J < 10^{-4} \text{ A/cm}^2$ ,  $E = 3\text{--}30 \text{ keV}$ ) and photoreflexion (PR) were studied at  $40\text{K}$  and  $300\text{K}$ . Fig.2 illustrates the CL and PR spectra. The CL intensity of ZnCdSe MQWs exciton radiation was more than 3 order stronger in comparison to ZnSe barrier and top layer radiation at  $40\text{K}$ , and was about 2 order stronger in comparison to long-wavelength radiation due to deep level defects at  $300\text{K}$ . The FWHM of the CL spectrum was  $15 \text{ meV}$  at  $40\text{K}$ , and this curve displays good quality of the grown SLS. Interference maximums and minimums being below the exciton resonance is due to full structure thickness. Their decreasing near  $484 \text{ nm}$  is real manifestation of the DBR mirrors.

The laser characteristics were studied under scanning electron beam pumping with the velocity of  $(0.8-4.0) \cdot 10^3$  m/s, and the frequency of 50Hz. For the decreasing of the threshold current the  $\text{SiO}_2/\text{ZrO}_2$  dielectric mirrors ( $R > 95\%$ ) were deposited in addition on the MBE grown structure after the etching of GaAs substrate and partly of the buffer layer. Then, the investigated structure was epoxyed down to sapphire substrate. Under room temperature the minimum threshold current density was equal to  $60\text{A}/\text{cm}^2$  for the electron beam energy of 40 keV. Fig.3 demonstrates the output spectra near and above threshold. The modes of the Fabri-Perot resonator were observed below and near the threshold. The increasing of the pumping current results the VCSEL action, being single longitudinal mode generation at 485 nm. The output mode diameter was equal to 15-30  $\mu\text{m}$  and increased with e-beam current, and the divergence angle was not more than  $20^\circ$ .

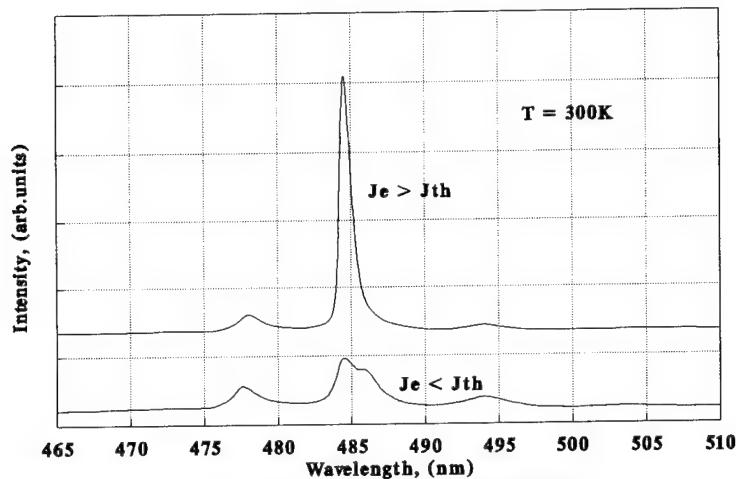


Fig.3 Output spectra of the electron-beam pumped VCSEL

In conclusion, we have demonstrated for the first time the room-temperature blue-green electron beam pumped VCSEL based on the MBE grown  $\text{ZnCdSe}/\text{ZnSe}$  SLS. Significant threshold and efficiency improvement compared with bulk devices was obtained by using of the SLS. This work demonstrates the possibility of the low threshold current operation of the LCRT based on the MBE grown SLS.

#### References.

1. R.N.Bhargava, J.of Cryst.Growth, 1992, 117, pp.894-901.
2. K.Derbyshire, Solid State Technology, 1994, Nov, pp.56-65.
3. A.S.Nasibov, V.I.Kozlovsky, P.V.Reznikov, Ya.K.Skasyrsky, and Yu.M.Popov, J. of Cryst. Growth, 1992, 117, pp.1040-1045.
4. M.A.Haase, J.Qiu, J.M.DePuydt, and H.Cheng, Appl. Phys. Lett., 1991, 59, p.1272.
5. E.M.Dianov, A.M.Prokhorov, P.A.Trubenko, E.A.Shcherbakov, Fizika i Technika Poluprovodnikov, 1994, 28, pp.1278-1281 (in Russian).

## 1.5 $\mu\text{m}$ Vertical-Cavity Surface-Emitting Lasers

M.A. Fisher, Y.-Z. Huang, A.J. Dann, D.J. Elton, M.J. Harlow, S.D. Perrin, J. Reed, I. Reid, H.J. Wickes and M.J. Adams

124/B54, BT Laboratories, Martlesham Heath, Ipswich IP5 7RE, UK

Tel. +44 1473 646793

Fax. +44 1473 637400

Y.-Z. Huang: Permanent Address: Institute of Semiconductors, Chinese Academy of Sciences, PO Box 912, Beijing 100083, China

VCSELs emitting in the 1.3 and 1.55  $\mu\text{m}$  regions could be particularly useful as low cost sources for optical fibre telecommunications applications because mode-matched devices can be coupled to single-mode fibres with high efficiency and good alignment tolerance. The absence of cleaved facets also permits on-wafer characterisation of devices.

Progress in devices at these wavelengths has been slower than that in the 0.8 - 1.0  $\mu\text{m}$  range, principally due to technological difficulties in producing high quality epitaxial mirrors with the high reflectivity required and intrinsically higher non-radiative losses in the active material. The first near room temperature (14°C) electrically pumped cw VCSEL at 1.3  $\mu\text{m}$ <sup>1</sup> and low threshold current room temperature pulsed lasing at 1.5  $\mu\text{m}$ <sup>2</sup> have recently been achieved, both in structures with two dielectric reflectors, which require removal of the substrate.

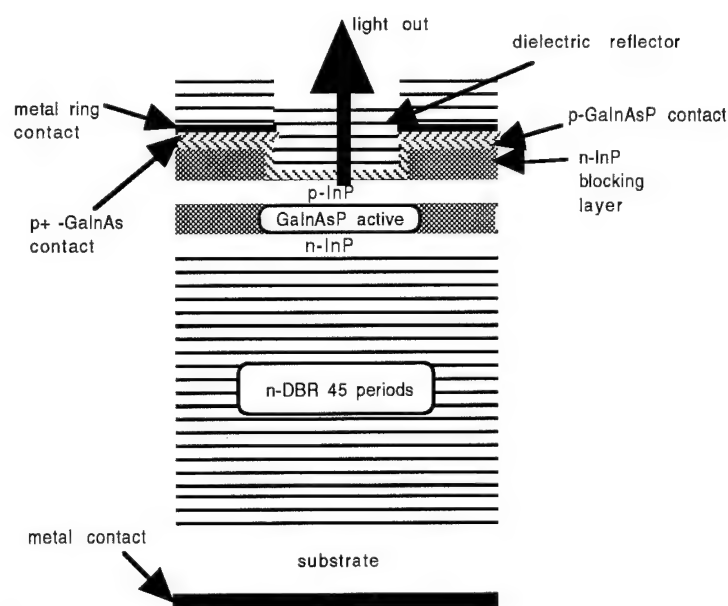


**Fig.1** Schematic diagram of VCSEL structure



Recently, very encouraging results have been reported using wafer fusion to allow the use of GaAs based reflectors with InP based active material<sup>3</sup>. Here we describe pulsed operation, both photopumped and electrically injected, of VCSELs with one epitaxial and one dielectric reflector and a bulk active region, operating close to 1.5  $\mu\text{m}$ .

Devices without electrical contacts (but fully doped structures) in which matching of the gain peak to the cavity resonance was optimal close to room temperature have been characterised by pulsed photopumping at 1064 nm with 100 ns pulses at a repetition frequency of 750 Hz. Devices were mounted on a Peltier heater and lasing at mount temperatures up to 357 K was achieved<sup>4</sup>. The minimum equivalent threshold current density of 6 kA/cm<sup>2</sup> was observed close to 295 K (Fig.2). The lasing wavelength at 295 K was 1.560  $\mu\text{m}$ . These results indicate that the quality of the reflectors and the active material is sufficient for room temperature operation in our devices.

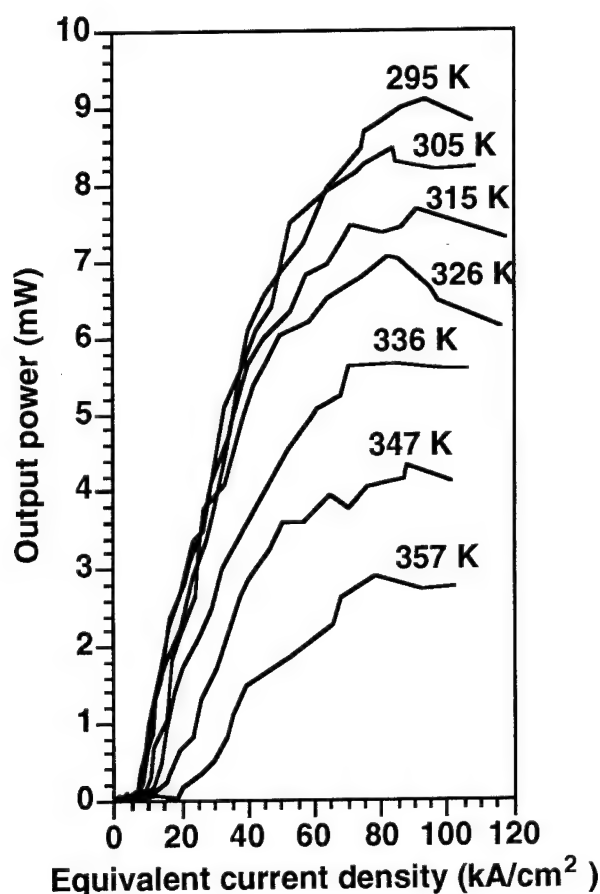


**Fig.2** Pulsed light vs. photopumped equivalent current density for a 15  $\mu\text{m}$  square VCSEL at different temperatures

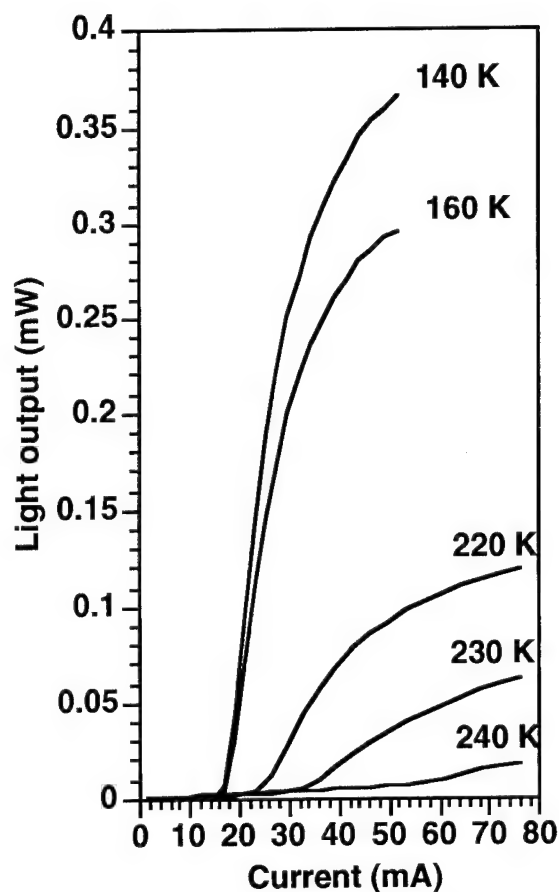


**Fig.3** Pulsed light vs. current plots for a 10  $\mu\text{m}$  square VCSEL at different temperatures

Electrical characterisation was carried out by wire-bonding and mounting of devices in a Joule-Thomson cryostat operating with high pressure nitrogen gas. This allows measurements to be made in the range 80-320K. Light vs. current characteristics for a 10  $\mu\text{m}$  square device are shown in Fig.3.

A voltage pulse generator was used for electrical injection into the VCSELs with a pulse length of 100 ns at a repetition frequency of 100 kHz (1 % duty cycle) to avoid thermal effects. The current was monitored using an inductive current probe, and the output light detected using a calibrated optical power meter. A clear threshold is observed at temperatures up to 240 K. A minimum in the threshold current was found at 140 K with a value of 16 mA. This increased to ~40 mA at 240K. The light output above threshold is linearly polarised with a single emission peak observed, within the 0.1 nm resolution of an optical spectrum analyser, across the lasing temperature range. The lasing wavelength was 1.504  $\mu\text{m}$  at 220 K, with a temperature coefficient of the cavity resonance wavelength of 0.07 nm/K. Similar light/current results were obtained with duty cycles of up to 25 %, though with some spectral broadening and saturation of the output power at higher current levels.

The threshold minimum at 140 K indicates that the cavity resonance is matched best to the material gain at this temperature. Achievement of higher temperature electrically injected lasing depends on a good match between the material gain peak and the cavity mode at the operating temperature. There will be a performance penalty with electrical injection arising from ohmic heating and non-uniform pumping across the device but, at least under pulsed conditions, this will have a weak temperature dependence. We can therefore expect good room temperature performance from an electrically injected device with improved matching of the cavity resonance to the material gain.

The results presented here indicate that there are good prospects for practical VCSELs operating in the 1.5  $\mu\text{m}$  wavelength region.

<sup>1</sup>Baba, T., Yogo, Y., Suzuki, K., Koyama, F., Iga, K., "Near Room Temperature Continuous Wave Lasing Characteristics of GaInAsP/InP Surface Emitting Laser", *Electron. Lett.*, **29**, pp.913-914, (1993)

<sup>2</sup>K. Uomi, S.J.B. Yoo, A. Scherer, R. Bhat, N.C. Andreadakis, C.E. Zah, M.A. Koza, T.P.Lee, "Low threshold, room temperature pulsed operation of 1.5 $\mu\text{m}$  vertical-cavity surface-emitting lasers with an optimized multi-quantum well active layer", *IEEE Phot. Tech. Lett.* **6**, 317-319, (1994)

<sup>3</sup> Dudley, J.J., Babic', D.I., Yang, L., Mirin, R.P., Miller, B.I., Ram, R.J., Reynolds, T., Hu, E.L., and Bowers, J.E., "Wafer fused Long Wavelength Vertical Cavity Lasers", *Proc. 1993 LEOS Annual Mtg.*, paper SCL4.1 (1993)

<sup>4</sup> Fisher, M.A., Dann, A.J., Davies, D.A.O., Elton, D.J., Harlow, M.J., Hatch, C.B., Perrin, S.D., Reed, J., Reid, I., Adams, M.J., "High Temperature Photopumping of 1.55  $\mu\text{m}$  Vertical Cavity Surface Emitting Lasers", *Elect.Letts.*, **29**, 1548-1550 (1993)

## Accurate Growth of Submilliampere Threshold Current Vertical Cavity Surface Emitting Laser using Diode Laser Reflectometry in a Molecular Beam Epitaxy System

G. S. Li, W. Yuen, S. F. Lim, K. Toh, L. E. Eng and C. J. Chang-Hasnain

E. L. Ginzton Laboratory, Stanford University, Stanford, CA 94305-4085

Telephone: (415) 725-2284 Fax: (415) 725-2533

**Introduction:** Vertical cavity surface emitting lasers (VCSELs) and resonant cavity detectors are of great interest for optical communications applications. In order to obtain high performance devices with high yield, the epilayer thickness and growth rate must be controlled to within  $\pm 1.5\%$ . Conventional molecular beam epitaxy calibration method such as reflection high energy electron diffraction (RHEED) and ion-gauge beam flux measurements are limited to an accuracy of a few percent. To achieve higher accuracy, various *in situ* optical techniques have been investigated for growth rate calibration [1]-[2] and for real time growth control [3]-[4]. The former is desirable because of its versatility and cost-effectiveness.

In this work, we performed the first extensive growth rate calibrations for VCSEL growth in a molecular beam epitaxy system (MBE). We have successfully grown and fabricated submilliampere threshold current VCSELs and widely tunable micro-machined filters [5] and detectors [6] with this technique. Average growth accuracy of 0.25 % with a 0.40 % standard deviation are achieved. Continuous wave (CW) room temperature operation is obtained from all VCSEL wafers.

**Experimental procedure:** The calibration system is schematically shown in Fig. 1. To perform laser reflectometry calibration, a 1 mW 973 nm laser beam is directed onto the center of a rotating calibration wafer through a bakable viewport while a layer of GaAs and AlAs for each of the Ga and Al effusion cells is grown. The intensity of the reflected beam varies sinusoidally and is monitored by a broad area Si detector.

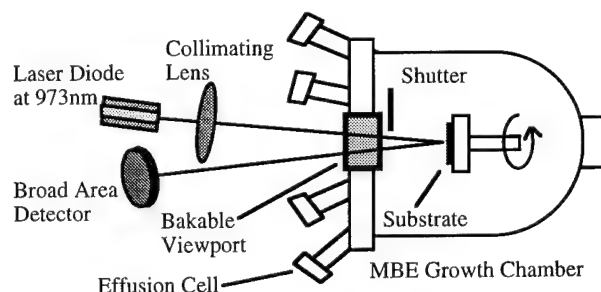


Fig. 1. Schematic of the calibration setup.

Precise growth rates for each cell can be deduced from as short as half a period of these oscillations with growth temperature refractive indices [7]. Growth rate and alloy composition of ternary material grown with a combination of these cells can also be accurately determined. We found that growth rates obtained by ion-gauge beam flux measurements alone could be off by as much as 8 % compared to the rates obtained by diode laser reflectometry.

**Growth results:** The precision of this technique is demonstrated by many different structures grown over the span of six months with chamber openings in between. These structures include twelve VCSEL structures with different designed lasing wavelength and with one to three quantum wells (QWs); four coupled vertical cavity structures; and four distributed Bragg reflectors (DBRs), each consisting of both binary and ternary layers.

Fig. 2 shows the measured wavelengths (mirror stop band centers for DBR mirrors and Fabry-Perot resonance wavelength for cavity structures), designed wavelengths, and the percentage deviations of the wafers grown.

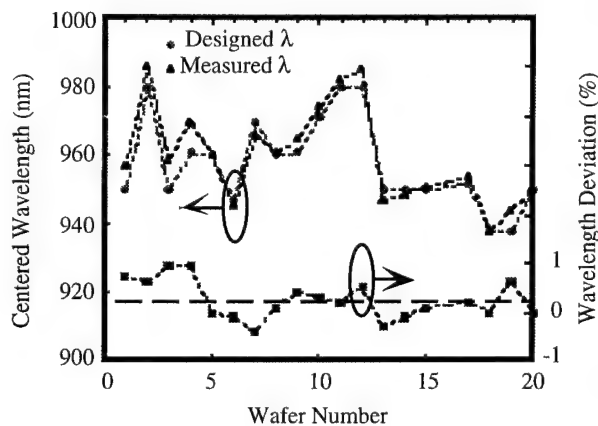


Fig. 2. Growth accuracy of various structures grown with diode laser reflectometry calibration. Average growth accuracy of 0.25 % is achieved.

Average growth accuracy of 0.25 % with a 0.40 % standard deviation is achieved. The large variety of the different structures grown indicates that this technique is very versatile and is not limited to the growth of one type of structures. We believe the nonzero average growth accuracy is due to lack of information

of the high temperature refractive indices and is not intrinsic to the calibration technique. Part of the standard deviation is attributed to the uncertainty in the growth temperature and hence the refractive indices during calibration.

The long-term stability of the growth rates is proven by the consecutive growth of five equivalent VCSEL wafers after a single initial calibration. The Fabry-Perot wavelengths and their relative deviation are shown in Fig. 3. It can be seen that the Fabry-Perot

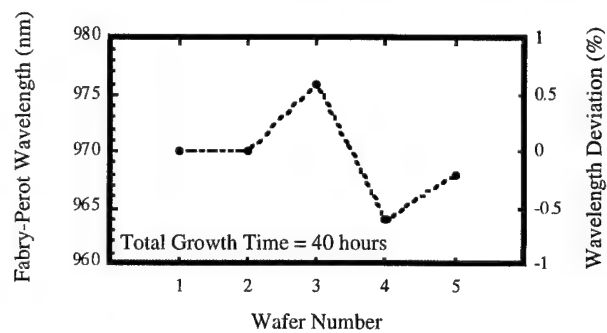


Fig. 3 Fabry-Perot wavelength of five VCSEL wafers grown with a single calibration. Growth rates drifts less than  $\pm 0.6\%$  in 40 hours.

wavelengths and thus the growth rates drift less than  $\pm 0.6\%$  over the span of 40 hours growth time.

**Device Results:** Numerous devices that require growth precision were successfully fabricated from these wafers. Low threshold CW room temperature operation is achieved from all the VCSEL wafers. Threshold current density as low as  $280 \text{ A/cm}^2$  and maximum power of 11 mW are obtained from broad area ( $40 \mu\text{m} \times 40 \mu\text{m}$ ) VCSELs with 2 QWs.

To obtain good current confinement for small area devices, an air gap confinement

VCSEL schematically shown in Fig. 4 was developed. The device was fabricated with a simple self-aligned process. Using the gold contact pad as a mask, the top  $\text{Al}_{0.7}\text{Ga}_{0.3}\text{Ga}/\text{GaAs}$  DBR was isotropically etched down to just above the active region.

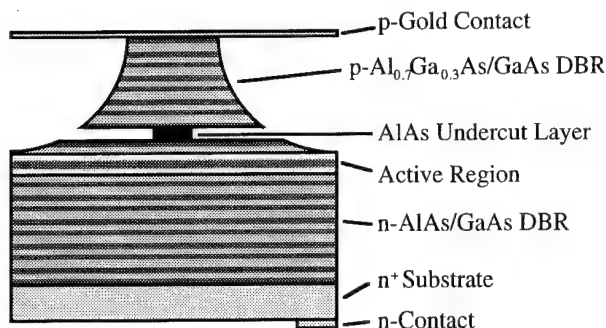


Fig. 4. Schematic of an air gap confinement VCSEL.

The exposed AlAs layer sandwiched between the top DBR and the active region was then undercut to various sizes with a selective wet etch to restrict current flow. Fig. 5 shows the characteristics of a  $\sim 4\ \mu\text{m}$  diameter device with a single QW active region. Pulse and CW

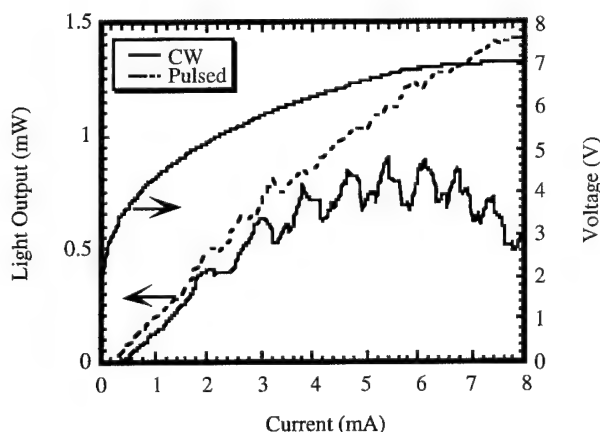


Fig. 5. Characteristics of an air gap confinement VCSEL. Pulsed and CW threshold current of 0.29 mA and 0.41 mA are obtained respectively.

threshold currents of 0.29 mA and 0.41 mA are obtained respectively. The large difference

in pulsed and CW threshold current is attributed to the lack of a heat sink. Threshold voltage and current of 2.0 V and 0.6 mA are achieved respectively with a  $\sim 4\ \mu\text{m}$  diameter device from a 2 QW VCSEL wafer with better mirror grading.

**Conclusions:** We present accurate MBE growth using diode laser reflectometry as an extremely simple, versatile compact and low cost pre-growth calibration tool. Highly accurate growth rates of both binary and ternary materials have been obtained. We have achieved average growth accuracy of 0.25 % with a 0.40 % standard deviation. We also demonstrate multiple growths of complicated structures can be accurately obtained using a single calibration step to reduce the calibration time. Using this technique, submilliampere threshold VCSELs with threshold currents as low as 0.29 mA (pulsed) and 0.41 mA (CW) are achieved with an air gap confinement VCSEL. Finally, we obtain a 100% VCSEL wafer yield.

## References

- [1] K. Bacher et al., *Appl. Phys. Lett.*, Vol. 61, pp. 1387-1389, 1992.
- [2] N. C. Frateschi et al., *Electron. Lett.*, Vol. 27, pp. 155-157, 1991.
- [3] S. A. Chalmers et al., *Appl. Phys. Lett.*, Vol. 63, pp. 3131-3133, 1993.
- [4] Y. M. Houn et al., *J. Vac. Sci. Technol. B*, Vol. 12, pp. 1221-1224, 1994.
- [5] M. S. Wu et al., in *Proceedings LEOS '94*, paper PD2.5, Boston (MA), 1994.
- [6] E. C. Vail et al., in *OFC '95*, paper PD18, San Diego (CA), 1995.
- [7] J. H. Shin et al., in *Technical Digest CLEO '94*, paper JThC6, Anaheim (CA), 1994.

## Low threshold current vertical-cavity surface-emitting lasers with enhanced resistance to heating

Gye Mo Yang, Michael H. MacDougal, and P. Daniel Dapkus

*Department of Electrical Engineering/Electrophysics, University of Southern California, Los Angeles, CA 90089-0483*

*Tel: 213-740-4414, Fax: 213-740-8684*

Vertical-cavity surface-emitting lasers (VCSEL's) fabricated by selective oxidation are attractive to achieve ultralow threshold currents [1-3]. Efficient heat dissipation, along with low threshold, is critical for uses as optical interconnects where massive integration is required. In this paper, we report an ultralow threshold of 8.7  $\mu\text{A}$  and a high output power over 1.9 mW in single quantum well VCSEL's fabricated by selective oxidation from an all epitaxial structure with intracavity p-contact layers grown by metalorganic chemical vapor deposition. The design of this structure is optimized for low thermal resistance by using distributed Bragg reflectors (DBR's) composed completely of binary materials. Fig.1 shows a schematic cross-section of the fabricated VCSEL's. The epitaxial structure consists of a 30-pair n-doped AlAs/GaAs quarter-wave stacks, an  $\text{Al}_{0.22}\text{Ga}_{0.78}\text{As}/\text{GaAs}/\text{In}_{0.2}\text{Ga}_{0.8}\text{As}$  resonant  $\lambda$ -cavity, p-doped contact layers, and a 22-pair undoped AlAs/GaAs quarter-wave stacks. The p-doped contact layers are formed from a  $0.25 \lambda$  AlAs current constriction layer and a  $0.75 \lambda$  GaAs intracavity contact layer. After growth, the top DBR is selectively wet etched into 14 and 5  $\mu\text{m}$  square mesas down to the p-type GaAs contact layer. Then, 50  $\mu\text{m}$  square mesas, whose centers coincide with the centers of the top mesas, are formed by wet chemical etching. Current flow apertures of 10 and  $\sim 3 \mu\text{m}$  are formed below the 14 and 5  $\mu\text{m}$  square top mirrors, respectively, by selective oxidation.

10  $\mu\text{m}$  square VCSEL's have very low threshold currents as low as 140  $\mu\text{A}$ , as shown in Fig. 2. To find the optimized number of top DBR pairs in this structure, we have systematically measured the light vs. current characteristics after removing each pair of the top stacks in another device. The device with 18-pair stacks in the top mirror shows a very high output power over 1.9 mW while maintaining a very low threshold current of 212  $\mu\text{A}$ . (see Fig.2). A slope efficiency of

55 % and a maximum power conversion efficiency of 16 % are achieved in this device. The lowest threshold observed in  $\sim 3 \mu\text{m}$  square devices is  $8.7 \mu\text{A}$  (see Fig. 3). This device operates with a slope efficiency of 10 % and produces a maximum output power of  $160 \mu\text{W}$ . The spectral emission at  $980.37 \text{ nm}$  from this device shows a continuous increase in the side mode suppression ratio. At  $160 \mu\text{W}$  output power, the side mode suppression ratio is 18 dB. The continuous variation of characteristics is characteristic of the behavior expected for microcavity lasers in which there is efficient coupling of the spontaneous emission into the cavity mode [4,5].

The effect of temperature change on the threshold for  $10 \mu\text{m}$  square device is shown in Fig. 4. A minimum threshold occurs around room temperature where the cavity mode matches the gain peak. This threshold current shows only  $30 \mu\text{A}$  change in the range of  $0 - 50^\circ\text{C}$ . The thermal resistance of the lasers are determined by measuring the wavelength shift as a function of electrical input power and stage temperature. The lasing wavelength shifts are  $0.094$  and  $0.035 \text{ nm/mW}$  for  $3$  and  $10 \mu\text{m}$  square devices, respectively. From the  $0.07 \text{ nm/K}$  wavelength shift (see Fig. 4), the thermal resistances correspond to  $1.35$  and  $0.5 \text{ K/mW}$ , respectively, which is much lower than previously reported VCSEL's [3,6]. The monolithic binary-material stacks with abrupt interfaces in both mirrors and intracavity p-contact give a reduction in the thermal resistance.

In conclusion, extremely low threshold VCSEL's have been fabricated from all epitaxial structure based on selective oxidation. This specially-designed structure also shows a enhanced resistance to heating.

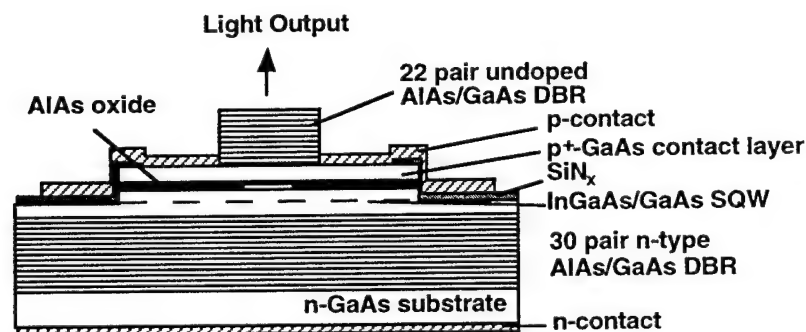


**Fig. 1** Schematic cross section of VCSEL with a native-oxide constriction layer and binary material DBRs.

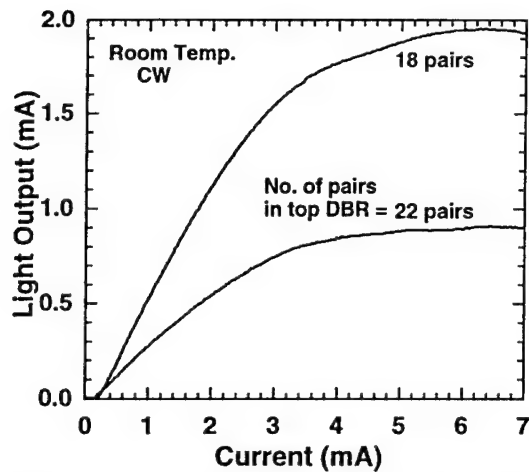


Fig. 2 Light output vs. current curves for 10  $\mu\text{m}$  square VCSELs with 22- and 18-pair stacks in the top DBR mirror.

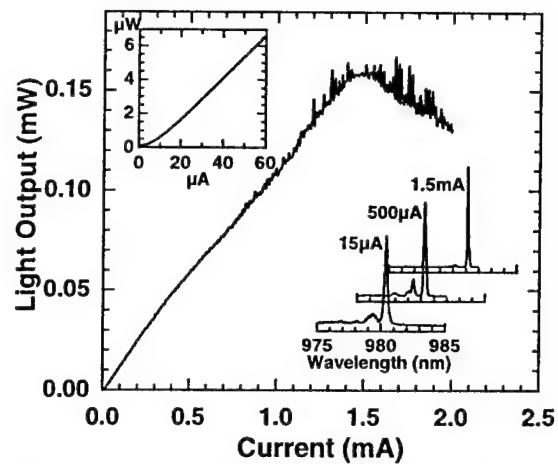


Fig. 3 Light output vs. current curve for approximately 3  $\mu\text{m}$  square VCSEL. Lasing spectra are shown at different currents.

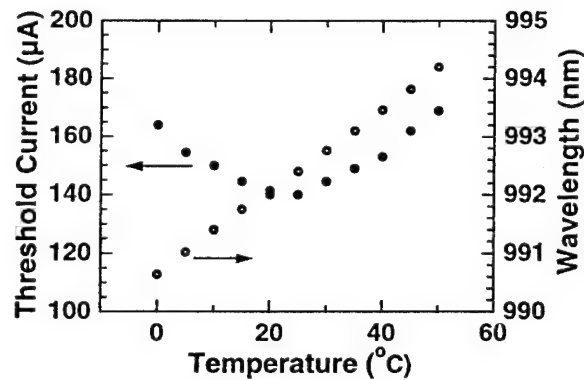


Fig. 4 Device temperature dependent threshold current and emission wavelength at 200  $\mu\text{A}$  for 10  $\mu\text{m}$  square VCSEL.

- [1] D. L. Huffaker, J. Shin, and D. G. Deppe, *Electron. Lett.* **30**, 1946 (1994).
- [2] M. H. MacDougall, P. D. Dapkus, V. Pudikov, H. Zhao, and G. M. Yang, *IEEE Photonics Technol. Lett.* **7**, 229 (1995).
- [3] K. L. Lear, K. D. Choquette, R. P. Schneider, Jr., S. P. Kilcoyne, and K. M. Geib, *Electron. Lett.* **31**, 208 (1995).
- [4] Y. Yamamoto, S. Machid, and G. Björk, *Opt. Quantum Electron.* **24**, S215 (1992).
- [5] H. Yokoyama, K. Nishi, T. Anan, Y. Nambu, S. D. Brorson, E. P. Ippen, and M. Suzuki, *Opt. Quantum Electron.* **24**, S245 (1992).
- [6] T. Wipiejewski, D. B. Young, M. G. Peters, B. J. Thibeault, and L. A. Coldren, *Electron. Lett.* **31**, 279 (1995).



# High Power Highly Efficient Vertical-Cavity Surface-Emitting Laser Diodes with a Au-Plated Heat Spreading Layer

T. Wipiejewski, M. G. Peters, B. J. Thibeault, D. B. Young, L. A. Coldren

University of California, Santa Barbara  
Department of Electrical & Computer Engineering  
Santa Barbara, CA 93106  
Phone: (805) 893-7163, Fax: (805) 893-4500

## Introduction

Vertical-cavity surface-emitting lasers (VCSELs) are gaining increasing attention due to their interesting properties. The ultimate device performance of VCSELs has exceeded in-plane laser data already regarding minimum threshold currents [1] and highest wall plug efficiency except for high output power pump lasers [2]. Whereas VCSELs are poised to prove their usefulness in short distance data link applications, high efficiency lasers are also attractive for high power applications like laser diode pumped solid state lasers. In general, the maximum output power of VCSELs is thermally limited. Improved heat sinking is therefore necessary to increase the maximum output power. A record high output power of 113 mW has been previously demonstrated with an up-side down mounting of a single VCSEL on a diamond heat sink [3]. Here we show how the thermal heat sinking in a 2D laser array can be improved by using a Au-plated heat spreading layer. The improved heat sinking results in an increase in maximum output power from 20 mW to 42 mW for a 64  $\mu\text{m}$  diameter device. To our knowledge this is the highest output power for an unmounted VCSEL reported to date.

## Fabrication

Fig. 1 shows a schematic of one laser element of the 2D array. The spacing between elements is 360  $\mu\text{m}$ . We use molecular beam epitaxy (MBE) to grow the epitaxial layers on n-GaAs substrates. The active region contains three 8 nm thick  $\text{In}_{0.18}\text{Ga}_{0.82}\text{As}$  strained quantum wells with 8 nm thick GaAs barriers. It is surrounded by  $\text{Al}_{0.5}\text{Ga}_{0.5}\text{As}$  layers to form a one wavelength long optical cavity. The bottom Bragg reflector is n-type doped and consists of 18.5 periods  $\text{AlAs-GaAs}$ . The p-type doped top reflector consists of 30 periods  $\text{Al}_{0.67}\text{Ga}_{0.33}\text{As-GaAs}$  with linearly graded, heavily Be-doped interfaces. Details of the laser structure are described elsewhere [4].

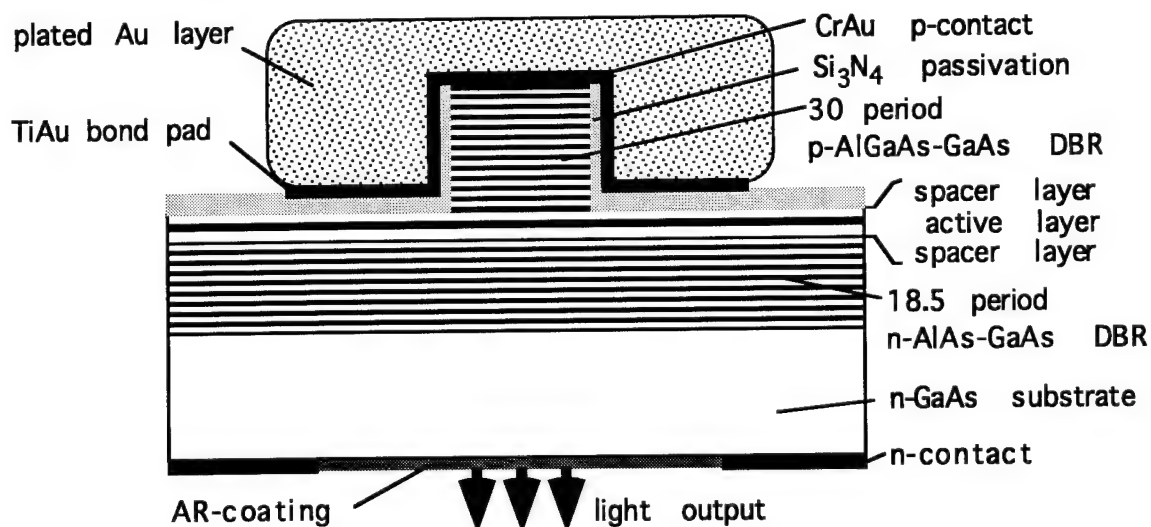


Fig. 1: Schematic of vertical-cavity laser element with a Au-plated heat spreading layer.

Individual lasers are defined by etching pillars using Cl-reactive ion etching (RIE). The etching is stopped above the active layer. A  $\text{Si}_3\text{N}_4$  layer passivates the mesa sidewalls and the surface area around them. CrAu on top of the mesa serves as p-contact and also boosts the reflectivity of the top DBR. Bond pads are formed out of sputtered TiAu and the n-contact is a broad area Au metallization. The substrate backside is AR-coated with SiO for light output. After initial testing a 15  $\mu\text{m}$  thick Au heat spreading layer is electro-plated on the  $300 \times 300 \mu\text{m}^2$  bond pads around the lasers.

#### Device Characteristics

The laser performance is measured before and after Au-plating. First, we are interested in the thermal properties of the devices. We determine the heat resistance  $R_{th}$  of the lasers by measuring the emission wavelength shift  $\Delta\lambda$  with increasing dissipated electrical power  $P_{in}$ . We obtain a linear relationship where the gradient  $\Delta\lambda/\Delta P_{in}$  depends on the device diameter. The comparison with the emission wavelength as function of the ambient temperature  $T$  gives the thermal resistance of the lasers:  $R_{th} = (\Delta\lambda/\Delta P_{in})^{-1} \Delta\lambda/\Delta T$ . We measure  $\Delta\lambda/\Delta T = 0.68 \text{ \AA/K}$  for the temperature wavelength shift of all device sizes.

Fig. 2 shows the heat resistance of the lasers for the various device diameters. In agreement with a simple theoretical model [5] the heat resistance is inversely proportional to the device diameter  $d$ . We find the relations  $R_{th} = 1.05 \text{ (cmK/W)} / d$  for etched pillar devices without the heat spreading layer and  $R_{th} = 0.64 \text{ (cmK/W)} / d$  for the Au-plated lasers. Thus, the heat spreading layer reduces the thermal resistance to approximately 60% of the initial values. The largest devices have thermal resistances of about 100 W/K. For the smaller devices of 8  $\mu\text{m}$  diameter the thermal resistance rises to 830 K/W and 1400 K/W for the Au-plated and etched pillar lasers, respectively. The thermal resistance of these lasers is slightly lower than that for our previously reported devices of a corresponding size [6]. We attribute the difference to the larger and thicker heat spreading layer in this case.

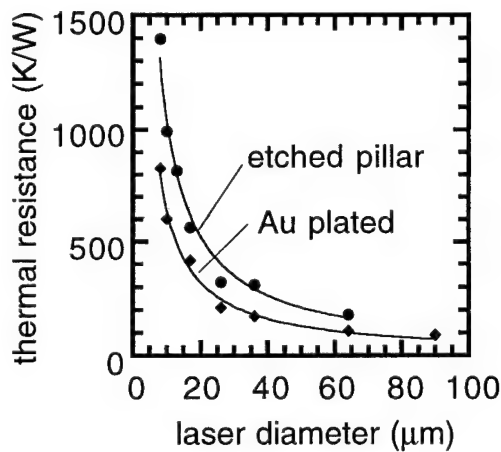


Fig. 2: Thermal resistance as function of the laser diameter.

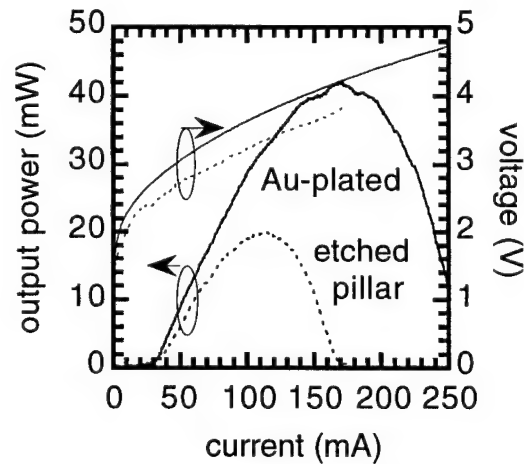


Fig. 3: Output characteristics of a 64  $\mu\text{m}$  diameter laser with and without Au-plating.

The improved heat sinking increases the maximum output power of the lasers. The output characteristics of a 64  $\mu\text{m}$  diameter device are depicted in Fig. 3. The threshold current is 32 mA. The heat spreading layer causes a rise of the maximum output power by more than a factor of two from 20 mW to 42 mW. The differential quantum efficiency is increased from 28% to 35%. We can ignore the slight increase in the drive voltage for the Au-plated case, because it is caused by an

accidental degradation of the n-contact during processing. The maximum wall plug efficiency is improved from 6.4% to 7.9% for this large diameter device. For the 20  $\mu\text{m}$  diameter device we measure the highest wall plug efficiency of 16.2%. From the thermal resistance data we can infer an effective temperature rise in the laser of about 70 K for the thermal roll-over point with and without the heat spreading layer for all device sizes.

In Fig. 4 we compare the maximum output power for plated and non-plated lasers. The maximum laser output power increases linearly with diameter for the smaller devices. The power saturates at laser diameters around 50-60  $\mu\text{m}$  and decreases for the 90  $\mu\text{m}$  device. The benefits of the better heat sinking are more pronounced for the larger devices. For the smallest devices the improvement in output power is only 40% compared to a factor of 370% increase for the 90  $\mu\text{m}$  diameter device.

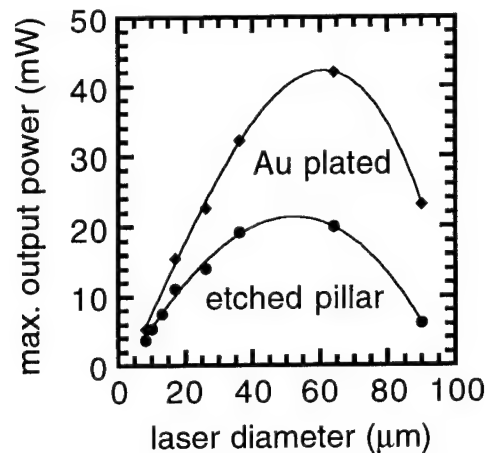


Fig. 4: Maximum output power versus laser diameter for Au-plated and standard etched pillar devices.

The linear increase in maximum output power with laser diameter is caused by the linear increase of the thermal conductivity  $1/R_{th}$  which determines how much heat can be dissipated in the device before the temperature for the thermal roll-over is reached. On the other hand, the dissipated input power below threshold scales approximately with the active area at a constant threshold current density. Thus it is proportional to the square of the device diameter. Therefore the maximum output power saturates and finally decreases for larger laser diameters.

### Conclusion

In conclusion, we demonstrate highly efficient vertical-cavity surface-emitting laser diodes with high output power levels up to 42 mW for an unmounted device. Improved output power is achieved by plating a Au heat spreading layer around these pillar-etched devices. With expected further improvements in heat sinking and efficiency, these devices will be very attractive for high power applications like laser diode pumped solid state lasers.

- [1] D. L. Huffaker et al., Electron. Lett., vol. 30, pp. 1946-1947 (1994).
- [2] K. L. Lear et al., Electron. Lett., vol. 31, pp. 208-209 (1995).
- [3] F. H. Peters et al., Electron. Lett., vol. 29, pp. 200-201 (1993).
- [4] M. G. Peters et al., IEEE Photon. Techn. Lett., vol. 6, pp. 31-33 (1994).
- [5] W. Nakwaski et al., Electron. Lett., vol. 28, pp. 572-574 (1992).
- [6] T. Wipiejewski et al., Electron. Lett., vol. 31, pp. 279-281 (1995).

## Impurity Induced Disordering for Improved Vertical Cavity Lasers

P. D. Floyd, M. G. Peters, L. A. Coldren  
Department of Electrical and Computer Engineering, Box #118  
University of California, Santa Barbara, CA 93106  
Voice: (805) 893-8679, Fax: (805) 893-8170

J. L. Merz  
Department of Electrical Engineering, University of Notre Dame, Notre Dame, IN 46556  
Voice: (219) 631-9177, Fax: (219) 631-4393

Vertical cavity surface emitting lasers (VCSELs) are interesting due to their single longitudinal mode operation, a circularly symmetric optical mode profile, and surface normal light emission. These characteristics make them ideal light sources in both free space optical communication systems and in short haul optical fiber communication systems.

Impurity induced disordering (IID) has been used to successfully fabricate low threshold edge-emitting laser diodes. [1]-[4]. By disordering of the quantum well active region, injected carriers are prevented from diffusing laterally out of the active region or recombining non-radiatively at exposed active region surfaces, reducing leakage currents.

In this work we use IID to improve VCSEL characteristics. We demonstrate suppression of higher transverse modes in VCSELs by IID and present initial results on IID of VCSEL active regions for carrier confinement.

The laser structures are grown by molecular beam epitaxy. The bottom reflector is a Si doped, 17.5 period GaAs/AlAs distributed Bragg reflector (DBR). The top reflector consists of 30 periods of quarter-wavelength GaAs/AlGaAs layers with a design discussed elsewhere. [5] The active region consists of three 80 Å  $\text{In}_{0.185}\text{Ga}_{0.815}\text{As}$  quantum wells with 80 Å GaAs spacer layers surrounded by 0.12  $\mu\text{m}$   $\text{Al}_{0.5}\text{Ga}_{0.5}\text{As}$  confinement layers.

### Impurity Induced Disordering for Mode Filtering

Fabrication begins by defining discs of evaporated Si of varying diameters, forming a mask for Zn diffusion. Zn is diffused at 640 °C for 4 hours. The moderate diffusion time and temperature are not expected to have adverse effects on the device structure. [6] After diffusion the mask is removed and layers of Cr/Au/Ni are evaporated in discs larger and concentric to the previous location of the Si diffusion masks. Pillars are etched by reactive ion etching (RIE), stopping just above the active region. A broad area Cr/Au metallization contacts the  $n^+$  GaAs substrate.

Figure 1 shows a schematic of the finished devices. RIE creates the pillar diameter ( $d_p$ ) and the Zn IID defines an inner diameter ( $d_i$ ). The continuous wave (CW) light-current (L-I) characteristics are shown in Figure 2 (a) for devices with an interdiffused aperture ( $d_i$ ) of 9  $\mu\text{m}$  and varying pillar diameters ( $d_p$ ). Oscillations in the L-I curves are due to residual reflection from the substrate backside which is not anti-reflection coated. For all the curves shown the output remains single transverse mode even for pillar diameters well above 10  $\mu\text{m}$ . This is in contrast to non-filtered etched-pillar VCSELs that typically exhibit multiple transverse mode emission for device diameters above 5  $\mu\text{m}$ . [7]

For comparison, lasers without the Zn-diffused mode filter were fabricated from the same wafer. The L-I characteristics for these devices are shown in Figure 2 (b). The threshold currents are only slightly less than those of the mode filter lasers.

Figure 3 shows the L-I characteristic for a laser with  $d_p=11$   $\mu\text{m}$  and  $d_i=7$   $\mu\text{m}$ , which was also shown in Fig. 1. The threshold current is significantly smaller than in previously reported devices with a Zn diffused mode filter [8], and is comparable to threshold currents reported for lasers using contact metallization for mode filtering. [9] [10]

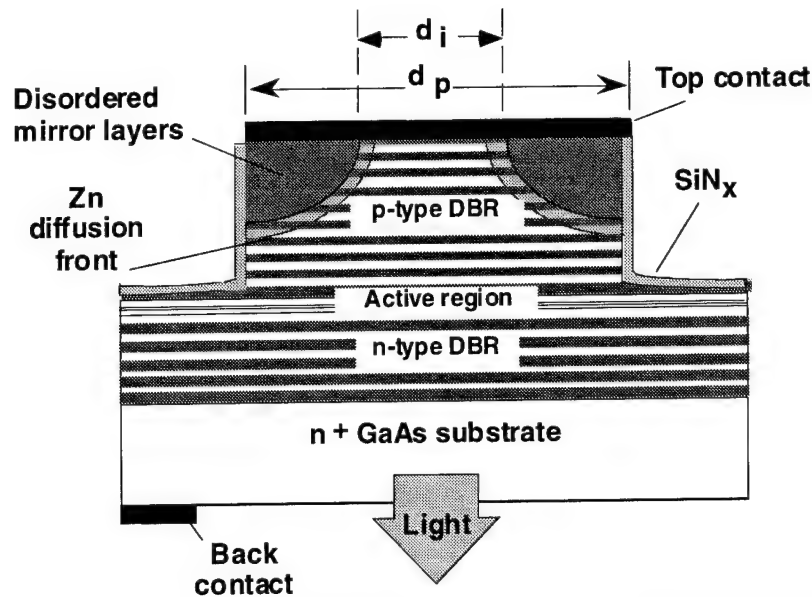
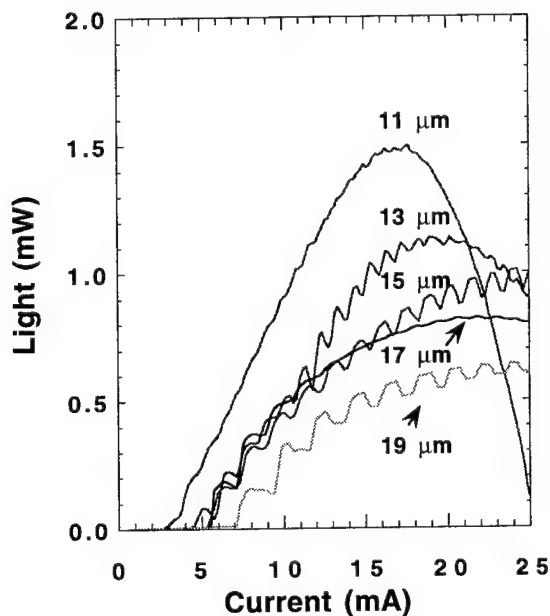


Figure 1. Finished device structure schematic for the mode filtered vertical cavity lasers. Devices with various pillar diameters ( $d_p$ ) and inner diameters ( $d_i$ ) were fabricated.

The transverse mode behavior is inferred from spectral measurements taken under CW operation. The inset of Figure 3 shows the spectra for currents of  $\sim 3.5$  and  $\sim 6.5$  times threshold respectively. The mode suppression exceeds 25 dB in both cases.

(a)



(b)

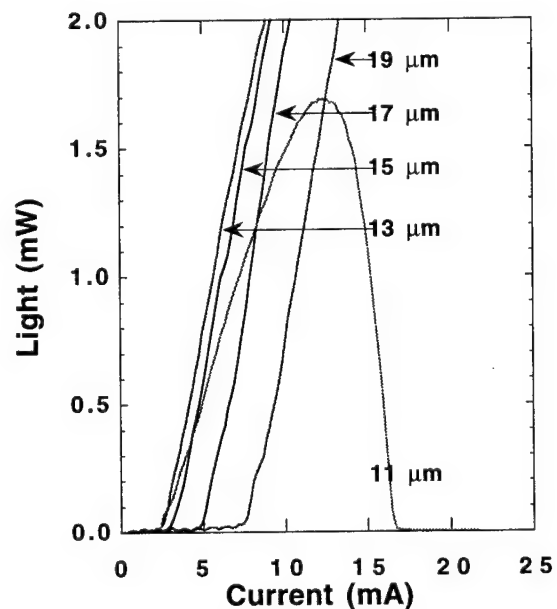


Figure 2. (a) CW light-current curves for a laser with an aperture fixed by the disordered material ( $d_i$ ) of  $9 \mu\text{m}$  and increasing pillar diameters ( $d_p$ ). Oscillations in the L-I characteristics are due to residual reflections from the substrate which is not anti-reflection coated. (b) CW light-current curves for lasers fabricated without a Zn diffused mode filter. The devices were fabricated from the same wafer as the mode-filtered devices.

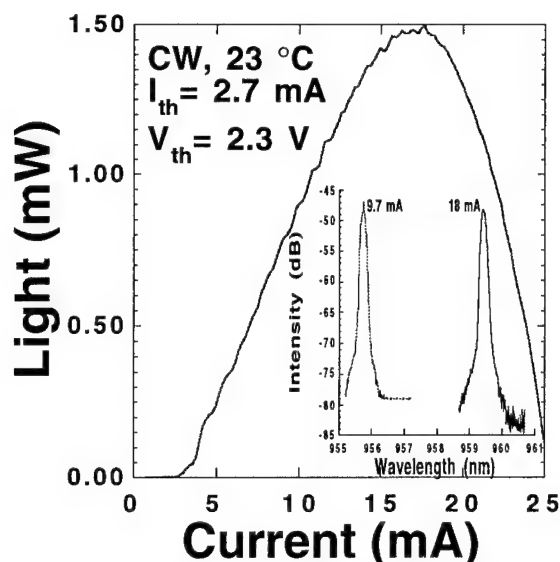


Figure 3. CW L-I characteristics for a mode filtered laser with  $d_p=11\mu\text{m}$  and  $d_i=7\mu\text{m}$ . The external efficiency is 9.5%. The spectra in the inset shows mode suppression  $>25$  dB.

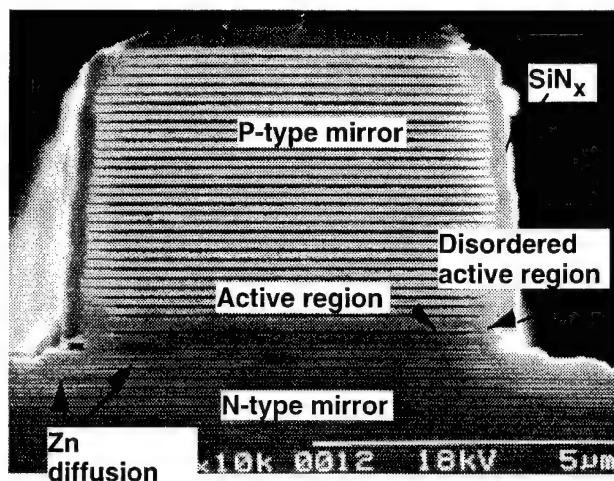


Figure 4. Scanning electron microscope image of laser structure after Zn diffusion for 100 minutes at 600 °C. The active region becomes mixed with the AlGaAs spacer region, near the etched surface.

### Impurity Induced Disorder for Carrier Confinement

We are also investigating the use of IID for carrier confinement in vertical cavity laser active regions by lateral diffusion of Zn into etch-pillar structures. Ridges are etched by RIE into laser material with a layer structure similar to that described earlier. The ridge is masked with  $\text{SiN}_x$  and Zn diffusion is performed at 600 °C for 100 minutes. Figure 4 shows a scanning electron microscope image of the structure after diffusion. The quantum well active region is pinched off near the edge of the ridge, indicating that it is intermixed with the AlGaAs spacer layers. The should provide a wide bandgap barrier for lateral confinement of injected carriers, preventing lateral diffusion and/or non-radiative recombination of carriers at etched surfaces.

In summary, Zn IID has been used to achieve single transverse mode operation with minimal effect on laser threshold currents. The lasers have threshold currents as low as 2.7 mA with a peak power of 1.5 mW, and mode suppression ratio greater than 25 dB.

Preliminary experiments indicate that both transverse mode control and lateral confinement of carriers in the active region can be achieved by Zn impurity induced disordering, enhancing vertical cavity laser performance.

1. R. L. Thornton et al, Appl. Phys. Lett. **47**, p. 1239, 1985
2. W. X. Zou et al, IEEE Photon. Technol. Lett. **5**, p. 591, 1993
3. P. D. Floyd et al, IEEE Photon. Technol. Lett. **5**, p. 1261, 1993
4. S. Y. Hu et al, Accepted for publication in IEEE Photon. Technol. Lett, 1995
5. M. G. Peters et al, Appl. Phys. Lett. **63**, p. 3411, 1993
6. P. D. Floyd et al, J. Appl. Phys. **76**, p. 5524, 1994
7. C. J. Chang-Hasnain et al, Appl. Phys. Lett. **57**, p. 218, 1990
8. T. G. Dziura et al, Electronics Lett. **29**, p. 1236, 1993
9. R. A. Morgan et al, IEEE Photon. Tech. Lett. **4**, p. 374, 1993
10. R. A. Morgan et al, Appl. Phys. Lett. **66**, p. 1157, 1995



## Robust and Wavelength Insensitive Performance of Selectively Oxidized Vertical-Cavity Lasers

Kent D. Choquette, R. P. Schneider, Jr. K. L. Lear,  
M. Hagerott Crawford, K. M. Geib, J. J. Figiel, and Robert Hull\*

Photonics Research Department  
Sandia National Laboratories  
Albuquerque, NM 87185  
(505)844-7287 phone (505)844-8985 FAX  
kdchoqu@sandia.gov

The unique properties of vertical-cavity surface emitting lasers (VCSELs), such as circular output beam, single longitudinal mode, and 2-dimensional array capability, make them promising light sources for a variety of applications, including optical data links, data storage, display and printing systems. Moreover, on-wafer testing and compatibility with traditional integrated circuit fabrication technologies make VCSEL manufacture feasible and potentially inexpensive. Recently, VCSELs fabricated using "wet" oxidation<sup>1</sup> have demonstrated the lowest threshold current ( $91\mu\text{A}$ ),<sup>2</sup> lowest threshold voltage (45mV above photon gap),<sup>3</sup> and highest power conversion efficiency (52%)<sup>4</sup> ever reported in VCSELs. The latter two results were obtained from an all semiconductor VCSEL structure that utilizes selective oxidation to form buried oxide layers. The low index oxide layers form current apertures sandwiching the active region to efficiently confine injected carriers as well as transversely confine the emitted photons. In this paper we show that the fabrication uniformity we have obtained using our selective oxidation process can reproducibly yield high performance VCSELs that are attractive for potential applications. In addition, these lasers exhibit high performance over a wide emission wavelength range from a given wafer. Finally, our selectively oxidized device structure is demonstrated to be robust and amenable to a variety emission wavelengths, currently extending from the infra-red to visible.

Our monolithic VCSEL structure for top emitting lasers is shown in Fig. 1. The 2-inch diameter wafers are grown by metalorganic vapor phase epitaxy (MOVPE) in an Axitron reactor on a rotating susceptor. The interfaces between the layers of the distributed Bragg reflectors (DBRs) have a parabolic composition grade for low series resistance with C and Si used as dopants. After growth, we fabricate buried oxide layers between the top and bottom DBRs surrounding the multiple quantum well active region. Mesas are reactive ion etched to expose the AlGaAs layers for lateral oxidation. The oxidation is done in a furnace at 400-450°C in water vapor. A reproducible and linear lateral oxidation rate without an induction period is achieved. We can thus controllably fabricate uniformly sized current apertures which produce uniform device performance, as described below. Furthermore, a high degree of oxidation selectivity between various AlGaAs layers in the DBRs can be obtained with only a small change in Al concentration.<sup>3</sup> Hence, through design of the Al composition of the constituent layers of the VCSEL, specific layers can be laterally oxidized further into the interior of the mesa to form current apertures.

Fig. 2 is a cross section transmission electron micrograph of an actual 980 nm selectively oxidized VCSEL. The oxide layer shown in Fig. 2 is located between the top DBR and the 3 InGaAs quantum well active region. The terminus of the oxide layer is denoted at the arrow; the unoxidized region beyond this point corresponds to the current aperture which defines the transverse laser cavity. Notice that no dislocations or other defects are apparent along the oxide layer or near the oxidation terminus. The implication of Fig. 2 is that the formation of the oxide layer does not precipitate defects which could lead to degraded VCSEL lifetimes.

In Fig. 3 we show the threshold current,  $I_{th}$ , and the threshold wavelength of VCSELs with  $5 \times 5 \mu\text{m}$  current apertures as a function of distance from the wafer center. Similar device characteristics have been found from other VCSEL wafers with the same epitaxial structure which utilize a relatively high reflectivity top DBR and 3 InGaAs quantum wells. Notice that  $I_{th}$  varies relatively smoothly from the wafer center to the edge due to the uniformly sized current apertures across the wafer. In addition,  $I_{th}$  remains less than 0.5 mA over a wavelength range of nearly 40 nm, and under 1 mA over the entire 56 nm operating range found on this wafer. The variation of  $I_{th}$  across the wafer arises from the spectral mismatch between the cavity resonance and the laser gain. The minimum  $I_{th}$  (and maximum output power) occurs at  $\approx 970$  nm, corresponding to the optimum resonance/gain overlap. Note that the maximum output power for the VCSELs in Fig. 3 vary between 0.4-0.9 mW.

Fig. 4 depicts the power conversion (wall plug) efficiency obtained at 1 mW output power from VCSELs fabricated in another wafer with reduced output coupler reflectivity. In Fig. 4 greater than 20% efficiency is obtained at 1 mW output over more than a 50 nm wavelength range. In addition, over most of this range  $I_{th}$  remains less than 1 mA. The best efficiencies from a given VCSEL on this wafer typically occur at output powers slightly greater than 1 mW; the maximum efficiency observed is 30%. It is important to note that 1 mW of output power is appropriate for many applications, and that maintaining wavelength insensitive performance in VCSEL arrays is important. Hence our selectively oxidized VCSELs provide high efficiencies irrespective of the varying emission wavelengths. New growth reactors currently under development to achieve better growth uniformity will lead to higher levels of uniform VCSEL performance.

The selectively oxidized VCSEL structure can also be modified for use at a variety of wavelengths. Exploiting the reduced threshold currents and voltages of the selectively oxidized VCSELs has allowed us to extend the cw operation of visible AlGaInP VCSELs<sup>5</sup> to shorter wavelengths. For example, Fig. 5 shows the device characteristics of a  $4 \times 4 \mu\text{m}$  selectively oxidized VCSEL emitting at 652 nm. The 1.2 mA (2.3 V) threshold current (voltage) and nearly 0.3 mW maximum cw power represent the best reported results to date for VCSELs operating at this short wavelength. Finally, Fig. 6 depicts the output characteristics from a 980 nm VCSEL during >650 hrs of constant operation at room temperature (no heat sinking) on a probe station. Over the duration of the test, no change in the VCSEL characteristics were observed, corroborating the lack of defects observed in Fig. 2. The tested VCSEL exhibited identical L-I-V characteristics at the completion of the testing as at the start. These preliminary results imply robust and long lifetimes for our selectively oxidized VCSELs.

In summary, not only do selectively oxidized VCSELs exhibit benchmark performance records, they also exhibit wavelength insensitive performance levels which are attractive for applications employing these devices. We have developed a uniform and reproducible selective oxidation process to produce robust lasers. Moreover, high performance VCSELs have been fabricated at emission wavelengths near 980, 850, and 650 nm, which indicates the universality of our selectively oxidized VCSEL structure. Manufacture of high performance selectively oxidized VCSELs at a variety of wavelengths will be important to emerging applications and markets considered for VCSELs. The work at Sandia National Laboratories is supported by the United States DOE under contract No. DE-AC04-94AL85000.

\*Dept. of Materials Science, University of Virginia, Charlottesville, VA 22903

<sup>1</sup>J. M. Dallesasse, *et al.*, Appl. Phys. Lett. **57**, 2844 (1990).

<sup>2</sup>D. L. Huffaker, *et al.*, Electron. Lett. **30**, 1946 (1994).

<sup>3</sup>K. D. Choquette, *et al.*, Electron. Lett. **30**, 2043 (1994).

<sup>4</sup>K. L. Lear, *et al.*, Electron. Lett. **31**, 208 (1995).

<sup>5</sup>R. P. Schneider, Jr., *et al.*, Photonics Tech. Lett. **6**, 313 (1994).



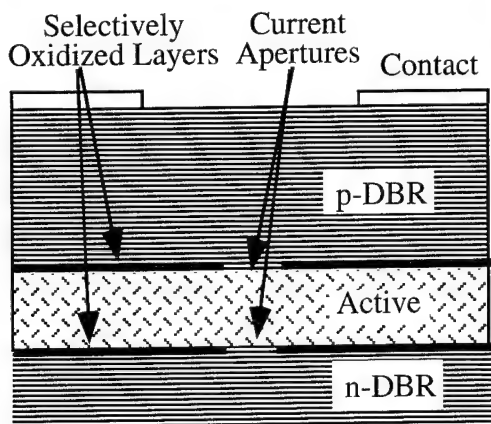


Fig. 1. Sketch of an oxidized VCSEL.

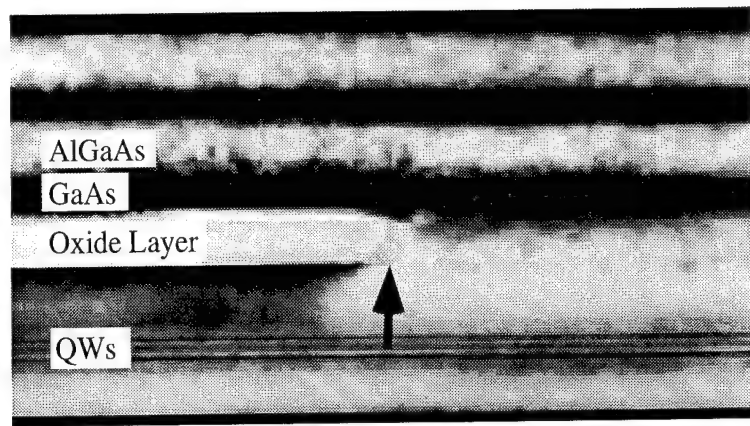


Fig. 2. TEM cross section view of an oxidized VCSEL.

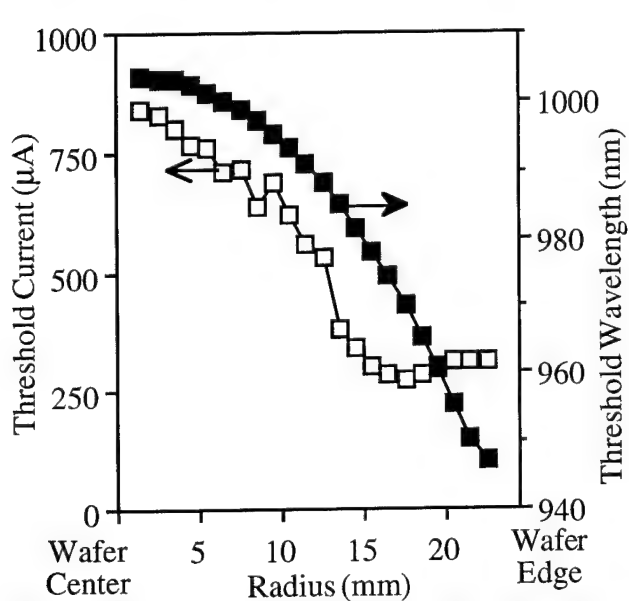


Fig. 3. Threshold properties of wafer XF114b

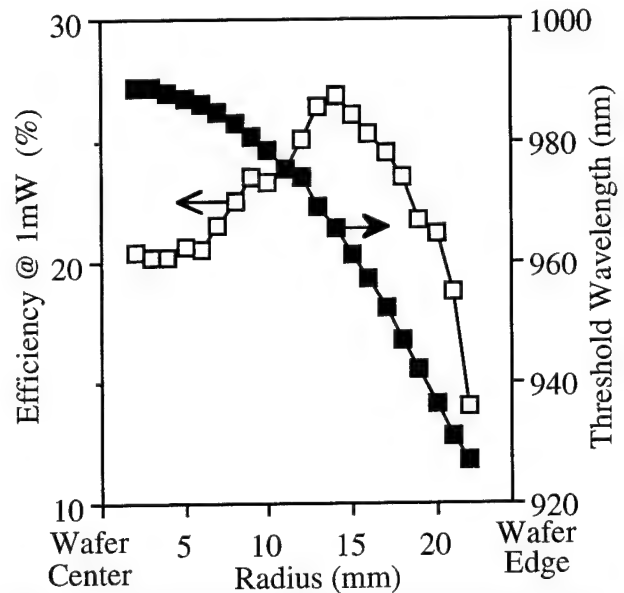


Fig. 4. Conversion efficiency of wafer XF130b

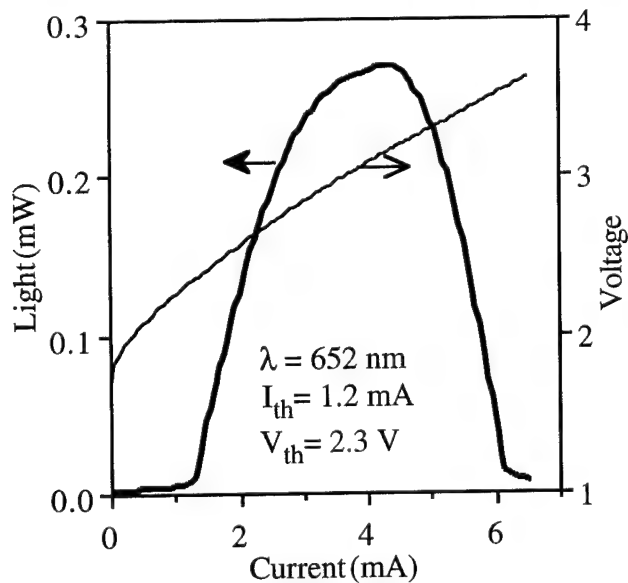
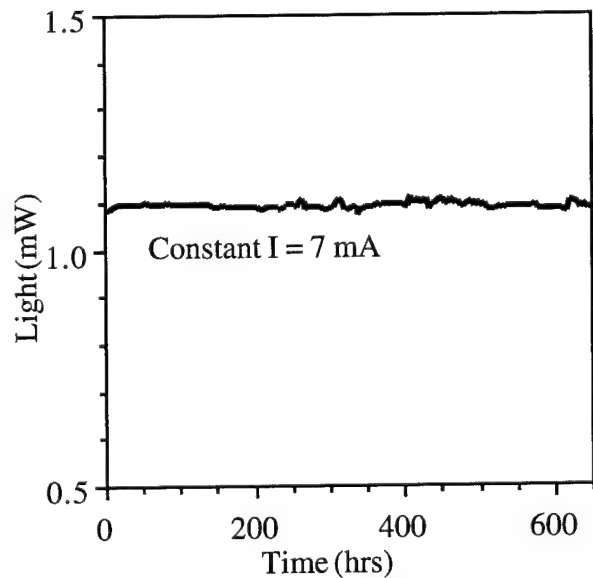
Fig. 5. L-I-V curves from 4x4  $\mu$ m red VCSEL

Fig. 6. Oxidized VCSEL output vs. time

## High-performance folded-cavity surface-emitting InGaAs/GaAs lasers fabricated by ion-beam-etching technique

Yong Cheng, Gye Mo Yang, and P. Daniel Dapkus

Department of Electrical Engineering/Electrophysics, University of Southern California, SSC505, Los Angeles, CA 90089-0483

High performance folded-cavity surface emitting lasers (FCSEL's) utilizing  $45^\circ$  deflection mirrors to couple the light in the horizontal cavity towards the surface are attractive devices for applications to optoelectronic integrated circuits. We report here low threshold current and high efficiency InGaAs/GaAs FCSEL's that employ high quality internal  $45^\circ$  deflectors. A simplified process involving a stop etch to position the surface emitting output mirror close to the waveguide and ion-beam-etching (IBE) to form the  $45^\circ$  deflecting mirror is presented.

The laser structure designed for FCSEL's is a single quantum well graded-index separate-confinement heterojunction grown by metalorganic chemical vapor deposition. Fig.1 shows a schematic diagram of FCSEL's we present. The FCSEL design positions the output mirror as close to the waveguide as possible to reduce the light path through unguided region to minimize the diffraction loss. A GaAs etch stop layer is employed to form output mirrors. Ion beam etching (IBE) is performed at  $9 \times 10^{-5}$  Torr with an  $\text{Ar}^+$  ion beam at 800eV. A single layer of photoresist is chosen as mask for IBE of the  $45^\circ$  deflecting mirrors.

The lasers are tested under pulsed operation. The emission spectra exhibit multiple modes centered around  $\sim 990\text{nm}$ . Fig.2 shows a typical L-I curve for a FCSEL ( $L = 640\mu\text{m}$ ) consisting of one vertical output mirror and one cleaved facet. The threshold current density is  $133\text{A/cm}^2$  and the external quantum efficiencies are 41% ( $0.52\text{W/A}$ ) and 38% ( $0.48\text{W/A}$ ) for the light output from the top surface and the cleaved facet, respectively. For comparison, broad-area cleaved lasers ( $L = 650\mu\text{m}$ ) made from this material have the threshold current density of  $108\text{A/cm}^2$  and the external quantum efficiency of 78%. Fig.3 shows a typical L-I curve for a broad area FCSEL ( $L = 800\mu\text{m}$ ), consisting of two vertical output mirrors and two internal  $45^\circ$  deflectors. The threshold current density is  $112.5\text{A/cm}^2$  and the external quantum efficiency is 65% ( $0.82\text{W/A}$ ) for surface emission, which are the best results reported for broad area FCSEL's. The

additional loss due to the folded-cavity design is estimated as  $4.2\text{cm}^{-1}$ . The devices are candidates for incorporation into monolithic high power arrays, into addressable arrays for printing applications, and as elements in OEIC's. The performance of narrow stripe devices and two dimensional array for these applications will be presented.

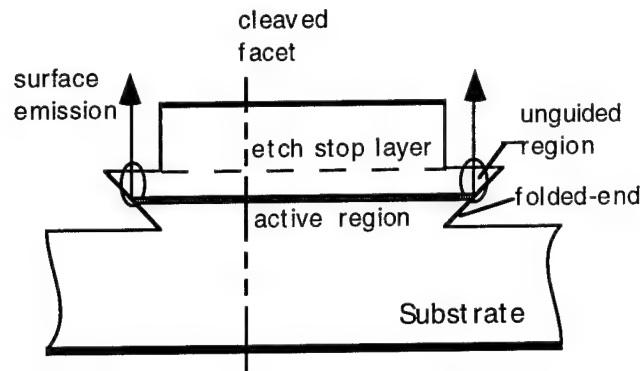


Fig. 1, A schematic diagram of FCSEL's

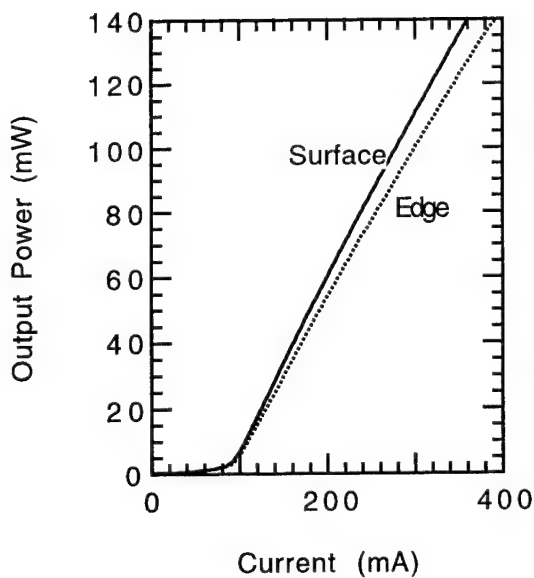


Fig.2, L-I curve for a FCSEL ( $L = 640\mu\text{m}$ ) consisting of one vertical output mirror and one cleaved facet.

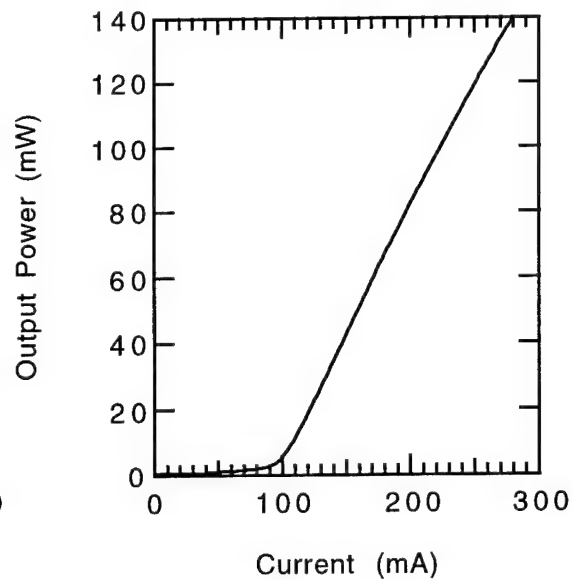


Fig.3, L-I curve for a FCSEL ( $L = 800\mu\text{m}$ ) consisting of two vertical output mirrors and two internal  $45^\circ$  deflectors.

Tuesday, August 22, 1995

## Poster Session

**TuE** 7:30 pm-8:30 pm  
Shavano Peak

## Efficiency and Spectral Properties of Integrated Optoelectronic Laser-Diode-Based RF Frequency Mixers

E.A. Avrutin, I.G. Thayne, D.A. Barrow, J.H. Marsh  
*Dept of Electronics & Electrical Engineering, University of Glasgow,  
Glasgow G12 8QQ, SCOTLAND, UK; phone +44-141-339 88 55; fax +44-141-330 49 07*

E.L. Portnoi  
*A.F. Ioffe Physico-Technical Institute, Polytechnicheskaya 26, St. Petersburg 1941024, RUSSIA;  
phone +7-812-247 93 76, fax +7-812-247 10 17*

V.B. Gorfinkel  
*Dept. of High Frequency Engineering, University of Kassel,  
Wilhelmshoeherallee 73, Kassel D-34121, GERMANY*

Frequency up/down conversion of optically transmitted RF signals may be useful for a number of microwave-over-fibre applications. In the earlier works [1-2], we have proposed to perform such conversion by means of operating passively Q-switched (self-pulsing) or passively mode locked semiconductor laser diodes (LDs) as integrated optoelectronic frequency mixers, i.e. as a local oscillator and a mixing element integrated within one device. Theoretical calculation proved the feasibility of RF frequency conversion due to parametric effects in such LDs. The calculations considered the input signal applied to a laser as either an electrical signal (optoelectronic scheme) or an RF modulated optical signal (all-optical scheme), the frequency-converted output being in the form of a modulated stream of optical pulses, convenient for further transmission, with an electrical signal as a by-product. In [3], optoelectronic up-conversion has been performed using self-pulsating lasers with subcarrier modulation in optical communications in view. The results of both [1-2] and [3] experimentally demonstrate the feasibility of frequency mixing in GHz range using self-pulsing lasers, but little study has been performed so far of the mixing efficiency, and the spectral properties of the device have been only studied theoretically [2] for the case of mode locked extended-cavity lasers. Here, we investigate, in more detail, the issue of the efficiency of the optoelectronic frequency conversion in dependency of frequency (in different frequency ranges) and intensity of the modulation signal for monolithic cavity Q-switched and mode locked lasers.

**1.** For optoelectronic mixing within the frequency range of **1-10 GHz**, a self-pulsing LD is the most appropriate device. Here we report results obtained using a 960 nm strained QW, two-section laser similar to that reported previously [1-2]. The two sections were a gain section and a saturable absorber (SA, 30  $\mu\text{m}$  out of the total cavity length of 400  $\mu\text{m}$ ). The threshold current of the device, with both sections in forward bias, was 20 mA. The optical output was detected using a fast photodiode (with a bandwidth of 20 GHz) and the resulting electrical signal displayed on a RF spectrum analyser with a resolution of 100 kHz. The self-pulsation frequency of the laser (the local oscillator frequency  $f_{LO}$ ) was 1.5 GHz. The input signal was applied as RF modulation of bias current of the gain section at  $f_s=0.9$  GHz. Under modulation, the measured output spectra contain the heterodyne frequencies  $f_{\pm}=f_{LO}\pm f_s$  [1-3], in addition to  $f_{LO}$  and the modulation signal frequency  $f_s$ . The conversion efficiency  $\eta$  was defined as the ratio of power of the output signal at  $f_{LO}+f_s$  (up-conversion) or  $f_{LO}-f_s$  (down-conversion) to the power of the input signal. The measured results are plotted in Fig. 1a (dots) vs. modulation current. The efficiency of up-conversion is of the order of unity at the laser power levels studied. The down-converted line is

about an order of magnitude lower; this asymmetry was also observed in [3] and explained as being due to a combination of AM and FM effects. The solid lines in Fig. 1a are theoretical results, obtained by means of a rate-equation model with parameters fitted to simulate the properties of the experimental structure *without* the modulation. As the measured and calculated results are in reasonable agreement without additional fitting, we have used the same model to study how  $\eta$  depends on the modulation frequency (plotted for the up-conversion case in Fig. 1b). The efficiency increases as  $f_s \rightarrow 0$  ( $f_+ \approx f_{LO}$ ) and as  $f_s \rightarrow f_{LO}$  ( $f_+ \approx 2f_{LO}$ ). This is due to the fact that the local oscillator frequency for a Q-switched laser is the same as the electron-photon resonance frequency in the system, an effect which may present problems for subcarrier modulation.

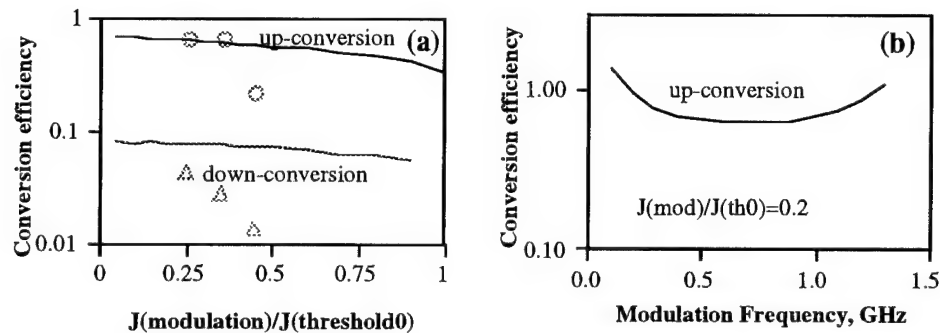


Fig. 1: Frequency conversion efficiency in a Q-switched laser vs. modulation current amplitude (in units of threshold current of a fully forward biased laser) (a) and frequency (b)

2. For the frequency range **10-100 GHz**, we consider mixing using monolithic extended-cavity passively mode-locked lasers [2] in linear or ring geometries; the modulation signal may be applied either to the saturable absorber section electrooptically or in the form of external modulated light incident noncoherently on one of the sections. The frequency dependence of the conversion efficiency is found to contain sharp peaks at  $f_s \approx f_{res}$  and  $f_s \approx f_{res}$ ,  $f_{res}$  being the electron-photon resonance frequency, with a flat region for  $f_s \ll f_{res}$ . This behaviour is unlike the case of Q-switched lasers, but is similar to the modulation curve of an ordinary LD. The modulation efficiencies for all-optical modulation are of the order of 0.01-0.1 (at  $f_s \ll f_{res}$ ) and about an order of magnitude higher at the frequency resonance. The theoretical efficiency values for electrooptic modulation were very high, predicting mixing with gain of about 10 dB at modest optical powers, but in practice these values are expected to be lower due to the effect of parasitics.

3. We also assess theoretically, for what we believe to be the first time, a feasibility of frequency conversion at **sub-terahertz** local oscillator frequencies using a monolithic-cavity mode locked LD. The simulated laser is 200  $\mu\text{m}$  long with a SA section in the middle (colliding-pulse geometry), providing a stream of subpicosecond pulses at  $f_{LO} = 372$  GHz. The theoretical approach utilised the distributed fully-time-domain model [2]. The modulation signal was simulated as direct modulation of the absorption coefficient of the SA with an amplitude of about 1% of its initial value; in reality this is likely to be achievable all-optically by means of a stream of external optical pulses acting on the absorption through fast nonlinearities in the SA medium. The RF spectrum of the simulated output signal (Fig. 2) clearly shows a down-converted line in the GHz range. The frequency dependence of the conversion efficiency is qualitatively the same as in the extended-cavity case; conversion efficiencies of 0.01-0.1 at  $f_s \ll f_{res}$  are predicted to be achievable with the all-optical modulation mechanism.

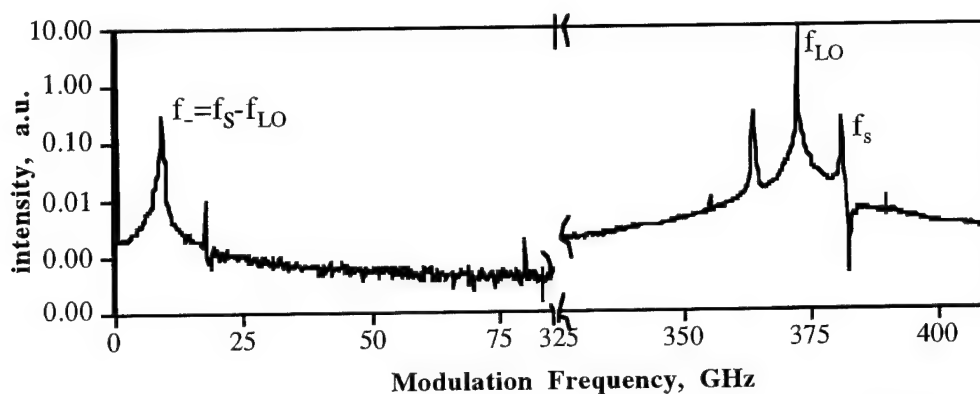


Fig.2: Part of the simulated RF spectrum of the optical output from a monolithic colliding-pulse mode locked LD under direct modulation of the saturable absorber

#### References:

- [1] E.L. Portnoi, V.B. Gorfinkel, D.A. Barrow, I.G. Thayne, E.A. Avrutin, J.H. Marsh, *Electron. Lett.*, V. **31**, P.289-290 (1995)
- [2] E.L. Portnoi, V.B. Gorfinkel, D.A. Barrow, I.G. Thayne, E.A. Avrutin, J.H. Marsh, *IEEE J. Special Topics in Quantum Electron.*, No.7 (1995)
- [3] Xiaolu Wang, Guifang Li, C.S. Ih, *IEEE J. Lightwave Technol.*, V.**11**, P. 309-15, 1993

# Dynamics of electro-optical synchronization of self-pulsating laser diodes

A. Egan, P. Rees, J. O'Gorman, J. Hegarty, G. Farrell, P. Phelan

Physics Department, Trinity College, Dublin 2, Ireland.  
Tel: +353-1-6081987 Fax: +353-1-6798412

## Introduction

Higher speed requirements in communication systems have led to demands for fast optical sub-systems. Important aspects of such sub-systems will be the synchronization of self-pulsating laser diode (SP LD) emission to electrical or optical signals and timing extraction, aspects which have already been demonstrated experimentally [1,2,3]. Consequently, these devices may play important roles as functional elements in transparent transmission systems. Effective implementation of these functions in communications systems using these devices depends on a more complete understanding of synchronization of SP LDs than exists at present. In this paper we address a number of important timing issues relating to electro-optical synchronization. We have experimentally observed for the first time that a phase difference exists between the input electrical signal and the output optical signal of a synchronized SP LD and we have experimentally and theoretically investigated the nature and behaviour of this phase difference. We have also numerically investigated the impact of synchronization of SP LDs on timing jitter in the emitted optical pulses.

## Phase Behaviour: Results and Discussion

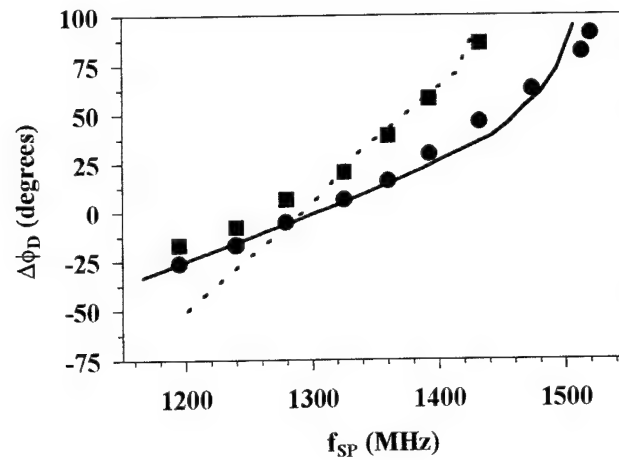
The SP LD used in our experiments is a two section Fabry-Perot laser diode that self-pulsates when one section is dc biased above threshold (gain section) using a constant current source and the other (absorber) section is dc biased below threshold using a constant voltage source [3]. The occurrence of controllable self-pulsation in such twin-section devices is well established and is explained on the basis of standard saturable absorption models [4]. The free-running self-pulsation frequency ( $f_{SP}$ ) of the laser emission can be controlled by varying the bias applied to either section. For our experiments, it is controlled by varying the absorber voltage. A sinusoidal input electrical signal is applied to the laser gain section in addition to a constant current. When synchronization is achieved, the relative phase shift between the input signal and the emitted laser pulses is measured on an oscilloscope and its behaviour is measured when  $f_{SP}$  is varied. The variation in the relative phase offset between the LD SP and the input electrical signal is shown for two different applied electrical signal levels in Figure 1. For an applied RF signal frequency of  $f_{IN}=1300\text{MHz}$ ,  $\Delta\Phi_D$  is the measured phase difference between the electrical and optical signals relative to the phase difference measured when  $f_{SP}=f_{IN}$  ( $\Delta\Phi_D=0$  when  $f_{SP}=f_{IN}$ ). The total variation in phase shift for each electrical input level is approximately  $0.61\pi$  radians. The existence of a phase shift between the applied electrical signal and the laser has not previously been reported or discussed. In order to determine the origin of this behaviour we have simulated the synchronization process in self-pulsating lasers.

Figure 1 also shows the result of a numerical simulation using a standard single mode rate equation model. The model is based on three rate equations for the carrier and photon density temporal evolution in the laser [5,6] describing the carrier dynamics in the gain section, the carrier dynamics in the absorber section and the mean photon density in the combined laser cavity. We note that for the simulations in this figure, noise terms are not included in the model. For  $f_{SP}>1300\text{MHz}$  the agreement between the theoretical curves and experimental data is excellent. For  $f_{SP}<1300\text{MHz}$  the agreement is not as good for the low signal level, we believe this is due to the low quality of synchronization achieved. Nevertheless, the agreement between calculation and experiment is excellent considering the simplicity of the model and the fact that standard parameters are used in the calculations - literature values have been used for standard parameters [5].

Our results show that an absolute phase difference exists between the applied signal and the pulsation, i.e. frequency synchronization does not automatically imply phase synchronization. Our numerical



simulations show that the signal applied to the laser synchronizes the pulsating emission by perturbing the carrier density and seeding the emitted optical pulse. This interaction results in the observed phase shift and also allows us to describe the dynamics of electro-optical synchronization in SP LDs.



**Figure 1:** The variation in the phase difference, DFD, between the applied electrical signal (at  $f_{IN} = 1300\text{MHz}$ ) and the laser output pulsation relative to the phase difference at  $f_{SP} = 1300\text{MHz}$  versus the free-running self-pulsation frequency varies. The experimental data and theoretical predictions are represented by (a) the circles and solid line for the large applied signal level and (b) the squares and dashed line for the small applied signal level (3dB less than in case (a)).

The phase dependence on  $f_{SP} - f_{IN}$  has important consequences for communication systems using SP LDs for clock extraction and distribution or for any other application which involves electrical injection of a periodic signal to a SP LD (e.g. in self-synchronization schemes for the stabilization or enhancement of self-pulsation). This phase variation may be a desirable effect for example, in fine tuning the clock delay in clock extraction systems or it may be preferable if the effect is minimized. Consequently, an understanding of the origin of this phase shift and its behaviour is essential.

### Jitter Behaviour: Results and Discussion

When spontaneous emission noise is included in the laser rate equations [5,6] it is possible to analyze the pulse-to-pulse jitter properties of the LD emission. Figure 2 illustrates the behaviour of the full width at half maximum (FWHM) of the pulse-to-pulse jitter distribution (the distribution of the time between successive pulses, the instantaneous period) as the ratio of gain current ( $I_g$ ) to threshold current ( $I_{th}$ ) is varied for the case of periodic electrical injection and that of no injection. The curve for the latter case shows that as  $I_g$  is increased jitter decreases. The two curves show a comparable jitter level only within the region where the laser with electrical injection is synchronized. At the extremes of the synchronization range jitter increases for the laser with electrical injection.

The fact that the level of pulse-to-pulse jitter in the laser is not substantially changed by synchronization with a periodic electrical signal is an important one, since it indicates that self-pulsating lasers may not be useful devices for generating reduced jitter optical pulse trains by synchronizing injected electrical signals. We conclude that spontaneous emission noise in the laser introduces timing jitter into the emitted pulse at the pulse-to-pulse level which the injected electrical signal cannot prohibit. However, our simulations show that the mechanism of synchronization tends to ensure that jitter does not accumulate over the pulse train, in the way it would if the laser did not have the synchronizing signal. Consequently, timing jitter with respect to some external signal is reduced when jitter is considered over the longer time scales. This, of course, is the essence of clock extraction.

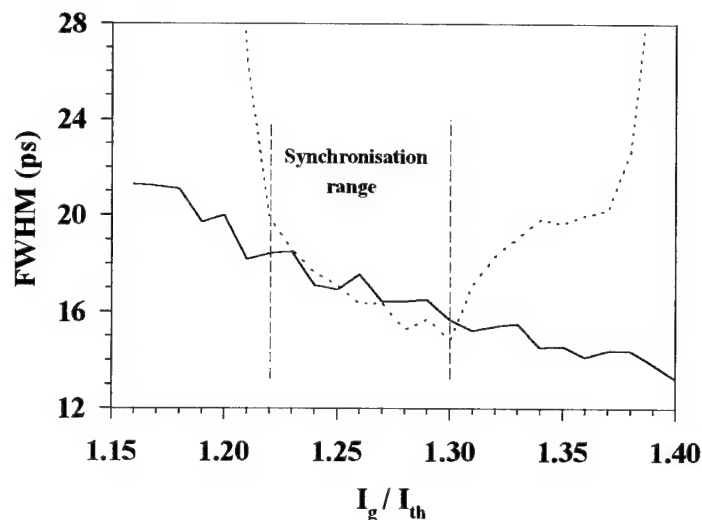


**Figure 2:** FWHM of pulse-to-pulse jitter distribution as a function of  $I_g/I_{th}$ . The solid line is for the case of a SP LD without electrical injection and the dashed line is for the case of sinusoidal electrical injection at a frequency of 2.5GHz.

### Conclusions

We have observed and explained significant new aspects to electro-optical synchronization and clock extraction using SP LDs, which have not been fully appreciated previously. We have shown that when a SP LD synchronizes to an external electrical signal, the phase difference between the electrical input and the laser emission depends on the free running SP frequency. We have modeled the behaviour of pulse jitter in a synchronized SP LD and have shown that synchronization does not lead to a reduction in the short term pulse jitter, but only in the long term pulse jitter. On-going work is addressing the issues of phase relationship and pulse jitter for all-optical synchronization. Initial investigations show that similar effects exist in the all-optical domain - these results are also important for a comprehensive understanding of the mechanism of all-optical synchronization of SP LDs. These results have important implications for SP LDs applied to communication systems. Improving understanding of the synchronization mechanism in these devices will hasten their exploitation.

### References

1. Barnsley, P., "All-optical clock extraction using two-contact devices", IEE Proceedings J, Oct. 1993, Vol. 140, No. 5, pp. 325-336.
2. Barnsley, P.E., Wickens, G.E., Wickes, H.J. and Spirit, D.M., "All-optical clock recovery from a 5GB/s RZ data signal using a self-pulsating 1.56 $\mu$ m laser diode", IEEE Photonics Tech. Lett., Vol. 3, No. 10, 1991, pp. 942-945.
3. Farrell, G., Phelan, P., Hegarty J. and Shields J., "All-optical timing extraction with frequency division using a twin section laser diode", IEEE Photonics Tech. Lett., Vol. 5, No. 6, 1993, pp. 718-721.
4. Dixon, R.W. and Joyce, W.B., "A possible model for sustained oscillations (pulsations) in (Al,Ga) As double-heterostructure lasers", IEEE J. Quantum Electronics, QE-15, No. 6, 1979, pp. 470-474.
5. Avrutin, E.A., "Analysis of spontaneous emission and noise in self-pulsing laser diodes", IEE Proceedings J, 1993, Vol. 140, No. 1, pp. 16-20.
6. Adams M.J., "Theory of two-section laser amplifiers", Optical and Quantum Electronics, 1989, Vol. 21, pp. S15-S31.

# Numerical Analysis of Distortions in Directly Modulated Semiconductor Lasers in the Presence of Weak Optical Feedback.

M.K. Haldar, F.V.C. Mendis and J. Wang

Department of Electrical Engineering

National University of Singapore

10 Kent Ridge Crescent

Singapore 0511

Tel. : +(65)7722575 Fax : +(65) 7791103

Subcarrier multiplexed (SCM) optical communication systems have been studied by many researchers for their attractiveness in providing simple, low-cost and broad-band optical fibre communications. In practical SCM systems, some light unintentionally fed back into the laser diode through various discontinuities such as splices adversely affect the performance of directly modulated semiconductor lasers. Many studies have been done carried out both theoretically and experimentally[1-4]. Using small signal perturbation method, Helms[2] gave expressions for modulation response, third order two carrier intermodulation distortion and second harmonic distortion which were shown to be in reasonable agreement with experimental results, especially when the modulating signals are small. Nevertheless, when modulating signals are large, small signal analysis may lose its accuracy and validity. In this paper, we use numerical methods to study the distortion produced by a directly modulated laser diode with weak coherent optical feedback.

The rate equations with weak coherent optical feedback given in reference [2] are solved numerically using a variable time step Runge-Kutta algorithm and Fast Fourier Transform algorithm. The laser parameters used for calculation are also taken from reference [2]. In order to obtain the time-delayed photon number  $S(t - \tau)$  and optical phase  $\phi(t - \tau)$ , we store the values of  $S(t)$  and  $\phi(t)$  in the memory and use them after the round-trip time  $\tau$  of the external cavity as has been done in [5]. For calculating the modulation response, we use a single sinusoidal tone of fixed amplitude. For multitone signals, we define the optical modulation depth (OMD) of  $j$ th frequency as  $OMD_j = S_j / S_0$  ( $j=1,2,\dots$ ), where  $S_j$  is the optical output amplitude of the  $j$ th frequency component and  $S_0$  is the DC value of  $S$ . This definition of OMD is chosen for consistency with reference [2] whose experimental and analytical results are compared with our results.

Fig.1a and b show the normalized modulation response. For small modulating current, the response as shown in Fig.1a has ripples of frequency equal to the reciprocal of the round-trip delay time of the external cavity as reported in [2]. For a larger modulating current, a peak appears in between two adjacent peaks of the small signal response as shown in Fig.1b. This has not been reported by theoretical calculation[2], but has been observed experimentally[3]. Similar extra peaks are also exhibited in plots of third order two carrier intermodulation distortion and second order harmonic distortion against frequency for large OMD. We believe that the occurrence of extra peaks result from the single mode laser entering a dynamic multimode state under large signal modulation[6]. We also find that the peak-to-peak amplitudes of the ripples decrease with increase in OMD (i.e., with large modulating currents).

Because of the reduction of peak-to-peak amplitude of the ripples arising from the dynamic multimode state, we expect the numerically computed distortions to be significantly different from those predicted by small signal theory for large modulating currents. This is indeed shown by the numerically computed values (shown as o, x and  $\Delta$ ) of two carrier third order intermodulation distortions IMD/C and second harmonic HD/C in Figs. 2 and 3. The small signal analytical results, indicated by solid lines, and experimental points, indicated by black dots, are obtained from Figs. 7 and 9 of ref. [2]. The computed values are in better agreement with experimental results at high external feedback levels. At lower feedback levels, the computed values also exhibit better agreement with experimental results, particularly for high OMD (m).

In practical SCM systems, although the OMD of individual channels is small, the number of channels is large and therefore large signal conditions may be expected to exist. Summing small signal results for distortion may not provide a good estimate of total distortion. We have simulated an eleven-channel SCM system with a spacing of 10 MHz between adjacent channels. The OMD of each channel is 0.09. We suppress the center channel signal and calculate the total distortion due to the remaining ten channels falling into this center channel. As the channels are uncorrelated, we introduce a random initial phase in each modulating signal and average distortions over the results from several runs as has been done for simulating the effect of over modulation [7]. A total of 20 runs is found to be adequate for our calculations. The result is shown in Figure 4, where the total distortion in the absence of reflections, obtained using the same averaging technique, is also plotted. We find that the increase in distortion in the presence of reflection over its value in the absence of reflections is very much smaller under large signal conditions than under small signal conditions.

#### References:

- [1] M.K.Haldar, J.Wang and F.V.C.Mendis, "Equivalent circuit of semiconductor lasers with weak coherent optical feedback", *Electron.Lett.*, Vol.31, pp.366-367, 1995.
- [2] J.Helms : "Intermodulation and harmonic distortions of laser diode with optical feedback," *J. Lightwave Technol.*, Vol.9, pp.1567-1575, 1991.
- [3] W.I.Way and M.M.Choy, "Optical feedback on linearity performance of 1.3 $\mu$ m DFB and multimode lasers under microwave intensity modulation," *J. Lightwave Technol.*, Vol.6, pp.100-108, 1988.
- [4] M.M.Choy, S.G.Menocal and T.P.Lee, " Reduced frequency chirp and suppressed harmonic distortion of a DFB-GRECC 1.5  $\mu$ m laser under 3-GHz large-signal modulation," *OFC/IOOC '87*, pp.210-211.
- [5] N.Schunk and K.Petermann, "Numerical analysis of the feedback regimes for single-mode semiconductor lasers with external feedback," *IEEE J. Quantum Electron.*, Vol. 24, pp.1242-1247, 1988.
- [6] K.Petermann, *Laser Diode Modulation and Noise*. Dordrecht, The Netherlands: Kluwer Academic, 1988.
- [7] N.R.Phillips and T.E.Darcie, "Numerical simulation of clipping-induced distortion in analog lightwave systems", *IEEE Trans. Photonics. Tech. Lett.*, Vol.3, pp.1153-1155, 1991, .

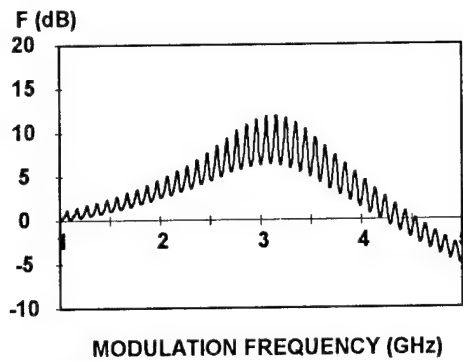


Fig.1 a

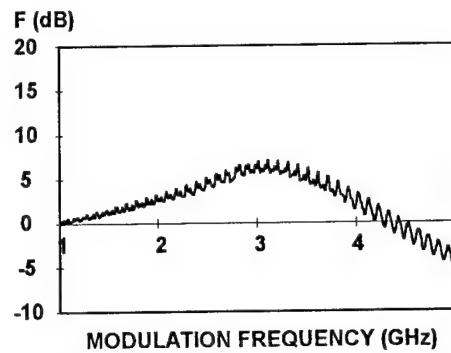


Fig.1 b

Fig1. Modulation transfer function. Optical feedback level (as defined in Ref. 2)  $=10^{-5}$ ; Bias current-Threshold current= 9mA. Fig.1 a. Peak driving current=0.09mA; Fig.1 b. Peak driving current=0.18mA.

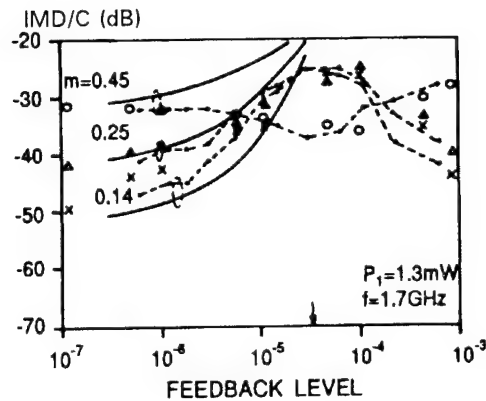


Fig.2. IMD/C versus feedback level (defined as Ref. 2)

---- experiment, \_\_\_ analytical,  $\Delta \times O$  computed values.

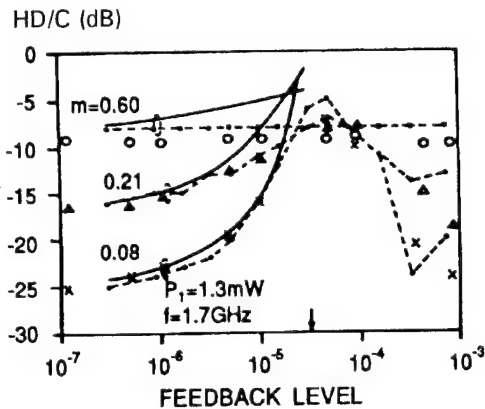


Fig.3 HD/C versus feedback level (defined as Ref.2)

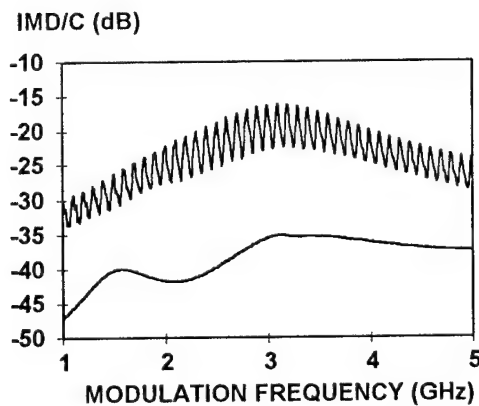


Fig. 4. IMD/C versus modulation frequency of 11 channels with center channel suppressed and OMD=0.09 for each channel. Feedback level  $=10^{-5}$ . Upper plot \_\_\_ with reflections, lower plot \_\_\_ without reflections.

# A Correct Way to Model Arbitrary Complex Distributed FeedBack (DFB) Lasers in The Above Threshold Regime.

Wei Hsin

Institute of Electro-Optical Engineering  
National Chiao Tung University  
1001 Ta Hsueh Rd  
Hsinchu 300, TAIWAN, R.O.C.

Tel: 886-35-712121 ext. 56376

Fax: 886-35-716631

Most of the published papers on the above-threshold simulation for DFB lasers utilize the powerful transfer matrix method (TMM) to include the longitudinal variations of the carrier and photon profiles caused by spatial hole burning and gain saturation effects at high output power<sup>[1]-[7]</sup>. However the approaches used to calculate the above-threshold behaviors were not correct. The most general mistakes are: (i). The use of the wrong threshold condition for the lasing mode both at and above threshold<sup>[2]-[5],[7]</sup>. (ii). The iteration algorithm used to solve the above-threshold behavior for higher order DFB modes did not include the influence of the lasing mode properly<sup>[1],[2],[4],[5],[7]</sup>.

The main reasons for these mistakes are: (1). People have used only three equations to model the above-threshold behavior of the DFB modes, i.e., the two coupled mode equations and the carrier's rate equation<sup>[2]-[7]</sup>. This is not enough. **Photon's rate equation must be included** as well. (2). People considered all the DFB modes separately in the above-threshold regime without considering the fact that they all share the same carrier reservoir and mode competition between them is important<sup>[2],[4,5],[7]</sup>.

The simulation results for an AR-coated quarter-wave-phase-shifted (QWPS) DFB laser due to above mentioned mistakes are: (A). Rapid increase of the threshold gain  $g_{th}L$  of the lasing mode in the above-threshold regime. This can be clearly seen in curve (1) of Fig.1. This curve is reproduced by using the old TMM method<sup>[2]</sup> for comparison. (B). Prediction of a "red shift" of the lasing mode in contradiction to the "blue shift" observed experimentally<sup>[9,10]</sup>. This is seen in curve (b) of Fig.2 which we reproduce here by the old TMM algorithm<sup>[2]</sup>. (C). Side DFB mode (here, the +1 mode) will never reach threshold even for very strong coupling ( $\kappa \cdot L = 3$ ). This is seen in curve (a) of Fig.2 which tells us that the laser will maintain stable single mode behavior forever. This is obviously ridiculous and is contradictory to many of the experimental results<sup>[8]</sup>.

We have developed a new and correct TMM approach to fix all the mistakes mentioned above. We solve the two coupled mode equations and the two rate equations simultaneously and self-consistently, and obtained new formula for the threshold condition of the lasing mode and its threshold gain variation in the above-threshold regime. We have noticed that the spatial hole burning and gain saturation effects are only caused by the lasing mode and all the other below-threshold side DFB modes have to obtain their gain

under the same carrier profile (i.e. the gain profile) which is dominated by the lasing mode. Therefore, our TMM method also includes the gain competition between the side DFB modes and the lasing mode correctly. The detailed derivation of equations and our numerical approaches will be presented at the conference. In the following, we only show the results obtained by our newly developed approach. Our results compare favorably to that of the experimental observations[8]-[10].

Curve (2) of Fig.1 shows the threshold gain increase of the dominant lasing mode in the above-threshold regime by our new TMM method. It is clear that the increase with injection current is much less than that obtained by the old TMM method. This result suggests that the old TMM method[1]-[7] has overestimate the effect of spatial hole burning and gain saturation. However, Fig.3-(a) shows that at  $4.5I_{th}$  the +1 mode reaches threshold which corresponds well to the experimental observations[8]. By comparing Fig.2-(a) and Fig.3-(a), we see that the extreme stable single mode behavior predicted by the old TMM method is not predicted by our new model. Therefore, even though our model results in less spatial hole burning and gain saturation effect for the lasing mode, the side mode will eventually reach threshold. This resolved the conflicting results between the experimental observation and the old TMM approach.

Fig.3-(b) shows the slight blue shift of the lasing mode predicted by our new approach in the above-threshold regime. This corresponds well with the experimental results[9,10]. In our present model, the thermal effect is not included and, therefore, can not predict the red shift of the lasing mode at high injection level due to heating. However, the thermal effect can also be included in our present model easily, but this is not the major point of this paper.

In conclusion, we have newly developed a correct TMM method to simulate DFB laser in the above-threshold regime by solving the two coupled mode equations and the two rate equations all together in a self-consistent way. This model can easily include the effect of spatial and spectral hole burning and the thermal heating at high injection level. Since we are using the TMM method, this model can apply to any complex DFB structures with any complex form of the coupling coefficient. Some of the simulation results by our new approach for the pure gain-coupled and complex-coupled DFB lasers will be presented at the conference.

### **References:**

- [1]. G. Bjork, O. Nilsson; IEEE J. Lightwave Technol., Vol. LT-5, No.1, pp.140-146, (1987).
- [2]. I. Orfanos, *et al*; IEEE J.Q.E., Vol. 27, No. 4, pp.946-956, (1991).
- [3]. H. Bissessur, IEEE J. Lightwave Technol., Vol. 10, No. 11, pp.1617-1630, (1992).
- [4]. G. P. Agrawal, A. H. Bobeck; IEEE J.Q.E., Vol. 24, No. 12, pp.2407-2414, (1988).
- [5]. K. Kikuchi, H. Tomofuji; IEEE J.Q.E., Vol.26, No.10, pp.1717-1727, (1990).
- [6]. R. Bonello, I. Montrosset; IEEE J. Lightwave Technol., Vol.10, No.12, pp.1890-1900, (1992).
- [7]. P. Correc, IEEE J.Q.E., Vol.30, No.11, pp.2467-2476, (1994).
- [8]. H. Soda, *et al*; IEEE J.Q.E., Vol. QE-23, No.6, pp804-814, (1987).
- [9]. Y. Nakano, *et al*; paper H-2, pp102-103, 11th IEEE International Semi. Laser Conf., Aug.29-Sept.1, (1988).
- [10]. H. Hillmer, *et al*; IEEE J.Q.E. Vol. 30, No. 10, pp.2251-2261, (1994)

### **Figures:**

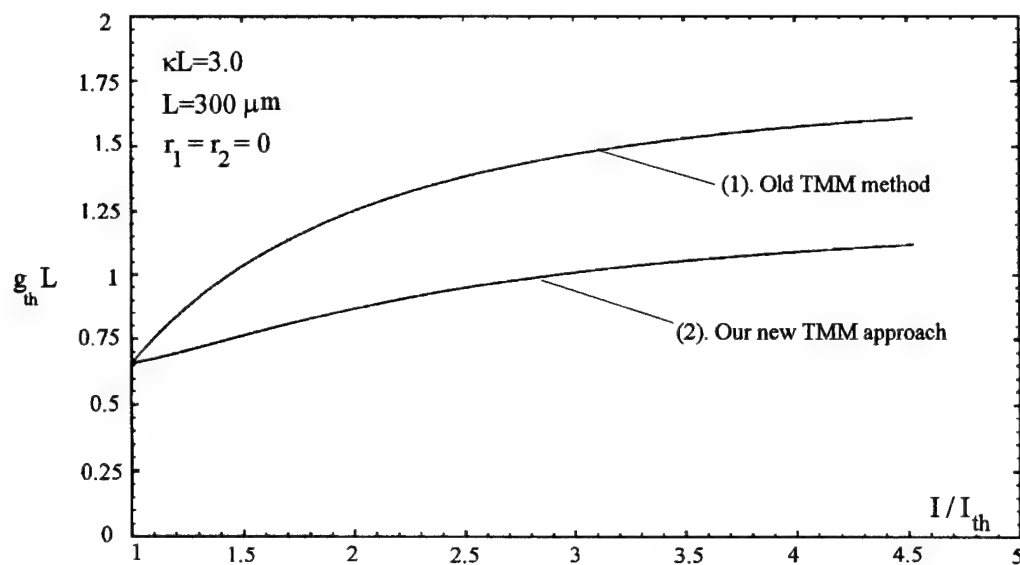


Fig.(1). Lasing mode's normalized threshold gain v.s. current injection level for a QWPS-DFB laser with both facets anti-reflection coated.

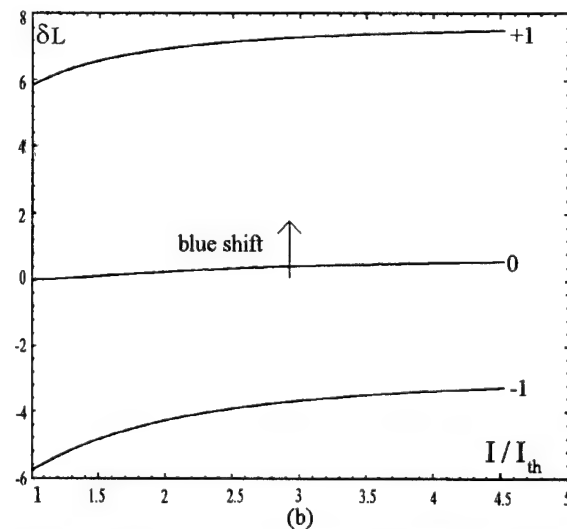
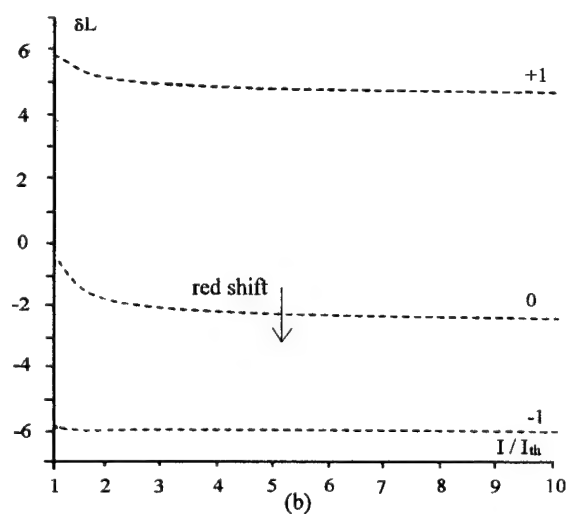
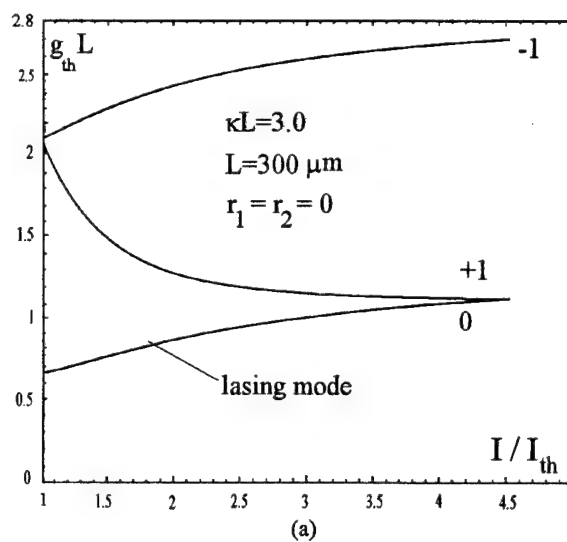
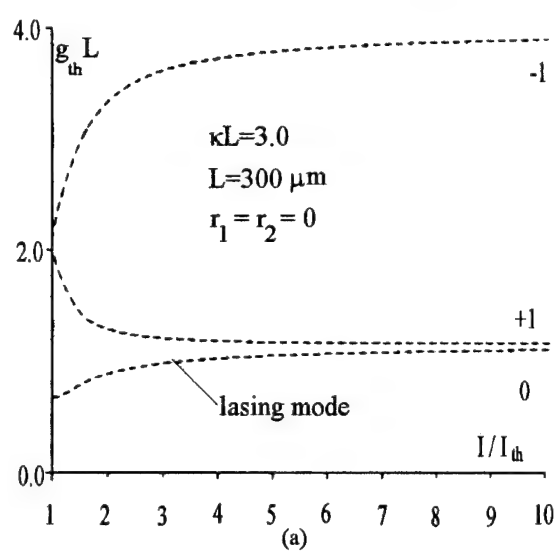


Fig.(2). First three modes behaviors of an AR-coated QWPS-DFB laser calculated by old TMM approach.<sup>[2]</sup>

Fig.(3). First three modes behaviors of an AR-coated QWPS-DFB laser calculated by our new TMM method.



# High power diffraction-limited ultrashort pulse generation from double tapered semiconductor laser diodes

Ziping Jiang<sup>1</sup>, I.H. White, F. Laughton, R.V. Penty, M.W. McCall\* and H.K. Tsang<sup>†</sup>.

School of Physics, University of Bath, Bath BA2 7AY.

<sup>†</sup>Department of Electronic Engineering, Chinese University of Hong Kong, Hong Kong.

\* Applied Optics, Department of Physics, Imperial College, London, SW7 2BZ.

Fax No:852-2603-5558

E-mail: zpjiang@ee.cuhk.hk

One promising way of generating high power diffraction-limited output from a semiconductor laser diode is to fabricate a double tapered device by varying the stripe width along the cavity, in order to produce wide stripes at the facets and a narrow stripe at the center. The narrow stripe near the middle of the cavity acts as a spatial filter to maintain a good quality spatially coherent output, whilst the wide stripes at the facets have the dual benefits of increasing the active volume (thus increasing optical power generation) and increasing the threshold power before catastrophic facet damage occurs. High power single lateral mode operation has already been demonstrated by using various tapered devices[1, 2, 3] and much work has been carried out on tapered semiconductor laser amplifiers [5, 4]. However, the nature of double tapered device in obtaining high power and diffraction limited output is still poorly understood and optimization in design is badly needed.

In this paper, the operation of various tapered stripe devices have been investigated theoretically by using generalized travelling wave equations[6], where the effects of diffraction and carrier-induced refractive index variation are taken into account. The partial differential equations are solved by using a modified beam-propagation-method[7, 8], which is computationally intensive, requiring a large number of longitudinal segments and lateral mesh points. The simulation also involves calculating the carrier density by integrating the carrier diffusion equation at time increment of less than 0.5ps, and obtains the full dynamics of filament formation.

The simulation results provide a good understanding of the dynamics of filament formation during gain-switching operation. In the following discussion, conventional stripe devices are considered first, before considering tapered devices. The length of devices is assumed to be  $500\mu\text{m}$  and the same injected current density is used in all the simulations. For a  $5\mu\text{m}$  narrow stripe device, the output optical pulse and the time evolution of the nearfield profile can be seen in Figure 1, where the intensity profiles are shown in the forms of (a) a spatial-temporal plot and (b) a contour map. The near field profile remain approximately Gaussian throughout the formation of the pulse, and the phase across the lateral axis is almost constant. The maximum beam width at  $\frac{1}{e^2}$  is about  $6.5\mu\text{m}$  and the far field consists of a single lobe averaging  $10^\circ$  FWHM during pulse formation. Broader stripe widths of  $10\mu\text{m}$

---

<sup>1</sup>Present address: the Department of Electronic Engineering, Chinese University of Hong Kong, Hong Kong.

and  $20\mu\text{m}$  have been simulated and the corresponding contour maps can be seen in Figure 2(a) and 2(b). The near field width at the tail of the pulse oscillates considerably, resulting in the formation of complex multi-lobe far-field patterns[9]. The physics of this is due to the non-uniform carrier depletion along the stripe laterally, so that the refractive index in the center part of stripe starts to increase and self-focusing reduces the laser beam size until the effects of diffraction prevent the beam from collapsing further.

Double tapered devices consisting of a  $250\mu\text{m}$  long  $5\mu\text{m}$  wide stripe in the middle and linear tapers to increase the stripe width to  $20\mu\text{m}$  at the facets has also been simulated for the same injected current density. Figure 3 show the dynamics of pulse formation in the tapered device. The maximum near-field( $\frac{1}{e^2}$ ) width is  $14\mu\text{m}$  and a single lobe far-field pattern averaging  $4^\circ$  FWHM is produced. In contrast to the broad stripe devices, the double tapered structure has a good single lobe far-field pattern whilst maintaining high power operation. It is also found that there is an optimum center

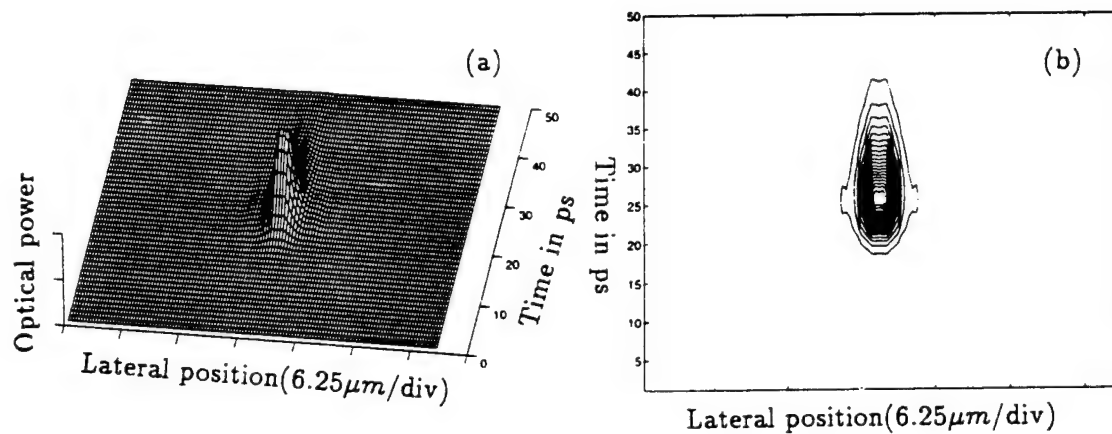


Figure 1. Simulation results for a laser diode with stripe width of  $5\mu\text{m}$  during gain-switching; (a). dynamical near field, (b). its contour map.

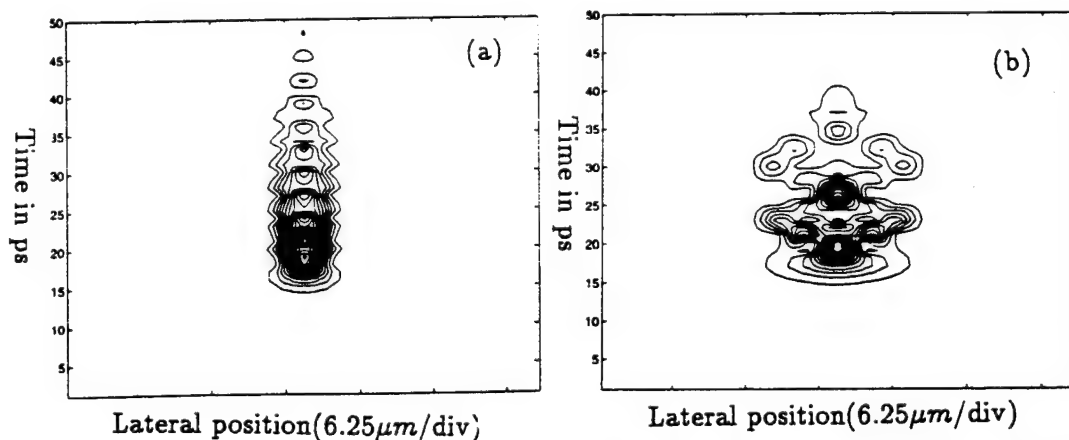


Figure 2. Contour map of near field for stripe width of (a)  $10\mu\text{m}$ , and (b)  $20\mu\text{m}$  device, respectively, during the gain-switching operation.

stripe width for a given device structure: too narrow a center stripe leads to mode break-up due to spatial hole-burning and nonlinear effects in the center region, while too wide a center stripe leads to multi-lobe far-field operation due to insufficient spatial filtering. Optimization in the terms of the length of center region, the coating at facets, and the pumping conditions have been investigated and will be presented at the conference.

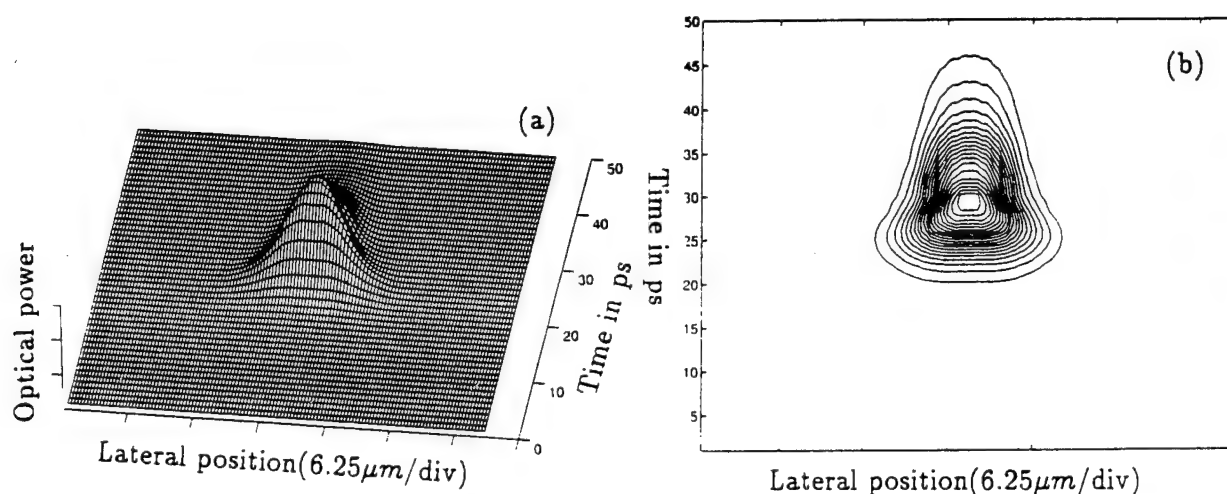


Figure 3. Gain-switching a double tapered laser with a  $250\mu\text{m}$  long,  $5\mu\text{m}$  center stripe width, and linearly tapered to  $20\mu\text{m}$  at facets. (a) Dynamical near field, and (b) its contour map.

## References

- [1] D.F. Welch, P.S. Cross, D.R. Scifres, W. Streifer and R.D. Burnham, *Applied Physics Letter*, Vol.50, No.5, pp233-235(1987).
- [2] K. Shigihara, T. Aoyagi, S. Hinata, Y. Nagai, Y. Mihashi, Y. Seiwa, K. Ikeda, and W. Susaki, *Electronic Letters*, Vol.24, No.18, pp117-118(1988).
- [3] K.A. Williams, J. Sarma, I.H. White, R.V. Pentty, I. Middlemast, T. Ryan, F.R. Laughton, and J.R. Roberts, *Electronic Letters*, Vol.30, No.4, pp320-321(1994).
- [4] D. Mehuys, L. Goldberg, and D.F. Welch, *IEEE Photonics Technology Letters*, Vol. 5, No. 10, pp1179-(1993).
- [5] R.J. Lang, A. Hardy, R. Parke, D. Mehuys, S. O'Brien, J. Major and D. Welch, *IEEE Journal of Quantum Electronics*, Vol.29, No.6, pp2044-2051(1993).
- [6] O. Hess, S.W. Koch, and J.V. Moloney, *IEEE Journal of Quantum Electronics*, Vol.31, No.1, pp35-43(1995).
- [7] G.P. Agrawal, *IEEE Journal of Quantum Electronics*, *Journal Applied Physics*, Vol.56, No. 11, pp3100-3109(1984).
- [8] E.A. Sziklas and A.E. Siegman, *Applied Optics*, Vol.14, No.8, pp1874-1889(1975).
- [9] P.R. Selway, P.A. Kirkby, A.R. Goodwin, and G.H.B. Thompson, *Solid-state and electron devices*, Vol. 2, No. 1, pp38-40(1978).

## Influence of small radiation doses on the parameters of injection lasers

A. V. Khaydarov\*, A. I. Koifman, I. V. Mart'yanova

Scientific-Research Institute of Applied Physics, Tashkent.

\*Current address: 1545 Parkhill Rd. Cleveland HTS, OH 44121

The effects of small doses ( $\sim 10^3 - 10^4$  rad) have not been studied sufficiently thoroughly, although these effects are of interest both from the point of view of the possibility of identification of the micromechanisms of radiation-defect formation and deliberate changes in the parameters of the structures, i.e., from the point of view of radiation technology.

The samples subjected to irradiation with  $^{60}\text{Co}$  gamma rays and mixed gamma-neutron radiation were laser structures in which the active elements consisted of InGaAsP-InP-InP (type 1) and AlGaAs-GaAs (type 2) heterojunctions grown by the liquid phase epitaxy method. These were mesa-stripe structures with horizontal and vertical confinement of both carriers and of the optical field. The width and the thickness of the active layer were 3-4 and 0.12-0.30 microns respectively, whereas the resonator length was 100 microns.

We used a well-type gamma-rays source with a "squirrel cage", containing the  $^{60}\text{Co}$  isotope, and a water reactor. The gamma radiation intensity was in the range 8-10 R/sec. At the center of the squirrel cage the gamma-rays field was homogeneous and isotropic. The flux density of neutrons (of energy at least 1.5 MeV) was  $\sim 10^9 \text{ cm}^{-2} \text{ sec}^{-1}$  and the intensity of the concomitant gamma radiation was approximately 2.5 R/sec.

The current-voltage characteristics of the injection lasers were not greatly affected by gamma irradiation. In the case of type 1 structures there were significant changes manifested by an increase in the forward voltage drop after a dose of  $\sim 5 \times 10^3 \text{ R}$ , whereas in the case of type 2 structures this happened after a dose of  $10^3 \text{ R}$ .

An investigation of the watt-ampere characteristics of laser structures showed that the power of the lasers was not greatly affected or it increased. Further irradiation resulted in degradation of the watt-ampere characteristics, which sometimes occurred abruptly.<sup>3</sup>

The threshold current  $J_{\text{th}}$  also changed abruptly after small doses. It either fell up to  $\sim 20\%$  (in the case of type 1 lasers) or increased by to 60% (type 2 lasers). However, under constant pumping conditions, the value of  $J_{\text{th}}$  increased up to 5% at doses up to  $10^3 \text{ R}$ , fell up to 5% at doses up to  $10^4 \text{ R}$ , and then rose slightly on increase in the dose. Under pulsed conditions the  $J_{\text{th}}$  only decreased as a result of irradiation.

The spectral characteristics of the lasers exhibited a greater sensitivity to the radiation doses. We observed a shift of the maximum of the fundamental mode resulting in an increase (by up to 4 nm) or a reduction (by 1.5 nm) in the wavelength in the range of doses  $10^3$ - $10^4 \text{ R}$  under multistage irradiation conditions.

The threshold current after neutron irradiation obtained under different loading conditions decreased by up to ~20% as a result of flux densities up to  $10^{12}$ - $10^{13}$   $\text{cm}^{-2}\text{sec}^{-1}$ . An increase in this density (in excess of  $10^{14}$   $\text{cm}^{-2}\text{sec}^{-1}$ ) increased  $J_{\text{th}}$  by the average of 70% under constant-current conditions and by 60% in the case of current pulses.

The threshold wavelength changed mainly in the range of flux densities  $10^{12}$ - $10^{13}$   $\text{cm}^{-2}\text{sec}^{-1}$  and the largest shift toward longer wavelengths was ~7nm, whereas that toward shorter wavelength was ~6nm. However, an increase in the neutron flux density in excess of  $10^{14}$   $\text{cm}^{-2}\text{sec}^{-1}$  resulted only in slight shift toward longer wavelengths.

The changes in the threshold wavelengths caused by neutron irradiation were practically the same irrespective of whether the pump current was constant or applied in the form of pulses. Hence, we concluded that at the excitation threshold the temperature effects could be ignored under constant excitation conditions.

We found that gamma irradiation resulted in three consecutively dominant processes governing the degradation of semiconductor lasers: 1) "short-range" radiation-stimulated diffusion and healing of radiation defects; 2) "long-range" radiation-stimulated diffusion and migration of excess dopants to the "sinks"; 3) radiation defect-formation and formation of stable defect complexes as a result of radiation-stimulated migration of the defects.

In the case of the action of gamma-neutron radiation one should bear in mind that, firstly, we were dealing here with the effects of transmutation doping due to the nuclear reactions<sup>2</sup> and, secondly, that the rate of radiation-stimulated processes increased at a rate characterized by a power-law dependence on the radiation intensity. In the case of steady-state gamma-neutron irradiation the small-dose effects were observed at doses equivalent to  $\sim 10^3$ - $10^4$ R. Transmutation doping manifested itself at neutron flux densities in excess of  $10^{14}$   $\text{cm}^{-2}\text{sec}^{-1}$  and had a significant influence on the distribution of the doping only in the case of InP structures.

The interaction of gamma radiation with energies in excess of 10KeV and in doses of  $10^3$ - $10^4$  R could be used at low temperatures to modify deliberately the parameters of injection lasers made of InGaAsP and AlGaAs materials. However, the suitability of such methods should be considered in each specific case and for a particular structure. It would also be desirable to carry out deliberate investigations of radiation-stimulated heterodiffusion and self-diffusion in ternary and quaternary compounds (films) containing  $A^3B^5$  materials in order to determine more accurately the radiation-stimulated diffusion coefficients.

<sup>1</sup> M. Kitagava, J. Endo, Y. Dei, Annu. Rep. Radiation Center Osaka Prefect. 16, 211 (1985)

<sup>2</sup> A. Koifman, O. Niyazova, Phys. Status Solidi A 10, 59 (1972)

# Theory of Sub-Picosecond Semiconductor Lasers

Jan A. Leegwater

Faculteit Natuurkunde en Sterrenkunde, Vrije Universiteit Amsterdam

De Boelelaan 1081, 1081 HV Amsterdam

The Netherlands, E-mail: leegwate@nat.vu.nl

tel: (00) 31 - 20 - 444 7863, FAX: (00) 31 - 20 - 444 7899

Theories of laser mode-locking were developed in the seventies for dye lasers. However, semiconductor lasers are characterized by quite different parameters and the approximations that can be justified for dye lasers break down for semiconductor lasers. In this paper we study the resulting pulse duration using the model introduced by New and Haus [1, 2] with both slow and fast absorbers. In the fast-and-slow-absorber model of Haus the electric field of the pulse after round-trip  $i$  is given by  $a_i(t)$ . While propagating through the cavity the pulse is modified by each of the elements of the cavity in some way. After passage through the gain section the pulse is expressed as

$$a_i^{(g)}(t) = \exp(g(t))a_i(t) \quad (1)$$

where the gain  $g(t)$  is time dependent due to gain saturation

$$g(t) = g_i \exp \left( -\frac{1 + j\alpha_g}{E_{G,sat}} \int_{-\infty}^t |a_i(t)|^2 dt \right) \quad (2)$$

Here  $g_i$  is the gain just before the pulse, the saturation energy [1, 2] is  $E_{G,sat}$ , and the line-width enhancement factor  $\alpha_g$  models self phase modulation. It is not clear at all whether this  $\alpha_g$  is the same as the Henry parameter  $\alpha$ . The saturable absorber is modeled in a similar manner with initial absorption  $q_i$  and a saturation energy  $E_{A,sat}$  resulting in a pulse  $a_i^{(a)}(t)$ . In addition we take into account an overall cavity loss  $q_0 \equiv 1$ , due to for instance the outcoupling. Moreover the gain and absorption depend on frequency. In the frequency domain this can be modeled as a Gaussian so that

$$a_{i+1}(t) = (1 + D^2)^{1/4} (2\pi\omega_L^2)^{-1/2} \int dt' \exp \left[ -\frac{\omega_L^2 t'^2}{1 + jD} \right] a_i^{(a)}(t - t') \quad (3)$$

Here  $\omega_L$  is the gain bandwidth, and  $D$  describes the (dimensionless) round-trip dispersion. The eventually resulting pulse shape is the solution to  $a_{i+1}(t) = a_i(t)$ . Due to the non-commuting properties of the various pulse modifications, a complicated set of equations results, that moreover is not instantaneous as the gain and absorption depend on the past pulse shape [Eq. (2)]. In spite of the complex nature of these equations, Haus has solved the resulting pulse shape [2] by expanding the various exponentials to first or second order. The result is a chirped hyperbolic secant pulse

$$a(t) = a_\infty \frac{1}{\cosh(t/\tau)} \exp(j\beta \log(\cosh t/\tau)). \quad (4)$$

A  $\text{sech}^2$  intensity pulse shape is universally assumed in the fitting of experimental results.

We have extended the work of Haus [2] by including the slow self phase modulation of the gain and absorber sections. In contrast to [3] we also allow for a fast saturable absorber in the

cavity. We will not present here the details of the solution of the round-trip equations, which are very similar to the equations obtained in [3]. Using the notation and the procedure outlined by Koumans and van Roijen [3] we find that the solution to the round trip equation follow as the solution to a set of 6 equations, the first of which can be solved to yield the pulse duration

$$\tau = \frac{\left[ (2q_F/P_F)^2 + 8(q_i - g_i s^{-2})(2 - \beta^2 - 3\beta D)E_{A,sat}^2 \omega_L^{-2} \right]^{1/2} - 2q_F/P_F}{(q_i - g_i s^{-2})E} \quad (5)$$

Here  $q_F$  is the absorption of the fast saturable absorber which saturates with a power  $P_F$  and we have introduced New's parameter  $s = E_{L,sat}/E_{A,sat}$ . While the other five equations appear to be quite complicated they are very useful and can be solved by reversing the problem: start with a certain desired pulse and calculate the parameters required. This then gives values of the required self phase modulation parameters  $\alpha_A$  and  $\alpha_L$  as well as other parameters. In the end we are then left only with two equations, which are Eq. (5) and Eq. (7) below.

From Eq. (5) trivially follows that when there is no fast saturable absorber in the cavity ( $q_F = 0$ )

$$\tau = \frac{4E_{A,sat}}{\omega_L E} \left( \frac{2 - \beta^2 - 3\beta D}{2(q_i - g_i s^{-2})} \right)^{1/2} \quad (6)$$

This expression suggests guidelines on how to achieve short pulses: maximize the energy  $E$  and the pre-pulse saturable absorption  $q_i$ . It also suggest that a chirped pulse with  $\beta \neq 0$  can improve the performance. The obtainable improvement is however quite limited. One of the equations of Koumans and van Roijen [3], which also holds in the presence of a fast saturable absorber, reads

$$1 + q_i - g_i - (q_i - g_i/s) \frac{E}{2} + (q_i - g_i s^{-2}) \frac{E^2}{4} + \xi^2 + \frac{-1 + \beta^2 + 2\beta D}{\omega_L^2 \tau^2} = 0 \quad (7)$$

The sum of terms on the first line must be positive which follows from requiring that noise before and after the pulse is not amplified [2, 3]. It follows that  $\beta^2 + 2\beta D < 1$  so that

$$2 - \beta^2 - 3\beta D = 2 - \frac{3}{2} (\beta^2 + 2\beta D) + \frac{\beta^2}{2} > \frac{1 + \beta^2}{2} \quad (8)$$

Substituting this inequality into Eq. (6) we find that self-phase modulation by a slow medium can shorten the pulse by at most a factor 2. A careful inspection of the round-trip equation of Haus reveals that its validity is based on the assumption that the total energy is less than the saturation energy of the saturable absorber. In semiconductor lasers this is a desirable regime to be in. For larger energies effects occur which are hard to model and hence make the design of such a semiconductor mode-locked laser cumbersome. These effects include, but are not limited to, free-carrier absorption and non-linear self-phase modulation. Due to the presence of the strong field caused by the reverse bias that is typically used to create an absorber that relaxes sufficiently rapidly, these are hard-to-model processes. The upshot of considerations such as these is that it is reasonable to impose an additional constraint on the solution of the round-trip equations, namely that the energy of the pulse is less than the absorber saturation energy,  $E < E_{A,sat}$ . This additional constraint has major implications for the parameters characterizing mode-locked semiconductor lasers. As for semiconductor lasers the pulse energy is limited, the only parameter

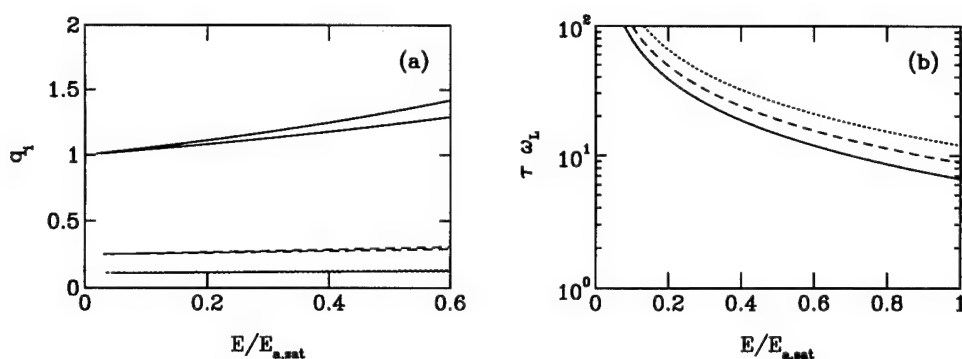


FIG. 1. (a) The area between the curves is the range of allowable amount saturable absorption  $q_i$  as a function of pulse energy for various values of the parameter  $s = E_{L,sat}/E_{A,sat}$ . Solid:  $s = 2$ , dashed  $s = 5$ , dotted  $s = 10$ . (b) The resulting pulse duration as a function of pulse energy. Shorter pulses result when  $s$  is smaller. While the pulse duration varies somewhat depending on other parameters, this variation is of the order of the thickness of the lines.

determining the pulse duration that can still be changed is the amount of saturable absorption  $q_i$ . This also can not be increased at will as then the laser becomes unstable. In Fig. 1a the regime of stable operation is presented and in Fig. 1b the resulting pulse durations are presented as a function of the pulse energy. It is clear that shorter pulses result when  $s$  is smaller. The conclusion is that a ring laser configuration can be expected to produce shorter pulses, simply because one of the effects of a colliding pulse configuration is to double  $s$ . Another consequence is that shorter pulses are to be expected from a laser constructed from bulk material as for a bulk material the gain is almost linearly dependent on the carrier density [5]. Indeed the shortest pulses generated by a monolithical semiconductor laser have been obtained from a bulk semiconductor laser [4]. The performance is expected to be quite modest, as is illustrated in Fig. 1 the shortest attainable pulse width has a time duration of eight times the inverse gain bandwidth. In order to obtain shorter pulses a fast saturable absorber must be introduced into the cavity.

## References

- [1] G. H. C. New, IEEE J. Quantum Electron. **10**, 115 (1974).
- [2] H. A. Haus, IEEE J. Quantum Electron. **11**, 736 (1975); J. C. Chen, H. A. Haus, E. P. Ippen, IEEE J. Quantum Electron. **29**, 1228 (1993).
- [3] R. G. M. P. Koumans and R. van Roijen, submitted to IEEE J. Quantum Electron. (1995).
- [4] R. G. M. P. Koumans, R. van Roijen, B. H. Verbeek, M. B. van der Mark, and C. T. H. F. Liedenbaum, to appear in the proceedings of the Optical Fiber Conference, San Diego, February 1995.
- [5] W. W. Chow, S. W. Koch, M. Sargent III, *Semiconductor-Laser Physics* (Springer, Berlin, 1994).



## Selected Multi-Wavelength Oscillation of a Semiconductor Laser in an External Cavity

Ching-Fuh Lin

Graduate Institute of Electro-Optical Engineering  
and

Department of Electrical Engineering

National Taiwan University

Taipei, Taiwan, R.O.C.

Tel: 886-2-3635251 ext. 339

Fax: 886-2-3638247

A multi-wavelength laser source is important for applications in areas such as wavelength-division multiplexing (WDM), interferometry, lidar and optical data storage. Simultaneous oscillation of multiple wavelengths have been demonstrated in several methods including spatially chirped Bragg reflector vertical cavity surface emitting laser (VCSEL) arrays,<sup>1</sup> multichannel grating cavity (MGC) laser,<sup>2</sup> multistripe array grating integrated (MAGIC) laser,<sup>3</sup> and multi-wavelength DFB laser array by control selective area MOVPE.<sup>4</sup> In those devices, arrays are required for the generation of multi-wavelength oscillation. Each array element is responsible for its individual wavelength oscillation. In this work, it is demonstrated that a single-stripe Fabry-Perot laser diode is able to oscillate at selected multiple wavelengths with a wavelength separation  $\geq 1.3$  nm, several times larger than the Fabry-Perot longitudinal mode spacing.

A schematic of the experiment is shown in Fig. 1. The laser diode has a 4  $\mu\text{m}$  wide ridge-waveguide structure fabricated on an AlGaAs/GaAs substrate.

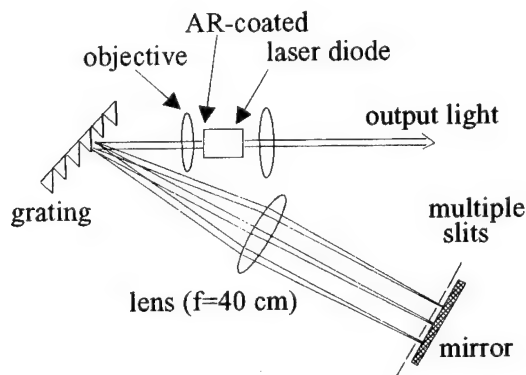


Fig. 1 Schematic diagram of the experimental setup.

The light emitted from the AR-coated facet ( $R \sim 4.6 \times 10^{-3}$ ) is collimated by a 60-X objective and incident on the grating at an angle of  $\sim 38^\circ$ . Output light is obtained from the uncoated facet. A reflected-type grating telescope configuration is used in the external cavity. With the lens at a focal length (40 cm) from the grating (1200 lines/mm), the beams of different wavelengths dispersed by the grating become in parallel, while each wavelength component is focused at another focal length from the lens. According to the grating principle, the beams of different wavelengths are spatially separated by  $W$ , which is determined by

$$W \sim L \frac{1}{\Lambda \cos \theta_R} \Delta\lambda \quad (1)$$

where  $\Delta\lambda$  is the spectral separation,  $\Lambda$  is the grating period;  $\theta_R$  is the first-order diffraction angle, and  $L$  is the distance from the grating to the lens. As a mirror is placed at a focal distance (40 cm) from the lens, as shown in Fig. 1, different wavelengths will return into the same gain region although they travel along different paths in the external cavity. Oscillation wavelengths are selected by placing slits in front of the mirror. The spectral separation of these oscillating modes is controlled by the slit separation, according to equation (1). In principle, the spectral width of each mode can also be controlled by the slit width. However, because the beam size in the external cavity is  $\sim 3$  mm, the grating resolving capability is limited to only  $\sim 0.25$  nm, corresponding to approximately a laser-diode mode.

V-shaped double slits and comb-type multiple slits have been used for the experiment. As the V-shaped double slits are used, two modes are oscillating. The mode spacing varies with the slit spacing and can be as far as 13.2 nm. The dual-mode oscillation can be tuned by moving the slits horizontally, but only within 0.4 mm for the situation of mode spacing 1.56 nm. Beyond this range, one of the two modes dominates possibly due to a strong competition between the two oscillating modes. With the comb-type multiple slits inserted, oscillation can occur at one, two, or three dominant modes, depending on the horizontal position of the comb-type slits. As the configuration is readjusted so that the mode spacing is reduced, oscillation at four modes is also observed. Fig. 2 shows output spectra of three and four dominant modes, which are approximately located around the maximum of the gain profile. For a single-stripe Fabry-Perot laser diode, multi-wavelength oscillation is a natural characteristics and is, in general, determined by the Fabry-Perot cavity structure.<sup>5</sup> With the reflected-type grating telescope configuration in the external cavity and the slits in front of the mirror, those unwanted modes are efficiently

suppressed. However, oscillation of more than four dominant modes with a mode spacing  $\Delta\lambda \geq 1.3\text{nm}$  is not observed in this experiment. The reason is probably because the gain bandwidth is not wide enough and gain competition causes other modes at two sides to be significantly quenched even though their paths are not blocked. For laser diodes fabricated from other materials (such as GaInAsP/InP) with a much broader gain bandwidth, oscillation of more modes with a similar mode spacing is expected.

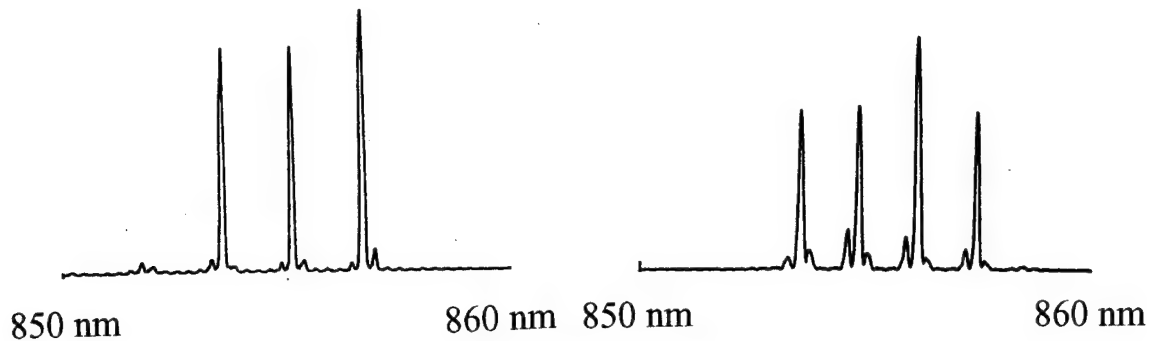


Fig. 2 Output spectra of three and four dominant modes.

### References

1. C. J. Chang-Hasnain, M. W. Maeda, N. G. Stoffel, J. P. Harbison, L. T. Florez, and J. Jewell, *Electron. Lett.*, **26**, 940 (1990).
2. K. O. Nyairo, I. H. White, C. J. Armistead, P. A. Kirkby, *Electron. Lett.* **28**, 261 (1992).
3. J. B. D. Soole, K. R. Poguntke, A. Scherer, H. P. LeBlance, C. Chang-Hasnain, J. R. Hayes, C. Caneau, R. Bhat, and M. A. Koza, *Appl. Phys. Lett.* **61**, 2750 (1992).
4. Masahiro Aoki, Tsuyoshi Taniwatari, Makoto Suzuki, and Takayuki Tsutsui, *IEEE Photon. Technol. Lett.* **6**, 789 (1994).
5. Yoshihisa Yamamoto, *Coherence, Amplification, and Quantum Effects in Semiconductor Lasers*, John Wiley & Sons, Inc., 1991.

# Thermal Modeling of VCSEL-based Optoelectronic Modules

N. D. Morozova

Center for Optoelectronic Computing Systems

Y. C. Lee

Department of Mechanical Engineering

University of Colorado, PO Box 427

Boulder, Colorado 80309-0427

(303) 492-0429, FAX (303) 492-3498

## Introduction

In recent years, many papers have been published about the thermal properties of a single vertical cavity surface emitting laser (VCSEL) and two-dimensional (2-D) arrays. However, a thermal model of VCSEL-based optoelectronic modules has needed to be developed, since the temperature distribution and heat dissipation in optoelectronic packaging affect the device's output characteristics. The device heating places upper limits on the maximum obtainable power as well as on the temperature range of operation. The development of reliable VCSEL-based optoelectronic modules strongly depends on proper thermal management.

## Thermal Model for VCSELs and VCSEL-based Optoelectronic Modules

A comprehensive thermal model for VCSEL-based optoelectronic modules has been developed at the University of Colorado - Boulder. A flow chart of the thermal model is shown in Fig.1, where  $r$  and  $z$  - cylindrical system coordinates,  $V$  - applied voltage,  $\eta$  - differential quantum efficiency,  $I_{th}$  - threshold current,  $K$  - thermal conductivity,  $\sigma$  - electrical conductivity,  $T$  - temperature,  $\eta_{int}$  - internal quantum efficiency,  $I$  - pumping current,  $L$  - light output power,  $Q$  - heat power density,  $\lambda$  - wavelength,  $V_{p-n}$  - voltage drop at the p-n junction, and  $K_p$  - VCSEL package thermal conductivity.

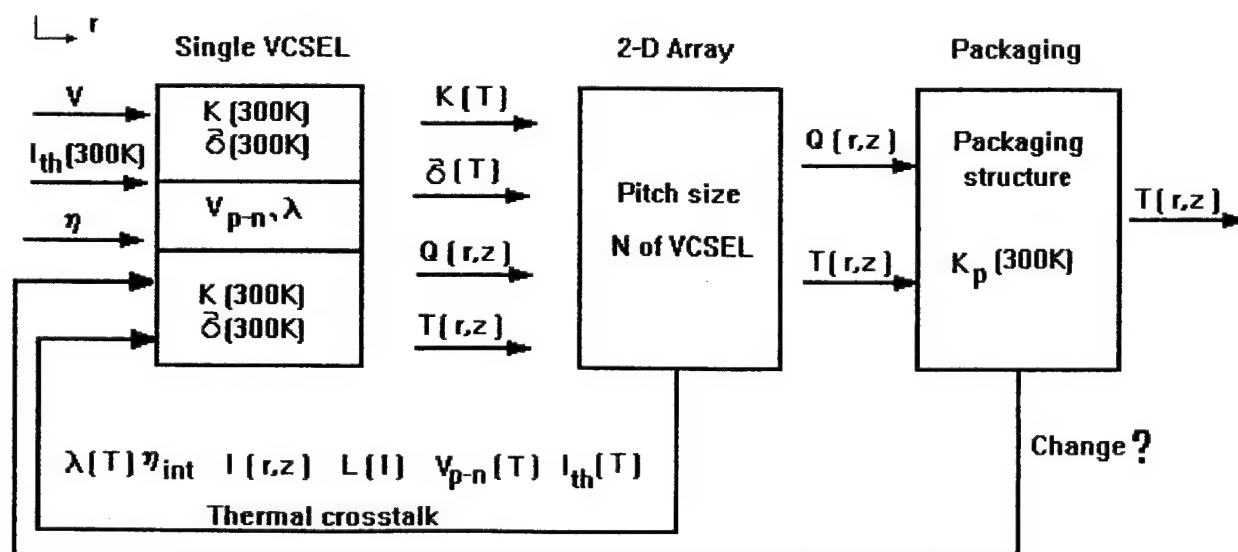


Fig. 1. Flowchart of Thermal Model

### VCSEL Thermal Modeling

A flowchart of a single VCSEL thermal model as a part of the thermal model of VCSEL-based optoelectronic modules is shown in Fig.1. In our thermal modeling, first the temperature distribution and heat dissipation in the single VCSEL are calculated. Three major heat sources are considered: the active region (primarily caused by nonradiative recombination), the P-type Bragg mirror (Joule heating), and the N-type Bragg mirror (Joule heating) [1]. The thermal dependence of electrical resistivity, thermal conductivity, threshold current and voltage, and external quantum efficiency are taken into account. Some of the results of our thermal modeling studies are discussed below.

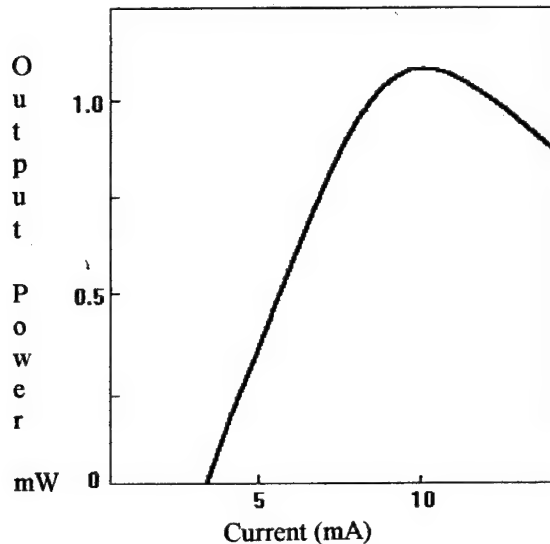


Fig. 2. Calculated Light-Current Characteristic

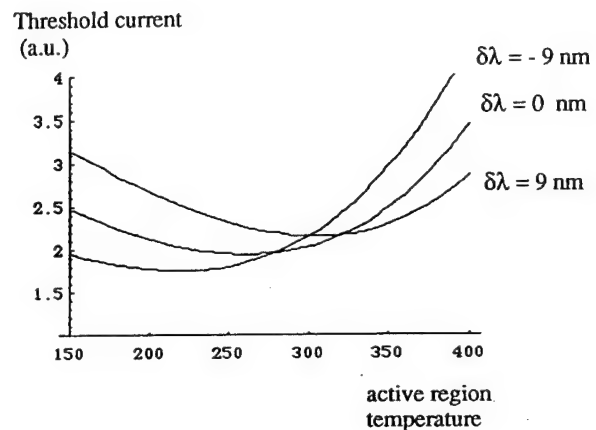


Fig. 3. Temperature Dependence of the Threshold Current

In our modeling, the VCSEL active region temperature as a function of the pumping current is calculated. Since the active region temperature is known, the light output characteristic is defined. Fig.2 shows the results of our calculation, the device under consideration is a gain-guided GaAs/AlGaAs VCSEL with the active region diameter  $D_A = 8 \mu\text{m}$ , continuously graded mirrors, and a CW operation [2].

To demonstrate the functionality of the developed thermal model and show how specific optoelectronic packaging affects the VCSEL characteristics, we have assumed a 2-D VCSEL array to be mounted on a heat sink providing the temperature in the device active region to be within the range of 150° to 400° K. It is known that the thermal behavior of the threshold current is a function of the relative position of the optical mode and the gain peak wavelength, and the threshold is minimum at the temperature where their positions coincide. Fig. 3 shows the threshold current of the VCSEL as a function of the temperature for three different cases:  $\delta\lambda = 0$ ,  $\delta\lambda = 9 \text{ nm}$ , and  $\delta\lambda = -9 \text{ nm}$ , where  $\delta\lambda$  is the shift between the gain and optical mode at room temperature. Calculating the optimum relative position of the optical mode and the gain peak wavelength is necessary for designing the VCSEL-based optoelectronic modules for specific temperature applications.

It is known that excessive heating limits the output power of an individual VCSEL. In the large 2-D arrays, the thermal crosstalk even more deteriorates the device's performance. After the temperature distribution and heat dissipation of the single VCSEL are calculated, the thermal crosstalk in the 2-D arrays can be defined.

### Thermal Modeling of VCSEL-based Optoelectronic Modules

One of the critical components of reliable VCSEL-based optoelectronic modules operation is the thermal path from a device to a heat sink which is affected by packaging technologies and materials. A 3-D numerical model has been developed to study the packaging affects on temperature control. Studies have been made on specific assembly technology, packaging design and materials, and types of heat removal. [3]. One of the results of our study is discussed below.

To demonstrate how the thermal properties of materials used for optoelectronic packaging affect the temperature in the VCSEL active region, the temperature distribution across 2-D arrays mounted on different materials is calculated. In Fig. 4, you can see the temperature distribution across a 2-D VCSEL array when it is mounted on a silicon, and in Fig. 5, you can see the temperature distribution across the same 2-D array, when it is mounted on a glass.

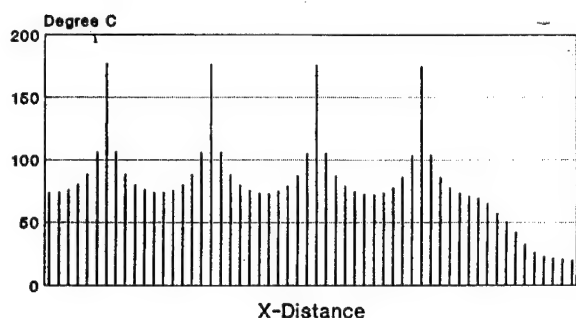


Fig. 4. Temperature Distribution Across a 2-D VCSEL Array Mounted on a Silicon

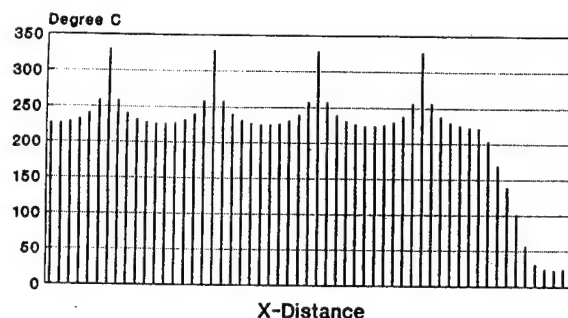


Fig. 5. Temperature Distribution Across a 2-D VCSEL Array Mounted on a Glass

### Conclusion

Experimental and modeling studies have been conducted to characterize the thermal performance of different configurations of VCSEL based optoelectronic modules [3]. The thermal model describe above allows for the design of application-specific VCSEL-based optoelectronic modules and predicts the device's performance under a variety of operation conditions.

### References

1. W. Nakwaski, M. Osinski, "Self-Consistent Thermal-Electrical Modeling of Proton-Implanted Top-Surface-Emitting Semiconductor Lasers", *SPIE Vol. 2146*, pp.365-386, July 1994.
2. P. Zhou, J. Cheng, C. F. Schaus, S. Z. Sun, K. Zheng, E. Armour, C. Hains, W. Hsin, D. R. Myers, and G. A. Vawter, "Low Series Resistance High-Efficiency GaAs/AlGaAs Vertical-Cavity Surface-Emitting Lasers with Continuously Graded Mirrors Grown by MOCVD", *IEEE Photon. Techn. Lett.*, Vol.3, pp. 591-593, July 1991.
3. Y. C. Lee, S. E. Swirhun, W. S. Fu, T. A. Keyser, J. L. Jewell, and W. E. Quinn, "Thermal Management of VCSEL-based Optoelectronic Modules", *IEEE Electronic Technology and Components Conference*, May, 1995.

## **Development of a Tritium Powered Semiconductor Laser**

H. E. Ruda and L. Jedral

*Department of Materials Science, University of Toronto, Ontario, Canada M5S 1A4*

*Tel. (416)978-4556: Fax. (416)978-4155*

and

L. Mannik

*Ontario Hydro Technologies, 800 Kipling Avenue, Toronto, Ontario, Canada M8Z 5S4*

*Tel. (416)207-6732: Fax. (416)207-5551*

Tritium is a radioisotope that emits beta radiation on its decay with a half life exceeding twelve years. The average emitted beta particle energy is  $\sim 6$  keV. Typically for a semiconductor with bandgap on the order of  $\sim 1$ -2 eV for example, one incident beta particle could result in the production of  $\sim 1000$  electron-hole pairs in the semiconductor. Beta decay thus represents an interesting generation source for the design of semiconductor-based light sources requiring no external energy supply. In this work we study the luminescence mechanisms resulting from such excitation in materials from the GaInAsP alloy system.

Work focused on GaInAsP grown by Liquid Phase Epitaxy (LPE) owing to this being one of the most well developed materials in current use for bright high efficiency Light Emitting Diodes (LED's). Epilayers were grown on both (100) and (111) GaAs and GaP substrates using a horizontal multibin slider system to grow layers with thickness up to tens of  $\mu\text{m}$ . Undoped buffer layers were grown prior to layer growth to isolate active layers from the substrates.

Tritium excitation of the material was studied by simulations involving photons and electrons, as well as actual tritium testing. The former studies were conducted using photoluminescence (PL) and panchromatic cathodoluminescence (CL) measurements as a function of temperature; from 12K to room temperature for the PL and 77K to room temperature for the CL studies. Tritium tests were conducted by using ultra-high vacuum cells within which the GaInAsP samples were placed for testing. After evacuation and purging cells, total panchromatic light output was measured as a function of tritium gas pressure using an optical fiber probe, light chopper, calibrated silicon diode with phototopic filter and lockin amplifier. Stability of light output was investigated by holding cells at a fixed pressure. PL measurements were conducted by placing the samples in a temperature-

controlled closed-cycle helium refrigerator controlled and exciting samples using focused radiation from a 10 mW argon ion laser (488 nm). Luminescence was collected using a calibrated silicon diode, 0.5 m monochromator, and lockin amplifier. CL studies were conducted in a scanning electron microscope using low beam current density excitation and under controlled incremental electron energy to cover the complete range of energies characteristic of the tritium beta energy spectrum. A specially designed cold stage was designed to permit low temperature CL measurements to be made.

PL was used to study the dominant radiative recombination pathways in the material and the spectral distribution of radiated light under photoexcitation[1]. Typically emission was in a strong narrow spectral band centered around 650-670 nm. CL measurements were made as a function of excitation energy, at constant beam current; beam current was independently measured in all experiments using a Keithley 617 electrometer. CL intensities were found to be limited by strong non-radiative recombination through surface states[2]. Surface passivation using ammonium sulfide proved to be essential to obtaining high efficiencies. By measuring CL ratios before and after surface passivation improvements in the low energy response were dramatic (over an order of magnitude at ~6 keV) compared to no significant change at high beam energies (say 20 keV, for example)[2]. This may simply be explained by the fact that at low beam energies the electron beam penetration depth is very small (sub-micron) and only samples the surface field where efficient non-radiative recombination is occurring. However, at higher beam energies most of the pair generation occurs deep in the bulk of the material where efficient radiative recombination prevails. Studying the energy dependence of CL also provided us with a means of calibrating our progress with regards to tritium excitation. Since the energy spectrum of tritium is well known, by adjusting the electron flux at each incremental electron energy we were able to simulate tritium excitation and optimize material for tritium testing.

Tritium tests on material optimized as discussed above resulted in the first observation of visible (red) radioluminescence in such materials. By studying the pressure dependence of the luminescence, we found that the luminescence initially rose approximately linearly with increasing tritium pressure and then reached a plateau, typically at about 500 torr of tritium in the cell. The initial rise may be explained by the dependence of the number of tritium encounters with the semiconductor as a function of pressure through the ideal gas law, whereas at higher gas pressures, self absorption of the tritium limits the beta flux arriving at the semiconductor surface. Initial tests



with GaP:Zn,O samples showed that over time light output was decreasing. Annealing experiments were able to show that de-activation of zinc-oxygen centers was occurring in the GaP: Zn,O samples, as the tritium diffused into the samples. This behavior is analogous to that reported for atomic hydrogen passivation of zinc acceptors in other III-V semiconductors. This was most convincingly demonstrated by experiments using the direct bandgap GaInAsP/GaAs samples emitting at  $\sim 650$  nm. With these materials, initial studies have resulted in red radioluminescent lights with  $\sim 5 \times 10^{-6}$  Lamberts of output. Further work on optimization of these materials using appropriate structures is anticipated to yield lights with brightness of  $\sim 1 \times 10^{-4}$  Lamberts, as determined from low temperature (77K) tritium tests. This technology could then be used in the development of radioisotope powered lasers. In progressing from incoherent to coherent light emitters, we will be concerned with cavity designs; initial designs are focusing on double heterostructures, while future designs are expected to look at quantum well active regions and also graded index confinement. Such designs would avoid many of the design concerns with current injection and by occluding the radioisotope within a confinement structure, carrier generation can be efficiently assured in the region where it is desired. Our studies have shown that radiation damage by these relatively low energy beta particles does not produce lattice damage and degrade luminescent output, rather, that the tritium decay is a long-lived source of carrier injection with high gain. We therefore anticipate a bright future for such an approach in areas such as fiber optic communications, optical gyroscopes and display applications.

The authors are indebted to Mr. Stewart Brown for providing assistance with tritium tests and gratefully acknowledge Ontario Hydro International and the NSERC for financial support of this research, and Sumitomo Metal Mining Company for contributing substrates for these studies.

#### References.

1. H. E. Ruda, L. Jedral and L. Mannik, Phys. Rev. B44(16), 8702(1991)
2. L. Jedral, H. E. Ruda and L. Mannik, J. Luminescence, 60/61, 899(1994)

# A CW External Cavity Surface Emitting Laser

J. V. Sandusky, A. Mukherjee, and S. R. J. Brueck

*The University of New Mexico, Center for High Technology Materials, EECE Building, Room 125, Albuquerque, NM 87131-6081. Phone (505) 277 - 3317. Fax (505) 277 - 6433*

We report the first continuous wave, external cavity, optically pumped surface emitting laser. The device is a resonant periodic gain (RPG) vertical cavity surface emitting laser (VCSEL) with the top mirror stack replaced by an epitaxially grown antireflection (AR) coating, as shown in Fig. 1.

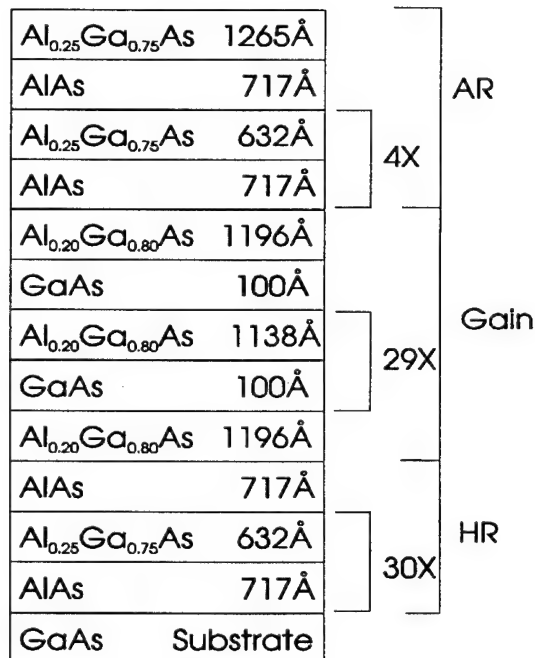


Fig. 1. Design of RPG VCSEL with AR coat.

The bottom stack is a standard high reflector (HR) composed of alternating quarter wavelength slabs of AlAs and Al<sub>0.25</sub>Ga<sub>0.75</sub>As, producing a theoretical reflectance of 99.8% at a wavelength of 860 nm. The gain region contains 30 10-nm thick GaAs quantum

wells with the Al<sub>0.20</sub>Ga<sub>0.80</sub>As barrier thickness chosen to satisfy the standing wave criterion while accounting for reflections between quantum well and barrier. The final AR stack is designed to minimize reflectance between air and the first barrier region in order to avoid coupled cavity oscillation when the wafer is used in an external resonator. The aluminum composition is chosen to be higher in both the HR and AR regions than in the gain region to provide a spectral window where the barrier and quantum well will absorb the pump beam but the HR and AR regions will not. A test antireflection coating exhibits a minimum reflectance of 0.05% at 858.5 nm, the reflectance doubling at 860.0 nm. Compared to the  $\geq 10$  nm gain bandwidth of the quantum wells, and the  $\geq 100$  nm bandwidth of the high reflector stack, it is clear that the antireflection coating will determine the lasing wavelength.

The theoretical reflectance spectra of the overall wafer shown in Fig. 2 closely matches the measured spectrum. Note that the spectrum is radically different from that of a conventional VCSEL design in that there is no region of high reflectance and the reflection dip at resonance is very broad. This is due to the antireflection coating which allows us to see the effect of absorption into the gain region. If absorption is removed, the

location of maximum reflectance coincides with the design wavelength of 860.0 nm.

#### Theoretical Reflectance Spectra

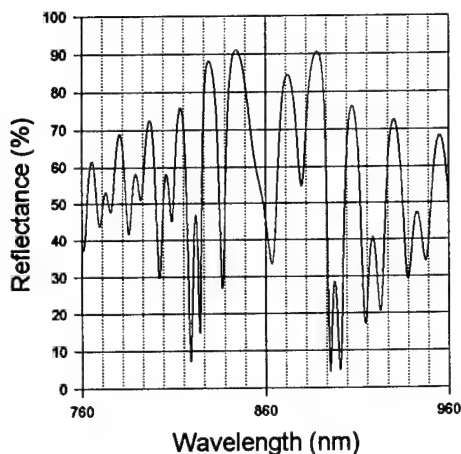


Fig. 2. Theoretical wafer reflectance spectrum.

The external cavity is a near hemispherical resonator using a 50 mm radius of curvature external mirror dielectrically coated to have  $\geq 99.8\%$  reflectance at 860.0 nm. This external mirror serves as the output coupler for the laser cavity. The Gaussian beam waist radius for the  $TEM_{00}$  mode at the wafer will be 8 to 20  $\mu\text{m}$ , depending sensitively on the length of the resonator.

Excitation is accomplished with a cw ring dye laser dye operating at 715 nm. The pump beam is focused to a beam waist of radius of 10-15  $\mu\text{m}$  and the power incident on the wafer is 50 mW at threshold. This yields a pump power density of  $\leq 20 \text{ kW/cm}^2$ , comparable to monolithic VCSELs<sup>1</sup>.

Fig. 3 shows a light input-light output curve for the device. Output power is that observed through the output coupler; input power is that incident on the wafer (uncorrected for reflection). Note the clear threshold at  $P_{th} \approx 50 \text{ mW}$ , indicating that lasing has been achieved.

Heating effects are believed responsible for the decrease in output power beyond  $\approx 1.8XP_{th}$ . The device operates at room temperature, and no attempts have been made to heat sink the wafer beyond backside contact mounting to an aluminum block.

#### Typical Input-Output Curve

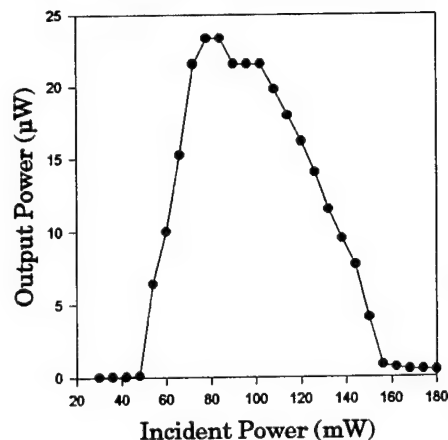


Fig. 3. Input-Output curve for external cavity laser.

A 2-meter double pass spectrometer was used to analyze the lasing mode spectrum. A typical spectrum is shown in Fig. 4a. The measured spacing of the modes is  $0.0074 \pm 0.0006 \text{ nm}$ , which agrees with the  $c/2L$  theoretical mode spacing for this resonator. Note that it cannot be ascertained from this data whether the modes are transverse or longitudinal, since the even transverse modes are degenerate with the longitudinal modes in the hemispherical resonator. The theoretical beam waist for the  $TEM_{00}$  mode on the external mirror is 700 to 1700  $\mu\text{m}$ . If an intra-cavity aperture of diameter 6000  $\mu\text{m}$  is inserted over the external mirror the number of oscillating modes is significantly reduced (Fig. 4b),

suggesting the presence of multiple transverse modes.

Although an AlGaAs crystal should have no polarization selective properties for surface emission, most researchers find that the lowest order mode from a standard VCSEL structure is highly linearly polarized along a crystal axis, higher order modes being orthogonally polarized<sup>2</sup>. Recently Choquette et. al. have determined that the dominant polarization mode can be selected by heating the wafer<sup>3</sup>. Also, polarization control has been achieved by anisotropic stress techniques applied to the wafer<sup>4</sup>.

It is interesting to note, then, that although our beam is oscillating in about 90 modes, at least some of which are transverse as evidenced by the reduction in mode spectrum obtained using an intra-cavity aperture, the output is highly linearly polarized along a crystal  $\langle 110 \rangle$  axis. This effect does not appear to be due to any peculiar stress induced by the wafer mounting technique, as the wafer can be mounted and remounted repeatedly while the polarization remains tied to the same axis. Since there are no polarization selective optics in the cavity, the polarization must be due to some property of the wafer. We have been successful in inserting an etalon into the cavity as a Brewster surface at  $45^\circ$  to the usual polarization direction, and lasing is achieved with polarization determined by the inserted etalon. Further experiments will study the variation in threshold as the Brewster surface is rotated with respect to the crystal axes.

In summary, we have demonstrated the first operation of a cw external-cavity surface-emitting laser.

The operation is highly multimode while maintaining a high degree of linear polarization. The capability of inserting polarization and mode control elements in the external cavity will allow both study of the physics of the RPG gain structure and applications requiring tunable, single frequency radiation.

### Lasing Mode Spectra

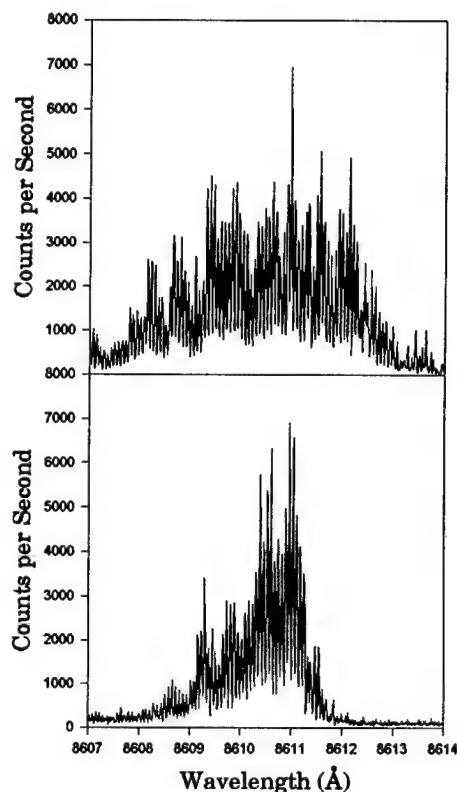


Fig. 4. External cavity lasing mode spectra. Top graph (a) shows the aperture fully open; bottom graph (b) shows the aperture open to 6000  $\mu\text{m}$ .

The authors would like to thank S. Sun and S. D. Hersee for growing the wafer used in these experiments.

1. D. L. McDaniel et. al., IEEE Photon. Tech. Lett., **2**, 156 (1990).
2. Fumio Koyama et. al., IEEE Jour. of Quant. Electron., **QE-27**, 1410 (1991)
3. Kent D. Choquette and D. A. Richie, Appl. Phys. Lett. **64**, 2062 (1994).
4. T. Mukaiyara et. al., IEEE Photon. Tech. Lett., **5**, 133 (1993).

## JITTER MEASUREMENTS IN GAIN SWITCHED DFB SEMICONDUCTOR LASERS COUPLED TO OPTICAL FIBERS

Adalberto Sapia and Jaume Dellunde \*

*Fondazione Ugo Bordonì - ISPT, via B. Castiglione, 59 I-00142 Rome, Italy.*

*Phone: (396) 5480 2222 Fax : (396) 5480 4402*

*\* Permanent address: Dept. d'Estructura i Constituents de la Matèria, Facultat de Física,  
Universitat de Barcelona, Diagonal 647, E-08028 Barcelona, Spain.*

*Phone: (343) 402 11 83 Fax: (343) 402 11 98*

Time jitter measurements in a repeatedly gain switched laser diode subject to a weak optical feedback are reported in this work. Reflections were induced by the tip of an optical fiber placed at a very short distance ( $10\text{ }\mu\text{m}$ ) from the output laser facet. The results point out the importance of controlling the reflections due to optical elements inside dense packaged devices.

Several works dealt with experimental and theoretical analysis of the transient dynamics of gain switched laser diodes both under repetitive gain switching [1-3] and periodic or pseudo-random word modulations [4]. The main results were related to the dependence of the statistical properties of the switching dynamics on the operating conditions such as bias current, data rate and modulation format. Two quantities have usually been analyzed: the mean turn-on time (MTOT), defined as the average time elapsed between the current switch-on and the achievement of a reference output intensity, and the time jitter (TJ), given as the standard deviation of the turn-on time probability distribution.

Only recently, studies of the feedback effect on the dynamical properties of current modulated semiconductor lasers have also been included [5,6]. Laser diodes subject to optical feedback exhibit, with respect to the unperturbed condition, a modification of their steady state characteristics, which depends both on the feedback level and the phase of the reinjected optical field [7]. The presence of feedback increases also the complexity of the dynamics involved in the switch-on process of laser diodes. In fact, in recent papers [6,8,9] large variations of both MTOT and TJ have been predicted when low or moderate feedback is added to the rate equations governing the laser dynamics during the turn-on process. The theoretical analysis developed in [8] for semiconductor lasers biased below threshold predicts a sinusoidal dependence of the MTOT on the reflector position and a TJ quite insensitive. Light fed back into the laser should accelerate the turn-on when it is in phase with the internal field, adding constructively to the seeding process after the carrier population has crossed its threshold value. Instability of the off state is described in terms of an effective threshold current. Nevertheless, no experimental evidence of such a behavior has been reported yet to the best of our knowledge.

### Experimental results

The laser diode used in this experiment was a  $\lambda/4$  shifted distributed feedback (DFB) laser emitting at  $1.3\text{ }\mu\text{m}$ , with a threshold current of 13.3 mA. The set-up employed is in Fig. 1. Pulses of 7 mA with a rise time of 80 ps, a duration of 1 ns and a repetition rate of 50 kHz

were superimposed to a variable bias current. The tip of a fiber was placed close to the output facet of the laser at an average distance of 10  $\mu\text{m}$ . Both tapered and untapered fibers have been employed in order to reproduce more accurately a feedback mechanism commonly encountered in fiber coupled devices. No coatings were used on the fiber tips and reflections from the far end of the fiber were carefully avoided. The chip-fiber distance was changed by tiny amounts by means of a piezoelectric element and the measurements have been performed at different and equally spaced fiber positions. MTOT and TJ have been measured using a PIN diode having a response time of 45 ps (FWHM) and a sampling oscilloscope with statistical analysis facilities.

Different bias currents have been explored: below, above and approximately at threshold. In all cases oscillations of the MTOT with the fiber position have been observed. The results shown in Fig. 2 refer to a bias current close to threshold and have been obtained using a fiber with a simple cut. The difference between the measured MTOT and the value assumed when no reflections are present is reported as a function of the chip-fiber distance. MTOT oscillates with a period corresponding to one half of the optical wavelength and the average amplitude is 25 ps. A relevant oscillation of TJ as large as 6 ps is also observed for bias close to threshold where, as shown in [10], its dependence on bias current is the strongest. When a bias current far from threshold is chosen, oscillations with slightly lower amplitudes remain both for MTOT and TJ. The results obtained when a tapered fiber has been used as a source of reflections are presented in Fig. 3 and show the same behavior, but with lower oscillation amplitudes of both MTOT and TJ.

## Conclusions

A fiber positioned at very short distances from the output facet of a DFB laser diode is shown to induce variations of both mean turn-on time and time jitter during gain switching. The measured values follow the phase of the reinjected field and their amplitudes are relevant even for very small feedback levels.

## REFERENCES

- [1] A. Mecozzi et al, *Optics Letters* **15** pp.1067-1069, 1990
- [2] S. Balle et al, *IEEE J. Quantum Electronics*, **QE-29**, pp.33-41, 1993
- [3] P. Spano et al, *IEEE J. Quantum Electronics*, **QE-25**, pp.1440-1449, 1989
- [4] C. R. Mirasso et al, *IEEE J. Quantum Electronics*, **QE-29**, pp.23-32, 1993
- [5] L. N. Langley and K. A. Shore, *IEEE J. Photonics Technology Letters* **4**, pp.1207-1209, 1992
- [6] L. N. Langley and K. A. Shore, *IEEE J. Lightwave Technology* **11**, pp.434-441, 1993
- [7] K. Petermann, *Laser Diode Modulation and Noise*, Kluwer Academic Publish., Dordrecht, 1988
- [8] E. Hernandez-Garcia et al, *IEEE J. Quantum Electronics*, **QE-30**, pp.241-248, 1994
- [9] C. R. Mirasso et al, *IEEE J. Quantum Electronics*, **QE-30**, pp.2281-2286, 1994
- [10] A. Mecozzi et al., *Appl. Phys. Lett.* **55**, pp.769-771, 1989

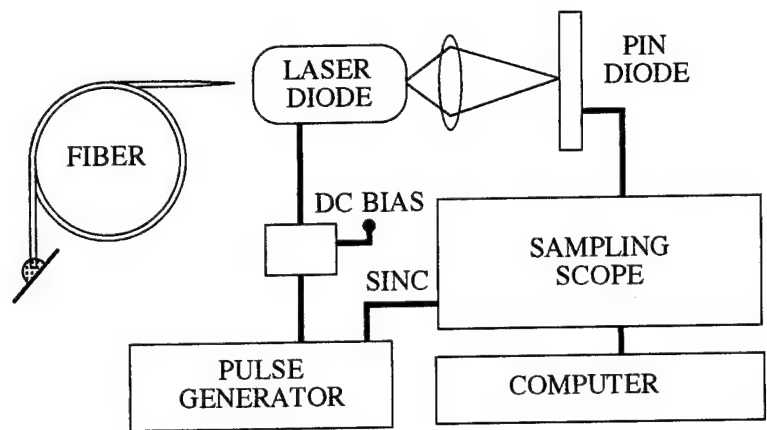


Fig. 1 Experimental set-up

Fig. 2 MTOT and TJ variations with respect to the solitary laser values at a bias current of 13.3 mA. The fiber has a simple cut.

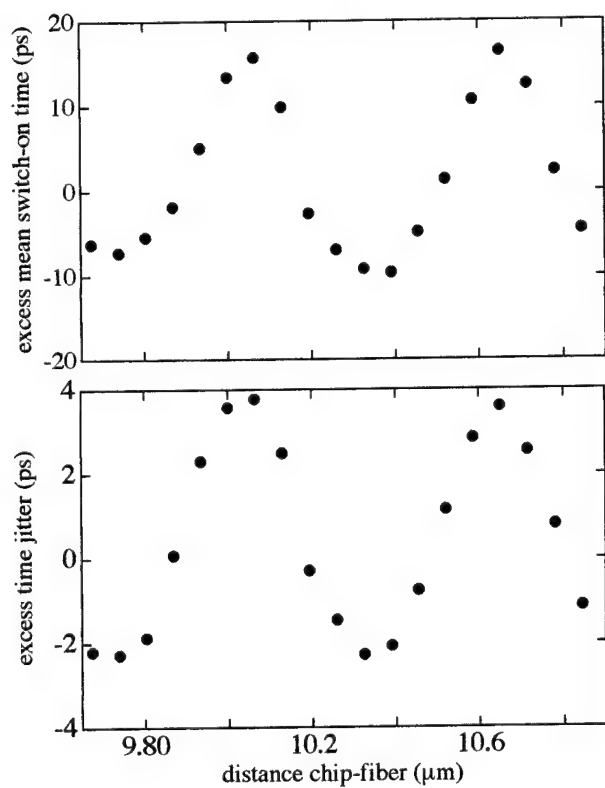
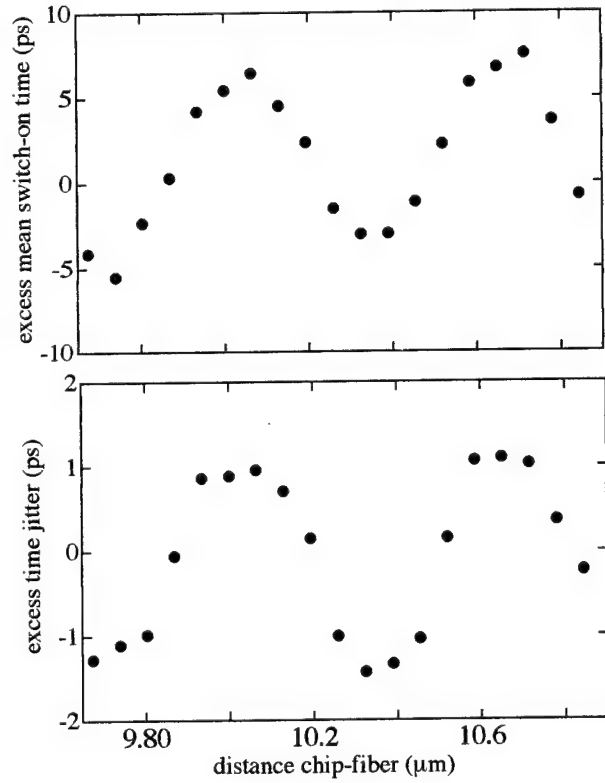


Fig. 3 MTOT and TJ variations with respect to the solitary laser values at a bias current of 13.1 mA. Measurements with the tapered fiber.



# Oscillation wavelength shift characteristics of a semiconductor laser in a magnetic field —Observation using a beat note—

Takashi Sato, Shin'ya Matsuda, Kazunori Shibata, Shigeki Yamamoto,  
Masashi Ohkawa, Takeo Maruyama, and Minoru Shimba\*

Faculty of Engineering, Niigata University  
8050 Ikarashi 2-no-cho, Niigata, 950-21 Japan  
Tel. +81-25-262-6723 Fax. +81-25-263-3174

\*Faculty of Engineering, Tokyo Denki University  
2-2 Kanda Nishikicho, Chiyoda-ku, Tokyo, 101 Japan  
Tel. +81-3-5280-3324 Fax. +81-3-5280-3324

## 1. Introduction

Since the development of the first semiconductor lasers, we know that the oscillation wavelength of a semiconductor laser depends on injection current, laser temperature and magnetic field. Among these factors, injection current and laser temperature are the principal means by which to control the wavelength of laser diodes, in many practical applications. The wavelength shift of laser diodes subjected to strong magnetic fields in low temperature was reported from a physical point of view in the early 60's[1]. Even after such work was further progressed, little time was spent actually testing semiconductor lasers in a magnetic field except for the spin-flip Raman[2] and quantum well[3] lasers.

We observed a red shift in a relatively weak magnetic field at room temperature, whereas the previous works reported a blue shift at low temperature. The theory based on the Landau level was used for explaining this blue shift, but our experimental conditions and results differ from the previous works. We have observed the wavelength shift through high-resolution observation systems, using the Rb absorption line[4] or a monochromator[5]. However, these methods cannot provide the transient result, which is important to know the shift mechanism. We, therefore, use a beat note to observe the transient frequency shift precisely and introduce a new shift mechanism in which a current-flow in a laser diode is important.

## 2. Wavelength shift in a magnetic field

Figure 1 shows the experimental setup used for observing a beat note in this work. The sample laser diode (LD1) was placed between the poles of an electromagnet. Standard laser diodes come with caps which protect against the influence of magnetic fields. This protective cap was cut away, so that the laser could be placed in the magnetic field. The laser beam from LD1 was coincided with the other laser beam from LD2 into an avalanche-photo diode to detect



the beat note. In order to control the operation, the variation of laser case temperature was maintained within 0.01K. The directional relation between the magnetic field and the laser diode was changed only by re-aiming the laser diode fixed in the magnetic field. Our previous experiments highlighted the importance of this directional relation, so the magnetic flux density vector  $B$  and the normal direction  $n$  of the layered surface of the laser diode were arranged parallel to each other ( $B//n$ ), as shown in Fig.2(a); or they were perpendicular ( $B \perp n$ ), as shown in Fig.2(b)[4],[5].

As the beat note expresses the difference between two laser frequencies, we can obtain the wavelength shift as this beat frequency shift  $\Delta f$  in a magnetic field. The frequency shift  $\Delta f$  vs. magnetic field  $B$  at a stationary condition is shown in Fig.3. This figure shows  $\Delta f$  is proportional to  $B^2$ . An example of the time dependence of  $\Delta f$  is shown in Fig.4. This figure also shows changes of coil current  $i$ ,  $B$  and  $B^2$ . The observed time delay between  $\Delta f$  and  $B^2$  was about 0.07s when the magnetic field was applied.

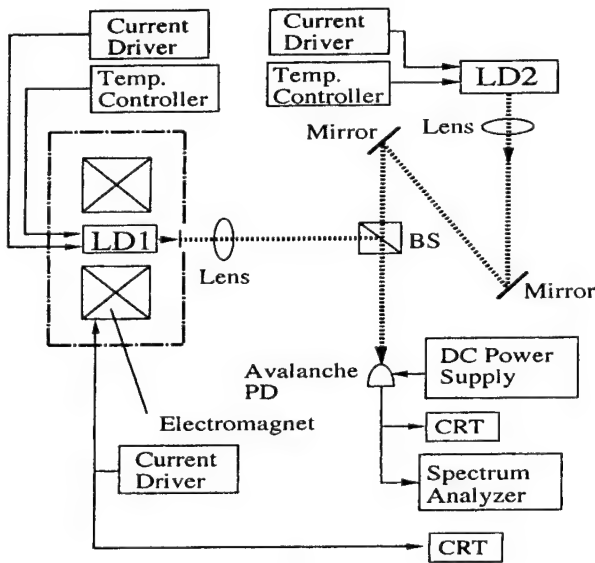
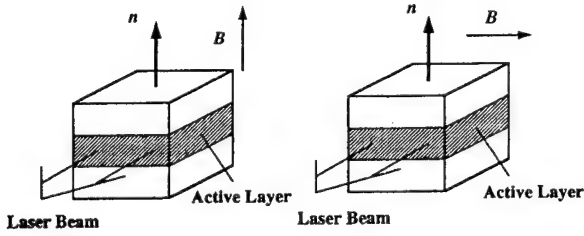


Fig. 1 Experimental setup.



(a)  $B//n$  (b)  $B \perp n$   
Fig. 2 Definition of magnetic field direction.

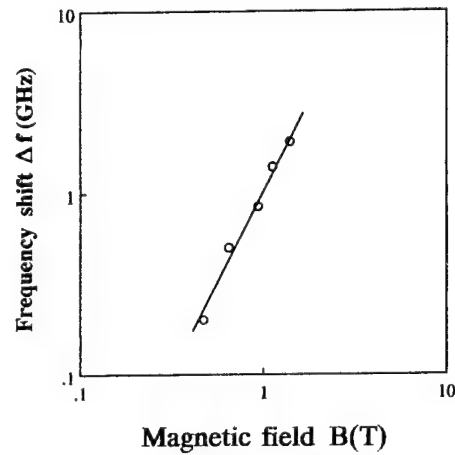


Fig. 3 Frequency shift vs. magnetic field characteristics.

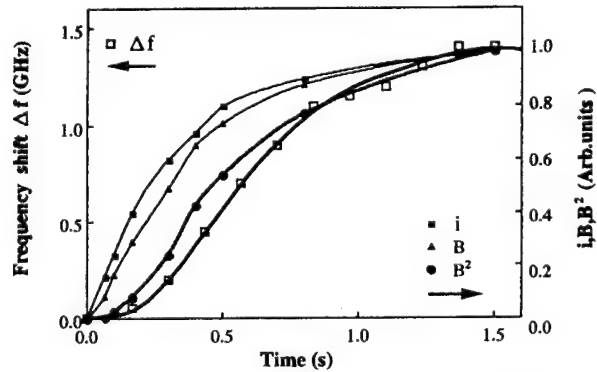


Fig. 4 Time dependences at  $B=1.12T$ .

### 3. Summary

The blue shift observed in high magnetic fields, at very low temperatures, is clearly understood in terms of the Landau level. However, the Landau level cannot be created, at room temperature, in weak magnetic fields, nor can we explain the red shift.

We have measured the frequency and threshold current shifts of laser diodes at room temperature, in relatively weak magnetic fields. The shifts have been observed in certain types of laser diodes oriented in the  $B//n$  direction. The observed frequency shift was proportional to  $B^2$  and its time delay was about 0.07s. The threshold current increased by 0.05 mA, at  $B=1.4T$ , in our previous work. When the direction of current  $i$  and magnetic field  $B$  are parallel, which is the case  $B//n$  in our sample laser diode (Inner stripe type), current diffusion is suppressed and current density and laser temperature increase. The current density increase usually causes a blue shift, while a temperature increase causes a red shift. Finally, and as a result, the red shift took place, which leads us to believe that the temperature increase effect is larger than that of any increase in current density.

The other conclusion arrived at, during the course of our study, also suggests that the temperature increased. The threshold current increased, when a magnetic field was applied  $B//n$ . This change in threshold current is usually observed, at higher temperatures. The threshold current increased at  $B=1.4T$  is corresponding to the temperature increase about 0.4K, whereas the wavelength shift is corresponding to about 0.08K.

We now believe that the current density increases in the neighborhood of the active region, as well as in the region itself. Temperatures in neighboring areas are also thought to rise, and are considered to be quite large, compared to the effect of the current density increase in the active region. Finally, the red shift occurs at  $B//n$  condition. The difference between calculated temperature increases corresponding to the shifts of the threshold current and wavelength is not clearly understood yet. However, we believe that the oscillation wavelength of certain types of laser diode is controllable by a magnetic field.

### References:

- [1] I. Melngailis, et al., Appl. Phys. Lett., 2, 11, pp.202 (1963).
- [2] A. Calawa, et al., Phys. Rev. Lett., 23, 1, pp.7 (1969).
- [3] Y. Arakawa, et al., Jpn. J. Appl. Phys., 22, 12, pp.L804 (1983).
- [4] T. Sato, et al., Electron. Lett., 22, 19, pp.979 (1986).
- [5] T. Sato, et al., QELS'89, WDD38 (1989).

## Asymmetric Cladding Ridge Waveguide Laser by Selective Area MOCVD

G.M. Smith, D.V. Forbes, R.M. Lammert, and J.J. Coleman

Microelectronics Laboratory  
University of Illinois  
208 N. Wright St.  
Urbana, IL 61801 USA  
(217) 333-2555  
(217) 244-7645 FAX

Stable fundamental mode operation of a semiconductor laser is a requirement for nearly all laser applications and the method to achieve that goal is usually an index guided laser. Two common index guided laser structures are the buried heterostructure (BH) and the ridge waveguide (RW). Both of these structures have been shown to have stable fundamental mode operation to several times threshold [1-3]. Generally, BH lasers have more stable operation but RW lasers are simpler to fabricate. RW lasers are commonly fabricated by etching trenches into the top cladding layer to within a few tenths of a micron of the active region, thus reducing the effective index of the mode in the etched region. The index step for the waveguide is a strong function of the etch depth and precise control of the etch mechanism is necessary to provide an adequate amount of waveguiding without introducing unnecessary loss by etching too deep.

We describe an asymmetric cladding ridge waveguide laser by selective area MOCVD designed to overcome the difficulty of etch depth control by eliminating etching altogether and using accurately controlled epitaxial growth to obtain the critical thickness control. Buried heterostructure lasers with very low thresholds have been demonstrated using three step selective area MOCVD [4,5]. The approach taken in the ridge waveguide fabrication is to use an asymmetric cladding structure with a thin upper cladding layer that utilizes the overlap of the mode with the surface metal to provide modal control [6]. Since this structure is very sensitive to changes in the surface material composition and thickness, it should be simple to change the mode structure using a thin regrown layer. Waveguide calculations can be performed using the layer thickness, composition, and doping to determine the effect of changing the

cap layer thickness on the optical mode [7]. If this layer is grown too thick and with low doping, a second waveguide will be formed between the top cladding layer and the metal resulting in poor overlap of the optical mode with the active region. However, by keeping the layer thin and highly doped (lossy) as a contact layer usually is, the optical mode in the active region is only slightly perturbed and the effective index change can be as large as 0.01. Unfortunately, the modal loss of the waveguide is strongly dependent on the thickness of the index increasing layer. As the layer thickness increases so does the modal loss since the optical mode is being pulled toward the lossier (more highly doped) layers. Hence, the index increasing layer thickness must be carefully chosen to provide an adequate index step for the ridge waveguide while resulting in only a small increase in the modal loss.

In this paper, two step selective area MOCVD grown asymmetric cladding ridge waveguide lasers are reported. An InGaAs-GaAs-AlGaAs separate confinement heterostructure is utilized with an initial MOCVD growth of the lower cladding, active region, and upper cladding. A silicon dioxide mask is deposited and patterned with twin stripes to define the selective growth, as has been previously reported [4,5]. A thin GaAs cap layer is then grown by selective area MOCVD to act as the contact layer as well as an index increasing layer for the ridge waveguide. A RW laser fabricated by this method with a ridge width of 3  $\mu\text{m}$  and cavity length of 425  $\mu\text{m}$  has a threshold current of 12.6 mA, slope of 0.26 W/A, and operates in a stable fundamental mode to 20 times threshold.

A cross-sectional schematic of a ridge laser by selective area MOCVD growth is shown in Fig. 1. The initial MOCVD growth of the

asymmetric separate confinement heterostructure consists of a  $1.0\text{ }\mu\text{m}$   $\text{Al}_{0.6}\text{Ga}_{0.4}\text{As}$  lower cladding layer ( $n = 10^{18}\text{ cm}^{-3}$ ), symmetric  $600\text{ }\text{\AA}$  GaAs barrier layers (undoped) around a  $75\text{ }\text{\AA}$   $\text{In}_{0.21}\text{Ga}_{0.79}\text{As}$  quantum well, a  $0.3\text{ }\mu\text{m}$   $\text{Al}_{0.6}\text{Ga}_{0.4}\text{As}$  upper cladding layer ( $p = 10^{18}\text{ cm}^{-3}$ ), and a  $100\text{ }\text{\AA}$  GaAs cap ( $p = 10^{18}\text{ cm}^{-3}$ ). The growth was then interrupted and a  $1200\text{ }\text{\AA}$  silicon dioxide mask was deposited and patterned to define twin  $20\text{ }\mu\text{m}$  wide stripes separated by  $3\text{ }\mu\text{m}$ . The sample was then returned to the MOCVD system to grow a nominally  $750\text{ }\text{\AA}$  thick GaAs contact and index increasing layer ( $p = 10^{19}\text{ cm}^{-3}$ ). The growth rate enhancement due to the oxide pattern on the substrate increases the layer thickness of the ridge by a factor of two [4], resulting in a GaAs layer thickness of  $0.15\text{ }\mu\text{m}$ . These layer thicknesses, compositions, and dopings can be used to calculate the effective index step for the ridge waveguide after Casey and Panish [7]. For this structure the calculated effective index step is  $9.5 \times 10^{-3}$ , adequate for index guided operation for a  $3\text{ }\mu\text{m}$  wide ridge. After growth, a second silicon dioxide layer is deposited and patterned to open electrical contact windows just over the ridge. The sample was thinned to  $100\text{ }\mu\text{m}$ , Ge/Au n-metals evaporated and alloyed, and a Au p-metal evaporated [6].

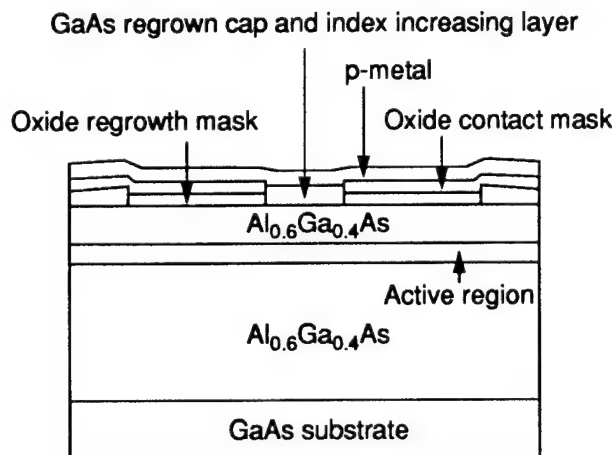


Fig. 1. Cross-sectional schematic of an asymmetric cladding ridge waveguide laser by selective area MOCVD.

Fig. 2 shows the cw performance of a typical uncoated ridge laser with a width of  $3\text{ }\mu\text{m}$  and cavity length of  $425\text{ }\mu\text{m}$ . This device has a threshold current of  $12.6\text{ mA}$ , slope of

$0.26\text{ W/A}$ , and peak emission of  $1008\text{ nm}$ . The slope of the output power versus current curve begins to decrease above  $75\text{ mA}$  due to heating effects in the laser. The slope efficiency of these lasers is slightly lower than that of typical ridge waveguide lasers since the index increasing layer also increases the modal loss of the waveguide. With further optimization of the thickness of the index increasing layer, the modal loss can be decreased yielding increased slope efficiency for the lasers.

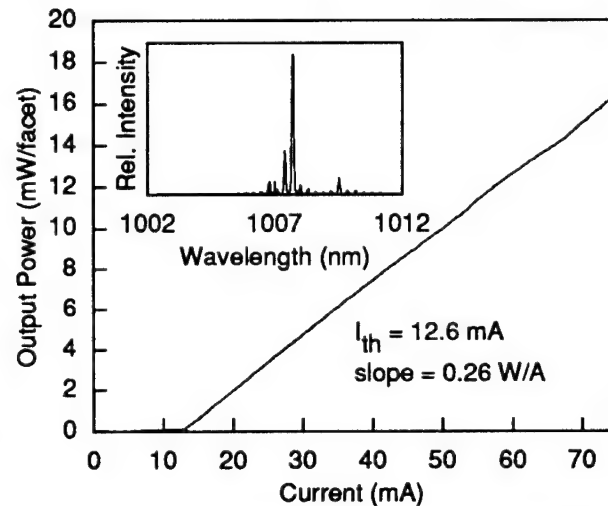


Fig. 2. CW output power versus current and emission spectra at 20% over threshold for a  $3\text{ }\mu\text{m} \times 425\text{ }\mu\text{m}$  uncoated ridge waveguide laser.

To demonstrate the performance of these lasers at higher currents, pulsed measurements ( $2\text{ }\mu\text{sec}$  pulses,  $0.1\%$  duty cycle) were performed up to  $250\text{ mA}$  where thermal roll-over again limited operation. These results are shown in Fig. 3 for the same device as Fig. 2 as well as a typical HR coated device. The HR coating is a three pair quarter-wave dielectric stack of  $\text{Al}_2\text{O}_3$  and silicon applied to one facet increasing its reflectivity to  $95\%$ . The HR coating on a device with cavity length of  $250\text{ }\mu\text{m}$  provides single-ended output from the uncoated facet of nearly  $100\text{ mW}$  at  $250\text{ mA}$  with a threshold current of  $8.9\text{ mA}$  and slope of  $0.42\text{ W/A}$ .

To confirm that the index step for the ridge waveguide is adequate, near-field measurements were performed on the uncoated device of Figs. 2 and 3. The near-field at  $20\text{ mA}$ ,  $100\text{ mA}$ , and  $250\text{ mA}$  corresponding to  $1.6$ ,  $8$ , and  $20$  times threshold are shown in Fig. 4. The laser operates in a fundamental

lateral mode throughout this entire range with a full width at half maximum (FWHM) of  $2.4\ \mu\text{m}$ . This demonstrates that the index step of  $9.5 \times 10^{-3}$  is adequate for very good confinement of the field under the ridge and excellent ridge waveguide laser stability. Transverse far-field measurements were performed to determine if the index increasing layer effects the transverse mode of the laser. The far-field is single lobe and gaussian-like with a FWHM of  $29^\circ$ , typical of a SCH structure of this sort, indicating that the index increasing layer has no noticeable negative effect on the modal emission properties of the laser.

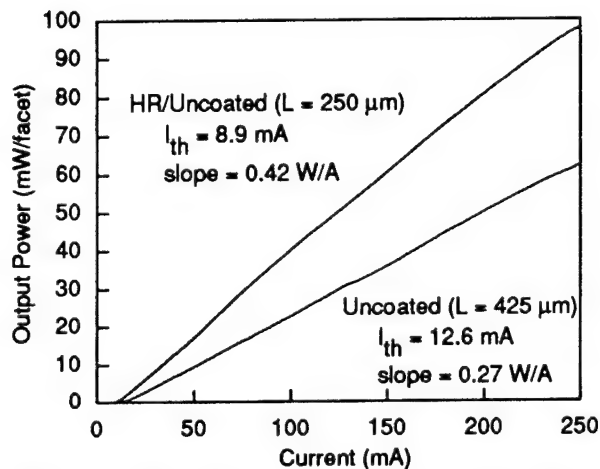


Fig. 3. Pulsed output power versus current for an uncoated device and a device with one facet HR coated.

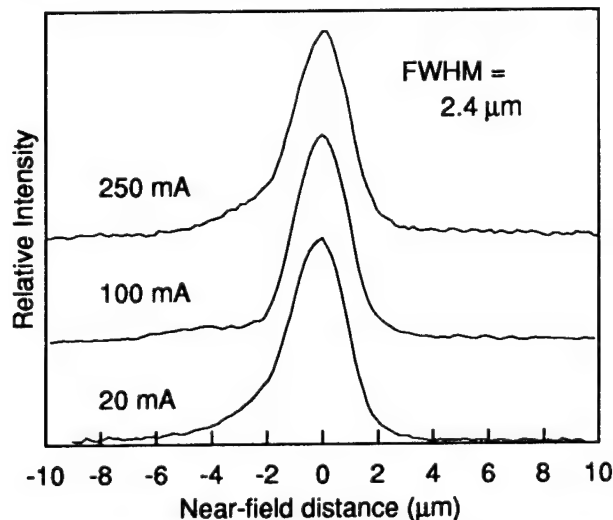


Fig. 4. Lateral near-field intensity profile of an uncoated ridge waveguide laser at 1.6, 8, and 20 times threshold showing a stable fundamental mode with a FWHM of  $2.4\ \mu\text{m}$  over the entire range.

In conclusion, asymmetric cladding ridge waveguide lasers by selective area MOCVD utilize the overlap of the tail of the optical field with the regrown cap layer to increase the refractive index underneath the ridge providing a calculated index step of  $9.5 \times 10^{-3}$  for the reported devices. Uncoated ridge lasers have a threshold current of 12.6 mA and slope of 0.26 W/A for a  $3 \times 425\ \mu\text{m}$  device. An HR/uncoated ridge laser has a single-ended output power of 100 mW at 250 mA, a threshold current of 8.9 mA, and a slope of 0.42 W/A for a  $3 \times 250\ \mu\text{m}$  device. These devices operate in a fundamental transverse mode and stable fundamental lateral mode to 20 times threshold. Further optimization of the thickness of the index increasing layer should result in increased slope efficiency and lower threshold lasers.

- [1] P.K. York, K.J. Beernink, G.E. Fernandez, and J.J. Coleman, "InGaAs-GaAs strained-layer quantum well buried heterostructure lasers ( $\lambda > 1\ \mu\text{m}$ ) by metalorganic chemical vapor deposition," *Appl. Phys. Lett.*, vol. 54, pp. 499-501, 1988.
- [2] S.E. Fischer, D. Fekete, F.B. Feak, and J.M. Ballantyne, "Ridge waveguide laser with a GaInAs strained-layer quantum well ( $\lambda = 1\ \mu\text{m}$ )," *Appl. Phys. Lett.*, vol. 50, pp. 714-716, 1987.
- [3] D.P. Bour, N.A. Dinkel, D.B. Gilbert, K.B. Fabian, and M.G. Harvey, "980 nm diode laser for pumping  $\text{Er}^{3+}$ -doped fiber amplifiers," *IEEE Photon. Technol. Lett.*, vol. 2, pp. 153-155, 1990.
- [4] T.M. Cockerill, D.V. Forbes, J.A. Dantzig, and J.J. Coleman, "Strained-layer InGaAs-GaAs-AlGaAs buried-heterostructure quantum-well lasers by three-step selective-area MOCVD," *IEEE J. Quantum Electron.*, vol. 30, pp. 441-445, 1994.
- [5] R.M. Lammert, T.M. Cockerill, D.V. Forbes, G.M. Smith, and J.J. Coleman, "Submilliampere threshold buried-heterostructure InGaAs/GaAs single quantum well lasers grown by selective-area epitaxy," *IEEE Photon. Technol. Lett.*, vol. 6, pp. 1073-1075, 1994.
- [6] C.H. Wu, P.S. Zory, and M.A. Emanuel, "Contact reflectivity effects on thin p-clad InGaAs single quantum well lasers," *IEEE Photon. Technol. Lett.*, vol. 6, pp. 1427-1429, 1994.
- [7] H.C. Casey, Jr. and M.B. Panish, *Heterostructure Lasers, Part A: Fundamental Principles*. New York: Academic, 1978.

# Analysis of Segmented Tapered Rib-Waveguide Semiconductor Optical Amplifiers.

P.S.Spencer, I.Middlemast, R.Balasubramanyam, J.Sarma, and K.A.Shore  
University of Bath, School of Electronic and Electrical Engineering,  
Bath, UK. BA2 7AY.

Tel. + 44 1255 826826, Fax. + 44 1255 826305.

## 1 Introduction

A single stripe semiconductor laser typically produces about 10mW of output power. This figure can be increased to about 50-60 mW by using some complicated fabrications techniques, but the goal of achieving higher powers and maintaining single mode operation has proved elusive. When the drive current to a single stripe laser is increased two effects may occur to limit the output power: the inversion population starts to saturate, and Catastrophic Optical Damage, (COD), starts to destroy the facets. Several approaches to these problems have been tried, eg., increased active area, and laser arrays, and have generally been found to be unsatisfactory. Increasing the active area does indeed result in increased output power but at the expense of the far-field pattern; and, unfortunately, increasing the active area generally leads to multi-mode operation, and hence a poor far-field.

Tapered waveguide devices have been proposed as a means of maintaining single mode operation and increasing the active area of the device, [1,2]. In order to maintain single mode operation the flare should be adiabatic, i.e divergence typically of  $2 - 3^\circ$ .

A theoretical model to analyse tapered waveguide devices is outlined in the next section, and results for the case of a segmented tapered rib-waveguide optical amplifier structure are presented. In general each segment is driven by a different current density, figure(1).

## 2 Theoretical Model

A step transition Effective Index Method, [3], has been used to analyse tapered, index guided, semiconductor optical devices. In this approach the tapered index profile is approximated by a series of small rectangular sections, figure(1), and within each small section the material parameters are assumed to be constant. The tapered waveguide can then be modelled as a cascade of parallel rib-waveguides of varying width.

The propagation characteristics of the device can be determined by calculating the degree of coupling between the normal modes of adjacent consecutive sections, [4]. In the present analysis the taper angle has been assumed to be sufficiently small that coupling to radiation modes and reflections at each boundary can be neglected. The normal modes are found by using the thin-film transfer matrix formulation, [3]. The refractive index profile used in the analysis includes the effects of the geometrical parameters, (the distribution of the "in-built" refractive index of the different semiconductor alloys), and the dependence of the refractive index on the carrier density. When the modal profiles have been found the transmission coefficients at the interface between two sections can be calculated.

The carrier profile of each longitudinal section has been determined by solving the time independent diffusion equation, [5]. The distribution of the carriers and optical field are not



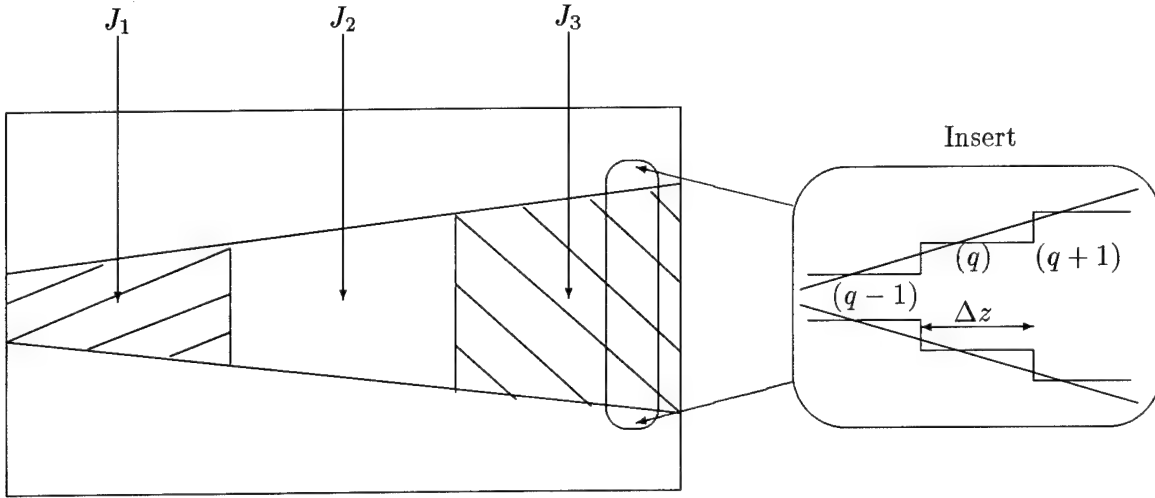


Figure 1: Segmented tapered optical amplifier. In general the current densities  $J_1$ ,  $J_2$ , and  $J_3$  are different. Insert shows sections used to approximate the taper waveguide.

independent of each other, and in this analysis they have been solved in a self-consistent manner by using the Piecewise Constant Inversion Population model, [6].

Within each longitudinal section ( $q$ ), the carrier profile has been assumed to be  $z$  independent. The amplitude of each mode will therefore either grow or decay exponentially; amplified spontaneous is assumed to be negligible.

### 3 Results

The rib widths of the narrow and wide ends of the amplifier to be considered are  $2\mu m$  and  $70\mu m$ , respectively. The effect of current segmentation on the optical power distribution within a  $960\mu m$  long tapered device, segmented into three equal sections, is shown in figure(2). By increasing the current density in the narrow end and decreasing the current density in the wider end the same output power can be obtained for less total current than that needed for case(a) - an unsegmented device. It can be seen from figure(2) that even when the current density of the first section is doubled, the amplification of the 860nm optical beam is still low in this region; virtually all the amplification occurs in the last two sections. Indeed, it is evident from figure(3) that the first segment of the device is actually attenuating the incident beam; the photon density at the end of first segment is lower than the input value for all but case(d). The effect of inversion population on the refractive index has been ignored in these calculation, but will also be described, as will the influence of other current segmentation geometries.

### 4 Conclusion

A model for analysing semiconductor tapered devices has been outlined and applied to the case of a three segment tapered amplifier. The results obtained indicate that due to the diffusion induced reduction in the carrier density the first segment actually attenuated the incident optical beam. It has also been shown that to obtain the same overall amplification less total current was needed in the segmented case than in the unsegmented case. This was achieved by increasing the current density in the narrow end and decreasing the current density in the last two sections.

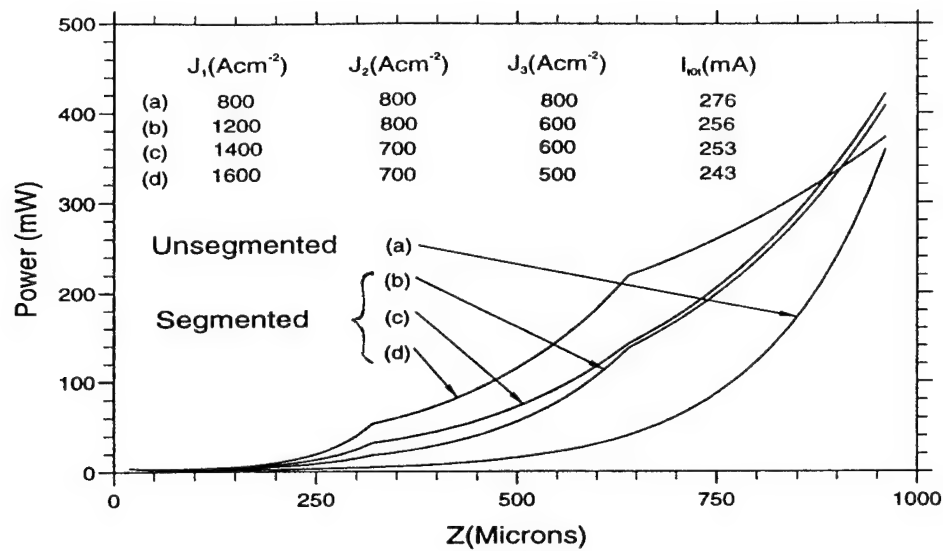


Figure 2: Variation of the optical power along the length of a three segment amplifier.

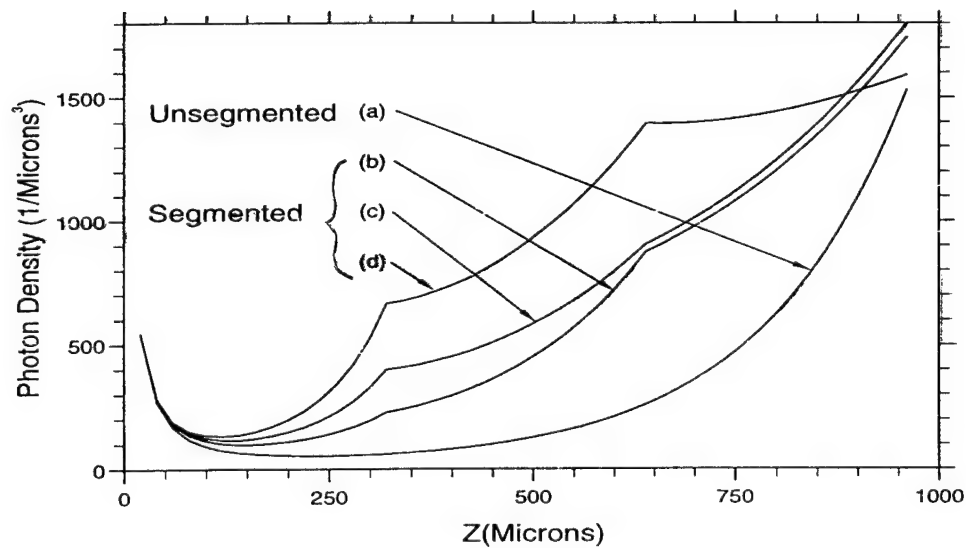


Figure 3: As above but showing photon density variation along the device.

## 5 References

- [1] K.A.Williams *et al*, Electron. Lett, **30**, 330, (1994).
- [2] R.J.Lang *et al*, IEEE J. Quant. Electron., **QE-29**, 2044, (1993).
- [3] M.Born, and E.Wolf, "Principles Of Optics (6<sup>th</sup> Ed.)," Pergamon:London,(1986).
- [4] S.F.Mahmoud, "Electromagnetic Waveguides: Theory and Application," Peregrinus:London,(1991).
- [5] G.P.Agrawal & N.K.Dutta, "Long wavelength semiconductor lasers, " VNR:New York, (1986)
- [6] I. Middlemast *et al*, IEE Proc-J, **138**, 301, (1991).



## Quantum Interference Effect and Electric Field Domains in Multiple Quantum Well Structures

Yuanjian Xu, Ali Shakouri, and Amnon Yariv

*Department of Applied Physics 128-95*

*California Institute of Technology*

*Pasadena, CA 91125*

Tel.: (818) 395-4413, Fax: (818) 405-0928

There has been great interest in studying optical and transport properties of multiple quantum well (MQW) structures. In these "artificial molecules", energy quantization and the wave nature of the carriers have been used to design new devices, e.g., intersubband lasers. The understanding of carrier transport in MQWs is important for the design of lasers with high modulation speed. In this talk, we report on a new observation of a quantum interference effect in the photocurrent spectrum of weakly coupled bound-to-continuum MQWs. Using this effect, we analyze the electric field domain (EFD) formation in the superlattice [1].

The absorption spectrum of a quantum well (QW) structure with parameters allowing only one state in the well (i.e. bound-to-continuum QW) is not Lorentzian. Because the continuum states above the barriers are extended over the barriers and several neighboring wells, an electron interference effect can be observed in the absorption spectrum. At zero external bias, due to the potential translation symmetry there are well known minibands in the continuum states of the superlattice which can be calculated using Kronig-Penney model, for example. The miniband energy gaps can be designed large enough to be observable in the absorption spectrum. However, under an applied bias, such that the voltage drop per period is bigger than these energy gaps, the miniband structure is destroyed. Features in the photocurrent spectrum which are due to electron interference effects over one or two periods of the superlattice (40 to 50nm) were observed for MQWs even under large biases.

The sample investigated for this study was grown by MBE on a (100) semi-insulating GaAs substrate (sample 1510). It consists of 50 periods of 4nm GaAs wells, uniformly doped with Si to  $n = 2 \times 10^{18} \text{cm}^{-3}$ , separated by 20nm  $\text{Al}_{0.22}\text{Ga}_{0.78}\text{As}$  barriers. Due to the well-known intersubband transition selection rule, the absorption measurement was performed in  $45^\circ$  multipass geometry. The experimental absorption spectrum at 79K (limited by experimental setup) is shown in the inset of Fig.1. The theoretical fit was calculated by solving Schrodinger's and Poisson's equations in the envelope function approximation. The effect of exchange-correlation was included through the one-particle exchange-correlation potential [2]. Non-parabolicity has been taken into account.

The experimental photocurrent spectrum as shown in Fig.1 shows the same experimental three-peak positions (at ~155, 187, and 220meV) for all biases between -0.2 and -4.3V. As the position of these peaks is a strong function of the applied bias, this invariance is explained through the formation of EFDs in the MQW region [3]. It should be noticed that the calculated electric field (~31kV/cm) for which the theoretical results match the experimental results does not correspond to an alignment between the ground state of one well with its neighboring well's resonant state. It is a little less than half of the alignment value. This seems to imply that the ground state of one well is aligned with the first resonance state of the second nearest neighbor. The formation of EFDs was further proved from the oscillatory behavior in the I-V characteristics, shown in Fig.2. The very irregular period of these oscillations ( $75 \pm 40\text{mV}$ ) might originate from the broad nature of

bound-to-continuum transitions. But the mean value of these oscillations is close to half of the voltage separation between the ground state and the first resonance state.

Our result was further substantiated on a different sample (sample 1511) with the same well width and barrier height but 40nm barrier width, shown in Fig.3. In this sample with very thick barriers, there is not enough coupling between wells to cause EFD formation. As expected, the peak positions in the photocurrent spectra move with the applied bias. The theoretical simulations predict these peak positions very well as shown for two biases in Fig.3.

In conclusion, we present a new observation of the quantum interference effect in the photocurrent spectrum which causes peaks in the later. We estimate the coherence length of the excited electrons and analyzed the sequential resonant tunneling induced EFD formation by comparing the theoretical calculation with the experimental results. A large energy level misalignment between two neighboring wells in the HFD was observed.

## References:

- [1] Y. J. Xu, A. Shakouri, A. Yariv, accepted for publication on Appl. Phys. Lett.
- [2] W. L. Bloss, J. Appl. Phys. **66**, 3639 (1989).
- [3] R. F. Kazarinov and R. A. Suris, Fiz. Tekh. Poluprovodn. **6**, 148 (1972) [Sov. Phys. Semicond. **6**, 120 (1972)]; L. Esaki and L. L. Chang, Phys. Rev. Lett. **33**, 495 (1974); F. Capasso, K. Mohammed, and A. Y. Cho, Appl. Phys. Lett. **48**, 478 (1986); K. K. Choi, B. F. Levine, R. J. Malik, J. Walker, and C. G. Bethea, Phys. Rev. B **35**, 4172 (1987).

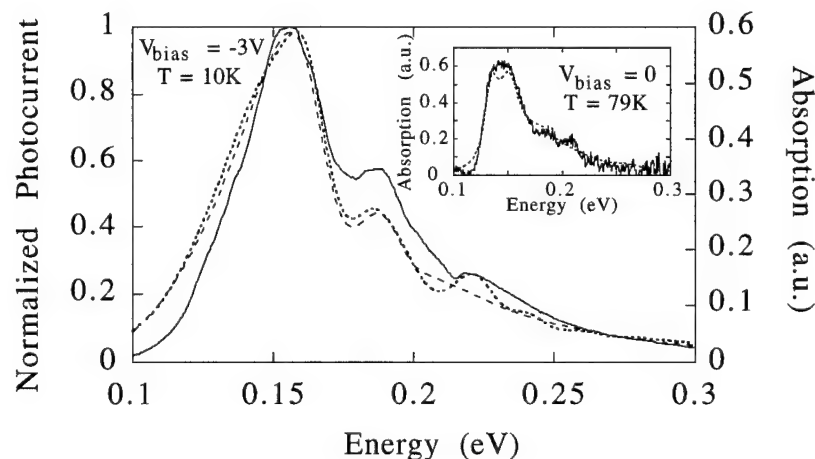


**Fig.1** The experimental photocurrent spectrum at  $V_{\text{bias}} = -3\text{V}$  (solid line) and theoretical absorption spectra (dashed line is for electrons which remain coherent over one period of the superlattice and dotted line is for two periods) of sample 1510 at  $T = 10\text{K}$ . It can be seen that the observed features are more consistent with electrons being coherent over two periods ( $\sim 40\text{nm}$ ). The inset is the experimental absorption spectrum at zero bias at  $T = 79\text{K}$  (solid line) and the calculated absorption spectrum (dotted line).

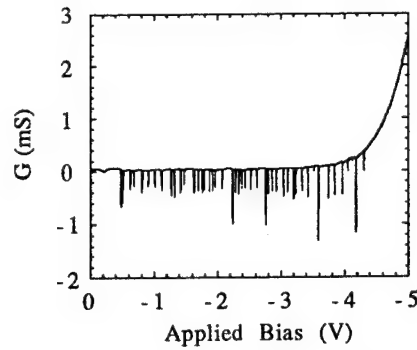


**Fig.2** The differential conductance vs. applied voltage at  $T = 10\text{K}$  in the dark. The number of negative differential oscillations (NDOs) for different devices processed out of the same wafer is between 45 to 49. A second sample with exactly the same quantum well parameters as sample 1510 but with half of the number of periods shows 23 to 24 NDOs.

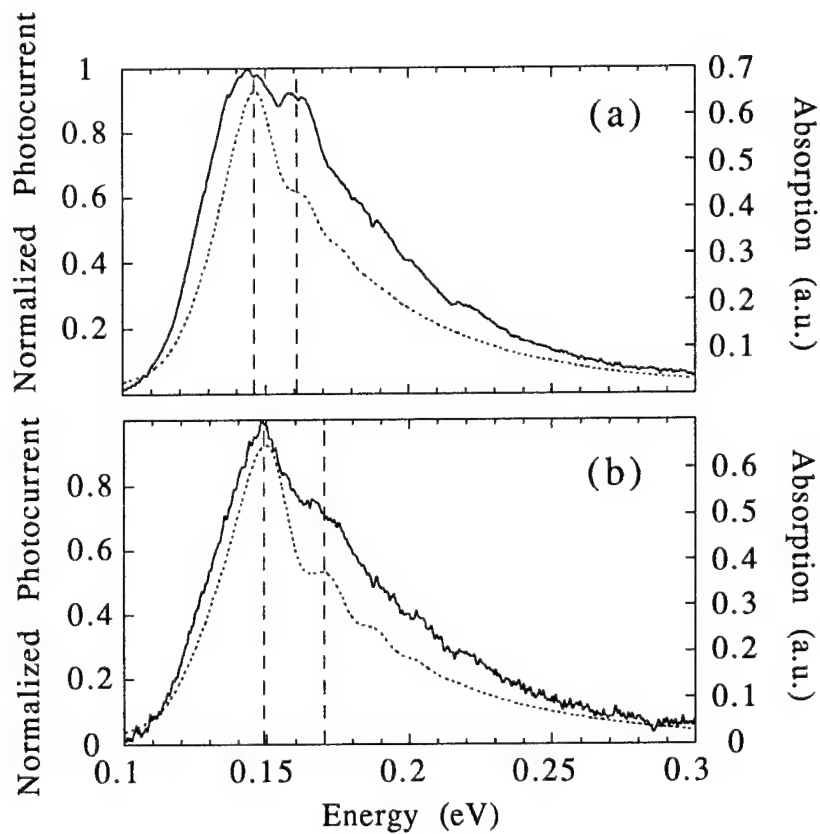


**Fig.3** The experimental photocurrent spectra (solid line) and theoretical absorption spectra (dotted line) at different biases of sample 1511 at  $T = 10\text{K}$ . (a)  $V_{\text{bias}} = -2.7\text{V}$ ; (b)  $V_{\text{bias}} = -3.8\text{V}$ .

## Lasing characteristics of pillar-type microcavity lasers

H. Yoshida, T. Tezuka, and S. Nunoue

Toshiba R&D Center

1, Komukai Toshiba-cho, Saiwai-ku, Kawasaki 210, Japan

TEL +81(44)549-2141, FAX +81(44)520-1286

Recently, spontaneous emission enhancement in pillar-type microcavities was reported for the first time by the authors.<sup>1)</sup> This type of cavity structure is relatively easy to fabricate and is suited to large scale integration of surface emitting laser arrays.<sup>2)</sup> It has been predicted that microcavity lasers, whose cavity size is of the order of one or a few times of the emission wavelength, have the potential for realizing ultralow thresholds ( $<1\mu\text{A}$ ) and ultrafast modulation ( $>20\text{GHz}$ ).<sup>3,4)</sup> Ultimately, low threshold lasers imply, to some extent, smaller lasers. To realize such lasers, reduction of losses of carriers and photons due to surface recombination and scattering of light in the cavity structures are very important points. In this paper we show lasing characteristics of micron size cavities up to  $2.5\mu\text{m}$  in diameter. We also show experimental studies of the cavity size dependence of lasing characteristics and microscopic reflection spectra of pillar-type microcavity lasers and discuss their relation to surface recombination and optical losses due to the scattering of light on the sidewalls.

The vertical structure of the sample was grown by metalorganic chemical vapor deposition (MOCVD) on an undoped GaAs substrate, consisting of an undoped one wavelength thick GaAs spacer layer with three 10nm-thick  $\text{In}_{0.15}\text{Ga}_{0.85}\text{As}$  quantum wells as well as DBRs.



Fig. 1. SEM image of pillar-type microcavities fabricated by ECR-RIBE.

The upper and lower DBRs consist of AlAs/GaAs quarter-wave stacks. A silicon dioxide ( $\text{SiO}_2$ ) layer was deposited on the upper DBR, then a circular  $\text{SiO}_2$  mask array was obtained by standard photolithography and wet etching. The diameters of the masks ranged from  $1\mu\text{m}$  to  $10\mu\text{m}$ . Pillar-type microcavities were fabricated by equirate etching of GaAs and AlAs by using electron cyclotron resonance-reactive ion beam etching (ECR-RIBE) as shown in Fig. 1.<sup>5)</sup> The samples without quantum well active layers were also prepared for the microscopic reflection spectra measurements.

Time-resolved photoluminescence (PL) experiments with picosecond laser pulse excitation were performed for the samples to observe lasing characteristics and to estimate the surface recombination velocity. At the lasing threshold, a sharp drop in the PL lifetime (Fig. 2) and a sharp increase in time integrated PL intensity (Fig. 3), were observed. For nominally fabricated samples, lasing characteristics were observed for cavities up to  $2.5\mu\text{m}$  in diameter at 77K. The values of surface recombination velocity deduced from the diameter dependence of the PL lifetime at 77K were about  $0.3\text{--}1 \times 10^6$  cm/s. These values, though resulting in considerable increase in lasing threshold in the

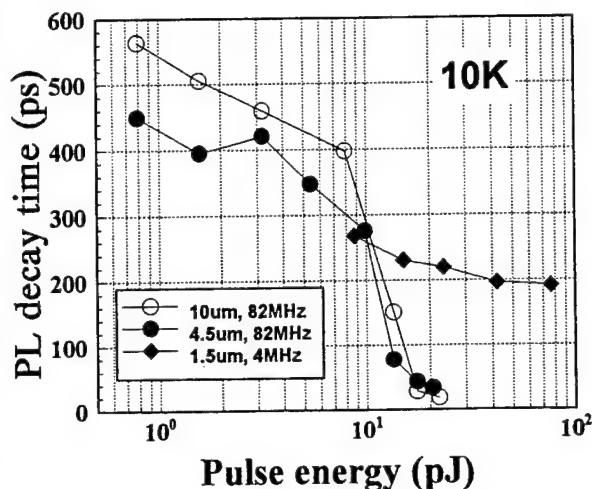


Fig. 2. PL decay time dependence on excitation laser pulse energy.

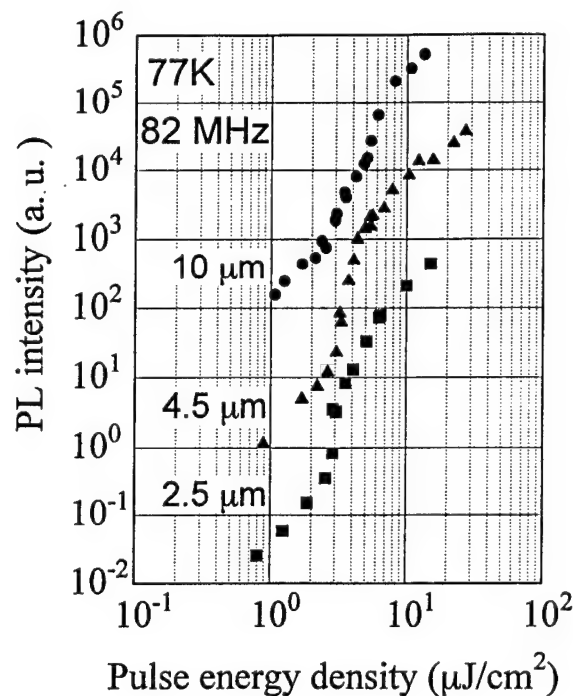


Fig. 3. PL intensity dependence on excitation laser pulse energy.

case of CW laser excitation, could not explain the difficulty in lasing for diameters less than  $2\mu\text{m}$  with short pulse excitation where the generation rate was far greater than the surface recombination rate.

The microscopic reflection spectra from single cavities were also measured to estimate the scattering loss in the cavities (Fig. 4). The

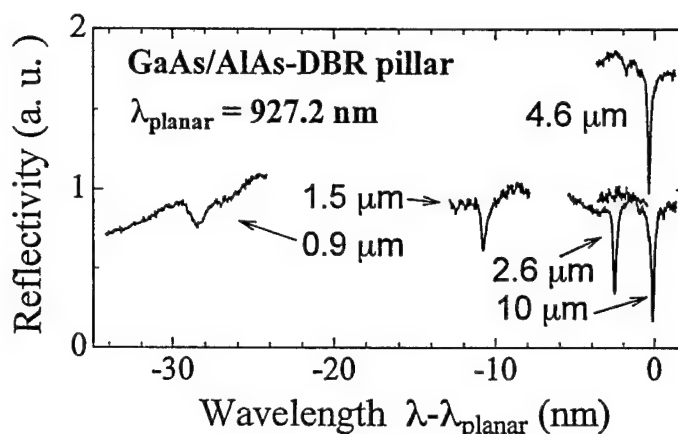


Fig. 4. Microscopic reflection spectra from single microcavities.

increase of the resonance width in smaller cavities, which originated from scattering on the rough surface of the sidewalls, was clearly observed. The Q-value estimated from these data showed a considerable decrease for diameters less than  $2\mu\text{m}$ , which explains the difficulty in lasing.<sup>6)</sup>

In conclusion, lasing of micron size pillar-type microcavities, which were fabricated by equirrate etching of GaAs and AlAs up to  $2.5\mu\text{m}$  in diameter was realized. For diameters less than  $2\mu\text{m}$ , reduction in not only surface recombination but also optical scattering loss were shown to be very important to realize lasing.

## References

- 1) T. Tezuka, S. Nunoue, H. Yoshida and T. Noda: Jpn. J. Appl. Phys. 32 (1993) L54.
- 2) Y. H. Lee, J. L. Jewell, A. Scherer, S. L. McCall, J. P. Harbison and L. T. Florez. Electron. Lett. 25 (1989) 1377.
- 3) Y. Yamamoto, S. Machida and G. Bjork: Phys. Rev. A 44 (1991) 657.
- 4) H. Yokoyama and S. D. Brorson: J. Appl. Phys. 66 (1989) 4801.
- 5) S. Nunoue and T. Tezuka: J. Vac. Sci. Technol. (to be submitted).
- 6) T. Tezuka and S. Nunoue: J. Appl. Phys. (to be submitted).



Wednesday, August 23, 1995

## Telecommunications Lasers

**WA** 9:00 am-11:00 am  
Torreys Peak I-III

P. Daniel Dapkus, *Presider*  
*University of Southern California*



## Market Requirements on Semiconductor Lasers for Telecommunications

N.A. Olsson, R.L. Hartman, and D.P. Wilt

AT&T Bell Laboratories  
Breinigsville, PA 18031

We review the key market and technological requirements on semiconductor lasers for commercial applications in telecommunications. We will cover high volume applications for access systems as well as high-reliability and high-performance requirements.

## High Temperature Uncooled Lasers

C. E. Zah, R. Bhat, and T. P. Lee

Bellcore, NVC 3Z385, 331 Newman Springs Rd., Red Bank, NJ07701, USA

Tel: (908) 758-3290, Fax: (908) 758-4372, e-mail: cez@nyquist.bellcore.com

**Introduction:** An uncooled laser transmitter is cheaper and more reliable than a thermo-electrically cooled laser transmitter because of its simplicity in packaging. A low-cost, highly-reliable uncooled laser may have a strong influence on pushing fiber deployment closer to the home. For loop applications, the laser transmitter must operate reliably over the temperature range from  $-40$  to  $85^{\circ}\text{C}$  [1]. It is rather difficult to make high performance uncooled lasers in the long wavelength region ( $1.3$ - $1.55\ \mu\text{m}$ ) using the conventional  $\text{Ga}_x\text{In}_{1-x}\text{As}_y\text{P}_{1-y}/\text{InP}$  materials system because the laser temperature performance suffers from Auger recombination in the low bandgap material and poor electron confinement resulting from the small conduction band offset ( $\Delta E_c = 0.4\Delta E_g$ ). We will discuss the design of uncooled lasers to minimize the changes in both threshold current and slope efficiency over the temperature range from  $-40$  to  $85^{\circ}\text{C}$  [2]. To prevent carrier overflow under high-temperature operation, the electron confinement energy is increased by using the  $\text{Al}_x\text{Ga}_y\text{In}_{1-x-y}\text{As}/\text{InP}$  materials system [2] instead of the conventional  $\text{Ga}_x\text{In}_{1-x}\text{As}_y\text{P}_{1-y}/\text{InP}$  materials system. Experimental results of the  $\text{Al}_x\text{Ga}_y\text{In}_{1-x-y}\text{As}/\text{InP}$  strained quantum well lasers show superior high temperature performances as discussed below.

**Design Considerations for High Temperature Operation:** Several approaches have been investigated to improve the laser temperature characteristics. Strained multiple quantum well active layers are used to reduce the laser threshold current, Auger recombination, and intervalence band absorption through reducing the in-plane hole effective mass by the combination of biaxial strain and quantum confinement. In quantum well structures, the carrier leakage through the barrier layer is one important factor causing laser performance to degrade at high temperature and high carrier density. Due to the difference in effective mass, the electron with its lighter effective mass requires a tighter confinement than the hole. To increase the conduction band offset beyond that of the conventional  $\text{GaInAsP}/\text{InP}$  quantum well structures, constant  $y$  quaternary quantum wells ( $\text{Ga}_w\text{In}_{1-w}\text{As}_y\text{P}_{1-y}/\text{Ga}_b\text{In}_{1-b}\text{As}_y\text{P}_{1-y}$ ) [3],  $\text{InAs}_x\text{P}_{1-x}$  ternary quantum wells [4], and quantum wells on ternary substrates ( $\text{InGaAs}$ ) [5] have been tried by various research groups. We have chosen the  $\text{Al}_x\text{Ga}_y\text{In}_{1-x-y}\text{As}/\text{InP}$  materials system instead, for its large conduction band offset ( $\Delta E_c = 0.72\Delta E_g$ ) to provide a strong electron confinement in the well and maintain uniform hole distribution among the wells [2]. Moreover, in this materials system, a graded-index separate-confinement heterostructure (GRINSCH) can be implemented by adjusting the Al to Ga ratio because the difference in the covalent radius of Gallium and Aluminum is very small. In contrast, in the case of the conventional  $\text{Ga}_x\text{In}_{1-x}\text{As}_y\text{P}_{1-y}/\text{InP}$  materials system, both  $x$  and  $y$  have to be adjusted nonlinearly to grow a GRINSCH. The GRINSCH provides not only strong carrier confinement but also efficient carrier injection. The design of high temperature lasers in terms of the quantum well number and the mirror loss is quite different from that of low-threshold-current lasers [2, 6]. To avoid gain saturation at high temperature operation (e.g.  $100^{\circ}\text{C}$ ), the optimum operating point should be designed using the gain curve of the highest operating temperature at the expense of a slightly high threshold current at room temperature [2].

**Material Growth and Device Fabrication:** The laser material was grown by low-pressure (76 Torr) organometallic chemical-vapor deposition at  $625^{\circ}\text{C}$  for  $\text{InP}$  and  $700^{\circ}\text{C}$  for  $\text{AlGaInAs}$  [7]. The quantum wells are either  $\text{Al}_{.161}\text{Ga}_{.102}\text{In}_{.737}\text{As}$  wells (5 nm each, 1.43 % compressive strain) or  $\text{Al}_{.07}\text{Ga}_{.54}\text{In}_{.39}\text{As}$  wells (11 nm each, 0.98 % tensile strain). The photoluminescence peak wavelength is around  $1.29\ \mu\text{m}$ . The multiple quantum wells are located in the middle of the graded-index separate-confinement heterostructure region. To provide a tight electron confinement in the growth direction,  $\text{Al}_x\text{Ga}_y\text{In}_{1-x-y}\text{As}$  quaternary layers (10 nm thick each) with a bandgap large enough to provide an electron confinement energy of 150 meV are used as the barrier layers, together with linearly graded waveguide layers (100 nm) on either side of the multiple quantum well region [2]. The graded regions are terminated at  $\text{Al}_{.48}\text{In}_{.52}\text{As}$  waveguide regions. Carriers and photons are laterally confined by a  $3\text{-}\mu\text{m}$  wide ridge waveguide fabricated by a self-aligned process to minimize the series resistance and provide uniform current injection.

**High Temperature Static Performances:** These lasers exhibit excellent temperature characteristics. When the heat sink temperature changes from 25 to 100 °C, a small reduction of 0.3 dB in slope efficiency has been demonstrated for a compressive-strained five-quantum-well (CS5QW) laser with rear facet high-reflection coated [8]. As shown in Fig. 1, a record high CW operating temperature of 185 °C has been obtained for a laser with both facets high-reflection coated [9].

**High Temperature Dynamical Performances:** The intrinsic small-signal modulation responses are measured in the range of 0.1-20 GHz by a parasitic-free optical modulation technique [2]. As shown in Fig. 2, the solid lines are the theoretical fittings to the measured data shown as dots for a CS5QW laser. The maximum intrinsic 3-dB bandwidths are measured to be 19.5, 15, and 13.9 GHz at 25, 65 and 85 °C, respectively [10]. Power roll-off caused by heating prevents further increase of the modulation bandwidth. The strong carrier confinement also results in small  $k$  factors (0.25 ns) which indicates the potential for high speed modulation up to 35 GHz.

**High Temperature Reliability:** In spite of the aluminum-containing active layer, no catastrophic optical damage was observed at room temperature up to 210 mW for CS5QW lasers and 103 mW for TS3QW lasers [2]. For aluminum-containing lasers such as AlGaAs lasers under CW operation, the nonradiative region caused by facet oxidation has been reported as a main reason for early stage degradation [11]. Thus, it is important to investigate the reliability of  $\text{Al}_x\text{Ga}_y\text{In}_{1-x-y}\text{As}/\text{InP}$  lasers under high temperature operation for subscriber loop applications. Thirty 300- $\mu\text{m}$  long CS4QW lasers have been undergoing a life test for 8,000 hours. The rear facets of the devices are coated with one-pair high-reflection dielectric coating and the front facets are coated with neutral coating. The aging condition is 10 mW output power launched into a 0.25 numerical aperture at 100 °C. The changes in threshold current are very small. The lifetime projection is made by the linear extrapolation method. Based on a widely accepted lifetime criterion of a 50 % increase of the original threshold current, the mean-time-to-failure (MTTF) is estimated to be 33 years ( $2.9 \times 10^5$  hours) for operating at 100 °C with more than 10 mW output power [12].

**Conclusions:** The favorable band offset of  $\text{Al}_x\text{Ga}_y\text{In}_{1-x-y}\text{As}/\text{InP}$  materials system enables us to design lasers with deep quantum wells and at the same time to maintain uniform hole distribution among the wells [2]. Following the design guide lines [2], we have demonstrated that the  $\text{Al}_x\text{Ga}_y\text{In}_{1-x-y}\text{As}/\text{InP}$  strained quantum well lasers perform well both statically and dynamically at high temperature. With these newly-designed uncooled lasers, low cost and reliable transmitters are being built for FITL applications.

**Acknowledgement:** The authors are grateful to Z. Wang, D. Darby, D. Flanders, and J. J. Hsieh of Lasertron for providing experimental data on laser static performances and reliability through research collaboration. We are also thankful to M. A. Koza, F. Favire, N. C. Andreadakis, B. Pathak, M. C. Wang, W. Lin, D. M. Hwang and C. Y. Chen of Bellcore for their help in crystal growth, device fabrication, laser characterization, bandgap calculation and TEM observations.

#### References:

- [1] "Reliability assurance practices for optoelectronic devices in loop applications," Bellcore, TA-TSY-000983, Issue 1, January 1990.
- [2] C. E. Zah, R. Bhat, B. Pathak, F. Favire, W. Lin, M. C. Wang, N. C. Andreadakis, D. M. Hwang, M. A. Koza, T. P. Lee, Z. Wang, D. Darby, D. Flanders, and J. J. Hsieh, "High performance uncooled 1.3  $\mu\text{m}$   $\text{Al}_x\text{Ga}_y\text{In}_{1-x-y}\text{As}/\text{InP}$  strained-layer quantum well lasers for subscriber loop applications," IEEE, J. Quantum Electron., vol. QE-30, pp. 511-523, February 1994.
- [3] A. Mircea, A. Ougazzaden, G. Primot and C. Kazmierski, "Highly thermally stable, high-performance InGaAsP: InGaAsP multi-quantum-well structures for optical devices by atmospheric pressure MOVPE," J. of Crystal Growth, vol. 124, pp. 737-740, 1992.
- [4] M. Yamamoto, N. Yamamoto and J. Nakano "MOVPE growth of strained InAsP/InGaAsP quantum-well structures for low threshold 1.3  $\mu\text{m}$  lasers," IEEE, J. Quantum Electron., vol. QE-30, pp. 3-9, January 1994.
- [5] H. Shoji, T. Uchida, T. Kusunoki, M. Matsuda, H. Kurakake, S. Yamazaki, K. Nakajima, and H. Ishikawa, "Fabrication of  $\text{In}_{0.25}\text{Ga}_{0.75}\text{As}/\text{InGaAsP}$  strained SQW lasers on  $\text{In}_{0.05}\text{Ga}_{0.95}\text{As}$  ternary substrate," IEEE, Photon. Technol. Lett., vol. 6, no. 10, pp. 1170-1172, October 1994.

- [6] P. W. McIlroy, A. Kurobe, and Y. Uematsu, "Analysis and application of theoretical gain curves to design of multi-quantum-well lasers" IEEE, J. of Quantum Electron., vol. QE-21, pp. 1958-1963, 1985.
- [7] R. Bhat, C. E. Zah, M. A. Koza, B. Pathak, F. Favire, W. Lin, M. C. Wang, N. C. Andreadakis, D. M. Hwang, T. P. Lee, Z. Wang, D. Darby, D. Flanders, and J. J. Hsieh, "High-performance 1.3  $\mu\text{m}$  AlGaInAs/InP strained quantum well lasers grown by organometallic chemical vapor deposition," J. of Crystal Growth, vol. 145, pp. 858-865, 1994.
- [8] C. E. Zah, R. Bhat, B. Pathak, F. Favire, M. C. Wang, W. Lin, N. C. Andreadakis, D. M. Hwang, M. A. Koza, T. P. Lee, Z. Wang, D. Darby, D. Flander and J. J. Hsieh, "High performance uncooled 1.3  $\mu\text{m}$  Al<sub>x</sub>Ga<sub>y</sub>In<sub>1-x-y</sub>As/InP strained-layer quantum well lasers for fiber-in-the-loop applications," Tech. Dig. of Optical Fiber Comm. ThG1, pp. 204-205, San Jose, CA, February 20-25, 1994.
- [9] Z. Wang, D. B. Darby, G. Pinelli, M. Matsuki, P. S. Whitney, D. C. Flanders, J. J. Hsieh, C. E. Zah, R. Bhat, and T. P. Lee, "High-reliability, high-performance, low-cost coaxial laser module at 1.3  $\mu\text{m}$  for local loop applications," Tech. Dig. of Optical Fiber Comm. W14, pp. 144-145, San Jose, CA, February 20-25, 1994.
- [10] C. E. Zah, M. C. Wang, R. Bhat, T. P. Lee, S. L. Chuang, Z. Wang, D. Darby, D. Flanders, and J. J. Hsieh, "High-temperature modulation dynamics of 1.3  $\mu\text{m}$  Al<sub>x</sub>Ga<sub>y</sub>In<sub>1-x-y</sub>As/InP compressive-strained multiple-quantum-well lasers," 14th IEEE Int. Semiconductor Laser Conf., Th1.3, pp. 215-216, Maui, Hawaii, September 19-23, 1994.
- [11] W. J. Fritz, L. B. Bauer, and C. S. Miller, "Analysis of aluminum gallium arsenide laser diodes failing due to nonradiative regions behind the facets," 27th Annual Proc. Reliability Phys., pp. 59-64, Phoenix, AZ, 1989.
- [12] C. E. Zah, R. Bhat, T. P. Lee, Z. Wang, D. Darby, D. Flanders, and J. J. Hsieh, "Recent progress on uncooled 1.3- $\mu\text{m}$  lasers for loop applications," Tech. Dig. of Optical Fiber Comm. ThG1, pp. 251-252, San Diego, CA, February 26-March 3, 1995.

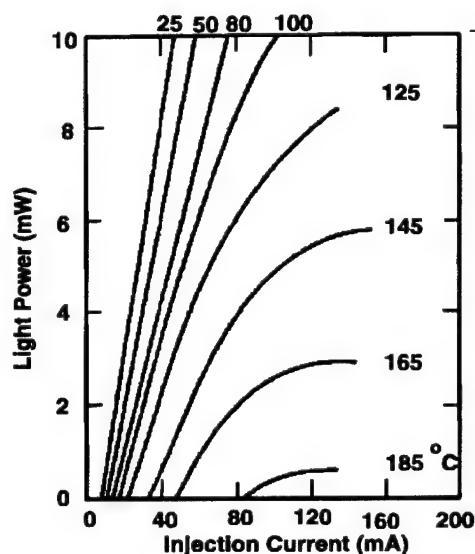


Fig. 1 Light-current characteristics of a 300- $\mu\text{m}$  long CS5QW laser with a 75 % (85%) high reflection coating on the front (rear) facet at various heat sink temperatures.

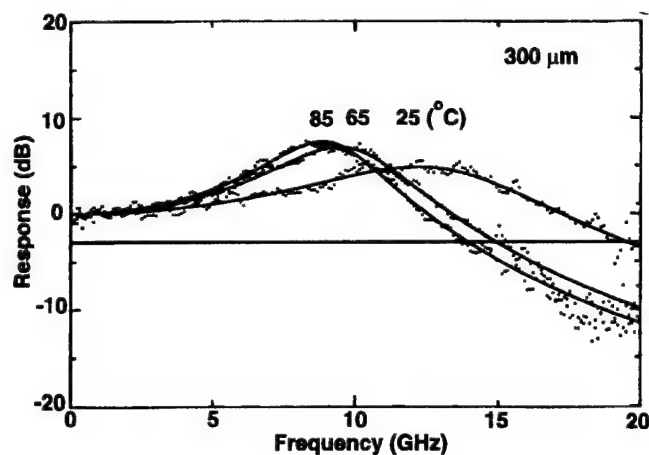


Fig. 2 Small-signal modulation responses of a 300  $\mu\text{m}$  long CS5QW laser at 25, 65 and 85  $^{\circ}\text{C}$  with bias currents of 153, 137 and 150 mA, respectively.

# Theoretical and Experimental Study on the Temperature Sensitivity of High-Efficiency 1.3- $\mu\text{m}$ InP-Based Strained MQW Lasers

S. Seki, H. Oohasi, H. Sugiura, T. Hirono, and K. Yokoyama

NTT Opto-electronics Laboratories

3-1 Morinosato Wakamiya, Atsugi, Kanagawa, 243-01 Japan

(Tel: 81-462-40-3173, Fax: 81-462-40-2859)

InP-based strained-layer (SL) multiple-quantum-well (MQW) lasers operating at a wavelength of 1.3  $\mu\text{m}$  have attracted much interest due to their potential applications to fiber-in-the-loop (FITL) or fiber-to-the-home (FTTH) systems [1], [2]. For these applications, it becomes important to improve the temperature sensitivity of device properties over a wide range of operating temperatures. We have recently derived the basic design rule for highly-efficient operation of InP-based SL-MQW lasers at elevated temperatures [3]. The SL-MQW lasers fabricated according to this design rule have exhibited high external differential quantum efficiency over 58% in the temperature range up to 363 K [3]. In this paper, we present a theoretical and experimental study on the temperature sensitivity of the differential quantum efficiency and threshold current of 1.3- $\mu\text{m}$  InP-based SL-MQW lasers.

The temperature dependence of differential quantum efficiency was analyzed by the following model. Applying the linear relationship between the internal loss of the QW ( $\alpha_i^{\text{QW}}$ ) and the temperature [4] as  $\alpha_i^{\text{QW}} = \alpha_1 + \gamma(T - T_1)$ , where  $\alpha_1$  is the internal loss of the well at  $T = T_1$  and  $\gamma = d\alpha_i^{\text{QW}}/dT$ , the external differential quantum efficiency ( $\eta_d$ ) is described as

$$\frac{\eta_d}{\eta_i} = \frac{\alpha_m}{N_w(\alpha_1 + \gamma(T - T_1)) + \alpha_i^{\text{SCH}}(T) + \alpha_m}, \quad (1)$$

where  $\eta_i$  is the internal quantum efficiency,  $\alpha_i^{\text{SCH}}$  is the internal loss of the separate confinement heterostructure (SCH) region,  $\alpha_m$  is the mirror loss, and  $N_w$  is the number of wells. When  $\alpha_i^{\text{SCH}}$  is small enough compared with  $\alpha_i^{\text{QW}}$ , Eq. (1) can be reduced to

$$\frac{\eta_d}{\eta_i} \propto \exp\left(-\frac{\gamma}{\alpha_m/N_w + \alpha_1}(T - T_1)\right). \quad (2)$$

Since  $\eta_i$  shows little temperature dependence in the temperature range in which we are interested [5], [6],  $\eta_d$  exhibits an exponential relationship with temperature when  $\alpha_i^{\text{SCH}}$  can be neglected.

The band structures were obtained by self-consistently solving the Poisson equation and the multiband effective-mass equations since electrostatic deformation in band profiles becomes important at elevated temperatures [7]. The threshold current was then calculated by taking into account the Auger recombination current ( $J_{\text{Aug}}$ ) in the quasi-two-dimensional system [8] as well as the radiative recombination current ( $J_{\text{rad}}$ ).

Following the design rule [3] for highly-efficient operation, we fabricated SL-MQW Fabry-Perot buried heterostructure (BH) lasers. The SL-MQW stack, which incorporates 5.5-nm thick, 1.5% compressively-strained  $\text{InAs}_y\text{P}_{1-y}$  ( $y = 0.52$ ) QWs with 10-nm

thick InGaAsP ( $\lambda_g=1.05\ \mu\text{m}$ ) barriers, was grown by chemical beam epitaxy [9]. The number of wells was varied from four to ten. The laser cavity was 300- $\mu\text{m}$  long with a high reflection coating ( $R_r = 96\%$ ) on the rear facet.

Figure 1 shows the temperature dependence of differential quantum efficiency for the SL-MQW lasers with various numbers of wells. There are two significant features in these characteristics. First, there exists a critical temperature ( $T_c$ ) in the temperature characteristics: the efficiency exhibits an exponential relationship with temperature below  $T_c$ , while it rapidly deviates from the exponential relationship above  $T_c$ . It is noted that  $T_c$  decreases with decreasing the number of wells. Secondly, the temperature dependence of the efficiency ( $|d\eta/dT|$ ) increases below  $T_c$  as the number of wells increases. The dashed lines in Fig. 1 indicate the calculated slope of  $d\eta/dT$  according to Eq. (2). For these lasers ( $\alpha_1=1.25\ \text{cm}^{-1}$  at room temperature [10]), the experimental results were consistently explained by assuming  $\gamma=0.025\ \text{cm}^{-1}/\text{K}$  regardless of the number of wells. These results clearly indicate that the temperature dependence of internal loss in the QWs plays a very important role in determining the temperature sensitivity of differential quantum efficiency below  $T_c$ .

A significant reduction in differential quantum efficiency above  $T_c$  is mainly caused by an increase in  $\alpha_i^{\text{SCH}}$  due to the pile-up of carriers in the SCH region at elevated temperatures [7], which agrees with the recent measurements in 0.98- $\mu\text{m}$  [5] and 1.55- $\mu\text{m}$  [11] lasers. The smaller the well number, the easier the carriers can spill over into the SCH region at elevated temperatures. Therefore,  $T_c$  becomes smaller with decreasing  $N_w$  as shown in Fig. 1. In most of the long-wavelength InP-based SL-MQW lasers reported so far,  $T_c$  was around or below room temperature. Hence, we could hardly separate  $\alpha_i^{\text{QW}}$  and  $\alpha_i^{\text{SCH}}$  from each other in the experiments. Since the carrier spillover is effectively eliminated in the SL-MQW structures used in this study,  $T_c$  becomes larger than room temperature, which makes them an ideal test device for analyzing the high-temperature characteristics.

The critical temperatures were also observed in the temperature dependence of threshold current as shown in Fig. 2, where the threshold currents were plotted as a function of temperature for the same devices. We then calculated the threshold current density on the basis of the self-consistent numerical method [7]. In these calculations, the threshold gain was determined from the results shown in Fig. 1. Figure 3 shows the calculated threshold current density plotted as a function of temperature for 4-well SL-MQW structures. The full calculation results (denoted by open circles) exhibit a similar temperature dependence as that observed in Fig. 2. These results clearly indicate that the self-consistent numerical method can give a good description of the temperature dependence of threshold current.

In this figure, the results when neglecting the temperature-dependent loss or the Auger recombination current are also shown for comparison. Below  $T_c$ ,  $T_0$  was more effectively improved when  $J_{\text{Aug}}$  was neglected. These results indicate that the Auger recombination plays a more significant role than the temperature-dependent loss in determining  $T_0$  below  $T_c$ . On the other hand, above  $T_c$ ,  $T_0$  was not improved that much even if  $J_{\text{Aug}}$  was ignored. Therefore, it is clear from these results that electrostatic deformation [7], which causes a significant increase in loss and  $J_{\text{rad}}$  in the SCH region, plays a more primary role in determining  $T_0$  in this temperature range.

In summary, we have analyzed the temperature sensitivity of the differential quantum efficiency and threshold current of 1.3- $\mu\text{m}$  InP-based SL-MQW lasers. We have shown that the critical temperature  $T_c$  exists in both temperature characteristics. Below  $T_c$ , the temperature dependence of internal loss in the QWs plays a very important role in determining the temperature sensitivity of the differential efficiency. On the other hand, above  $T_c$ , its temperature sensitivity is affected more by the internal loss in the SCH region. It has been shown that the Auger recombination current plays a more significant role in determining the temperature dependence of threshold current below  $T_c$ . However, above  $T_c$ , electrostatic band-profile deformation, which causes a significant increase in loss and radiative recombination current in the SCH region, plays the more dominant role than the Auger recombination current.

#### References

- [1] P. J. A. Thijs et al., IEEE J. Lightwave Technol. **LT-12**, 28 (1994).
- [2] C.E. Zah et al., IEEE J. Quantum Electron. **QE-30**, 511 (1994).
- [3] S. Seki et al., Digest of 1995 Integrated Photonics Research, Dana Point, PD7, 1995.
- [4] Y. Zou et al., IEEE J. Quantum Electron. **QE-29**, 1565 (1994).
- [5] E. C. Vail et al., IEEE Photon. Technol. Lett. **PTL-6**, 1303 (1994).
- [6] D. A. Ackerman et al., Digest of 14th IEEE Int. Semiconductor Laser Conf., Maui, Th3.3, 1994.
- [7] S. Seki et al., IEEE Photon. Technol. Lett. **PTL-7**, 251 (1995).
- [8] S. Seki et al., to be published in Appl. Phys. Lett.
- [9] H. Sugiura et al., J. Cryst. Growth **147**, 1 (1995).
- [10] M. Yamamoto et al., IEEE J. Quantum Electron. **QE-30**, 554 (1994).
- [11] V. Mikhaelashvili et al., IEEE Photon. Technol. Lett. **PTL-6**, 1293 (1994).

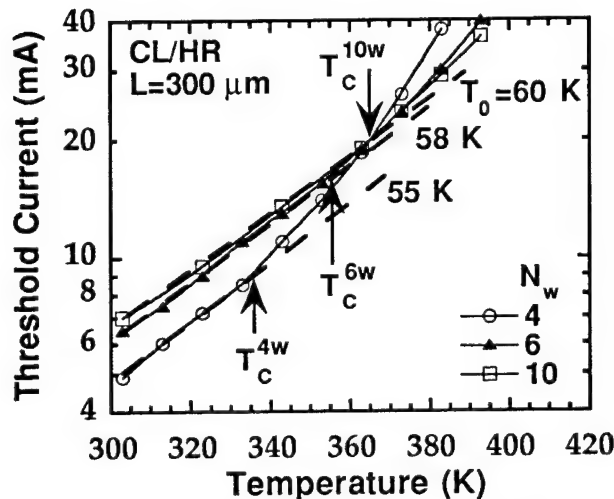


Fig. 2 Measured threshold current plotted as a function of temperature.  $T_0$  is obtained in the temperature range below  $T_c$ .  $T_c^{nw}$  is the critical temperature of  $n$ -well MQW structures.

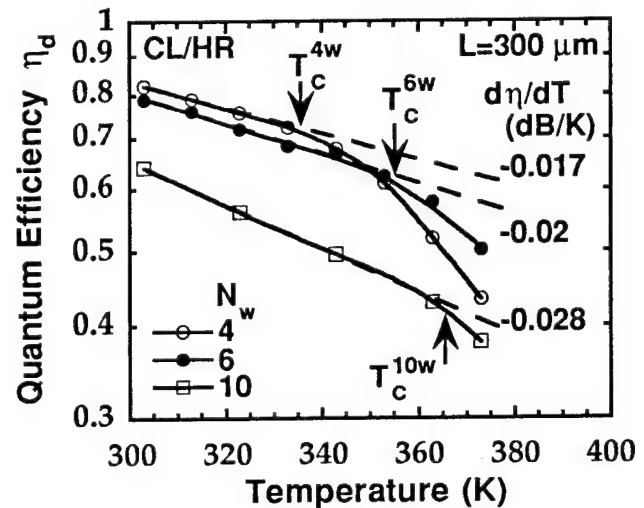


Fig. 1 Measured quantum efficiency plotted as a function of temperature. The number of wells is varied from 4 to 10.  $T_c$  is the critical temperature. The dashed lines are the calculated slope of  $d\eta/dT$  according to Eq. (2).

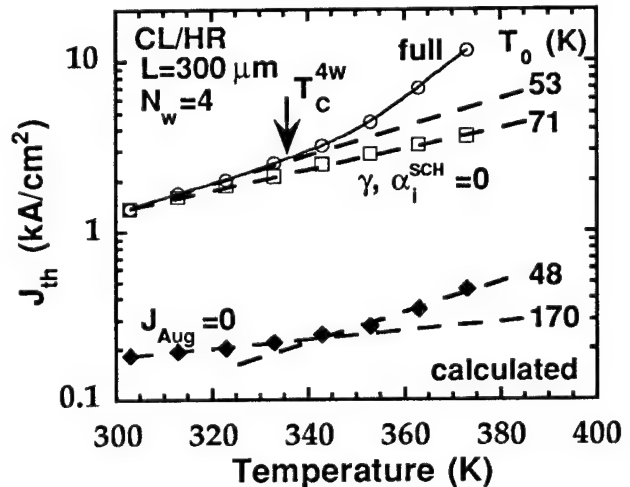


Fig. 3 Calculated threshold current density plotted as a function of temperature. The circles indicate the full calculation results. The results when neglecting the temperature-dependent loss (squares) or Auger current (diamonds) are also shown for comparison.



## A bi-directional transceiver PIC for Ping-Pong local loop configurations operating at 1.3 $\mu\text{m}$ wavelength

R. Ben-Michael, U. Koren B.I. Miller, M.G. Young, T.L. Koch, M. Chien, R.J. Capik, G. Raybon, K. Dreyer

AT&T Bell Laboratories

Holmdel, NJ 07733. Phone (908) 949 1545, Fax (908) 949 8988

For deployment of a single mode fiber to the home, one wishes to develop an inexpensive optical data link. In order to reduce the cost of a such a local loop communication system operating at 1.3  $\mu\text{m}$  wavelength, the preferred mode of operation of transmitters and receivers operation in such a configuration is uncooled operation. To further reduce the cost, the transmitters would be Fabry-Perot cavity lasers, with a relatively broad spectral range of  $\pm 10$  nm around the desired 1.3  $\mu\text{m}$  lasing wavelength. The combination of uncooled operation and broad temperature range requires the receiver in such a configuration to have broad spectral responsivity of  $\pm 35$  nm around the lasing wavelength. This is calculated taking into account the worst case scenario in temperature changes, and a  $\sim 6$   $\text{\AA}/^\circ\text{C}$  wavelength change by temperature.

One proposed configuration is a Ping-Pong link, where transmitting and receiving occurs through a single fiber at different time slots with time division multiplexing (TDM). A possible solution for a transceiver operating in such a system would be to use a bulk laser, which would be operated part of the time as a detector<sup>[1,2]</sup>. By using a *bulk*, instead of an MQW laser, polarization independent detection would be possible. The use a laser as a transceiver yields the following advantages: (I) Relatively inexpensive uncooled lasers are commercially available. (II) Elimination of the need for a separate receiver, located either on a separate fiber or after an optical splitter. The problem with this approach is that the responsivity, even of a bulk laser, is not broad enough to account for the extremely broad spectral responsivity range needed in a low cost configuration. Therefore, a specially designed detector seems a necessity, in order to meet the broad spectral responsivity demand. Thus, a simple photonic integrated circuit (PIC) which is potentially inexpensive, that would have the two benefits of a laser mentioned above, plus the desired broad spectral responsivity range, would be potentially useful in low cost local loop applications.

In this work we propose and demonstrate a PIC transceiver operating in the 1.3  $\mu\text{m}$  wavelength range. The transceiver is a simple new single in-line waveguide device, with integration of a gain section, a specially designed detector and a beam expander. All three sections are integrated inside the Fabry-Perot cavity of the laser, along an underlying waveguide. The detector has a broad spectral responsivity range by using a 1.4  $\mu\text{m}$  bulk quaternary layer in that section. This design has optimized gain and detector sections, by making use of the high gain provided by MQW layers together with the benefit of polarization independent response of the bulk active layer in the detector section. The device operates without significant degradation of performance when the transceiver operates as a laser. The purpose of the beam expander is to reduce the cost of packaging the PIC. With the beam expander there is no need for a lensed fiber, as good coupling is achieved to a cleaved (flat) single mode fiber<sup>[3,4]</sup>. Moreover, alignment tolerance of the cleaved fiber to the output of the beam expander is significantly enhanced, suggesting possible use with a passive alignment or hybrid integration scheme<sup>[5,6]</sup>, that potentially would further reduce the cost of packaging this PIC.

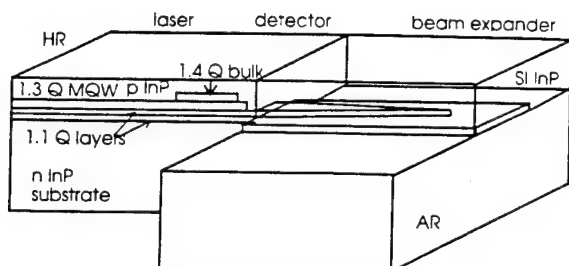


Figure 1 shows a schematic structure of the transceiver. The transceiver includes three sections: a laser, a detector, and a beam expander integrated along an underlying backbone waveguide. The underlying waveguide consists of two InGaAsP quaternary layers, with  $\lambda_p = 1.1 \mu\text{m}$  (1.1 Q), separated by an InP etch stop layer. The bottom waveguiding layer is 800 Å thick and the top 1400 Å thick. The gain section of this PIC is referred to as the laser section, and consists of 6 compressively strained (0.9%) 70 Å thick quantum wells, and 150 Å 1.1 Q tensile strained barriers. The length of the laser section is 500  $\mu\text{m}$ . The detector is separated electrically from the laser section. The active layers of the detector section consists of the underlying MQW layers and a 800 Å 1.4 Q bulk layer. In order to reduce the capacitance of the detector, the length of this section is 85  $\mu\text{m}$ . The detector ohmic contact stripe is 10  $\mu\text{m}$  wide, connected with a 100 x 100  $\mu\text{m}$  contact pad on top of a 0.5  $\mu\text{m}$  thick SiO<sub>2</sub>. The resulting zero bias capacitance of the detector section is approximately 2 pF. In the beam expander section, the top 1.1 Q layer is adiabatically tapered laterally from 3  $\mu\text{m}$  at the beginning of the beam expander to a sharp termination. The bottom layer remains in the same 5  $\mu\text{m}$  width along the entire 300  $\mu\text{m}$  long beam expander. The beam expander transforms the elliptical optical mode both laterally and vertically to better fit the shape of the optical mode in a single mode fiber<sup>[3]</sup>.

The following experimental results are with zero biasing the detector. In figure 2 we show the responsivity of the transceiver for wavelengths ranging from 1.28 to 1.36  $\mu\text{m}$ . The front facet of the device is anti-reflecting (AR) coated. The highest responsivity is 0.43 A/W, with very low polarization sensitivity. We attribute the extremely broad spectral responsivity range and the polarization independence to the structure of the active layers of the detector section, which include a bulk 1.4 Q layer. This spectral responsivity may meet the demand for broad spectral responsivity range in a low-cost network configuration, with a measured range of 33 nm above and 47 nm below the lasing wavelength.

In figure 3 we show the output power coming out of the front facet of the transceiver vs. the drive current at different temperatures. The detector was biased at 50 mA in this measurement. As can be seen in the figure, lasing up to 72°C is demonstrated with output power of 9 mW, and with characteristic temperature of the laser of  $T_0 = 31^\circ\text{C}$ . Typical insertion loss to a single mode optical fiber is -3.9 dB (41%), and at room temperature, typically 8 dBm is coupled to a single mode fiber, with drive current of 100 mA in the laser section and of 50 mA in the detector section. The beam expander greatly broadens the alignment tolerance to a single mode fiber. Fig. 4 shows the power coupled to a cleaved single mode fiber vs. lateral and vertical misalignments, with the conditions stated above, giving 8 dBm inside the fiber with optimal alignment. As seen in the figure, the 1 dB excess loss due to misaligning the fiber is  $\pm 2.2 \mu\text{m}$  vertically and  $\pm 3.2 \mu\text{m}$  laterally. This result is the same both when the operating as a receiver or a transmitter, and can possibly reduce the “pigtailling” cost of the transceiver due to the more relaxed alignment needed, together with the use of a cleaved, rather than a lensed, single mode fiber.

In conclusion, we have demonstrated a potentially low cost photonic integrated circuit that can operate as a transceiver in a Ping-Pong optical data link configuration, designed for uncooled operation, with integration of a laser, a detector, and a beam expander inside a Fabry-Perot cavity. The specially designed detector has broad spectral responsivity range of 80 nm, extending to 33 nm above the lasing wavelength of the device. The transmitter can couple 8 dBm of optical power into a single mode fiber, using a beam expander.



**Fig. 1** Schematic structure of the transceiver, with integration of a gain section, a detector section, and a passive beam expander.

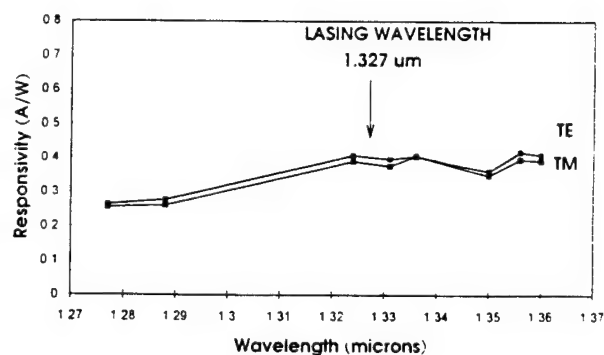


**Fig. 2** Responsivity of AR coated transceiver in wavelengths ranging from 1.28 to 1.36  $\mu\text{m}$ . The spectral and polarization induced variations in responsivity are smaller than 1 dB relative to the responsivity in the lasing wavelength of the device.

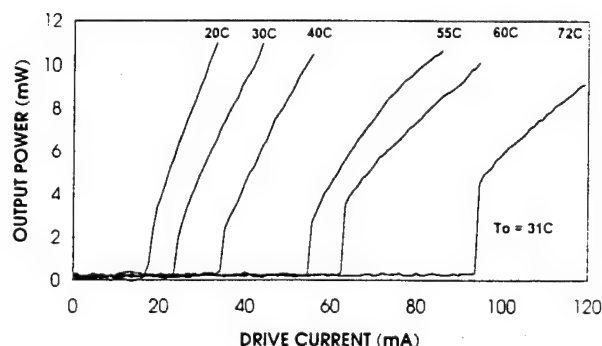


**Fig. 3** Output power coming out of the transceiver as a function of the laser section current, at different operation temperatures. The detector section current was a constant 50 mA in this measurement.

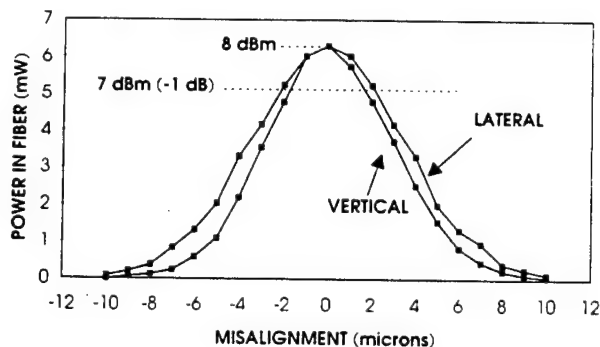


**Fig. 4** Power inside a cleaved single mode fiber vs. lateral and vertical misalignments of the fiber.

## References

- [1] H. Terui, T. Kominato, K. Yoshino, S. Hata, S. Sekine, M. Kobayashi, J. Yoshida, K. Okada, "Optical module with a silica-based planar circuit for fiber-optic subscriber systems," *Phot. Tech. Lett.*, vol. 4, pp. 660-662, 1992
- [2] T. Kurosaki, Y. Tohmori, M. Fukuda, M. Nakamura, H. Kimura, S. Matsumoto, T. Sugie, "Dynamic properties of 1.3  $\mu\text{m}$  semi-insulating BH light emission and detection diode module for subscriber TCM transmission systems" *Electron. Lett.*, vol. 31, pp. 189-191, 1995
- [3] R. Ben-Michael, U. Koren, B.I. Miller, M.G. Young, M. Chien, G. Raybon, "InP-based Multiple quantum well lasers with an integrated tapered beam expander waveguide," *IEEE Phot. Tech. Lett.*, vol. 16, pp. 1412-1414, 1994
- [4] U. Koren, R. Ben-Michael, B.I. Miller, M.G. Young, M. Chien, H.H. Yaffe, G. Raybon, K. Dreyer, "Electroabsorption modulator with passive waveguide spotsizers," *Electron. Lett.*, vol. 30, pp. 1852-1853, 1994
- [5] Y. Yamada, S. Suzuki, K. Moriwaki, Y. Hibino, Y. Tohmori, A. Akatsu, Y. Nakasuga, T. Hashimoto, H. Terui, M. Ynagisawa, Y. Inoue, Y. Akahori, R. Nagase, "A hybrid integrated optical WDM transmitter receiver module for optical subscriber systems utilizing a planar lightwave circuit platform", in *Post Deadline Proc. Opt. Fiber Commun. Conf. (OFC'95)*, San Diego CA, Feb. 1995, paper PD-16.
- [6] Y. Yamada, A. Takagi, I. Ogawa, M. Kawachi, M. Kobayashi, "Silica based optical waveguide on terraced silicon substrate as hybrid integration platform," *Electron Lett.*, vol. 29, pp. 444-446, 1993
- [7] U. Koren, B.I. Miller, G. Eisenstein, R.S. Tucker, G. Raybon, R.J. Capik, "Semi-insulating blocked planar buried heterostructure GaInAs-InP laser with high power and high modulation bandwidth," *Electron. Lett.*, vol. 24, pp. 138-139, 1988.

## An Fe-InP buried 1.3- $\mu$ m double heterostructure laser heteroepitaxially grown on Si

T. Yamada, M. Tachikawa, T. Sasaki, H. Mori, Y. Kadota,  
S. Matsumoto and K. Kishi

NTT Opto-electronics Laboratories, 3-1 Morinosato Wakamiya, Atsugi-shi,  
Kanagawa 243-01, Japan  
Phone +81 462 40 3254  
Facsimile +81 462 40 4304  
e-mail tyamada@aecl.ntt.jp

### Introduction

Opto-electronic integrated circuits (OEICs), especially photonic devices on Si, are attractive because of their potential to combine photonic functions with highly integrated silicon electronic circuits. We have already demonstrated long term cw operation of a 1.5- $\mu$ m multiple quantum well laser<sup>1)</sup> and high-temperature cw operation of a 1.3- $\mu$ m double heterostructure (DH) laser<sup>2)</sup> heteroepitaxially grown on Si. Low threshold current lasers are required to reduce the power consumption of OEICs. An effective approach to reduce the threshold current is burying lasers with semi-insulating InP. The semi-insulating buried structure is also indispensable to reduce parasitic capacitance for high-frequency operation. Though a semi-insulating InP layer has been successfully grown on a Si substrate,<sup>3)</sup> there are no reports on its application to devices on Si.

This letter presents, for the first time, a semi-insulating-InP buried laser heteroepitaxially grown on Si and its lowered threshold current compared to that of ridge waveguide lasers on Si.

### Device structure

Figure 1 shows a schematic diagram of a layer structure heteroepitaxially grown on a Si substrate. A 2- $\mu$ m-thick n-type GaAs layer and five pairs of strained layer superlattice consisting of InP and InGaAsP were grown on a Si substrate by low pressure metalorganic chemical vapor deposition (MOCVD). Then, 13- $\mu$ m-thick n-type InP was grown by hydride vapor phase epitaxy with thermal annealing. The InP layer has the highest quality ever reported: etch pit density (EPD) is  $5 \times 10^6 \text{ cm}^{-2}$  and full width at half maximum (FWHM) of x-ray diffraction is 65 seconds for (400) reflection.

A DH laser structure, shown in Fig. 1, was grown by MOCVD. The laser structure consists of a 0.1- $\mu$ m-thick InGaAsP confinement layer, a 0.15-

$\mu\text{m}$ -thick InGaAsP active layer of 1.3- $\mu\text{m}$  composite, a 0.1- $\mu\text{m}$ -thick InGaAsP confinement layer, a 1.5- $\mu\text{m}$ -thick p-InP layer and a 0.4- $\mu\text{m}$ -thick p<sup>+</sup>-InGaAsP contact layer. The laser structure was etched into a mesa structure using reactive ion etching (RIE) with a mixture of C<sub>2</sub>H<sub>6</sub> and H<sub>2</sub>. The mesa structure was then regrown by low pressure MOCVD using ferrocene as a precursor.<sup>4)</sup> The p-electrode was deposited on the laser stripe and the n-electrode was deposited on the n-InP layer. The laser structure on InP was grown simultaneously and processed in the same way to compare it to the laser on Si. The lasers were cleaved in 300- $\mu\text{m}$  long and had no coating.

### Results and discussion

Light-current characteristics of the buried laser on Si operating at cw are shown in Fig. 2 compared to those of the laser on InP at 20°C. The threshold current was 28 mA and the slope efficiency was 0.20 W/A for the lasers on Si. The threshold current was decreased by 8 mA compared to that of a ridge waveguide lasers made on other part of the same wafer. The buried laser on InP had a threshold current of 16 mA and a slope efficiency of 0.21 W/A, which is similar to that of the laser on Si. The difference in the threshold current between the buried laser on Si and the laser on InP is very similar to the difference in the case of the ridge waveguide lasers.

The temperature dependence of the threshold current is shown in Fig. 3. The laser on Si operated at up to 70°C and the laser on InP operated at up to 80°C. The maximum operating temperature of the laser on Si is similar to that of the ridge waveguide laser on Si. The characteristic temperature of the laser on Si was 53 K, which is similar to 50 K for the laser on InP.

These results clearly indicate the InP layer on Si has sufficient quality to bear dry etching and regrowth of the ion-doped InP processes. They also indicate that the Si substrate does not degrade the semi-insulating InP layer during regrowth. Consequently, the semi-insulating-InP buried laser on Si will be useful for future OEICs.

### Summary

We have made, for the first time, an Fe-doped semi-insulating-InP buried DH laser heteroepitaxially grown on a Si substrate. The threshold current was lowered to 28 mA compared to 36 mA of a ridge waveguide laser. The maximum operation temperature was 70°C and the characteristic temperature was 53K for the buried laser on Si.

## References

- 1) M. Sugo, et al. SSDM Extended Abstracts, 656 (1992) Tsukuba.
- 2) T. Yamada, et al. Tech. Digest of IPR, 181 (1995) Dana Point.
- 3) R. F. Schnabel, et al. IPRM'93, 115 (1993) Paris.
- 4) S. Matsumoto, et al. Electronics Lett., 30 (1994) 1305.

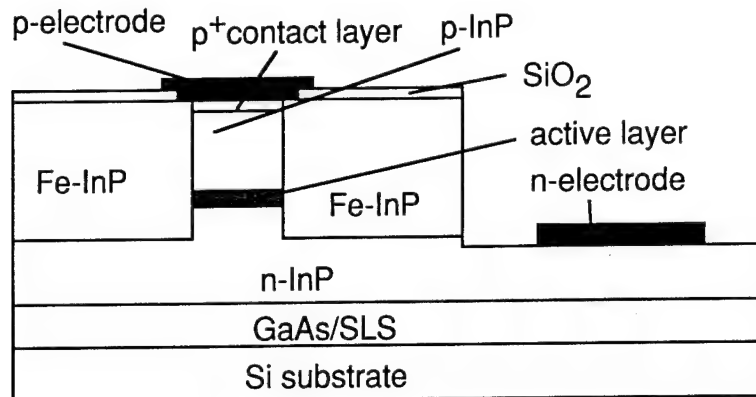


Fig. 1 Schematic diagram of the heteroepitaxially grown layers and the laser structure.

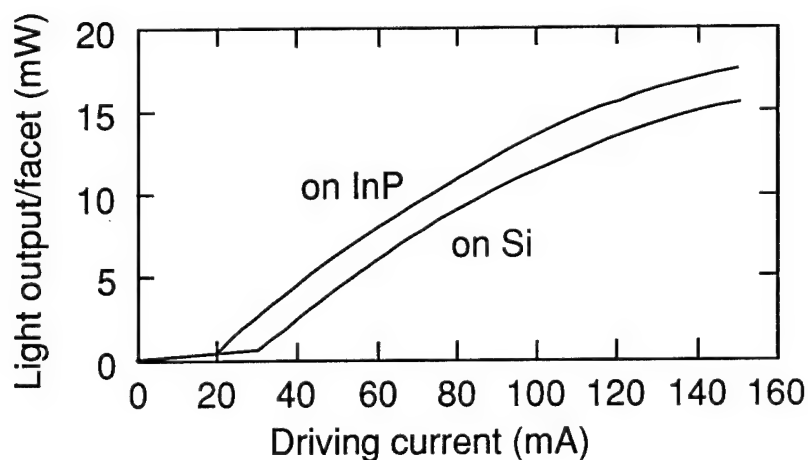


Fig. 2 I-L characteristics operated at cw.

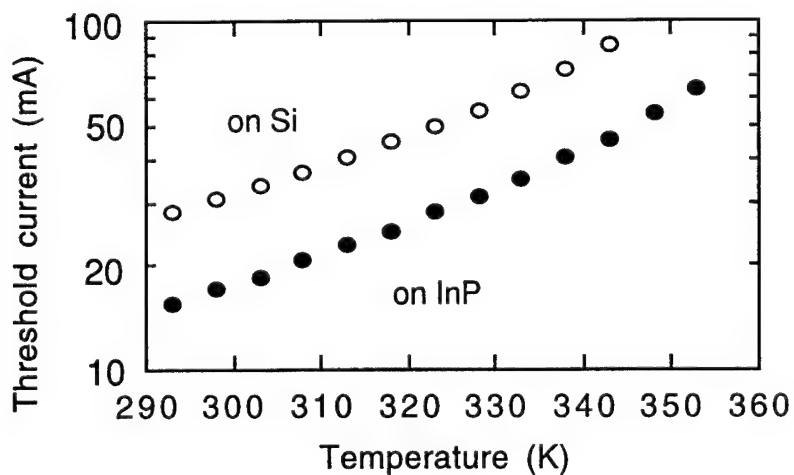


Fig. 3 Temperature dependence of threshold currents.

## Wavelength Uniformity in $\lambda/4$ -Shifted DFB Laser Array WDM Transmitters

M.G. Young, T.L. Koch, U. Koren, D.M. Tennant, B.I. Miller, M. Chien, K. Feder

AT&T Bell Laboratories, Holmdel, NJ 07733  
(908) 949-5974

Wavelength division multiplexed (WDM) optical transmission requires laser sources with wavelengths closely aligned to the pass-bands of demultiplexing optical filters at the receiving end. A common and simple strategy to meet this demand is the use of wavelength-stabilized discrete sources and passive demultiplexing filters without active tracking, i.e., both the source and the demultiplexing filter being independently responsible for maintaining the wavelength channel assignment within a prescribed accuracy. Properly engineered distributed feedback (DFB) laser resonators are well-known in their ability to offer exceptionally robust longitudinal mode stability, both in their long-term resistance to mode jumps with environmental and operating condition changes, and in basic side-mode suppression characteristics. Temperature-stabilized DFB lasers have been shown to have very low (0.1nm-level) wavelength drift with aging over system life[1,2].

Integrated arrays of DFB lasers offer the potential of either simultaneous transmission of a number of WDM channels, or arbitrary selection of a particular WDM channel, without forfeiting the spectral stability inherent to the independent, short, highly frequency-selective DFB resonators. However, the requirement of achieving the desired accuracy in wavelength places stringent demands on the fabrication processes. A number of physical phenomena contribute to deviations in the effective index of the laser waveguides, giving rise to typical  $\sigma$  values of 1 to 2 nm for the distributions of wavelengths for quantum well DFB lasers. However, we have hypothesized that the variations contributing to this spread may be more uniform within the smaller area of a particular array.

Figure 1 is a schematic diagram of a proposed DFB-array WDM source. A passive waveguide combiner brings the output of each DFB source together, and the lone output waveguide includes an amplifier to compensate for the inherent losses of the non-wavelength-selective combiner. With the addition of an output modulator, the device is designed for the transmission of a single, selectable wavelength, or broadcasting the same signal on several or all wavelengths. The rear detectors monitor the operation of the lasers, as well as provide an excellent sink to avoid facet reflections from the back facet. This design permits a different set temperature, perhaps stored in a PROM in the transmitter logic, for each laser channel. The result is a dramatically relaxed wavelength precision requirement, where each laser must only lie within a reasonable temperature tuning range (typically  $\pm 0.6\text{nm}$ ) from the assigned channel value.

We report here on the initial results of  $\lambda/4$ -shifted DFB arrays with 200 GHz ( $\sim 1.61\text{ nm}$ ) design spacings for the application described above. The abrupt  $\lambda/4$ -shifted design deterministically places a longitudinal mode in the center of the DFB stop-band, in contrast to the random placement, usually on either side of the stop band, that is achieved in a typical HR/AR-coated DFB laser design. The array is intended to offer a four-channel selectable WDM source. We will show that *relative* wavelength accuracy is excellent, but the *absolute* wavelength accuracy will still lie in the  $\pm 1\text{nm}$  range typical to state-of-the-art MQW DFB laser growth and fabrication. For this reason a six-element array is employed. The four adjacent devices, out of three such possible sets, that most closely align with the absolute WDM channel allocations, would be bonded to DC package leads, and the final adjustment to exact channel values is made under temperature control (at  $\sim 0.09\text{nm}/^\circ\text{C}$ ).

We employ a recently developed contact lithography technique to print DFB gratings using e-beam generated holographic or phase masks[3]. This technique offers the advantage of simultaneously printing all the required pitches in a single lithographic exposure, while maintaining the versatility of the



e-beam tool in creating the desired  $\lambda/4$ -shifts in the gratings. Furthermore, it has been modified to use a nearly conventional mercury arc lamp mask aligner instead of the usual UV laser and holography set-up required for DFB lasers

Wafers are grown using five metal-organic vapor phase epitaxial (MOVPE) growth steps. The lasers, amplifier, and modulator are processed using the semi-insulating planar buried heterostructure (SIPBH) configuration. The waveguides in the passive section employ a buried-ridge technique. The gain in the lasers and amplifier is provided by a strain-compensated stack of six compressively strained quantum wells. The use of a gas-diffusing frit and rotating substrate results in wavelength uniformity for these quantum wells of  $\pm 3$  nm over a 42 mm diameter on a 50 mm wafer.

Figure 2 shows the raw frequency data from fourteen randomly selected arrays from two wafers. This data reveals a spread in laser frequency at each channel that is comparable to the channel spacing of 200 GHz or 1.61 nm. However, careful inspection of the data reveals that the deviations to longer or shorter wavelength are nearly the same for all the elements in each array. In other words, the *spacing* in the arrays is much more precise than the overall spread observed in Figure 2 at each channel frequency. To make this graphically evident, the following procedure was followed. For the total data, a least square straight-line fit revealed a slope of 186 GHz rather than the design value of 200 GHz. This corresponds to a design error of 7%, comprised of potential errors in the group index used to determine the grating pitch, and in errors in the e-beam writing pitch changes for each successive grating in the quartz photomask. This slope can be corrected iteratively with new masks, and is not a concern here. What is of concern are the *deviations from the designed uniform slope*.

The origin of a 186 GHz/channel slope line was adjusted for a best fit for each array (physically corresponding to temperature tuning of the entire array), and all the arrays were then replotted with a common origin. This is shown in Figure 3. The resulting spread in uniformity is now seen to be much smaller than a channel spacing. Figure 4 plots the actual distribution of wavelength deviations from those values corresponding to a perfectly uniform frequency slope for each channel. The standard deviation,  $\sigma$ , of this distribution is 0.18nm, which is nearly an order of magnitude smaller than the values commonly observed for the distribution of wavelengths in wafer-wide measurements of DFB lasers.

The impact of this result on the yield of  $\lambda$ -selectable WDM sources using DFB arrays is very encouraging. Figure 5 shows the expected yield reduction due to wavelength inaccuracy assuming a Gaussian distribution. The result is plotted for various array sizes, as a function of the allowed tolerance in wavelength accuracy normalized to the  $\sigma$  of the fabrication process as discussed above. As an example, for a wavelength accuracy requirement of  $\pm 0.1$ nm, the observed  $\sigma$  of 0.18nm would lead to a yield of only  $\sim 3\%$  for a four-element array. This level of wavelength precision may be required for an array in which all lasers are operating simultaneously. However, since the wavelength-selectable design in Figure 1 allows a  $\pm 0.6$ nm temperature-tuned range for each laser, the yield for even an eight-element array will be in the 99% range.

In conclusion, we have shown that the intra-array standard deviation from uniform channel spacing is dramatically reduced from nm-scale wafer-wide values down to  $\sigma = 0.18$ nm for six-element  $\lambda/4$ -shifted DFB laser arrays fabricated using a holographic contact print grating process. This value is shown to be sufficient for high-yield for  $\lambda$ -selectable WDM arrays, but not yet sufficient for simultaneous multi- $\lambda$  transmission in a tight-tolerance dense WDM application. We are hopeful that continuing improvements in epitaxy, processing uniformity, and laser design will improve the yield even for the latter case.

## REFERENCES

- [1] R.S. Vodhanel et al., OFC'94, paper WG5, San Jose, Feb. 1994
- [2] Y.C. Chung and Jichai Jeong, OFC'94, paper WG6, San Jose, Feb. 1994
- [3] T.L. Koch et al., OFC'93, paper PD23, San Jose, Feb. 1993

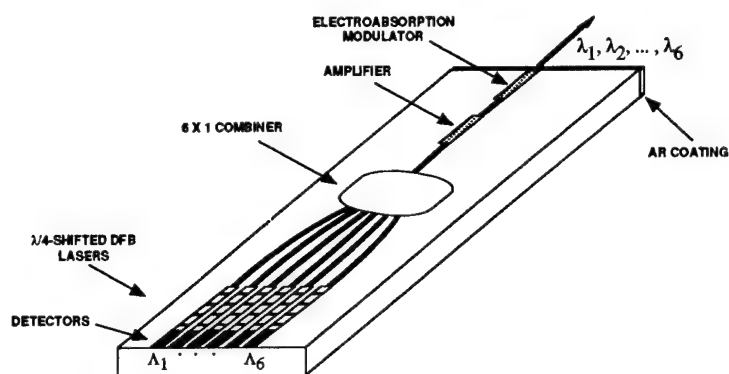


Fig. 1 Schematic diagram of a 6X1 DFB-array WDM source.

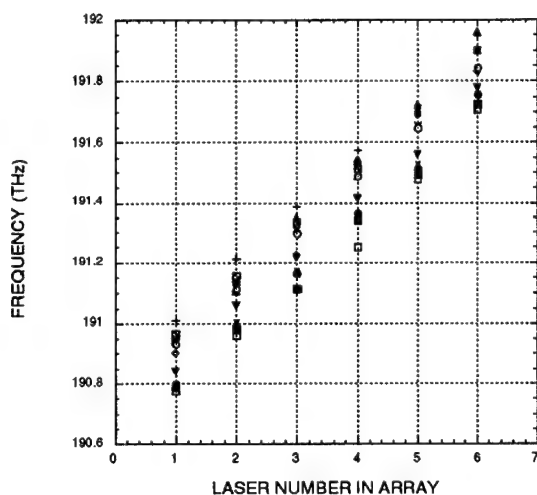


Fig. 2 Raw frequency data from fourteen 6X1 arrays.

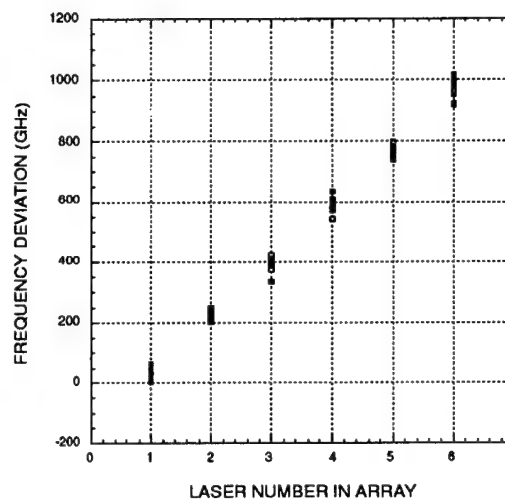


Fig. 3 Frequency deviation when fitted to a 186 GHz/channel slope.

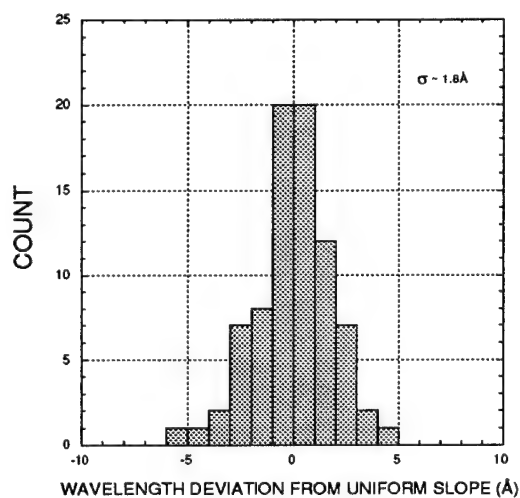


Fig. 4 Distribution of wavelength deviations.

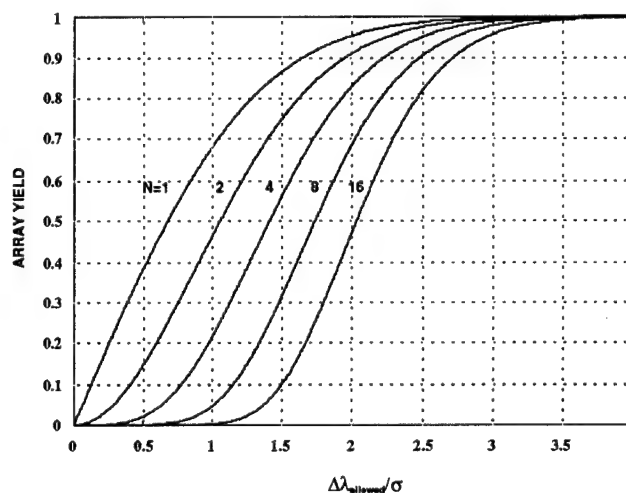


Fig. 5 Expected yield reduction due to wavelength inaccuracy.





Abshire, James B. — TuB1, TuB2, TuB5  
 Adams, M. J. — TuD2  
 Avrutin, E. A. — TuE1

Backbom, L. — MA2  
 Baer, Thomas M. — TuD  
 Balasubramanyam, R. — TuE15  
 Barrow, D. A. — TuE1  
 Basov, N. G. — TuD1  
 Ben-Michael, R. — WA4  
 Bennett, S. C. — MB3  
 Bhat, R. — WA2  
 Biellak, S. A. — TuC2  
 Bomse, David S. — MB1  
 Brueck, S. R. J. — TuE11

Caffey, David — MC4  
 Capik, R. J. — WA4  
 Chabran, C. — TuA2  
 Chang-Hasnain, Connie J. — MB6, TuA, TuD3  
 Chazan, P. — TuC5  
 Chen, T. R. — MA3, MA4  
 Cheng, Yong — TuD8  
 Chien, M. — WA4, WA6  
 Cho, D. — MB3  
 Choi, H. K. — MB6  
 Choquette, Kent D. — TuD7  
 Christian, Kent D. — TuB4  
 Clarkson, W. A. — MC4  
 Coldren, L. A. — TuD5, TuD6  
 Coleman, J. J. — MC3, TuE14  
 Cornwell, Jr., Donald M. — TuB3, TuC4  
 Crawford, M. Hagerott — TuD7  
 Curl, R. — MB4

Dai, Zheng — TuC6  
 Dann, A. J. — TuD2  
 Dapkus, P. Daniel — TuD4, TuD8, WA  
 Dellunde, Jaume — TuE12  
 Dianov, E. M. — TuD1  
 Doiron, Daniel R. — MC5  
 Dreyer, K. — WA4  
 Duan, G.-H. — TuA2  
 Dutto, Valerie — TuC4

Egan, A. — TuE2  
 Elton, D. J. — TuD2  
 Eng, L. E. — TuD3  
 Ershov, O. G. — MB5

Farrell, G. — TuE2  
 Feder, K. — WA6  
 Feng, J. — MA3, MA4  
 Field, Christopher T. — TuB4  
 Fields, Renny A. — TuB  
 Figiel, J. J. — TuD7  
 Fisher, M. A. — TuD2  
 Floyd, P. D. — TuD6  
 Forbes, D. V. — MC3, TuE14  
 Fox, R. W. — MB2

Gallion, P. — TuA2  
 Geib, K. M. — TuD7  
 Gorfinkel, V. B. — TuE1  
 Gupta, S. — TuC3

Haldar, M. K. — TuE3  
 Handa, Yuichi — TuA3  
 Harlow, M. J. — TuD2  
 Harnagel, Gary L. — TuB3, TuC1  
 Hartman, R. L. — WA1  
 Heath, L. — MC1  
 Hegarty, J. — TuE2  
 Hirono, T. — WA3  
 Hollberg, L. — MB2, MB4  
 Hopf, Daniel E. — TuB3  
 Hovde, D. Christian — MB1  
 Hsin, Wei — TuE4  
 Huang, Y.-Z. — TuD2  
 Hull, Robert — TuD7  
 Hunter, M. — MB2

Ikedo, Sotomitsu — TuA3

Jacquet, J. — TuA2  
 Jain, R. K. — TuC3  
 Jedral, L. — TuE10  
 Jiang, Ziping — TuE5  
 Jones, R. J. — TuC3

Kadota, Y. — WA5  
 Kane, Daniel J. — MB1  
 Khaydarov, A. V. — TuE6  
 Kishi, K. — WA5  
 Kjebon, O. — MA2  
 Koch, T. L. — WA4, WA6  
 Koifman, A. I. — TuE6  
 Koren, U. — WA4, WA6  
 Kozlovsky, V. I. — TuD1  
 Krainak, Michael A. — TuC4  
 Krysa, A. B. — TuD1  
 Kurokawa, Takashi — TuA1

Lammert, R. M. — MC3, TuE14  
 Landais, P. — TuA2  
 Lang, Robert J. — TuC1  
 Laughton, F. — TuE5  
 Lear, K. L. — TuD7  
 Lee, T. P. — WA2  
 Lee, Y. C. — TuE9  
 Leegwater, Jan A. — TuE7  
 Li, G. S. — TuD3  
 Lim, S. F. — TuD3  
 Lin, Ching-Fuh — TuE8  
 Lourdudoss, S. — MA2

MacDougal, Michael H. — TuD4  
 Majima, Masao — TuA3  
 Major, Jo — TuC1  
 Mannik, L. — TuE10  
 Marabella, Leonard J. — MC2  
 Marsh, J. H. — TuE1  
 Mart'yanova, I. V. — TuE6  
 Maruyama, Takeo — TuE13  
 Matsuda, Shin'ya — TuE13  
 Matsumoto, S. — WA5  
 McAdams, M. — WA3  
 McCall, M. W. — TuE5  
 Mehuis, David — TuC1  
 Mendis, F. V. C. — TuE3  
 Merz, J. L. — TuD6

Michalzik, Rainer — TuC6  
 Middlemast, I. — TuE15  
 Mikhailova, M. P. — MB5  
 Millar, Pamela S. — TuB3, TuB4, TuB5  
 Miller, B. I. — WA4, WA6  
 Moiseev, K. D. — MB5  
 Mori, H. — WA5  
 Morozova, N. D. — TuE9  
 Morton, Paul — MA  
 Moulton, Peter F. — MB  
 Mukherjee, A. — TuE11

Nabiev, R. F. — MB6  
 Nagarajan, Radhakrishnan — MA1  
 Nasibov, A. S. — TuD1  
 Nilsson, S. — MA2  
 Nonaka, Koji — TuA1  
 Nunoue, S. — TuE17

O'Brien, Stephen — TuC1, TuC4  
 O'Gorman, J. — TuE2  
 Oh, Daniel B. — MB1  
 Ohkawa, Masashi — TuE13  
 Ohlander, U. — MA2  
 Olsson, N. A. — WA1  
 Ono, Takeo — TuA3  
 Ohashi, H. — WA3  
 Osinski, Julian S. — TuC1  
 Osowski, M. L. — MC3  
 Ouchi, Toshihiko — TuA3

Paige, Mark E. — MB1  
 Parke, Ross — TuC1  
 Parker, M. A. — TuA4  
 Pentty, R. V. — TuE5  
 Perrin, S. D. — TuD2  
 Peters, M. G. — TuD5, TuD6  
 Petrov, K. — MB4  
 Pham, G. — TuA2  
 Phelan, P. — TuE2  
 Popov, Yu. M. — TuD1  
 Portnoi, E. L. — TuE1  
 Prokhorov, A. M. — TuD1

Rall, Jonathan A.R. — TuB1, TuB2  
 Ralston, John D. — TuC, TuC5  
 Raybon, G. — WA4  
 Reed, J. — TuD2  
 Rees, P. — TuE2  
 Reid, I. — TuD2  
 Ruda, H. E. — TuE10

Sahlen, O. — MA2  
 Sandusky, J. V. — TuE11  
 Sapia, Adalberto — TuE12  
 Sarma, J. — TuE15  
 Sasaki, T. — WA5  
 Sato, Takashi — TuE13  
 Schneider, Jr., R. P. — TuD7  
 Seki, S. — WA3  
 Shakouri, Ali — TuE16  
 Shcherbakov, E. A. — TuD1

Shibata, Kazunori — TuE13  
 Shimba, Minoru — TuE13  
 Shire, D. B. — TuA4  
 Shore, K. A. — TuE15  
 Shum, Frank — TuC1  
 Siegman, A. E. — TuC2  
 Silver, Joel A. — MB1  
 Simon, U. — MB4  
 Smith, G. M. — MC3, TuE14  
 Spencer, P. S. — TuE15  
 Stanton, Alan C. — MB1  
 Streubel, K. — MA2  
 Stutius, W. — MC1  
 Sugiura, H. — WA3  
 Sun, Xiaoli — TuB5  
 Sun, Yan — TuC2

Tachikawa, M. — WA5  
 Tang, C. L. — TuA4  
 Tennant, D. M. — WA6  
 Tezuka, T. — TuE17  
 Thayne, I. G. — TuE1  
 Thibeault, B. J. — TuD5  
 Tittel, F. — MB4  
 Toh, K. — TuD3  
 Trubenko, P. A. — TuD1  
 Tsang, H. K. — TuE5

Uchida, Mamoru — TuA3  
 Unger, Peter — TuC6

Wallin, J. — MA2  
 Walpole, J. N. — TuC3  
 Waltman, S. — MB4  
 Wang, J. — TuE3  
 Welch, David F. — TuC1  
 White, I. H. — TuE5  
 Wickes, H. J. — TuD2  
 Wieman, C. E. — MB3  
 Williamson, Richard — MC  
 Wilt, D. P. — WA1  
 Wipiejewski, T. — TuD5  
 Wong, S. — TuC2  
 Wood, C. S. — MB3

Xu, Yuanjian — TuE16

Yakovlev, Yu. P. — MB5  
 Yamada, T. — WA5  
 Yamamoto, Shigeki — TuE13  
 Yang, Gye Mo — TuD4, TuD8  
 Yariv, Amnon — MA3, MA4, TuE16  
 Yokoyama, K. — WA3  
 Yoshida, H. — TuE17  
 Young, D. B. — TuD5  
 Young, M. G. — WA4, WA6  
 Yu, Anthony W. — TuB3, TuC4  
 Yuen, W. — TuD3

Zah, C. E. — WA2  
 Zhao, B. — MA3, MA4





**SEMICONDUCTOR LASERS  
TECHNICAL PROGRAM COMMITTEE**

**Thomas M. Baer**, *General Chair*  
*Biometric Imaging*

**Thomas L. Koch**, *General Chair*  
*AT&T Bell Laboratories*

**Peter F. Moulton**, *Program Chair*  
*Schwartz Electro-Optics, Inc.*

**David F. Welch**, *Program Chair*  
*SDL, Inc.*

**Connie J. Chang-Hasnain**  
*Stanford University*

**P. Daniel Dapkus**  
*University of Southern California*

**Russ Dupuis**  
*University of Texas at Austin*

**Renny A. Fields**  
*Aerospace Corporation*

**Edward Gage**  
*Eastman Kodak Corporation*

**Leo William Hollberg**  
*National Institute of Standards and Technology*

**Paul Morton**  
*AT&T Bell Laboratories*

**Robert Olson**  
*Schwartz Electro-Optics, Inc.*

**John D. Ralston**  
*SDL, Inc.*

**Peter Roenpten**  
*IBM Research Division, Switzerland*

**Alan C. Stanton**  
*Southwest Sciences, Inc.*

**Wolfgang Stutius**  
*Polariod Corporation*

**Dick Williamson**  
*MIT Lincoln Laboratory*

**Mori Yoshifumi**  
*Sony Corporation, Japan*